Special Application of Bioactive Glass as Active Ingredient in Woundcare and Hemostasis

Thesis submitted

by

Payal Roy

For the Degree of

Doctor of Philosophy (Science)

Faculty of Science

Department of Life Science and Biotechnology
Jadavpur University
Kolkata, India
2024

Index No.: 139/21/life Sc./27

Thesis Title: Special application of bioactive glass as active ingredient in woundcare and hemostasis

Supervisor Name

Dr. Jui Chakraborty
Senior Principal Scientist
CSIR-Central Glass & Ceramic Research Institute
Jadavpur, Kolkata-700 032
India

Supervisor: Dr. Jui Chakraborty
Senior Principal Scientist
Bioceramics and Coating Division (BCCD)
CSIR-Central Glass and Ceramic Research Institute
Kolkata-700 032

CERTIFICATE FROM THE SUPERVISOR

This is to certify that the thesis entitled '**Special application of bioactive glass as active ingredient in woundcare and hemostasis'** submitted by Smt. Payal Roy (Index No.: 139/21/life Sc./27), who got her name registered having enrolment No. **SLSBT1113921**, **Dated: 06.12.2021**for the award of Ph.D. (Science) degree of Jadavpur University is absolutely based upon her own work under the supervision of the undersigned and that neither her thesis nor any part of the thesis has been submitted for any degree/ diploma or any other academic award anywhere before.

Jui Chakraborty
30/05/2024

(Signature of the Supervisor, date with official seal)
Dr. Jui Chakraborty
Senior Principal Scientist
Bioceramics and coating Division
CSIR-Central Glass and Ceramic Research Institute
Kolkata-700 032

Dr. (Mrs) J. CHAKRABORTY
SENIOR PRINCIPAL SCIENTIST
Central Glass & Ceramic Research Institute
(C.S.I.R., GOVT OF INDIA)
Jadavpur, Kolkata - 700 032

Declaration

I hereby declare that the work of 'Special application of bioactive glass as active ingredient in woundcare and hemostasis' was carried out by me under the supervision of Dr. Jui Chakraborty, Senior Principal Scientist, Bioceramics and Coating Division, CSIR-Central Glass and Ceramic Research Institute, Kolkata. This work is original and has not been submitted to anywhere in part or full for any other degree or diploma.

Payal Roy

(Payal Roy) 31.05.2024

Place: Kolkata

Date:

This Thesis is dedicated to my beloved Father, Late Sanjib Kumar Roy, may his memory forever be a comfort and a blessing

&

My dear Husband, Dr. Soumya Sarkar for his constant support

Acknowledgements

First and foremost, I am grateful to God, the Almighty, for granting me the strength and opportunity to undertake this life-changing journey of pursuing a PhD. I would like to extend my sincere thanks to all those who have supported and guided me throughout this endeavor.

I am deeply indebted to my supervisor, Dr. Jui Chakraborty, for her unwavering support and guidance. She not only welcomed me into her research group but also mentored me in developing my research and laboratory skills, as well as improving my writing skills for reviews and papers. Her dedication and assistance have been invaluable, and I credit her for much of the success of my work. Additionally, I am grateful to her for instilling in me a newfound appreciation for pets and nature, which has enriched my life beyond academia.

I would also like to thank Prof. Tapan Kumar Mandal, Head of the Department of Pharmacology and Toxicology, and Director of West Bengal University of Animal and Fishery Sciences, Kolkata, for his support in conducting the *in vivo* studies in animal models.

I am thankful to Prof. Parimal Karmakar (Chairperson), Department of Life Science and Biotechnology at Jadavpur University, Kolkata, and Dr. Soumi Sukla from TCG-CREST, Kolkata, for their insightful comments and suggestions during the Research Advisory Committee (RAC) meetings. Their input has significantly enhanced the quality of my work.

Special thanks to Dr. Vamsi Krishna Balla, Head of the Bioceramics and Coating Division (BCCD) at CSIR-Central Glass and Ceramic Research Institute, Kolkata, for his encouragement and for allowing me to use the division's facilities and for providing me with the freedom to conduct my research.

I am also grateful to Dr. (Mrs.) Suman Kumari Mishra, Director of CSIR-Central Glass and Ceramic Research Institute, Kolkata, for her valuable suggestions and cooperation throughout my research.

I extend my thanks to Dr. Samar Chakraborty, Head and Consultant Anaesthesiologist at AMRI Hospital, Kolkata, for generously providing various bacterial and fungal strains for my research.

I am grateful for the financial support from CSIR-HRDG, GOI, New Delhi, India, which has been instrumental in the completion of my PhD work.

I also want to acknowledge the valuable discussions with my seniors, Dr. Suman Saha and Sk. Hasanur Rahaman, as well as my junior, Rupam Saha, at BCCD, Kolkata. I am thankful to all my friends, juniors, seniors, and non-teaching staff at BCCD for their support and for the enjoyable moments we shared over the past four years.

I appreciate the assistance of all the staff members at the Central Characterization Facility, CSIR-CGCRI, Kolkata, for their help in characterizing different samples.

Lastly, I want to express my heartfelt gratitude to my late father, Late Sanjib Kumar Roy, for his blessings, and to my mother, Mrs. Mita Roy, my elder brother, Mr. Sumit Roy, and sister-in-law, Mrs. Sonali Roy and little nephew, Niladri Roy, as well as my in-laws, Mr. Sushanta Kumar Sarkar, Mrs. Sushmita Sarkar, Mr. Bimal Talukdar, and Mrs. Swapna Talukdar, for their constant support and blessings. I am also thankful to my husband, Dr. Soumya Sarkar, for his unwavering support, motivation, and enthusiasm throughout my PhD journey.

List of publications in peer reviewed journals

1. **Roy, Payal**, Rupam Saha, and Jui Chakraborty. "A novel composition of bioactive glass with potent haemostatic action and antibacterial competence." Ceramics International 49, no. 4 (2023): 6389-6400. **[IF: 5.2]**
2. **Roy, Payal**, Rupam Saha, Suman Saha, Debolina Dattaray, Tapan Kumar Mandal, Noha ElShazly, Mona K. Marei, and Jui Chakraborty. "Facile synthesis of electrospun antibacterial bioactive glass based micronanofibre (ABGmnf) for exalted wound healing: *in vitro* and *in vivo* studies." Materials Chemistry and Physics 305 (2023): 127874. **[IF: 4.6]**
3. **Roy, Payal**, Rupam Saha, Debolina Dattaray, Suman Saha, Tapan Kumar Mandal, Pooja Srivastava, and Jui Chakraborty. "Bioactive glass incorporated dressing matrix for rapid hemostatic action with antibacterial activity." Materials Chemistry and Physics 315 (2024): 128942. **[IF: 4.6]**
4. **Roy, Payal**, Rupam Saha, Justyna Pawlik, Zuzanna Samol, Michał Dziadek, Katarzyna Cholewa-Kowalska, and Jui Chakraborty. "Cobalt containing antimicrobial bioactive glass coated urinary catheter towards management of catheter associated urinary tract infection (CAUTI): Significant *in vitro* characterizations." Ceramics International 50, no. 7 (2024): 11625-11638. **[IF: 5.2]**
5. Saha, Rupam, **Payal Roy**, and Jui Chakraborty. "Synthesis and in-vitro evaluation of Zr-doped radiopaque bioactive glass: A possible biomaterial for endodontic application." Materials Chemistry and Physics (2024): 129416. **[IF: 4.6]**
6. **Roy, Payal,** Suman Saha, and Jui Chakraborty. "Looking into the possibilities of cure of the type 2 diabetes mellitus by nanoparticle-based RNAi and CRISPR-Cas9 system: A review." Journal of Drug Delivery Science and Technology 66 (2021): 102830. [**IF: 5.05**]
7. Saha, Suman, **Payal Roy**, and Jui Chakraborty. "Mesoporous silica-biopolymer-based systems in drug delivery applications." Tailor-Made and Functionalized Biopolymer Systems (2021): 313-347.

List of Patents

i) 'A bioactive glass composition and a process thereof', J.Chakraborty, P.Srivastava, **P. Roy**, S. Saha and R. Saha, App. No.202211057220, INDIA, Filed, published on 04.08.23 [DRDO]

ii) 'Antibacterial bioactive glass micronanofibre composition and process for preparation thereof', J. Chakraborty, S. Saha, **P. Roy**, R. Saha, App. No. 202111046618, INDIA, Filed, published on 14.04.23 [CSIR]

iii) 'In situ radiopaque bioactive glass and its composition thereof', J Chakraborty, R Saha, **P Roy**. Ref. No. 202211005734, App No. TEMP/E-1- 4985/2022-DEL, Dated: 02.02.2022, INDIA, Filed [CSIR]

iv) 'A method for the synthesis of a polymerceramic/bioactive glass composite material with biodegradable and antimicrobial properties for use as topsheet in female sanitary hygiene products and adult diapers' M. Majumdar, J. Chakraborty, S. Samanta, M. B. Narjinary, A. Banerjee, **P. Roy** and R. Saha, 2022, Indian patent, App. No. 202211028466, TEMP/E-1/26211/2022-DEL, published on 22.12.23 [CSIR]

List of Award/ Recognition/ Conference:

1. **1st Prize** for Best e-Poster Presentation, BIOCOM-2021, entitled 'Mesoporous antibacterial bioactive glass coated non-woven surgical cotton gauze-a novel haemostatic dressing material for profusely bleeding condition', **Payal Roy**, Suman Saha, Rupam Saha & Jui Chakraborty, held during 27-28 May, 2021

2. Participated in oral presentation at IvaCCT 2021, entitled 'A novel haemostatic dressing material impregnated with mesoporous antibacterial bioactive glass for profusely bleeding condition', Payal Roy, Rupam Saha & Jui Chakraborty; held during 13-14th December, 2021 [Virtual mode]

3. Participated in oral presentation at Glamics Fiesta, entitled 'A special application of novel antibacterial bioactive glass based micro-nanofibres as an active pharmaceutical ingredient in wound care', Payal Roy, Rupam Saha & Jui Chakraborty; held on 10.06.2022 at CSIR-CGCRI

4. Participated in Oral presentation at ICAGGC-2022, entitled 'Development of antibacterial bioactive glass based dressing with rapid hemostatic action'; Payal Roy, Rupam Saha and Jui Chakraborty, held during 23-25th August, 2022 at CSIR-CGCRI

5. **1st Prize** for the Best Poster Presentation, ICAGGC-2022, entitled 'Bioactive glass incorporated plexiglass bone cement: value addition for minimally invasive procedure for Osteoporotic Vertebral Compression Fracture (OVCF)', Rupam Saha, **Payal Roy** & Jui Chakraborty, held during 23-25th August, 2022 at CSIR-CGCRI

6. **1st Prize** for the Best Poster Presentation, ICAGGC-2022, entitled 'Biodegradable and anti-microbial ZnO/bioactive glass incorporated electrospunpolycaprolactone

membranes: synthesis, characterization and in-vitro studies', Arpita Banerjee, **Payal Roy**, ..& M. Majumder, held during 23-25th August, 2022 at CSIR-CGCRI

7. Participated in Oral presentation at International Conclave on Materials, Energy & Climate, 2022, entitled 'A novel antibacterial bioactive glass based micronanofibres as an active pharmaceutical ingredient in wound care', Payal Roy, held during 12-14th December, 2022 [Virtual mode].

8. **1st Prize for Best Poster Presentation** BIOCOM-2022, entitled 'A novel antibacterial bioactive glass based micronanofibres as an active pharmaceutical ingredient for chronic wound', **Payal Roy**, Rupam Saha & Jui Chakraborty, held during 20th December, 2022

9. **Won Best Poster presentation award** in 30th Annual Conference of Indian Pharmacological Society, West Bengal & East Zone Colloquium entitled 'A novel antibacterial bioactive glass based micronanofibres: can heal the wound?', **Payal Roy** et al., held on 11th March, 2023 at WBUAFS, Kolkata.

Membership

Materials Research Society of India (MRSI): Life Membership No. LMB3565

The Physiological Society of India (PSI): Life Membership ID PSI-LM888

List of tables

List of figures

Fig. 5.1. [A] XRD pattern of the as-prepared ABGmnf based wound care matrix.

[B] FTIR spectra of the ABGmnf based wound care matrix showing characteristic vibrations consigned to silicate structural groups and associated with Si-O-B, B-O bonds. ['ν' and 'δ' denotes stretching and bending vibrations, respectively] [Roy et al., 2023a].

Fig. 5.2. (a) TG-DSC curve of AgBG glass powder, calcined at 650^0C.

(b) FESEM image of AgBG glass powder.

Fig. 5.3. (a) Nitrogen adsorption/desorption isotherm for AgBG, (b) BJH for AgBG, and (c) Zeta potential measurement for AgBG.

Fig. 5.4. shows angle of repose of AgBG.

Fig. 5.5. [A] XRD pattern of the PVP matrix

[B] XRD pattern of the as-prepared ABGmnf woundcare matrix.

Fig. 5.6. (a) FTIR spectra of the PVP matrix and ABGmnf based wound care matrix heat treated at 600^oC showing characteristic vibrations consigned to silicate structural groups and associated with Si-O-B, B-O bonds and PVP related groups.

(b) TG-DSC plot of as-prepared ABGmnf based wound care matrix [AgBG was calcined at 600^oC].

Fig. 5.7. FESEM image (scale bar 10μm) shows the collection of (a) PVP fibre and (b) ABGmnf based wound care matrix with micro-nano ranged diameters of the fibres.

Fig. 5.8. Stress-strain curve of ABGmnf based wound care matrix and PVP matrix.

Fig. 5.9. The solubility assessment of ABGmnf based wound care matrix.

Fig. 5.10. Viability of NIH3T3 cells after 24, 48 and 72h extracts achieved from AgBG. Data shown is mean ± SD of three independent experiments.

Fig. 5.11. *In vitro* cytotoxicity assay of ABGmnf based wound care matrix showing excellent cell viability, using NIH3T3 cell line.

Fig. 5.12. Fluorescence images of cells (a) without any treatment (act as control) and (b) treated with ABGmnf based woundcare matrix extract and incubated for 24h and 72h. The images showed no adverse effects on the cellular morphology after treatment. Magnification: 10X and Scale bar: 50μm. (c) The cellular morphology was showed in higher magnification (20X) and scale bar: 20μm.

Fig. 5.13. Representative optical image of *in vitro* 2D wound healing assay showing higher cell migration when treated with ABGmnf based wound care matrix compared to the control group. Data shown is mean ± SD of three independent experiments ($p < 0.05$).

Fig. 5.14. Antibacterial activity of ABGmnf based wound care matrix (PVP-AgBG, showing ZOI) compared with control, pure PVP matrix (no ZOI) after 24h incubation on agar plate at 37^{o}C against (a) *S. aureus* and (b) *E. coli*.

Fig. 5.15. Determine the Minimum Inhibitory Concentration (MIC) of ABGmnf based wound care matrix's active ingredient on both Gram-positive strains (*S. aureus* and *S. pneumoniae*) and the Gram-negative strain (*P. aeruginosa*), in comparison to gentamicin [Roy et al., 2023a].

Fig. 5.16. (a) Macroscopic examination reveals the absence of any immune response from the host throughout the observation period. (b) The assessment involves a quantitative analysis of the concentration of the proinflammatory cytokine TNF-α. (c) Similarly, the IL-6 concentration is subjected to quantitative analysis [Roy et al., 2023a].

Fig. 5.17. Histological examinations were conducted on sections of the heart, liver, lung, and kidney (labeled A-H) in Wistar rats, with both control and ABGmnf based wound care matrix-treated groups (n>3) [Roy et al., 2023a].

Fig. 5.18. Serum concentration profile of Ca released from AgBG of ABGmnf based wound care matrix. All values are in mean ±SD (n=3/group) [$p < 0.05$].

Fig. 5.19. The tissue calcium concentration (in ppm) in different time points after application of ABGmnf based wound care matrix and compared to the control.

Fig. 5.20. Cascade of full thickness skin wound repair in rats at days 0, 7 and at day 14. Wound treated with ABGmnf based wound care matrix had restored the same texture of normal skin

unlike the wound treated with betadine and untreated wound, also it maintained a uniform wound edges throughout the follow up period. The statistical analysis of the % of wound closure in different groups at 0, 7, 10 and 14 days postoperative. All values are demonstrated as mean ± SD (triplicated), ($p \leq 0.05$).

Fig. 5.21. Histological analyses the sections of heart, kidney, liver, lung and kidney in control, betadine and ABGmnf based wound care matrix treated wistar rats (n=3).

Fig. 5.22 (a) XRD pattern of as-prepared Al-BAG powder, calcined at 650^0C.
(b)FTIR spectra of as-prepared Al-BAG calcined at 650^oC and bioactive glass.
(c) TG-DSC plot of as-prepared Al-BAG, calcined at 650^0C.
(d) Displays the N_2 adsorption-desorption isotherm and its associated pore size distribution for Al-BAG [inset of 5.22(d)].
(e) Particle size distribution measurement of Al-BAG.
Fig. 5.23. Image (a) depicts the Scanning Electron Microscope (SEM) image, while (b) represents the Energy Dispersive X-ray (EDX) pattern of the as-prepared Al-BAG [Roy et al., 2023b].

Fig. 5.24. The levels of (a) Ca^{2+}, (b) Al^{3+} and (c) Zn^{2+} were monitored over time during the initial 24 hours in solutions with two different pH values, 5.2 and 7.4. Additionally, (d) illustrates the variation in weight loss of Al-BAG samples under the aforementioned pH conditions [Roy et al., 2023b].

Fig. 5.25 Microscopic pictures of NIH3T3 cells (40X magnification) cultured with the Al-BAG sample are shown for different durations: (a) 24 hours, (b) 48 hours, and (c) 72 hours. (d) illustrates the viability of NIH3T3 cells after exposure to extracts from Al-BAG for 1, 2, and 3 days. The data, obtained through the MTT assay, did not show any statistically significant differences ($p > 0.05$) [Roy et al., 2023b].

Fig. 5.26 Fluorescence images of cells (a) without any treatment (act as control) and (b) treated with Al-BAG extract and incubated for 24h and 72h. The images showed no adverse effects on the cellular morphology after treatment. Magnification: 10X and Scale bar: 50μm. (c) The cellular morphology was showed in higher magnification (20X) and scale bar: 20μm.

Fig. 5.27 A comparison of turbidity was made between McFarland standard 0.5 (a) and a suspension of *Staphylococcus aureus* (b). The bacteriostatic effectiveness of Al-BAG against *S. aureus* is depicted in (c).

Fig. 5.28 presents the results: (a) a line of best fit was created by making 100, 50, 25, 10, and 1% dilutions, and (b) the hemolysis percentage standard error of the mean for the samples. Absorbance values were matched with the calibration curve to determine hemolysis percentage measurements, demonstrating a statistically significant decrease in hemolysis percentage for Al-BAG compared to PBS only (i.e., no treatment) with a p-value greater than 0.05 [Roy et al., 2023b].

Fig. 5.29 illustrates the absorption of Al-BAG samples in both PBS and blood at two distinct time intervals (1 and 2 hours). The findings indicate a higher absorption capacity in blood compared to PBS, and these differences are statistically significant with a p-value greater than 0.05 [Roy et al., 2023b].

Fig. 5.30 (a) The blood clot formed on Al-BAG surface, captured by a digital camera. (b) Quantitative results of thrombus formation after different incubation times [Roy et al., 2023b].

(c) PT and (d) aPTT results for the sample, observed statistically significant reduction (n=3, $p>0.05$) in PT specially and aPTT as well compared to control [Roy et al., 2023b].

Fig. 5.31 Thrombin generation over time as measured by the levels of thrombin-antithrombin (TAT) complex, $p<0.05$ by Al-BAG compared to control, n=4 [Roy et al., 2023b].

Fig. 5.32 (a) represents the clot formation time, contact with whole blood in the presence of Al-BAG as well as control (n=5).

(b) SEM micrograph exhibit red blood cells (RBCs) and platelets adhered onto the Al-BAG pellet surface, scale bar represents 20 μm and 3000x magnification.

Fig. 5.33 (A) Quantification of platelet adhesion on the Al-BAG surface. (Represented a significant difference, $p > 0.05$). (B), (C) and (D) SEM images illustrating platelet adhesion on the Al-BAG surface at 15, 30, and 60 min (magnification 10000X and scale bar 8 μm).The

arrows indicate the dendrites connecting the platelets. SD=Spread dendritic, S=Spreading, FS=Fully spread [Roy et al., 2024a].

Fig. 5.34 SEM image of erythrocyte adhesion [yellow arrow= RBCs] [Scale bar= 5µm, Mag=5 K X].

SEM image of a stable hemostatic blood clot, composed of platelet aggregates, erythrocytes, and leukocytes entrapped in the fibrin network [Scale bar= 2µm, Mag= 15 K X].

SEM image of fibrin network [Scale bar= 1µm, Mag= 30 K X].

Fig. 5.35 Effect of the Al-BAG on blood clotting rates, as calculated by absorbance of haemoglobin from lysed untrapped RBCs ($p< 0.05$) [Roy et al., 2024a].

Fig. 5.36 (a) The images depict the mixing of the test material with an appropriate vehicle at a specific ratio, which is then applied to the shaved skin area for the acute dermal study. (b) The images illustrate that the test material does not induce any indications of dermal toxicity after specific time intervals [Roy et al., 2023b].

Fig. 5.37 Histological examinations were conducted on sections of lung, liver, heart, kidney, and skin in both Al-BAG treated and control Wistar rats ($n>5$) [Roy et al., 2023b].

Fig. 5.38 (A) and (B) Photographic images illustrating the surgical process for creating a femoral artery injury. (C) Evaluation of the percentage of blood loss. (D) Application of Al-BAG, monitoring the time for hemostasis/clotting, and subsequent estimation of blood loss. (E) Graphical representation of clotting time/time for hemostasis. (F) Graphical representation of the percentage of blood loss before and after the application of Al-BAG ($p < 0.05$) [Roy et al., 2023b].

Abstract

Index No.: 139/21/life Sc./27

Thesis Title: Special application of bioactive glass as active ingredient in woundcare and hemostasis

Recently, bioactive glass (BG) has emerged as a promising solution for treating injuries such as diabetic and venous ulcers. BG release the therapeutic ions that helps in fibrin clot formation by aid in platelet aggregation, supporting the coagulation cascade and helping in the regeneration of soft tissue.

In the Part A of this thesis, we synthesized a binary glass composition (named, AgBG) containing varying mol% of SiO_2, CaO, B_2O_3, and Ag_2O using the sol-gel technique, followed by electrospinning with an FDA-approved polymer to fabricate a fibrous matrix named ABGmnf based wound care matrix. We then conducted various material characterization techniques including XRD, FTIR, TG-DSC, FESEM, BET, angle of repose, zeta potential, solubility assessment, and mechanical property testing. Biological studies included *in vitro* cytocompatibility, immunofluorescence staining for cellular proliferation and morphology, 2D wound healing assays, and antibacterial experiments to estimate zone of inhibition (ZOI) and determines minimum inhibitory concentration (MIC) using gram positive and gram negative strains. The *in vitro* material characterizations and biological studies confirmed the successful fabrication of ABGmnf based wound care matrix, its cytocompatibility, and antibacterial activity. Subsequently, *in vivo* pharmacokinetic and biodistribution studies along with biocompatibility study by assessing IL-6 and TNF-α confirmed its safety profile. This was followed by *in vivo* wound healing assay, which exhibited fast closure of wound, and histological assessment of various vital organs. These findings suggest that compositions like AgBG as ABGmnf based wound care matrix have great potential in the wound care market and could pave the way for new directions in tissue engineering.

In the Part B of the thesis, we report a unique composition of bioactive glass, 70 SiO_2: (30-x-y) CaO: x.Al_2O_3: y.ZnO, where x=10-18 mole% and y= 0-8 mole%, exhibiting haemostatic property as well as antibacterial activity. The as-prepared glass was characterized using XRD, SEM-EDX, FTIR, BET and TG-DSC along with *in vitro* degradation study and biological studies e.g., cytocompatibility, haemocompatibility, *in vitro* thrombus formation, *in vitro* blood absorption capacity, blood coagulation assays (PT, aPTT), erythrocyte adhesion assay, measuring blood clotting index (BCI), *in vitro* antibacterial assay against *S. aureus* as well as *in-vivo* acute dermal toxicity followed by histopathological analysis) and *in vivo* haemostasis efficacy were undertaken. The novel bioactive glass composition exhibits promises to be an efficient haemostatic agent with antibacterial activity.

Candidate's signature:

Payal Roy
30.05.2024

Forwarded by the Supervisor:

Jui Chakraborty
30/05/2024

Dr. (Mrs) J. CHAKRABORTY
SENIOR PRINCIPAL SCIENTIST
Central Glass & Ceramic Research Institute
(C.S.I.R., GOVT OF INDIA)
Jadavpur, Kolkata - 700 032

CONTENT

Chapter 1: Introduction

Chapter 2: Literature survey

Chapter 3: Objectives

Chapter 4: Experimental procedures

Chapter 5: Results and Discussions

Chapter 6: Conclusions

Chapter 7: Bibliography

Chapter 1: Introduction

1.1.Introduction:

Wound healing is a highly orchestrated and dynamic biological process that involves a sequence of intricate events aimed at repairing damaged tissue. The process can be broadly divided into four overlapping phases: hemostasis, inflammation, proliferation, and remodeling [Sun et al., 2014; Rodrigues et al., 2019]. Hemostasis initiates immediately after injury, involving vasoconstriction to reduce blood flow, platelet activation and aggregation to form a temporary plug, and the activation of the coagulation cascade to generate fibrin, which stabilizes the platelet plug and forms a clot to prevent excessive bleeding [Gale et al., 2011; Meddahi-Pelle et al., 2014 & Heher et al., 2018]. In the inflammatory phase, immune cells such as neutrophils and macrophages infiltrate the wound site to clear debris, pathogens, and damaged cells, releasing cytokines and growth factors that trigger the subsequent phases [Han et al., 2017]. During proliferation, fibroblasts play a crucial role by synthesizing collagen, the primary component of the extracellular matrix, which forms a scaffold for migrating cells [Gonzalez et al., 2016]. Formation of new blood vessels, or angiogenesis to supply oxygen and nutrients to the growing tissue. The remodeling phase involves the gradual realignment and remodeling of collagen fibers, as well as the removal of excess tissue [Schultz et al., 2003]. This phase can take months to years and results in increased tissue strength. The orchestrated interplay of cell types, growth factors, and signaling molecules is essential for effective wound healing, as dysregulation can lead to chronic wounds or excessive scarring. Understanding the molecular and cellular mechanisms underlying wound healing and hemostasis is crucial for developing therapies that enhance healing outcomes and promote tissue regeneration and to stop profusely bleeding condition.

1.2.Exploring the Demand for Innovative Materials in Tissue regeneration and Wound Healing: The Role of Bioactive Glasses

In recent years, bioactive glasses have emerged as a promising solution for wound healing. In tissue engineering, scaffolds, along with cells and ions, are used to aid tissue regeneration. These biomaterials can be used in the body without rejection and provide a surface for cell proliferation, facilitating tissue formation.

While research on bioactive glasses has primarily focused on bone healing, their unique ability to bond with bone was first demonstrated by Professor Larry Hench in 1969 with the development of Bioglass® [Hench, 2006]. This original composition, Bioglass 45S5, contains 46.1 mol. % SiO_2, 24.4 mol. % Na_2O, 26.9 mol. % CaO, and 2.6 mol. % P_2O_5. It has been commercially used as synthetic bone grafts (e.g., NovaBone® and Perioglas®) and as an ingredient in toothpaste for hypersensitivity (e.g., GlaxoSmithKline, UK). Since then, many other bioactive glass compositions have been developed [Rodriguex et al., 2008].

One significant advantage of bioactive glasses is their compositional flexibility. They can be produced using either a melt-derived or sol-gel derived route, allowing for the addition of different metal oxides that offer various beneficial properties for wound healing and other applications. One of the key advantages of these bioactive glasses is their potential to stimulate angiogenesis, the formation of new blood vessels, which is crucial for the development of a vascular network within tissue engineering scaffolds. Researchers have explored coating bioactive glasses like 45S5 with vascular endothelial growth factor (VEGF) to enhance their angiogenic properties. Studies have shown that 45S5, when coated with VEGF, can increase the vascular network inside a scaffold, making it a promising material for enhancing tissue regeneration in soft tissue engineering [Chen et al., 2006; Jones J R, 2013].

Furthermore, research has demonstrated that 45S5 bioactive glass is angiogenic even in low concentrations. It has been suggested that it may upregulate VEGF production from soluble reaction products when co-cultured with human microvascular endothelial cells *in vitro*. These findings make bioactive glasses like 45S5 intriguing materials for soft tissue engineering applications, particularly in wound care, where their angiogenic properties could help promote faster and more efficient wound healing [Day et al., 2005; Gorustovich et al., 2010 & Mao et al., 2015]. Numerous studies have shown that bioactive ions like Ca^{2+} and $SiO4^{4-}$ released from bioactive glasses (BG) can influence cell fate and interactions. These ions activate paracrine effects during wound healing, such as enhancing interactions between human dermal fibroblasts and human umbilical vein endothelial cells. This, in turn, promotes vascularization and the deposition of extracellular matrix proteins [Xu et al., 2017 & Kong et al., 2018].

Also, bioactive glass has been shown to possess antimicrobial properties, making it effective against a wide range of pathogens [Hu et al., 2009; da Silva Buriti et al., 2021]. This property is

particularly beneficial in wound care, as it helps prevent infections and promotes faster healing. Additionally, bioactive glass can absorb excess exudate from wounds, maintaining a moist environment that is conducive to healing [Homaeigohar et al., 2022].

Severe blood loss, known as exsanguination, is a significant contributor to mortality globally. Bioactive glasses (BGs) are increasingly recognized as effective hemostatic agents. They have shown promise in enhancing the activation of the intrinsic pathway of blood coagulation, making them valuable candidates for managing bleeding. Interestingly, bioactive glass, a silicate-based biodegradable material, serves a dual function in hemostasis. The calcium ions released from bioactive glass act as cofactors, aiding in the alignment of protein assemblies and the activation of enzymes involved in fibrin production and coagulation cascades. Additionally, the high surface area of bioactive glass is crucial for effectively facilitating thrombosis [Ostomel et al., 2006].

Overall, the special applications of bioactive glass in wound care and hemostasis highlight its immense potential in modern medicine. As researchers continue to explore its capabilities and refine its formulations, bioactive glass is poised to revolutionize the treatment of wounds and bleeding disorders, offering patients faster healing, reduced complications, and improved outcomes.

1.3.Background

A. The Cascade of Wound Healing

The wound healing cascade denotes a series of meticulously orchestrated physiological processes set in motion in response to tissue injury, with the ultimate goal of repairing damage and reinstating tissue integrity. This intricate sequence encompasses four distinct yet interconnected phases: hemostasis, inflammation, proliferation, and remodeling [Sun et al., 2014 & Rodrigues et al., 2019].

a. Hemostasis:

The hemostasis phase unfolds in two primary components—primary and secondary hemostasis—both swiftly activated in the immediate aftermath of an injury [Gale et al., 2011]. Initially, primary hemostasis initiates, involving vasoconstriction to minimize blood loss and the

formation of an initial platelet plug through the aggregation of platelets within the bloodstream [Broughton et al., 2006]. This platelet plug serves as the initial barrier to staunch bleeding [Schultz et al., 2003]. Subsequently, secondary hemostasis engages, working towards the formation of a fibrin clot that definitively arrests bleeding. The extrinsic coagulation pathway is promptly set in motion by tissue factors released from damaged endothelial cells, triggering a swift release of thrombin [Witte et al., 1997]. Concurrently, the intrinsic coagulation pathway is activated through the initiation of Factor XII, which occurs upon exposure of endothelial collagen due to endothelial damage [Schultz et al., 2003]. This pathway continues thrombin release once the extrinsic pathway deactivates. Thrombin plays a vital role by converting fibrinogen into fibrin, which then binds to the platelet plug. The resulting clot acts as a scaffold, facilitating the attachment of immune cells, endothelial cells, fibroblasts, growth factors, and cytokines [Schultz et al., 2003].

b. Inflammation:

After the hemostasis phase, the early stage of inflammation begins around 24-48 hours post-injury. This phase is marked by the migration of leukocytes, especially neutrophils, to the wound area. The clot formation increases vascular permeability, allowing leukocytes to enter the clot and eliminate pathogens, transforming them into exudates [Young et al., 2011; Broughton et al., 2006 & Han et al., 2017]. Neutrophils also release proteases and reactive oxygen/nitrogen species (ROS/RNS), aiding in tissue degradation [Schultz et al., 2003; Wu et al., 2018]. This stage creates a scaffold for cell migration and proliferation. Reactive oxygen species (ROS) such as hydroxyls, superoxide anions, and hydrogen peroxide are produced during cellular activities and increase during inflammation, influencing cellular responses [Dunnill et al., 2017]. ROS levels regulate proliferation, inflammation, and apoptosis. Reactive nitrogen species (RNS), like nitrogen oxide (NO), have functions similar to ROS but do not regulate vasoconstriction. In later inflammation, macrophages take over, clearing debris and producing proteases and ROS/RNS [Broughton et al., 2006; Bylund et al., 2014]. Macrophages also stimulate cytokines and growth factors, promoting inflammatory or proliferative responses [Dunnill et al., 2017; Raja et al., 2007; Shen et al., 2009 & Trachootham et al., 2008]. In the anti-inflammatory phase, macrophages favor the M2 phenotype [Koh et al., 2011], reducing inflammatory cytokines and increasing anti-inflammatory cytokines [Suzuma et al., 1998 & Gonzalez et al., 2016].

Macrophages also stimulate fibroblast proliferation [Riedel et al., 2007 & Kiritsi et al., 2018], which becomes an alternative source of cytokines and growth factors, facilitating the subsequent proliferation phase[Barrientos et al., 2008; Kiritsi et al., 2018 & Battegay et al., 1994].

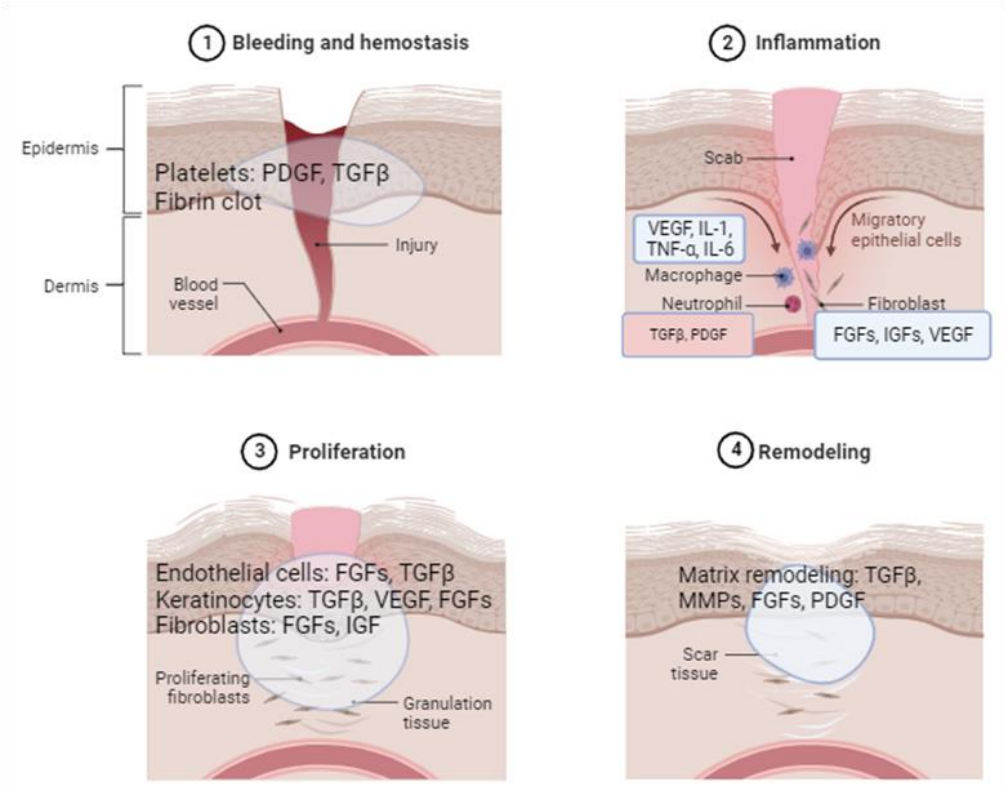

Fig. 1.1: Schematic representation of the wound healing cascade

c. Proliferation:

The proliferation phase begins once the wound is cleaned, providing a surface for fibroblasts to attach. It overlaps with the inflammation phase and lasts about three weeks, involving angiogenesis, re-epithelialization, and extracellular matrix (ECM) deposition.

Angiogenesis: Triggered by low oxygen levels leading to increased expression of Hypoxia-inducible Factor-1α (HIF-1α) [Riedel et al., 2007 & Kiritsi et al., 2018], angiogenesis involves the migration and proliferation of endothelial cells to repair and create blood vessels. Factors like VEGF, FGF2, TGF, KGF, PDGF, and TNF-α promote angiogenesis and stabilize the vasculature [Barrientos et al., 2008; Kiritsi et al., 2018 & Battegay et al., 1994].

Re-epithelialization: This process starts with the proliferation of epithelial cells at the wound edge, followed by migration to cover the wound [Broughton et al., 2006; Young et al., 2011]. Growth factors like EGF, KGF, and TGF-β [Grazul-Bilska et al., 2003; Fan et al., 2006 & Amendt et al. 1998] stimulate keratinocyte proliferation and migration [Ando et al., 1993], while factors like PDGF, IL-1, and IL-6 indirectly enhance re-epithelialization [Barrientos et al., 2008].

ECM Deposition: Fibroblasts become active and secrete ECM proteins like collagen, fibronectin, and hyaluronan [Schultz et al., 2003] in response to TGF-β and PDGF [Witte et al., 1997; Broughton et al., 2006 & Meckmong et al. 2008]. This forms a temporary matrix called granulation tissue, which matures over time. Wound contraction, signaling the end of the proliferation phase, starts around seven days after injury [Young et al., 2011].

d. Remodeling:

The remodeling phase activates following the initial wound closure, aligning with ongoing processes of ECM production and myofibroblast differentiation [Schultz et al., 2003]. During this phase, the balance between ECM production and degradation occurs, along with fibroblast apoptosis and the elimination of initial capillaries [Schultz et al., 2003]. Collagen and other ECM components reorganize, adopting a more aligned structure. Comprehensive wound regeneration is achieved, but the tissue never fully regains the same strength and functionality as normal tissue. Only around 50% recovery occurs within three months, and approximately 60-70% is achieved over the long term [Young et al., 2011 & Frykberg et al., 2015]. Excessive secretion of TGF-β, along with other contributors such as CTGF, PDGF, and IL-4, poses a risk of scarring [Branton et al., 1999]. Scarring can manifest as hypertrophic scars or keloids, both functionally impaired and susceptible to recurrent trauma, viral infections, and even the development of malignancies [Friedman et al., 2013 & Sun et al., 2011].

B. **Hemostasis**

Hemostasis is the complex physiological process that the human body utilizes to stop bleeding and maintain vascular integrity when blood vessels are injured. It involves a series of interrelated steps and biochemical reactions, collectively known as the hemostasis cascade [Hoffman et al., 2001 & Versteeg et al., 2013]. The cascade consists of three primary phases:

vascular phase, primary hemostasis, and secondary hemostasis. Here's an overview of each phase:

Vascular Phase:

The first response to blood vessel injury is vasoconstriction, which reduces blood flow to the site of injury [Waugh et al., 2001]. Endothelial cells that line the blood vessels release substances like endothelin and thromboxane A2 to help constrict the vessel [Sherwood et al., 2016]. Additionally, the endothelial cells become sticky and release von Willebrand factor (vWF), which plays a role in platelet adhesion [Atluri et al., 2006].

Primary Hemostasis:

This phase involves the formation of a temporary platelet plug at the site of injury. Platelets, which are small cell fragments in the blood, play a crucial role in primary hemostasis [Waugh et al., 2001]. When exposed to collagen and vWF from the damaged endothelium, platelets adhere to the site of injury. This adherence activates the platelets, causing them to change shape and release granules containing factors that enhance platelet aggregation [Ruggeri et al., 1999]. Platelet aggregation results in the formation of a plug that temporarily seals the damaged vessel [Martini et al., 2018].

Secondary Hemostasis:

Secondary hemostasis is a more complex phase involving a cascade of enzymatic reactions that lead to the formation of a stable blood clot. It primarily occurs through the coagulation cascade, which can be divided into the intrinsic and extrinsic pathways.

Intrinsic Pathway: Triggered when blood comes into contact with exposed collagen within the damaged blood vessel. This pathway involves factors VIII, IX, XI, and XII.

Extrinsic Pathway: The extrinsic pathway requires tissue factor, which is located in the tissue adventitia and comes in contact with blood only after vascular injury [Maynard et al., 1975, 1977; Weiss et al., 1989, Wilcox et al., 1989]. Activated by tissue factor (also known as factor III), which is released from injured tissues. This pathway involves factors VII, X, and the common pathway.

Both pathways converge into a common pathway that ultimately leads to the activation of factor X. Activated factor X converts prothrombin into thrombin in the presence of calcium ions and other cofactors. Thrombin, in turn, converts soluble fibrinogen into insoluble strands of fibrin, forming a mesh that traps blood cells to create a stable clot. The clotting process is carefully regulated by anticoagulant factors to prevent excessive clot formation.

Clot Retraction and Repair:

After the stable clot is formed, it undergoes clot retraction, where the fibrin strands contract and pull the edges of the broken vessel closer together. This process helps to minimize the size of the damaged area and promotes healing [Nurden A T, 2023].

Fibrinolysis:

Once the injury is repaired, the body initiates fibrinolysis, a process that gradually dissolves the clot. Plasmin, an enzyme, breaks down fibrin strands into soluble fragments, allowing the clot to be gradually removed [Kwaan H C., 2014; Hvan C L., 2023].

Hemostasis is a finely balanced process involving various factors and mechanisms to ensure that bleeding stops when necessary, but also to prevent excessive clotting within the bloodstream. Disruptions in this balance can lead to bleeding disorders or thrombotic conditions.

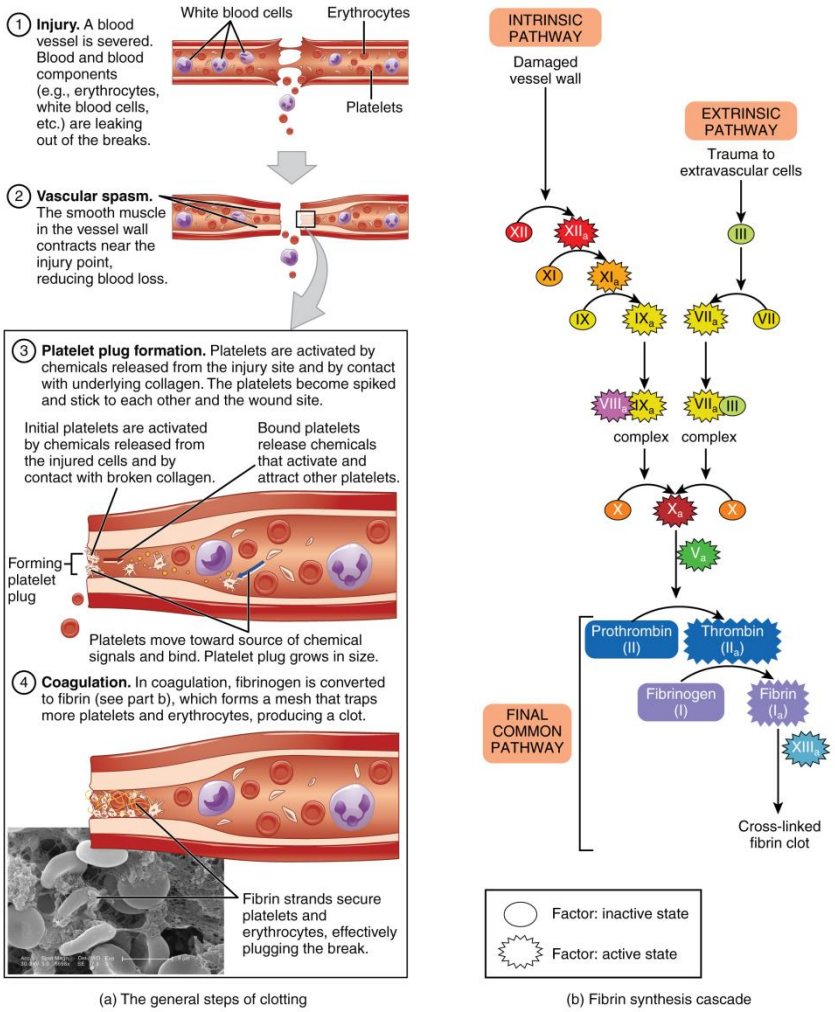

Fig. 1.2: Schematic representation of the coagulation cascade.

1.4.Brief description of the material under discussion:

Normal wound healing follows a four-stage process, and any disruption in these stages can lead to chronic wounds characterized by bacterial colonization, reduced blood supply, and weakened immune responses, causing significant health issues. Current clinical treatments for such chronic wounds primarily focus on protection but often fall short in promoting actual healing (Gao et al., 2021).

Bioactive glasses (BGs) are currently under intense research scrutiny due to their potential in facilitating soft tissue regeneration. They have been shown to enhance the migration of fibroblasts, stimulate the secretion of various growth factors, and reorganize the extracellular matrix [Tang et al., 2021]. BGs can also promote neovascularization by upregulating the

expression of angiogenic genes and facilitating gap junction formation in human umbilical vein endothelial cells (HUVECs).

Wound healing presents significant challenges in the medical field, spanning diverse clinical scenarios such as skin regeneration, chronic wounds (e.g., non-healing diabetic ulcers), mucous membrane damage, and the utilization of surgical sutures [Holl et al., 2021; Ding et al., 2022]. The skin serves a dual role in safeguarding the body from pathogens and maintaining bodily equilibrium. When the skin is injured, it is vital to promptly cover the affected area with a dressing that can establish a slightly moist environment, prevent infections, alleviate pain, and manage excess fluids [Ding et al., 2022].

In an intriguing animal study conducted by Gillete et al., the researchers explored the effects of incorporating bioactive glass (BAG) particulates into incisions during the healing of fully sutured, full-thickness skin wounds in dogs. Interestingly, the introduction of these glass particles into soft tissues did not induce a severe inflammatory response. Instead, it initially resulted in an increase in histological signs of inflammation, which gradually diminished over time. Moreover, at the 5-day mark, wounds treated with bioactive glass exhibited significantly higher subcutaneous breaking strength compared to control wounds. This suggests that bioactive glass may offer advantages in situations where early wound strength is crucial [Gillete et al., 2001].

In the field of wound healing, scientists have extensively explored the potential of specific metallic cations to act as antibacterial agents, providing an alternative to traditional antibiotics that may contribute to bacterial resistance. Bioactive glass proves valuable in this pursuit as it can be enriched with various metal oxides, enabling the controlled release of therapeutic ions directly at the wound site. Gallium (Ga), silver (Ag), and copper (Cu) have been studied for their antibacterial properties when incorporated into silicate and phosphate glasses [Pawar and Shinde, 2024].

For instance, even a modest concentration of 1 mol% of Ga_2O_3 in a phosphate glass has demonstrated effectiveness in delivering potent antibacterial effects through the gradual release of Ga^{3+} ions [Valappil et al., 2008; Valappil et al., 2009]. Similarly, silver has shown its ability to support the healing of sterile skin wounds by reducing inflammatory and granulation tissue

phases [Lansdown et al., 1997] while also exhibiting bactericidal action by damaging bacterial RNA and DNA [Lansdown et al., 2005]. The inclusion of 3 wt% Ag_2O in silicate glass has imparted antimicrobial properties without compromising the material's bioactivity [Bellantone et al., 2002a, Bellantone et al., 2002b]. *In vitro* studies have highlighted the antibacterial and antifungal effects of silver-coated glass particles. These principles have been applied to the development of surgical sutures that integrate bioactive and antibacterial components, resulting in versatile composite materials suitable for advancing wound healing applications.

Researchers have explored the clinical applications of bioactive glass (BG) for the healing of oral mucosal tissue [Stoor et al., 1998]. For instance, an implant made of S53P4 glass demonstrated strong and relatively fast antimicrobial properties, effectively inhibiting the growth of various oral pathogens. These granules and disks were successfully employed for closure in most cases, with no issues of implant extrusion or infections reported [Stoor et al., 1999]. Furthermore, these glass materials showed promise in treating atrophic rhinitis, effectively restoring normal to mucosal membranes. Additionally, certain commercial products containing silver-doped phosphate glass, such as wound care film dressings and tropical powders, are already available on the market, providing extended infection control benefits [Stoor et al., 2001].

The literature has conflicting findings regarding the anti-inflammatory effects of bioactive glasses (BGs). Some studies suggest that certain BGs, like sol-gel-derived SiO_2-P_2O_5-CaO BGs and bioactive glass-ceramics, can induce inflammation by stimulating macrophage proliferation. For example, the 45S5 BG was found to increase the expression of pro-inflammatory factors such as TNF-α and TNF-α-mRNAs in peritoneal macrophages and monocytes [Bosetti et al., 2002]. Additionally, the hydroxycarbonate apatite (HCA) formed from BG dissolution products can contribute to inflammation by up-regulating interleukins (IL) like IL-1, TNF-α, IL-6, and IL-8. However, other studies suggest that certain BGs, including 45S5, exhibit anti-inflammatory properties. Treatment with 45S5 was shown to significantly decrease IL-6 levels in macrophages and monocytes, with minimal changes in TNF-α and IL-10 [Bosetti et al., 2002; Zheng et al., 2021]. 45S5 BGs were also reported to activate macrophages toward the anti-inflammatory M2 phenotype, leading to a decrease in IL-1 and TNF-α expression and an increase in anti-inflammatory factors like IL-10, VEGF, FGF-2, and TGF-β. The effect of BGs on macrophage response depends on the BG dose used. Lower doses promoted a switch from pro-inflammatory

M1 to anti-inflammatory M2 macrophage phenotypes and reduced pro-inflammatory factors [Sridharan et al., 2015; Spiller et al., 2015; Spiller & Koh, 2017]. However, higher doses led to significant inflammation, characterized by increased pro-inflammatory factors and decreased cell numbers. Furthermore, the dissolution products of certain MBGs (75SiO2-20CaO-5P2O5) conditioned in DMEM for 24 hours reduced the number of macrophages while maintaining the percentage of M1 phenotypes. The anti-inflammatory responses of BGs are thought to be influenced by soluble silica released by BGs. Silicon-based materials, like coral sand and sodium metasilicate, have been used in treating inflammatory diseases due to their anti-inflammatory properties, including down-regulation of TNF-α and modulation of antioxidant enzymes [Liu et al., 2020, Zheng et al., 2021].

Research by Zhao et al. [2015] explored the effects of BG scaffold dissolution products (SiO_2:CaO:P_2O_5 = 80:15:5) on RAW cells in both inflammatory and anti-inflammatory states, showing increased expression of IL-1, IL-6, and Arginase (an anti-inflammatory gene) and decreased IL-10 and TNF-α in both conditions.

Similarly, the use of alginate hydrogels containing SiO_2-CaO-P_2O_5 BG increased the M2 macrophage phenotype (anti-inflammatory) and down-regulated inflammatory cytokines while up-regulating anti-inflammatory cytokines. These effects can promote tissue regeneration, including fibroblast proliferation, migration, expression of growth factors (VEGF, FGF-2, and TGF-β), and angiogenesis [Zhu et al., 2020]. These anti-inflammatory and regenerative effects have been demonstrated in diabetic rat models and in normal and macrophage-depleted mice, highlighting the potential of BGs in tissue regeneration and inflammation reduction, particularly in wound healing and other medical applications [Zhu et al., 2020; Nie et al., 2024].

Angiogenesis, the formation of new blood vessels, plays a crucial role in wound healing by facilitating the penetration of capillaries into wound clots. Bioactive glasses (BGs) have been found not only to exhibit antibacterial effects but also to stimulate angiogenesis in both laboratory experiments and living organisms. For example, studies involving the incorporation of 45S5 Bioglass into poly(glycolic acid) (PGA) meshes have demonstrated an increase in neovascularization, beneficial for engineering large soft tissue constructs [Day et al., 2004]. Recent research has explored the application of BAG ointments in cutaneous wounds, showing

that they expedited wound healing by promoting fibroblast proliferation and the growth of granulation tissue. Various bioactive glasses (BGs), including 45S5 BG and others, have shown promising pro-angiogenic properties, promoting blood vessel formation and tissue regeneration. Studies have demonstrated that these BGs stimulate the expression of pro-angiogenic factors like VEGF and FGF-2 and enhance blood vessel density in *in vitro* and *in vivo* models [Day R M, 2005, Pawar & Shinde, 2024]. Incorporation of BGs into scaffolds and hydrogels has also been found to promote angiogenesis and tissue healing. The release of ions, particularly $SiO4^{4-}$ and calcium, from BGs plays a crucial role in their pro-angiogenic effects [Dashnyam et al., 2017]. $SiO4^{4-}$ ions stimulate endothelial cell tubule formation and promote the expression of angiogenic factors like VEGF and FGF-2 through HIF-1α upregulation [de Laia et al., 2021]. Shi et al. [2021] examined how bioactive glass (BG) affects vascular endothelial growth factor (VEGF) paracrine signaling in cardiomyocytes. They discovered that BG stimulates the production and secretion of bioactive ions by cardiomyocytes. Importantly, they demonstrated that VEGF, derived from cardiomyocytes, plays a significant role in influencing endothelial cell behavior. Additionally, their research revealed that BG upregulates the phosphoinositide-3-kinase (PI3K)/protein kinase B (Akt)/hypoxia-inducible factor 1α (HIF-1α) signaling pathway in cardiomyocytes, which is responsible for the increased expression of VEGF [Shi et al., 2021]. Calcium released from BGs triggers calcium intake in cells, activating signaling pathways involved in angiogenesis and growth factor binding. Co-culturing BGs with other cell types, such as stem cells and endothelial cells, has shown synergistic effects on angiogenesis. BG fibers also provide a supportive network for endothelial cell attachment and migration, further promoting blood vessel formation. Nano-sized particles of 45S5 Bioglass have proven particularly effective in healing wounds and enhancing the production of growth factors like VEGF and FGF2, crucial in the wound healing process. Additionally, researchers have examined cobalt-doped glasses to encourage angiogenesis by releasing Co^{2+} ions, mimicking hypoxic conditions. However, it is crucial to exercise caution and consider potential risks associated with cobalt toxicity *in vivo* when exploring this approach further de [Laia et al., 2021]. In recent years, scientists have developed experimental constructs based on bioactive glasses (BGs) specifically for the field of skin tissue engineering. These constructs, available in both 2D and 3D forms, include nanofibrous gelatin/Bioglass composite hydrogels, composite membranes, and ultrathin mesoporous bioactive glass (MBG) hollow fibers. These innovative structures aim to provide

support for regenerating tissue and facilitate the controlled delivery of drugs, contributing to the wound healing process.

Moreover, bioactive glasses have shown promise in promoting the healing of internal wounds within the gastrointestinal tract, with an observed antacid effect beneficial in aiding the recovery of gastric ulcers. Notably, 45S5 Bioglass particles have actively played a role in healing superficial injuries to the intestinal mucosa by promoting the restoration of the epithelial layer.

These findings underscore the versatile applications of bioactive glasses in the realms of wound healing and tissue regeneration, offering promising solutions to a range of medical challenges.

Table 1.1. Brief discussion of the clinical status of the bioactive glass in wound healing

Application	Material used	Clinical use	MoA	Effect	Remarks
Wound healing	Polymeric sutures coated with Ag-doped BAG ointments, Fibrous glass or polymer glass composite constructs, composite films with Ag-doped BAG	Yes	Release of ion dissolution products (e.g. boron) promoting blood microvessels formation. The glass releases antibacterial ions (Ag^{+}, Cu^{2+}, Ga^{3+}) that disrupt bacterial RNA and DNA replication or induce damage to the bacterial cell membrane.	Antimicrobial and antifungal action (e.g. Inhibition of biofilm formation, inhibition of pathogen replication), Angiogenic action.	Trials conducted in humans, dogs, and rats have been undertaken, and certain commercial products are now accessible. The ions liberated by bioactive glass (BG) can induce advantageous antibacterial, antifungal, and/or angiogenic effects, particularly beneficial for the process of wound healing.

One crucial factor in the transition from the inflammatory phase to angiogenesis is connexin43 (Cx43), a protein that plays a pivotal role in cellular communication and tissue homeostasis. BGs have been found to modulate the expression of Cx43, thus aiding in angiogenesis, fibroblast migration, and the proliferation of keratinocytes, ultimately promoting wound healing (Li et al., 2016). Furthermore, the calcium ions released by BGs assist in cell migration and the re-epithelialization of dermal cells.

Bioactive glasses (BGs) have emerged as promising materials for promoting epithelialization, the process critical for wound healing. Epithelialization involves the proliferation and migration of epithelial cells, primarily keratinocytes, culminating in wound closure. BGs have been studied extensively for their ability to enhance this process through various mechanisms. One of the fundamental studies on BGs and epithelialization focused on gingival epithelium. It compared the efficacy of BGs in promoting epithelial cell proliferation with a bioabsorbable membrane, showing that BGs could significantly increase the proliferative index of epithelial cells compared to the membrane. This indicated BGs' potential to enhance epithelialization in clinical settings. In a co-culture system with intestinal epithelial cell monolayers and subepithelial fibroblasts, 45S5 bioactive glass powder demonstrated substantial epithelialization, with wound closure reaching 600% at a specific dose. This effect was attributed to the migration and restitution of original epithelial cells. Moreover, research has shown that culturing human dermal fibroblasts on 45S5 dissolution products led to a significant increase in epidermal growth factor (EGF) secretion, further indicating the potential of BGs in promoting re-epithelialization. The release of calcium ions from BGs plays a pivotal role in promoting epithelialization. Calcium ions regulate the growth and differentiation of epidermal cells, promoting their proliferation and differentiation. Silicates in BGs have also been found to promote EGF expression from keratinocytes, further supporting epithelialization. Additionally, BGs stimulate connexin 43, a protein involved in gap junction intercellular communication, which promotes epithelialization by facilitating cell-cell communication. Furthermore, BGs interact with macrophages to create an anti-inflammatory environment, which accelerates wound closure. This paracrine effect enhances the expression of transforming growth factor-beta (TGF-β) in macrophages, contributing to wound healing. Macrophages play a vital role in re-epithelialization, as evidenced by slower wound closure in macrophage-depleted mice compared to normal mice. Various formulations of BGs have demonstrated efficacy in promoting epithelialization. These include sol-gel and melt-derived

BGs, as well as BG-containing scaffolds and composites. For instance, Vaseline containing BGs led to faster wound closure *in vivo* on full-thickness wounds in rats. Collagen and polycaprolactone (PCL) fibrous scaffolds containing BG nanoparticles enhanced *in vitro* epithelialization in human epidermal keratinocytes (HaCaTs) and promoted wound closure *in vivo*. Additionally, BG-containing agarose-alginate composites and a poly(D,L-lactic acid) (PDLLA) electrospun membrane containing BGs exhibited accelerated wound healing rates in animal models.

In summary, BGs have demonstrated significant potential in promoting epithelialization through various mechanisms, including the release of calcium ions, promotion of growth factors secretion, enhancement of cell-cell communication, and modulation of the inflammatory environment. These findings highlight the therapeutic potential of BGs in enhancing wound healing and tissue regeneration.

BG-based electrospun fibers, as demonstrated by Gao et al. (2021), mimic the properties of fibrin clots, creating a microenvironment resembling the extracellular matrix (ECM) that covers the wound bed and facilitates the healing process. The porous and cottony texture of these micronanofibers provides a large surface area, regulates moisture levels at the wound site, and offers mechanical support, thereby promoting re-epithelialization during the later stages of healing. Additionally, they have the capacity to activate key factors such as vascular endothelial growth factor (VEGF), vascular cell adhesion protein 1 (V-CAM 1), and fibroblast growth factor receptor 1 precursor (N-sam), contributing to neovascularization [Saha et al., 2020].

Bioactive glasses (BGs) stimulate the expression of collagen and other extracellular matrix (ECM) proteins, aiding in tissue regeneration. BGs promote collagen type I expression from fibroblasts and induce MMP1 secretion from mesenchymal stem cells (MSCs). Recent studies show BGs' ability to stimulate collagen type II formation by chondrocytes, crucial for chondrogenesis. Ions released by BGs, like SiO_4^{4-} and Ca^{2+}, promote collagen and fibronectin production in skin ECM. BGs incorporated into scaffolds enhance collagen deposition in soft tissues and promote fibroblast migration and ECM protein expression. However, some BG formulations may down-regulate certain ECM proteins, possibly due to poor adhesion to ECM

proteins. *In vivo* studies demonstrate increased ECM deposition in systems containing BGs, indicating their potential for tissue engineering applications.

Bioactive glasses (BGs) have gained attention in various biomedical applications, including hemostasis. Their role in hemostasis primarily involves their ability to promote blood clotting and control bleeding. BGs have a surface chemistry that can initiate and accelerate the coagulation process. When BGs come into contact with blood, they activate the intrinsic and extrinsic coagulation pathways by interacting with blood proteins and platelets. This interaction promotes the aggregation of platelets and the formation of a stable blood clot at the site of injury. BGs can adhere to the wound site and serve as a hemostatic agent. They help control bleeding by providing a scaffold for platelets and blood proteins to adhere to, facilitating the formation of a clot. This is particularly beneficial in cases of surgical procedures or traumatic injuries where rapid hemostasis is essential. BGs release calcium ions, which play a crucial role in the coagulation cascade. Calcium ions are required for the activation of various coagulation factors and enzymes, including prothrombin to thrombin conversion. Therefore, the presence of calcium ions from BGs can enhance the efficiency of the clotting process. BGs interact with blood components such as fibrinogen and von Willebrand factor (vWF), which are involved in platelet activation and clot formation. These interactions promote the adhesion of platelets and the formation of a stable fibrin clot.

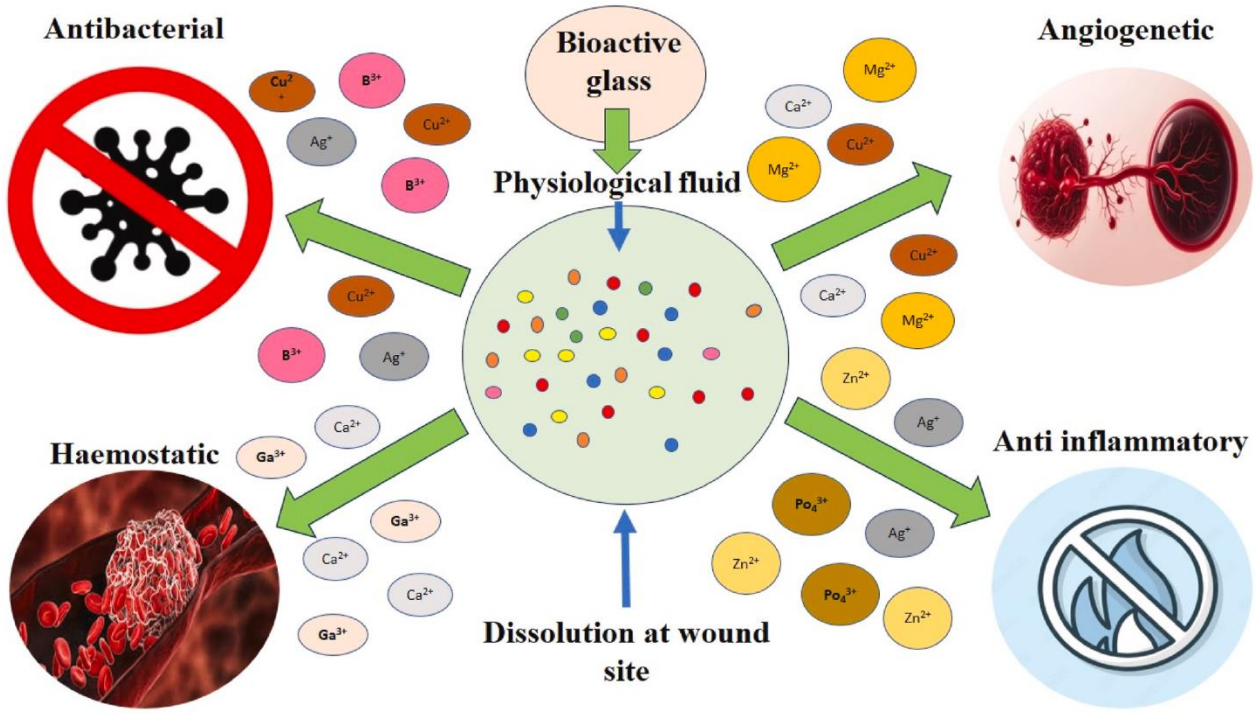

Fig. 1.3. Schematic illustration of the biological effects of various ions released from the bioactive glass

Chapter 2: Literature Survey

2.1.Literature Survey

Bioactive glasses have significantly influenced the healthcare sector and played a pivotal role in advancing modern regenerative medicine through biomaterials. Larry Hench's creation of the initial 45S5 glass composition fifty years ago marked a momentous breakthrough. This composition demonstrated the ability to bond with living bone and stimulates osteogenesis by releasing biologically active ions. Over time, medical products containing 45S5 glass have been implanted in millions of patients worldwide, mainly for treating bone and dental issues. Additionally, different formulations of bioactive glass have been suggested for novel biomedical purposes, such as soft tissue repair and drug delivery. Despite significant progress, the complete potential of bioactive glasses remains untapped, with many current achievements once considered impossible during the early stages of research. As a result, research in this field is vibrant and collaborative, requiring cooperation among glass chemists, bioengineers, and clinicians from various backgrounds.

2.2.FDA approved bioactive glass materials in woundcare and hemostasis application

Existing literature demonstrates that bioactive glasses (BGs) have predominantly found applications in connection with bone tissue, but there is emerging potential for their use in soft tissue repair as well. As far as the author is aware, there are currently only two BG-based commercial products explicitly designed to promote angiogenesis. One of these products is a biodegradable borate BG with a structure resembling that of a fibrin clot, which has been shown to accelerate wound healing in both animal and human patients. These BG nanofibers, known as DermaFuse®/ Mirragen®, have notably aided in the healing of chronic venous stasis ulcers in diabetic patients who did not respond to conventional treatments [Masoud et al., 2020]. Research conducted using a rat subcutaneous model has indicated that the angiogenic effect can be enhanced by incorporating a small amount of copper into the BG, which is gradually released into the surrounding biological environment. The veterinary medicine product 'RediHeal' is commercially available and received FDA approval for human clinical use in 2016.

Table 2.1. Brief description of the various market available bioactive glass based products in wound healing application

Commercial marketed formulation	Manufacturer	Application	Type of dosage form	Glass system	Biological application
Dermafuse®/ Mirragen®	ETS wound Care, USA	Human	Fibre	Borate	Diabetic pressure, trauma wounds, vascular ulcers, surgical incisions, burns [Masoud et al., 2020].
Dermfactor®	UEG Medical Group Ltd., China	Human	Powder	Silicate	Chronic wounds, diabetic ulcers, surgical incisions, burns, bedsores [Chen et al., 2018].
Tendaheal™	Tenda Horse products, LLC, USA	Animal	Fibre, spray, hydrogel, cream	Borate	Chronic and severe wounds, sores, cuts, scrapes, abrasions, scratches, hot spots, skin rashes, burns, abscesses and post surgical sites [Pawar & Shinde, 2024].
Arglaes®	Medline Industries,	Human	Powder, film	Phosphate (Ag doped)	Full thickness wounds and

	USA				management of infection [Baino et al., 2016; baino et al., 2018].
Rediheal™	Avalon Medical, USA	Animal	Ointment, fibre	Borate (Cu doped)	Promote angiogenesis, trauma wounds, surgical wounds, pressure sores, chronic and soft tissue wounds [Pawar & Shinde, 2024].
Theraglass®	Medcell, UK	Human	Powder	Silicate	Promote angiogenesis [Kargozar et al., 2018].

2.3.Bioactive glass in wound healing and hemostasis - ongoing research

Lin et al. (2012) conducted a study to investigate the effects of bioactive glass (BG) on the healing of cutaneous wounds in normal rats and rats with diabetes induced by streptozotocin. They used a BG ointment containing a mixture of sol-gel BAG 58S (SGBG-58S), nanobioactive glass (NBG-58S), and melt-derived 45S5 Bioglass powder with Vaseline (V) at 18 wt% to treat full-thickness excision wounds, with pure Vaseline used as a control. NBG-58S was found to consist of nanoparticles that were more dispersible and smaller in size compared to SGBG-58S. The results showed that bioactive glasses promoted efficient wound healing, with ointments containing SGBG-58S and NBG-58S demonstrating faster and more effective healing than the ointment containing 45S5 Bioglass. Histological analysis revealed that BGs promoted fibroblast proliferation and the growth of granulation tissue. Immunohistochemical staining showed increased production of growth factors such as VEGF and FGFs, which are beneficial for wound

healing. Transmission electron microscopy (TEM) observations indicated that fibroblasts in wounds treated with BGs exhibited more rough endoplasmic reticula and had formed new capillary microvessels by the 7th day. Both SGBG-58S and NBG-58S accelerated skin wound recovery in both normal and diabetic rat models, suggesting their potential for future use in wound repair. Mao et al. (2014) conducted a study to assess the healing effects of bioactive glass (BG) and Yunnan baiyao ointments in diabetic rats induced by streptozotocin. The ointments were formulated by combining 45S5 Bioactive glass powder (16% wt.) with Vaseline and different weight percentages of Yunnan baiyao. Full-thickness defect wounds were created on the backs of 130 SD rats and divided into 8 groups. Wound healing rates were evaluated at various time points, and tissue samples were collected for further analysis. Group 6, which received ointment with 5% Yunnan baiyao, demonstrated superior wound healing performance compared to other diabetic groups. This group exhibited reduced inflammatory responses, as evidenced by gross observations and confirmed through histological and TEM examinations. Additionally, fibroblast proliferation, granulation tissue formation, and vascularization were enhanced in group 6 compared to the other diabetic groups.

Mârza et al. (2019) evaluated the impact of bioactive glass (BG) and gold-nanoparticles (BG-AuNPs) composites on skin wound healing in experimental rat models over 14 days. Sol-gel derived BGs and BG-AuNPs composites mixed with Vaseline at 6, 12, and 18 wt% were used. The 18% BG-AuNPs-Vaseline treated group exhibited a strong vascular proliferation and complete wound regeneration, suggesting its potential as a promising candidate for wound healing applications.

Özarslan et al. (2023) developed a zinc-doped bioactive glass (BG) by incorporating 5 wt% zinc into 45S5 BG (16 wt%). They formulated an ointment for wound healing by mixing this zinc-doped BG with Vaseline. The ointment exhibited pseudoplastic behavior and viscoelastic properties, indicating its suitability for topical application. It was found to be non-toxic to L929 cells, confirming its cytocompatibility for topical use. *In vitro* wound healing assays showed that the ointment promoted wound healing by accelerating skin wound closure, likely due to the presence of zinc in the formulation.

Zeng et al. (2015) designed a BG/agarose-alginate (AA) hydrogel, has thermosensitivity allowing it to gel at physiological temperature through the interaction between the agarose and

alginate polymer chains. The hydrogel promote migration of fibroblasts and endothelial cells and it can also enhance the angiogenesis of endothelial cells in a fibroblast-endothelial cell co-culture model *in vitro*. The results demonstrate that the BG/AA hydrogel can enhance blood vessel and epithelium formation, which contribute to wound healing. Wang et al. (2016) prepared sol-gel derived bioactive glass nanoparticles (nBPs) with mean diameter of 12 nm (BP-12) and were mixed with gelatin to form an easy-to-use hydrogel as a dressing for skin wound. *In vitro*, the composite hydrogel of BP-12 and gelatin had good biocompatibility with the fibroblast cells. *In vivo*, rapid cutaneous-tissue regeneration and tissue-structure formation within 7 days was observed in the wound healing experiment performed in rats, exhibiting an easy-to-use wound dressing material. Zhou et al. (2018) developed a novel Bioglass/albumin composite hydrogel by utilizing dual-functional bioactive ions released from Bioglass, which on one side controls the gelling time by creating an alkaline environment to regulate the cross-linking reaction between human serum albumin and succinimidyl succinate modified poly (ethylene glycol) and on the other side stimulates wound healing. The *in vivo* experiment confirms that this composite hydrogel has good bioactivity to stimulate angiogenesis and enhance chronic wound healing. Gao et al. (2019) developed a unique bioglass (BG)/oxidized sodium alginate (OSA) composite hydrogel with adipic acid dihydrazide (ADH)-modified γ-polyglutamic acid (γ-PGA) as the cross-linking agent, in which the BG plays a multifunctional role to endow the hydrogel with both dual-adhesive and bioactive properties. The composite hydrogel showed excellent bioactivity to promote vascularization and accelerate tissue regeneration. Zhu et al. (2019) developed composite hydrogels named Gel-ZBG, consisting of zinc-doped bioactive glass (ZBG), succinyl chitosan (SCS), and oxidized alginate (OAL), as wound dressings to accelerate wound closure. The amino group from SCS and zinc ions released from ZBG exhibited strong antibacterial properties in the composite hydrogels, as confirmed by *in vitro* antibacterial tests. Additionally, the presence of silicon and calcium ions in ZBG played a crucial role in stimulating fibroblasts to produce beneficial factors for angiogenesis and wound closure. Furthermore, epidermal growth factor (EGF) was incorporated into the hydrogels to enhance cell proliferation and tissue remodeling in the wound bed. Zhu et al. (2020) studied the effects of a hydrogel made from bioactive glass (BG) and sodium alginate (SA) (BG/SA hydrogel) on macrophage behavior and their interactions with other repairing cells. They used macrophage-depleted mice to understand the role of macrophages in the regeneration of full-thickness skin wounds treated

with BG/SA hydrogel. The results showed that BG/SA hydrogel could induce macrophages to adopt an M2 phenotype, which is associated with anti-inflammatory effects, both *in vitro* and *in vivo*. This M2 polarization of macrophages led to increased expression of anti-inflammatory genes. Additionally, M2-polarized macrophages were found to recruit fibroblasts and promote vascularization of endothelial cells in both *in vitro* and *in vivo* experiments. Depletion of macrophages from the wound sites hindered the recruitment of repairing cells and reduced the formation of blood vessels and extracellular matrix (ECM), thereby slowing down skin regeneration. In a related study, Dong et al. (2017) investigated how bioactive glass (BG) influences the behavior of macrophages and the communication between macrophages and other repairing cells during wound healing. The findings revealed that BG's ionic products activated macrophages, prompting them to adopt the M2 phenotype and express a higher level of anti-inflammatory and angiogenic growth factors compared to control medium. When BG powder was applied to full-thickness excisional wounds in rats, the wounds closed more rapidly compared to the control group. Additionally, there was reduced inflammation in the initial stages of healing, as evidenced by fewer neutrophils and more M2 macrophages present in the wound sites treated with BG compared to those without treatment. Wu and Li (2021) incorporated bioglass (BG) into alginate/ carboxymethyl chitosan (SA/CMCS) hydrogel in order to obtain a bioactive alginate/CMCS/BG(SA/CMCS/BG) hydrogel wound dressing with improved mechanical stability, bioactivity and antibacterial and coagulation ability. The findings demonstrated that the hydrogel could expedite the closure of skin wounds by modulating the body's inflammatory responses, promoting the growth of new blood vessels, and improving the deposition of collagen in the wound area. This indicates that SA/CMCS/BG hydrogels have potential as effective wound dressings for clinical use. Zhang et al. (2021) prepared an injectable hydrogel made of DFO grafted to SA/BG (DFO-SA/BG). Degradation of SA/BG hydrogel was modulated by grafting deferoxamine (DFO) to SA. The funtionalized grafted DFO-SA (G-DFO-SA) was used to form G-DFO-SA/BG hydrogel. When the hydrogels were implanted subcutaneously, G-DFO-SA/BG hydrogel possessed a faster degradation and better tissue infiltration as compared to SA/BG hydrogel. In a rat full-thickness skin defect model, wound healing studies showed that, G-DFO-SA/BG hydrogel significantly accelerated wound healing process by inducing more blood vessels formation. Therefore, G-DFO-SA/BG hydrogel can promote tissue infiltration and stimulate angiogenesis. Mehrabi et al. (2022) developed a wound

dressing hydrogel by using thiolated chitosan (tCh)/oxidized carboxymethyl cellulose (OCMC) containing Cu-doped borate bioglass (BG) to improve wound healing in a full-thickness skin defect of mouse model. Thiolated groups incorporated into chitosan (Ch) to enhance its water solubility and mucoadhesion. Investigation of *in vitro* cytotoxicity assays demonstrated that the synthesized hydrogel showed good biocompatibility and promoted cell growth. The hydrogel containing borate BG was maintained in the defect site of the animal model, healing efficiency was accelerated by improving the angiogenesis and remodeling. Zhang et al. (2023) developed a multifunctional chitosan/alginate hydrogel decorated with β-cyclodextrin (β-CD) modified polydopamine (PDA)-Bioactive glass (BG) nanoparticles (NPs) integrating for photothermal performance and nitric oxide release activities for the treatment of bacterially infected wounds. The above mentioned nanocomposite hydrogel has multiple functions in preventing bacterial infections, accelerating angiogenesis and wound regeneration. Tomar and colleagues (2023) developed a novel composite hydrogel adhesive, which combines gelatin, chitosan, polydopamine-coated bioactive glass (BG), and curcumin-capped silver nanoparticles (Cur-AgNPs), aiming to address various aspects of wound healing. The polydopamine-coated BG contributes adhesiveness through its catechol groups and released calcium ions, while the silicon from BG promotes angiogenesis and vascularization. The Cur-AgNPs provide potent bactericidal and anti-inflammatory properties to the hydrogel. The results demonstrated the hydrogel's efficacy in wound healing, with significant wound closure observed by day 7, along with an upregulation of key genes involved in skin regeneration. Recently, Monavari et al. (2023) fabricated a wound dressing composed of alginate-dialdehyde-gelatin (ADA-GEL) hydrogel incorporated astaxanthin (ASX) and 70B (70:30 B_2O_3/CaO in mol%) borate bioactive glass microparticles was developed through 3D printing. The composite hydrogel constructs codelivered biologically active ions (Ca and B) and ASX, which should lead to a faster, more effective wound healing process. As shown through *in vitro* tests, the ASX-containing composite hydrogel promoted NIH3T3 cell adhesion, proliferation and VEGF expression and keratinocyte migration, due to the antioxidant activity of ASX, the release of cell-supportive Ca^{2+} and B^{3+} ions and the biocompatibility of ADA-GEL.

Lin et al. (2014) created bioactive borate glass 13-93B3 microfibers containing 0.4 wt% copper, which were found to stimulate significant angiogenesis compared to silica glass microfibers. To assess cytotoxicity, histological examination of kidney tissue collected from animals four weeks

after subcutaneous implantation of a large quantity of borate glass microfibers was conducted, revealing no signs of chronic histopathological alterations in the kidney. Yang et al. (2015) developed three types of microfibers, silica-based 45S5, borate-based 13-93B3 and 1605-based, added with CuO and ZnO. Evaluation on human skin cell line demonstrated that borate-based fibres though more toxic than silicate-based glass fibres under static condition, can significantly stimulated cell growth with higher cell proliferation rate and migration ability when appropriate pre-soaking time and dynamic flow rate were acquired. Another group, Zhou et al. (2016) fabricated borate bioactive glass microfibers to treat serious skin defects. The ionic extracts of BG and SiG (traditional material 45S5 Bioglass, SiG) microfibres were not toxic to HUVECs. *In vivo* experiments demonstrated that wound dressings made from borate glass (BG) microfibers notably promoted blood vessel formation and led to faster reduction in wound size compared to silicon glass (SiG) microfibers or control groups after nine days of application. The enhanced skin defect reconstruction ability of BG microfibers was attributed to the presence of boron in their composition, which enhances bioactivity and angiogenesis. Biomimetic electrospun nanofibers were crafted using a combination of fish collagen and bioactive glass (Col/BG) in a study by Zhou et al. (2016). They utilized a Sprague Dawley rat skin defect model to assess the nanofibers' impact on wound healing. Results demonstrated that compared to pure fish collagen, the Col/BG nanofibers exhibited enhanced tensile strength and displayed some antibacterial activity against *S. aureus*. Additionally, these nanofibers were found to enhance the attachment, multiplication, and movement of human keratinocytes. Animal trials further revealed that Col/BG nanofibers accelerated the healing process of rat skin wounds. In another study by Wang et al. (2016), biocomposites consisting of copper-containing mesoporous bioactive glass (Cu-MBG) and nanofibrillated cellulose (NFC) were developed for treating chronic wounds. The research highlighted a critical biological concentration of Cu^{2+} ions below 10mg/L for the viability and growth of 3T3 fibroblasts. Cu^{2+} ions released from the composite displayed significant angiogenic effects in a 3D spheroid culture of human umbilical vein endothelial cells. Additionally, Cu-MBG upregulated angiogenic gene expression in 3T3 fibroblasts and exhibited inhibitory effects on E. coli growth. In their study, Zhao et al. (2015) developed wound dressings comprising borate bioactive glass microfibers (with a diameter ranging from 0.4 to 1.2 μm) doped with varying amounts of CuO (ranging from 0 to 3 wt%). These dressings were evaluated both *in vitro* and *in vivo*. Upon immersion in simulated body fluid, the fibers underwent

degradation and transformed into hydroxyapatite within 7 days, releasing ions such as Ca, B, and Cu into the medium. *In vitro* cell culture experiments revealed that the ionic dissolution products of the fibers were non-toxic to both human umbilical vein endothelial cells (HUVECs) and fibroblasts. Moreover, they promoted HUVEC migration, tubule formation, and secretion of vascular endothelial growth factor (VEGF), while also stimulating the expression of angiogenic-related genes in fibroblasts.

When applied to treat full-thickness skin defects in rodents, the Cu-doped fibers demonstrated a significantly higher capacity to stimulate angiogenesis compared to the undoped fibers and the untreated control defects at both 7 and 14 days post-surgery. Additionally, the defects treated with Cu-doped fibers exhibited improved collagen deposition, maturity, and alignment compared to the untreated defects. However, the extent of improvement observed with Cu-doped fibers did not significantly surpass that of undoped fibers by the 14th day post-surgery. Hu et al. (2018) fabricated a novel organic-inorganic dressing of copper-doped borate bioactive glass/poly (lactic-co-glycolic acid) loaded with vitamin E (0-3 wt% vitamin E) to evaluate its efficiency for angiogenesis in cells and full-thickness skin defects in wounds. Cell culture suggested the ionic dissolution product of the copper-doped and vitamin E-loaded dressing showed excellent migration, tubule formation and VEGF secretion in HUVECs and higher expression levels of angiogenesis-related genes in fibroblasts *in vitro*. Furthermore, this dressing also suggested a significant improvement in the epithelization of wound closure and an obvious enhancement in vessel sprouting and collagen remodeling *in vitro*. Sharaf et al. (2022) developed cellulose acetate (CA) electrospun nanofibres containing BG nanoparticles (BGNPs). Biological wound healing capabilities for the prepared nanofibre dressing were assessed using *in vivo* diabetic rat model with induced wounds. The result demonstrated improved antibacterial activity against wide range of microbes including gram negative and gram positive bacteria with significant reduction of induced wound in diabetic rats with complete healing over limited period. Kermani et al. (2023) synthesized a series of Zn and Cu-doped 13-93B3 borate glasses by a modified sol-gel method in the presence of Pluronic P123. The synthesized doped glasses at a concentration of 0.5 mg/ml had no adverse effects on the viability of fibroblasts and showed suitable antibacterial activity, considered a useful substance for wound healing applications. Vinayak et al. (2023) utilized a waste product, eggshell membrane and coated with bioactive glass/ion-doped (Zn, Co) BG in the nanoscale range to develop different types of wound dressing mats and all mats were

cytocompatible with human dermal fibroblasts and maintained cytoskeletal and nuclear morphology upto day 14 of culture. On application of these mats over the full-thickness skin wounds in the rabbit model, enhanced wound closure was observed especially with the eggshell membrane/ion-doped BG mats. Saha et al. (2020) synthesized a silver-containing bioactive glass by sol-gel route, followed by fabrication of the antibacterial bioactive glass nanofibres using electrospinning technique. An *in vitro* cell proliferation assay was performed using SV-transformed GM00637 (skin fibroblast cell line), exhibited significant cell proliferation (82%) compared to the control (47%) in a period of 24h, thus establishing its wound healing potential. Ju et al. (2021) fabricated 3D cotton-wool-like sol-gel bioactive glass fibres by electrospinning technique that mimic the fibrous architechture of skin extracellular matrix (ECM) and the deliver metal ions for antibacterial (silver) and therapeutic (Ca and silica species) actions. The degradation products from the Ag-doped 3D non-woven sol-gel glass fibres were also found to promote fibroblast proliferation thus demonstrating their potential for use in skin regeneration. Another group [Mahmoudi et al. 2023], developed a biocompatible fibrous scaffold containing polyvinyl alcohol (PVA), 70S30C bioactive glass (BG), silver (Ag) nanoparticles and curcumin (Cur) was fabricated through electrospinning method. The viability of fibroblasts after 7 days of cell culture was 93%. The antibacterial activity against *E. coli* and *S. aureus* bacteria was illustrated using inhibition zones of 13 and 14 mm, respectively. Histological results revealed that tissue regeneration after 14 days of surgery was much higher for the dressing compared to the blank group. In more advanced research conducted by Sharifi et al. (2022) incorporated glass-ceramics (GC) doped with silver in chitosan and gelatin electrospun nanofibres scaffolds were biocompatible, hemocompatible and promote cell attachment and proliferation. The rate of biodegradation of the nanocomposite was similar to the rate of skin regeneration under *in vivo* conditions. Histopathological evaluation of full-thickness excisional wounds in BALB/c mice treated with mouse embryonic fibroblasts-loaded nanofibrous scaffolds showed enhanced angiogenesis and collagen synthesis as well as regeneration of the sebaceous glands and hair follicles *in vivo.* Liu et al. (2023) prepared a magnesium-doped silica bioactive glass (SiO_2/MgO) nanfibre by electrospinning. The result demonstrated that this SiO_2/MgO nanofibre membrane has good flexibility and hydrophilicity, which give it intimate contact with wound beds. *In vitro* assessments illustrated its good cytocompatibility and bioactivity that contribute to its robust cell proliferation and angiogenesis. In addition, *in vitro* assays prove its good antibacterial activity

against both gram positive and gram negative strains. In a full-thickness skin defect inoculated with *S. aureus* in mice, it effectively inhibits bacterial infection. Both gene expression and histological/ immunohistological analyses confirmed the down regulated pro-inflammatory factors, these desirable properties work in concert to contribute to the rapid healing of infected wounds and make it a good candidate for wound dressing materials. An anticancer drug, 5-FU containing mesoporous bioactive glass (MBG) was successfully loaded into core-shell nanofibres by Yuan et al. (2023) and sustained release of 5-FU was achieved, exhibited excellent cancer cell killing effect. Also, MBG-U-CSF could promote skin regeneration owing to the function of MBG. El-Okaily et al. (2023) prepared nanofibre membranes for wound healing using electrospinning process containing polycaprolactone (PCL). Integration of atorvastin and bioactive glass with PCL nanofibres showed superior wound closure results in the human skin fibroblast cell line.

Yu et al. (2016) demonstrated that bioactive glass (BG) can induce fibroblasts to produce essential growth factors and key proteins, such as vascular endothelial growth factor, basic fibroblast growth factor, epidermal growth factor, collagen I, and fibronectin. *In vivo* findings showed that fibroblasts within the bioactive skin tissue engineering grafts migrated into the wound bed, with BG enhancing their migration ability. These grafts contained higher levels of critical growth factors and extracellular matrix (ECM) proteins that are advantageous for wound healing compared to untreated grafts. Sharifi et al. (2023) doped zinc to bioactive glass-ceramic (Zn-BGC) and then incorporated into a porous scaffold of collagen (Col) and gelatin to promote angiogenic properties. The bioactive porous bionanocomposite (Col-Gel/Zn-BGC) exhibited improved cell attachment and proliferation. Mouse embryonic fibroblasts were loaded into Col-Gel/Zn-BGC scaffold and were applied on full-thickness skin wounds on the BALB/c mice, the results indicated that the biodegradation rate of the Col-gel/Zn-BGC nanocomposites was comparable to the rate of skin tissue regeneration *in vivo*. Macroscopic wound healing results showed that Col-Gel/Zn-BGC loaded with mouse embryonic fibroblast possesses the smallest wound size, indicating the faster healing process. Histological evaluations displayed that the optimal wound regeneration was observed in Col-Gel/Zn-BGC loaded with mouse embryonic fibroblasts indicated by epithelization and angiogenesis. Naseri et al. (2019) developed two different glass composition, $(46)B_2O_3$-$(27)CaO$-$(24-x)Na_2O$-$(3)P_2O_5$-$(x)Ag_2O$ where x=0, 0.15, 0.5 and 1 mol% and $(60)B_2O_3$-$(36)CaO$-$(4-x)P_2O_5$-$(x)Ag_2O$, where x=0, 0.3, 0.5 and 1 mol% by

sol-gel route, reported for the first time. The antibacterial activity against *E. coli* and *S. aureus* was correlated with silver ion release. Kermani et al. (2022) successfully synthesized silver-doped borate-based mesoporous BAG, exhibited potent antibacterial activity against gram-positive and gram-negative strains and had no adverse effect on the viability of fibroblasts.

Li et al. (2016) proposed that bioactive glass (BG) could influence cell behavior mediated by gap junctions to enhance wound healing. To investigate this hypothesis, they studied the effects of BG on endothelial cells' (ECs) behavior related to gap junctions to understand the underlying mechanism. *In vitro* studies demonstrated that BG ion extracts protected human umbilical vein endothelial cells (HUVECs) from hypoxia-induced cell death in a dose-dependent manner, potentially by modulating connexin hemichannels. BG also enhanced gap junction communication between HUVECs and upregulated the expression of connexin 43 (Cx43). Moreover, BG promoted the expression of vascular endothelial growth factor (VEGF), basic fibroblast growth factor (bFGF), their receptors, and vascular endothelial cadherin in HUVECs, all of which are beneficial for vascularization. *In vivo* wound healing experiments in rats showed that BG accelerated the closure of full-thickness excisional wounds, reduced inflammation during the initial stages of healing, and stimulated angiogenesis during the proliferation stage. This work revealed the relation between BG and Cx43 mediated endothelial cell behavior and elucidates one of the possible mechanisms through which BG stimulates wound healing. It has been reported earlier that experimental downregulation of connexin43 (Cx43) expression at skin wound sites appears to markedly improve the rate and quality of healing, but the underlying mechanisms are currently unknown. Mori et al. (2006) had compared physiological and cell biological aspects of the repair process with or without Cx43 antisense oligodeoxynucleotide treatment. *In vitro* knockdown of Cx43 in a fibroblast wound healing model also resulted in significantly faster healing. mRNA levels of CC chemokine ligand 2 and TNFα were reduced in the treated wound. In their recent study, Zhang et al. (2022) proposed that bioactive glass (BG) might facilitate wound healing by suppressing pyroptosis, a newly recognized form of programmed cell death implicated in various traumatic injury-related diseases. They investigated BG's potential impact on pyroptosis during wound healing both *in vitro* and *in vivo*. The findings revealed that BG accelerated wound closure, promoted granulation formation, enhanced collagen deposition, and facilitated angiogenesis. Moreover, BG was found to inhibit the expression of pyroptosis-related proteins both *in vitro* and *in vivo*, as confirmed by Western blot analysis and

immunofluorescence staining. Additionally, BG was observed to modulate the expression of connexin 43 (Cx43) while suppressing reactive oxygen species (ROS) production. Further experiments involving the activation and inhibition of Cx43 suggested that BG suppressed pyroptosis in endothelial cells by reducing Cx43 expression and ROS levels. This research suggests that BG promotes wound healing by inhibiting pyroptosis via the Cx43/ROS signaling pathway. Tang et al. (2021) discovered that extracts from 58S-bioactive glass (BG) significantly improved the barrier function of keratinocyte monolayers. This enhancement was attributed to the promotion of keratinocyte differentiation and the formation of tight junctions, as indicated by increased expression of key differentiation markers (K10 and involucrin) and tight junction proteins (claudin-1, occludin, JAM-A, and ZO-1). These effects were measured using transepithelial electrical resistance (TEER) and paracellular tracer flux. In an *in vivo* study using a diabetic rat wound model, BG extracts were found to expedite re-epithelialization, stimulate keratinocyte differentiation, and enhance the formation of tight junctions in the newly regenerated epidermis. Filip et al. (2021) synthesized three distinct bioactive glasses incorporating fluorine and boron, which were then assessed for their effects on oxidative stress and matrix metalloproteinases (MMP-2, MMP-9), followed by histopathological examination. Their findings revealed that the degradation rates of the bioactive glass compositions were exceptionally high, resulting in rapid release of calcium, fluorine, and boron. Moreover, animal groups treated with bioactive glass exhibited reduced lipid peroxidation and increased levels of nitric oxide, particularly at 14 days post-treatment, along with improved superoxide dismutase activity. Furthermore, there was a decrease in MMP-9 levels at 14 days, coupled with an increase in the proportion of normal collagen within the wound bed. Bioactive glass (BG) and zeolitic imidazolate framework-8 (ZIF-8) have been incorporated into poly(ε-caprolactone)/poly(vinyl alcohol) (PCL/PVA) composite skin scaffolds via microfluidic electrospinning. The addition of ZIF-8 further strengthens the BG stability and demonstrates better antibacterial effects. Utilizing the slow release of Zn, Ca, and Si ions, it also significantly promotes growth factor expression and skin regeneration. In addition, it is further demonstrated by *in vitro* and *in vivo* studies that the prepared composite skin scaffolds possess excellent biocompatibility, antibacterial capabilities, and mechanical properties [Hou et al., 2024].

The tunable *in vitro* blood clotting activity of high-surface area-hemostatic bioactive glass is evaluated by thromboelastograph, a clinical instrument for quantifying changes in blood during

coagulation. The hemostatic trends associated with hemostatic bioactive glass and new preparation of spherical hemostatic bioactive glass, along with similar Si-Ca containing oxides, and related to Si:Ca ratios, Ca^{2+} availabiblity and coordination environment (Ostomel et al., 2006a, 2006b). Pourshahrestani et al. (2016) developed mesoporous bioactive glass (MBG) containing varying concentrations of Ga_2O_3 (1, 2, and 3 mol%) using the evaporation-induced self-assembly (EISA) process, aiming to investigate the role of Ga^{3+} in hemostasis. Their findings revealed that incorporating a lower Ga_2O_3 content (1 mol%) into the MBG system improved structural properties such as specific surface area, mesopore size, and pore volume, as well as the release of silicon and calcium ions. The bioactive glass was observed to enhance blood coagulation, platelet adhesion, and thrombus generation, and exhibited antibacterial effects against both *E. coli* and *S. aureus*. Furthermore, Ga-doped MBGs demonstrated excellent cytocompatibility even after 3 days, with the 1 mol% Ga_2O_3-containing MBG showing the best biocompatibility, suggesting their suitability as safe hemostatic agents for controlling bleeding. Further, they constructed (2017) a series of 1% Ga_2O_3 containing mesoporous bioactive glass-chitosan composite scaffolds (Ga-MBG/CHT) by the lyophilization process and shown the hemostatic function compared to Celox Rapid Gauze, commercially available chitosan-coated hemostatic gauze. The results of coagulation studies showed that pure CHT and composite scaffolds exhibited increased hemostatic performance with respect to CXR. The cell viability results also demonstrated that Ga-MBG/CHT composite scaffold had good biocompatibility, which facilitates the spreading and proliferation of human dermal fibroblast cells even with 50 wt%-Ga-MBG loading. Then, they (2018) compared 1% Ga_2O_3 (1% Ga-MBG) with two commercial hemostats, Celox^{TM} (CX) and Quikclot Advanced Clotting Sponge Plus^{TM} (ACS^+). The result indicate that the number of adherent platelets were higher on the 1% Ga-MBG and CX surfaces than ACS^+ whereas a greater contact activation was seen on 1% Ga-MBG and ACS^+ surface than CX. 1%-Ga-MBG not only resulted in larger platelet aggregates and more extensive platelet pseudopodia compared to CX and ACS^+ but also significantly accelerated the intrinsic pathways of the clotting cascade. *In vitro* thrombin generation assays also showed that CX and ACS^+ induced low levels of thrombin formation while 1% Ga-MBG had significantly higher values. Another group, Nagrath et al. (2021) synthesized Ta-containing MBG with x mol% Ta_2O_5 added to the (80-x) SiO_2-15CaO-xT_2O_5 where x= 0-10 mol%. The hemstatic potential of Ta-MBG was confirmed by its negative zeta potential, which enhances the intrinsic pathway of

blood coagulation. Cytotoxicity analysis revealed that Ta-MBGs had no effect on bovine fibroblast viability. A reduction in both aPTT and PT signified enhancement of hemostasis compared to 'no treatment'. Next, they fabricated Ta-MBG containing fibrous mats using electrospinning [Nagrath et al., 2022]. The hierarchial micro-nano porosity of the mat is known to enhance the activation of coagulation proteins. The fibrous texture mats, containing tantalum in the composition can provide a stable matrix for hemostasis. Furthermore, they evaluated impact of Ta-MBG using a porcine fatal liver injury model, for that a class IV hemorrhage condition was stimulated on the animals, hemodynamic data and biochemical analysis confirmed the life-threatening condition. Ta-MBG was able to stop the bleeding within 10 min of their application while the bleeds in the absence of any intervention or in the presence of a commercial agent Arista^{TM} continued for up to 45 min [Nagrath et al., 2022]. Moreover, SEM of the blood clots showed that the presence of Ta-MBGs did not affect clot morphology. Rather, the connections seen between fibrin fibres of the blood clot and Ta-MBG powders point towards the powder's surfaces embracing fibrin. Histopathological analysis of the liver tissue showed 5Ta-MBG as the only composition reducing parenchymal hemorrhage and necrosis extent the tissue after their application. Additionally, 5 Ta was also able to form an adherent clot in worst case scenario bleeding where no adherent clot was seen before the powder was applied. Liu et al. (2022) prepared a two-step-acid-catalyzed-self-assembly method to synthesize cerium-containing mesoporous bioactive glass (Ce-MBG). The results exhibited that MBG without cerium and MBG with cerium slightly affected its surface area, and its water absorption rate was significantly higher. *In vitro* coagulation experiments showed that Ce-MBG significantly reduces PT and aPTT, indicating that MBG containing Ce could promote coagulation and platelet adhesion compared to MBG. Further, they prepared a composite hemostatic sponge (Ce-MBG/CHT) of cerium-containing MBG and chitosan (CHT) by a freeze-drying technique and compared with the commercially available gelatin sponge (GS) to evaluate hemostatic performance [Liu et al., 2022]. The *in vitro* coagulation studies showed that factor XII was activated by the addition of Ce-MBG, inducing the intrinsic coagulation pathway. Whole blood coagulation studies suggested that Ce-MBG/CHT has superior hemostatic properties to GS and validated *in vitro* thrombosis, platelet adhesion and hemocompatibility. Zhang et al. (2022) produced bismuth-containing mesoporous bioactive glass using a two-step-acid-catalyzed self-assembly (TSACSA) process. The Bi-doped MBG accelerated the intrinsic coagulation pathway

and did not show significant cytotoxicity to RBCs. Additionally, it demonstrated increased thrombus formation, fibrin polymerization rates, and platelet adhesion. Another group, Zheng et al. (2022) prepared bioactive glass based membrane-like structure camouflage composite particles (MBG@BSA/CS) by using layer-by-layer (LBL) method. The result showed that MBG@BSA/CS particles significantly improved the coagulation effect of MBG and could activated both intrinsic and extrinsic pathways of coagulation by forming a fibrin network by aggregating RBCs and activating platelets, thus rapidly aggregating required coagulation factors. MBG@BSA/CS particles had a significant hemostatic effect on surface bleeding and internal bleeding in SD rats, which could shorten the bleeding time and reduce the amount of blood loss effectively. Li et al. (2023) designed a composite cryogel by gelation of quaternized chitosan (QCS) and hydroxyethyl cellulose oxide (OHEC) at low temperature. Iron-doped bioactive glass (FeBG) as an active substance that was incorporated into the QCOC composite cryogel to promote RBCs aggregation by ion dissolution and activate intrinsic and extrinsic pathways. Additionally, the composite cryogel showed excellent antibacterial properties against S. aureus and E. coli as well as good cell biocompatibility. Further, QCOC/FeBG composite cryogel showed excellent hemostatic performance in the model of liver non-compressible hemorrhage with coagulation disorders and the hemostasis time and blood loss were much lower than the commercial gelatin sponge. Another research group, Lei et al. (2023) prepared a sharp-memory cryogel using Schiff-base reaction between alkylated chitosan (AC) and oxidized dextran (ODex) and then incorporated with a dry-laden and silver-doped MBG. Hydrophobic alkyl chains enhanced the hemostaic and antimicrobial efficiency of the chitosan, forming blood clots in the anti-coagulated condition. The Ag-MBG activated the extrinsic pathway by releasing Ca^{2+} and prevented infection through the release of Ag^{+}. The proangiogenic desferrioxamine (DFO) in the mesopores of MBG was released gradually to promote wound healing. They demonstrated that AC/ODex/Ag-MBG DFO (AOM) cryogels exhibited excellent blood absorption capability, facilitating rapid shape recovery. It provided a higher hemostatic capacity in normal and heparin-treated rat- liver perforation wound model than gelatin sponges and gauze. The AOM gels simultaneously promoted infiltration, angiogenesis and tissue integration of liver parenchymal cells. Alasvand et al. (2023) synthesized CuO containing borate-based BGs by melt-derived method. The results indicated that the BGs did not show any significant cytotoxicity and also showed antibacterial properties against *S. aureus* and *P. aeruginosa*. The investigation revealed

its hemocomaptibility. The incorporation of copper ions into the modified BGs could dramatically improve the endothelial cell proliferation, migration, vascular endothelial growth factor secretion, tube formation and expression of angiogenesis-related genes (VEGF, KDR, HIF-1α and endothelial NO), resulting in the promotion of angiogenesis properties. Further they (2023) developed the porous vascular graft tubes by 3D print using PCL, polyglycerol sebacate and the above mntioned BGs. The PCL sheath was then wrapped around the 3D-printed layer using the electrospinning technique to prevent blood leakage. *In vivo* angiogenesis and gene expression experiments showed that copper-releasing vascular graft considerably promoted the formation of new blood vessels, low-grade inflammation (reduce expression of IL-1β and TNF-α) and high-level angiogenesis (increase expression of angiogenic growth factors including VEGF, PDGF and HEBGF) [Alasvand et al., 2023].

2.4.An overview: Bioactive glass

2.4.1. Structure of the bioactive glass

Glass is a distinct state of matter, not in equilibrium and lacking a crystalline structure. It exhibits a glass transition phenomenon, sharing a microstructure with a supercooled liquid, though it would ultimately crystallize given infinite time [Zanotto et al., 2017]. When the temperature goes beyond the glass transition temperature (Tg), glass shifts from being brittle and solid to becoming more viscous, showing characteristics of flow [Scholze et al., 2012]. Glass structures are typically composed of three components: network formers, network modifiers, and intermediate oxides [Condon et al., 1954]. Network formers like silica (SiO_2), phosphorous pentoxide (P_2O_5), and boron trioxide (B_2O_3) can form glass independently [Shelby, 2005]. Silicate glasses are composed of SiO_4 tetrahedra linked together by Si-O-Si bonds, known as bridging oxygen atoms [Zarzycki et al., 1991]. These tetrahedra are classified as Q^n units, with 'n' indicating the number of bridging oxygen atoms attached to the tetrahedron [Shelby, 2005]. In vitreous silica, each tetrahedron connects to four others, resulting in four bridging oxygen (BO) atoms per tetrahedron (Q^4 units).

In contrast, network modifiers change the glass structure by converting bridging oxygen atoms into non-bridging oxygen atoms through covalent bonds, resulting in Si-O-M^+ linkages, which are predominantly ionic. Network modifiers often include alkali or alkali-earth metal oxides,

exhibiting higher coordination numbers compared to network formers. The representative examples are sodium (coordination number: 5.6 to 6), calcium (6-6.3), and strontium (6.7-7.1). Intermediate oxides can function as network modifiers or, in some cases, integrate into the glass structure like network formers.

The glass structure can be estimated based on its compositional ratio, and the network connectivity (NC) model quantifies the average number of bridging oxygen atoms per network-forming element, typically silicon (NC_{Si}). Network connectivity offers insights into the degree of network polymerization and assists in predicting various glass properties, including bioactivity, crystallization tendencies, and the glass transition temperature [Wu et al., 2009; Wu et al., 2014; Barbieri et al., 1999 & Hunault et al., 2016].

In bioactive glasses like SiO_2-P_2O_5-M_2O-M'O, where M_2O and M'O act as network modifiers, the connectivity of the network is determined using Equation 1. This equation accounts for a maximum of four bridging oxygen atoms per silicon atom, adjusting for the non-bridging oxygen atoms created by modifiers. The inclusion of P_2O_5 increases the number of bridging oxygen atoms, as it requires modifier cations to balance the charge of PO_4^{3-}. SiO_2, P_2O_5, M_2O, and M'O represent the molar percentages of each component.

$$NC_{Si} = [(4\times SiO_2) + (6\times P_2O_5) - \{2\times(M_2O+M'O)\}]/ SiO_2$$

Vitreous silica exhibits a network connectivity of four, which decreases as the content of network modifiers increases. Bioactive glasses generally exhibit network connectivities ranging from 2 to 3. For instance, the bioactive 45S5 glass displays a network connectivity of 2.11, indicating a composition mainly consisting of silicate chains (89% Q2). Additionally, 11% of all Q units serve as branching units (Q3), connecting the chains through bridging oxygen atoms.

On the other hand, the network rigidity model, also referred to as the "floppy networks" model, takes into account local structural differences, making a distinction between rigid and flexible regions. This model is particularly relevant for highly cross-linked glasses, such as bioactive glasses with a network connectivity exceeding 2.4. Based on concepts proposed by Phillips and Thorpe, the network rigidity model explains that in three-dimensional networks, rigidity emerges above a percolation point, corresponding to a network connectivity of 2.4. Below this threshold,

the network is characterized as flexible. Even in rigid networks, certain flexible regions persist, and their extent can be approximated based on the composition of the glass.

2.4.2. Synthesis of bioactive glass

a) Melt-derived approach

The melt-derived approach is a method used in the production of glass materials, including bioactive glasses (BG), which have applications in the field of medicine and biotechnology. This approach involves melting a mixture of various chemical compounds at high temperatures, typically exceeding 1300°C [Jones et al., 2013].

- ✓ Ingredients: The mixture used for this approach typically includes silicon dioxide (SiO_2), calcium carbonate ($CaCO_3$), sodium carbonate (Na_2CO_3), and phosphorus pentoxide (P_2O_5). Other metallic oxides or carbonates can also be added to the melt to incorporate trace elements into the final glass product.
- ✓ Melting Process: The ingredients are melted together in a platinum crucible at temperatures exceeding 1300°C. This high temperature is required to achieve a molten state, which is necessary for forming glass.
- ✓ Quenching: After the mixture has melted, it can be quenched in two different ways:
    - ➢ It can be quenched in a graphite mold to maintain a specific shape, which is particularly useful for creating glass products with predefined forms.
    - ➢ Alternatively, it can be quenched in water to obtain particulate glass. This process typically involves grinding and sieving to produce glass particles.
- ✓ Fiber Production: In some cases, fibers can be drawn from the molten glass before quenching [Jung e al., 2011].
- ✓ Commercial Production: The melt-derived approach is commonly used for commercial production because it is relatively easy to manufacture and tends to have a lower manufacturing cost compared to other methods.
- ✓ Drawback with Sodium (Na_2O): One drawback of the melt-derived approach is that sodium oxide (Na_2O) must be incorporated into the glass composition to lower the

melting point. However, this incorporation of sodium can make it challenging to precisely control the composition of the bioactive glass and its corresponding ion release kinetics [Jones and Clare, 2012]. Excessive levels of sodium ions, exceeding 25%, can lead to a toxic alkaline environment and may not provide the desired therapeutic effects.

- ✓ Process Duration: The entire process, from melting the ingredients to the final product, usually takes less than one day, but it might take longer if the ingredients are mixed and prepared overnight.

In summary, the melt-derived approach is a commonly used method for manufacturing bioactive glasses and other types of glass materials. While it offers advantages in terms of ease of manufacturing and cost-effectiveness, the need to incorporate sodium to lower the melting point presents challenges in controlling the glass composition and ion release kinetics, as excessive sodium content can be detrimental to the intended therapeutic effects.

b) Sol-gel derived approach

The sol-gel process usually comprises several stages where a precursor is transformed into the silica gel, which is then dried to form dry gels. Subsequently, sintering is employed to produce bioactive glasses (BGs) [Hench, 2002]. This detailed procedure involves hydrolysis and condensation, casting of gels, gel formation, aging, drying, stabilization, and sintering. In this method, tetraethyl orthosilicate (TEOS, $Si(OC_2H_5)_4$) serves as the precursor for silicon, while the precursors for metallic ions are typically their respective chlorides or nitrates.

In comparison to the melt-derived method for BG synthesis, the sol-gel process offers several advantages. It enables the production of bioactive glasses (BG) with a silicon content exceeding 70 mol% and eliminates the necessity for a modifier, Na_2O [Lin et al., 2009]. The synthesis temperature in the sol-gel process is much lower than the temperature required for melt-derived method. Additionally, sol-gel BGs naturally possess mesopores ranging from 6-17 nm, significantly increasing the glass's surface area [Yan et al., 2006; Saravanapavan et al., 2003]. The surface area of sol-gel BG particles (size range: 1-32 μm) is 70-130 m^2g^{-1}, whereas similar composition melt-derived BGs have a surface area of only 2.7 m^2g^{-1} [Sepulveda et al., 2001]. Furthermore, sol-gel BGs contain more OH^- groups that lower the network connectivity value compared to speculated values.

However, it's worth noting that sol-gel-derived glasses are more expensive to produce and require a longer synthesis time. The first product developed through the sol-gel method with the 58S composition was primarily used for bone regeneration.

- ✓ Hydrolysis and condensation

In case of acidic catalysis process, tetraethyl orthosilicate (TEOS) undergoes hydrolysis to produce $Si(OH)_4$ and ethanol as a result of condensation. During the condensation process, siloxane bonds (Si-O-Si) are created, and the primary particles start to join together to form secondary particles. The reactions are:

Hydrolysis: $Si(OC_2H_5)_4 + 4H_2O = Si(OH)_4 + 4\ C_2H_5OH$

Condensation: $Si(OH)_4 + Si(OH)_4 = (HO)_3Si\text{-}O\text{-}Si(OH)_3 + H_2O$ (aqueous)

Condensation: $Si(OH)_4 + Si(OH)_4 = (HO)_3Si\text{-}O\text{-}Si(OH)_3 + OH^-$ (as R-OH)

- ✓ Gelation

Following the hydrolysis and condensation stages, the resulting product is Sol containing silica nanoparticles with diameters of approximately 2 nanometers. This solution is composed of several silicon tetrahedral [Jones et al., 2013]. The gelation phase begins when a three-dimensional network forms from these colloidal particles. During this phase, viscosity experiences a significant increase, eventually leading to the formation of a gel.

One of the primary factors that influence the kinetics of hydrolysis and condensation is the pH value of the sol. The reaction kinetics are at their slowest point near the isoelectric point, which is approximately at pH 2.2 [Brinker et al., 2013]. Both acidic and alkaline environments expedite the synthesis of silanols due to the increase in free H^+ or OH^- ions [Hench, 2002], although the mechanisms involved in these processes differ slightly.

When treated with strong acids, H^+ is involved as the catalyst:

$$Si_nO_a(OH)_b + Si(OH)_3O^- + H^+ = Si_nO_a(OH)_{(b-1)}\text{-}O\text{-}Si(OH)_3^+ + H_2O$$

When treated with alkali or weak acids, OH- is involved as the catalyst

$$Si_nO_a(OH)_b + Si(OH)_3O^- + OH^- = Si_nO_a(OH)_{(b-1)}\text{-}O\text{-}Si(OH)_3^+ + H_2O$$

The surface hydrolysis of silica particles is represented by the formula $Si_nO_a(OH)_b$, where 'n,' 'a,' and 'b' are integers [Hench, 1990]. In the majority of cases involving the synthesis of bioactive glass (BG) microparticles, monoliths, fibers, or foams, acids are commonly employed as catalysts [Hench, 2002]. On the other hand, alkaline catalysts lead to a slower increase in reaction kinetics compared to acids and are typically used in the synthesis of BG nanoparticles [Iler et al., 1986].

The stoichiometric ratio (R) of water to tetraethyl orthosilicate (TEOS) plays a crucial role in sol-gel hydrolysis and condensation. The alkalinity of water affects proton activity and, in turn, influences the hydrolysis process. When R is less than 2, alcoholic condensation is favored, while when R is greater than 2, aqueous condensation prevails [Jones et al., 2002]. An R value of 2 is the optimal ratio for drawing fibers, resulting in the induction of viscosity within the range of 1-10 Pa·s [Sack et al., 1987; Sakka et al., 1982]. The water content also has a role in regulating the porosity in BGs, as its removal creates more voids during the stabilization process [Ishizaki et al., 1998]. Additionally, the inclusion of other solvents like dioxane, ethanol, and acetone during the synthesis can alter the rate of hydrolysis and condensation [Hench, 2002].

- ✓ Aging

Following gelation, the gel retains a liquid phase with dispersed ions, marking the onset of the aging phase. This phase encompasses four distinct stages: continued polycondensation, syneresis, phase transformation, and coarsening [Jones et al., 2002]. In the continued polycondensation stage, secondary particles continue to interconnect, forming larger networks and enhancing the gel's strength. The increase in particle size leads to the gel contracting and expelling liquid, a process termed syneresis. Once the degree of cross-linking reaches a critical point, phase transformation occurs, turning the gel into a solidified wet gel. Coarsening, the final step, commences when localized dissolution and reprecipitation processes induce the growth of larger pores at the expense of smaller ones, a phenomenon known as ‘Ostwald ripening’ [Jones et al., 2002]. This results in a high level of interconnection between secondary particles. Typically, this aging process takes approximately three days at a temperature of 60°C.

- ✓ Drying

The drying stage involves the elimination of liquid from both the surfaces and pores, resulting in the formation of a dry gel or xerogel. However, it's crucial to commence the drying phase only after a sufficient aging period. This delay is necessary because, without it, the removal of smaller pores with higher capillary forces can lead to structural cracking [Brinker et al., 2013]. Additionally, an important factor during the drying process is the rate of drying, which can be controlled through the use of surfactants, employing a supercritical drying method, or by reducing surface energy through the creation of monodisperse pore sizes, achieved by controlling the rate of hydrolysis and condensation. Following drying, ions precipitate onto the surface of secondary particles. The drying temperature typically increases from 80 to 130°C, and this process typically takes around 3-4 days.

While hydrolysis, condensation, and gelation reactions continue during the aging phase, it typically takes one day to stir the precursor materials before placing them in the aging oven.

- ✓ Stabilization

Stabilization is a critical step involving the removal of chemically active groups, such as OH^- and unreacted silanols, which render the glass unstable at room temperature. Typically, this is achieved through heat treatment at around 500°C, simultaneously resulting in structural relaxation due to rehydration [Hench 1990]. Additionally, during stabilization, NO_3^- groups from cation sources are eliminated. While conventional NO_3^- groups decompose at temperatures of 561°C, in the case of bioactive glass (BG), higher temperatures are required for complete removal [Pereira et al., 1994]. For example, Arcos et al. [2002] observed that 700°C removed 95% of NO_3^-, while 800°C removed 100% in two separate BG systems. Stabilization also serves to incorporate calcium into the glass network. After stabilization, tertiary particles are formed from clusters of secondary particles and precipitated ions, representing the final glass structure.

However, it's worth noting that while a high stabilization temperature is ideal for removing chemical groups, excessively high temperatures can impact other glass properties. Sintering BG above its glass transition temperature leads to the elimination of nanopores, resulting in a reduction in BG porosity and surface area. For instance, stabilizing 58S glass at 800°C

significantly reduces porosity and surface area [Lin et al., 2009]. This is because high temperatures activate viscous flow and diffusion of glass mesopores to a state with lower interfacial energy. Additionally, hydroxyapatite (HA) formation can occur around temperatures of 800-900°C, depending on the glass composition. The stabilization process typically takes about one day [Nayak et al., 2010].

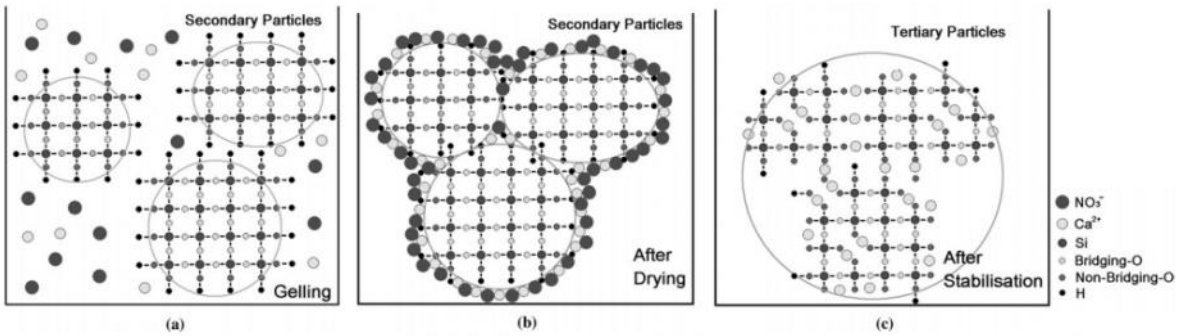

Fig. 2.1. The provided description refers to a schematic diagram illustrating the structural changes and distribution of alkali ions in sol-gel-based bioactive glass (BG) synthesized using tetraethyl orthosilicate (TEOS) and calcium nitrate ($Ca(NO_3)_2$) during different stages of the process [Lin et al., 2009].

(a) During the gelling stage, the schematic likely shows the formation of the initial gel structure, which contains liquid with dispersed ions.

(b) In the drying phase, the diagram probably depicts the removal of the liquid, resulting in the formation of a dry gel or xerogel. This stage may involve the elimination of smaller pores, as mentioned earlier.

(c) The image for stabilization is likely showing the heat treatment process at around 500°C. This phase serves to remove chemically active groups, such as OH^- and unreacted silanols, and to facilitate rehydration. It might also involve the removal of NO_3^- groups and the incorporation of calcium into the glass network.

These structural changes and ion distributions are key aspects of the sol-gel-based BG synthesis process.

2.4.3. Basic difference between melt quench and sol gel process

Compared to the traditional melt-quenching route, the sol-gel process offers the possibility to obtain more reactive materials in a wider compositional range (up to 90% of SiO_2) due to the unique textural properties (inherent nanoporosity) that directly derive from the synthesis process [Sepulveda et al., 2001; Sepulveda et al., 2002; Saravanapavan et al., 2003; Arcos et al., 2010; Izquierdo-Barba et al., 2015]. The sol-gel process offers several advantages over melt-quenching for bioactive glass production. Sol-gel chemistry enables the creation of a wide range of nano- and micro-structures and allows for precise control over surface chemistry, which is beneficial for biomedical applications. Sol-gel methods have been noted for their ability to explore a broader range of glass compositions and mesoporous structures compared to the melt-quenching method [Fiume et al., 2020]. This versatility allows for easy adjustment of the composition of bioactive glasses, giving them specific properties tailored to meet the requirements of various biomedical applications. Sol-gel processing of bioactive glass particles (BGs) provides convenience and versatility in adjusting BG properties like size, shape, and pore structure. Moreover, sol-gel derived materials have demonstrated superior bioactivity, compositions, and processing parameters compared to traditional melt-quenching methods, making them advantageous for tissue engineering applications [Kaur et al., 2016]. Sol-gel derived bioactive glasses also exhibit critical interactions with proteins post-implantation, and the sol-gel process allows for the modification of surface properties, impacting protein adsorption. In summary, the sol-gel process offers enhanced control and adaptability in producing bioactive glasses with customized properties for biomedical applications compared to melt-quenching.

As compared with the conventional melt quench synthesis, the sol–gel synthesis method allows the production of glasses with higher purity, high specific surface area and intrinsic porous structure owing to the advantages of low-temperature processing [Zhong & Greenspan, 2000]. Lin et al. [2012] demonstrated that sol-gel derived Na_2O-CaO-SiO_2 glass compositions exhibit bioactivity across a wider range of compositions compared to glasses derived from melt processes. The study used bioactive glass ointments made by mixing sol-gel synthesized silicate glass (58S) with a composition of 58% SiO_2, 33% CaO, and 9% P_2O_5, nano bioactive glass (58S), and melt-derived 45S5 bioglass powder with 18 wt% Vaseline to treat full-thickness excision wounds. In all cases, adding bioactive glass to Vaseline improved and accelerated

wound healing and vascularization. Furthermore, sol-gel derived silicate glasses showed significantly better healing rates compared to melt-derived 45S5 bioglass [Deshmukh et al., 2020].

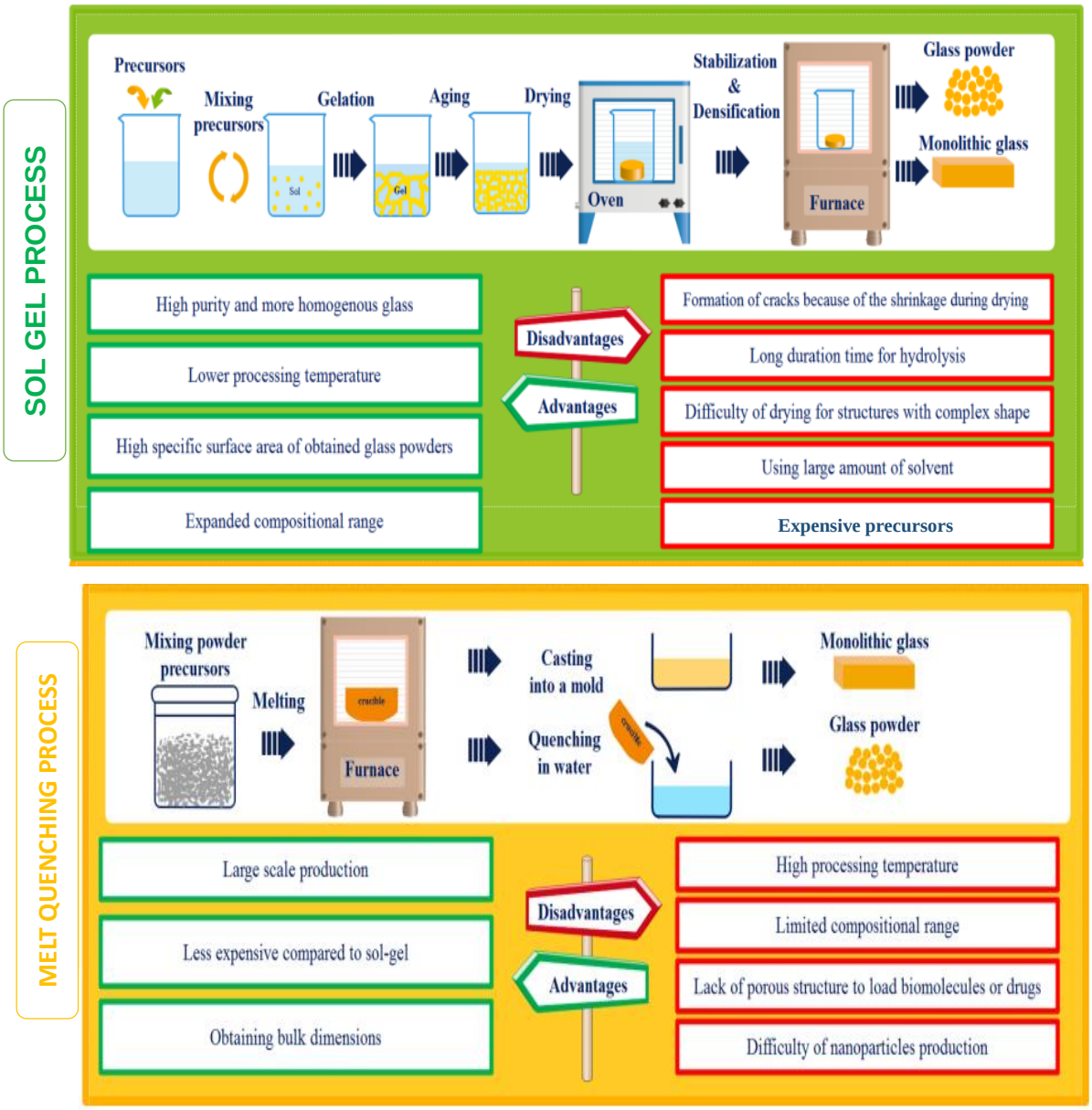

Fig. 2.2. Schematic representation of sol−gel and melt-quenching processes and the comparison of their advantages and disadvantages

2.4.4. Synthesis of bioactive glass based micronanofibres

Bioactive glass (BG) based micronanofibers have the ability to mimic the collagen and fibronectin fibrils present in the extracellular matrix (ECM). These fibers are favorable for the attachment, proliferation, differentiation, and migration of cells, making them promising materials for tissue engineering and regenerative medicine.

For fabrication of electrospun BG based micronanofibers, BG can be synthesized both via melt-quench or the sol-gel derived approach. Both methods offer the means to produce micronanofibers with properties that resemble the natural ECM, facilitating their use in a wide range of biomedical applications [Nagrath et al., 2019; Parham et al., 2020].

(a) Melt derived BG fibres

Jung et al. [2011] at Mo-Sci in Rolla, Missouri, patented a technique for directly extracting bioactive glass (BG) fibers from the melt during the rapid cooling process. This process resembles the synthesis of melt-derived BG, where oxides and carbonates are melted in a platinum crucible at 900^{o} to 1500°C. The fibers are then manually drawn out or extracted through a bushing using a rotary drum [Zhou et al., 2016]. However, this method faces challenges in controlling fiber diameter, resulting in shorter fibers, and has a low fiber yield, with approximately 25% of the produced material ending up as beads. In a modified fiber extraction method anticipated by Zhou et al., high-pressure airflow (0.35 MPa) can be utilized to obtain fibres with longer and thinner texture, enhancing the quality of the fibers compared to the previous method [Zhou et al., 2016].

An alternative method for synthesizing BG fibers involves processing melt-derived monoliths. Quintero et al. [2009] introduced the laser spinning technique, which generates uniformly long and cylindrical BG fibers with diameters ranging from 200 to 300 nm. This method is versatile and can be applied to various BG compositions incorporating therapeutic ions such as magnesium, zinc, and strontium, among others [Echezarreta-Lopez et al., 2017]. However, the fibers may not be entirely uniform in size, ranging from tens of nanometers to 5000 nanometers [Echezarreta-Lopez et al., 2014]. Additionally, the yield of usable fibers is limited, with the remaining material consisting of beads and colloids.

(b) Sol-gel derived BG fibres

The sol-gel method often employs electrospinning to generate very fine fibers. In this process, a sol-gel solution is ejected from a syringe needle under high voltage, whipping it into long and uniform fibers that are deposited on a collector [Homaeigohar et al., 2020; Xue et al., 2019]. Several factors such as voltage that had been applied, humidity, surrounding temperature, sol and cation content, viscosity, distance to the collector, and collector type can affect the morphology of the fibers produced [Reneker et al., 2000; Tan et al., 2005; Norris et al., 2020].

Electrospinning is a technique for generating ultrafine fibers by forcing a solution through a syringe needle under high voltage. Although the concept dates back to the 1600s and was patented in 1934 by Formhales, it gained significant attention at the beginning of this century. Electrospun fibers closely resemble the fibrils found in the extracellular matrix (ECM), such as collagen and fibronectin, with diameters typically ranging from 100 to 700 nanometers [Bhardwaj et al., 2010]. This structural similarity makes them highly favorable for cellular connection, proliferation, and migratory behavior. Polymers are frequently electrospun because they are typically soluble in organic solvents and can be easily processed.

- **Electrostatic Force and Charge Repulsion:**

At the heart of the electrospinning process is the fundamental principle of electrostatic repulsion. When a high voltage is applied to a polymer solution or melt, an electric field is generated. This electric field imparts an electric charge to the polymer solution or melt. The electrostatic repulsion within the charged polymer material overcomes the surface tension, causing the material to form a thin jet. This charged jet is ejected from the tip of the spinneret [Xue et al., 2019; Homaeigohar et al., 2020]. By rising up the intensity of the electric field, the hemispherical exterior of the formed solution globule extends, leading to the formation of a cone-shape [Taylor cone, Fig. 2.3.] [Stocco et al., 2018]. When the electric field approaches a crucial value (repulsive electrical forces exceed surface tension forces), a charged jet of the polymer solution can be expelled from the Taylor cone [Li et al., 2016].

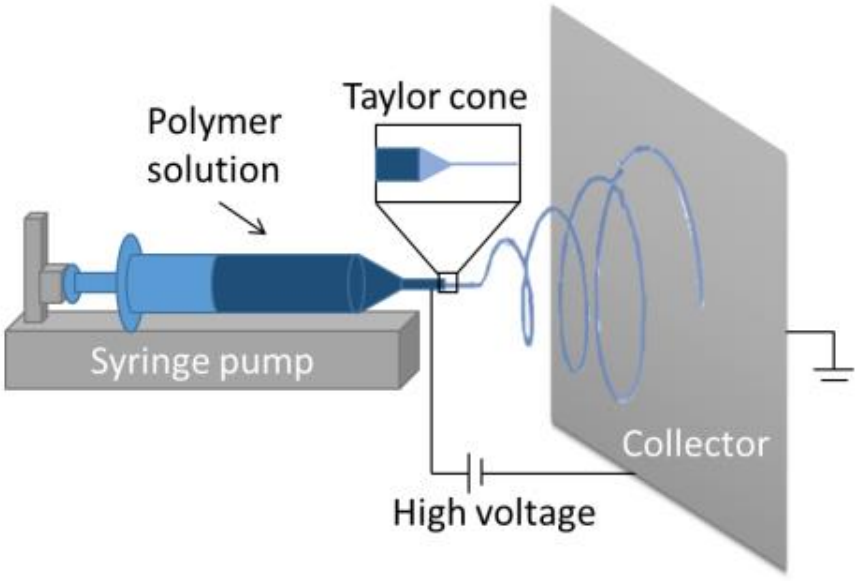

Fig. 2.3. Schematic overview of the electrospinning process.

- **Polymer Solution or Melt:**

The starting material for electrospinning is a polymer solution or polymer melt. The choice of polymer and, if applicable, the solvent is crucial, as it determines the physical and chemical properties of the resulting fibers. The polymer should have appropriate rheological properties and electrical conductivity for successful electrospinning [Haider et al., 2013, Pillay et al., 2013; Haider et al., 2018].

- **Spinneret Design:**

The spinneret, typically a needle-like device, plays a crucial role in shaping the electrospun fibers. The spinneret can have a single nozzle or multiple nozzles, and the size and shape of these nozzles influence the morphology and diameter of the resulting fibers [Baumgarten, 1971, Matabola and Moutloali, 2013, Wang and Kumar, 2006]. The choice of spinneret design can be tailored to specific applications, allowing for control over fiber characteristics.

- **Collector Setup:**

A grounded or oppositely charged collector is positioned at a certain distance from the spinneret. The collector serves as the target for the ejected jet of polymer material. As the charged jet travels toward the collector, it undergoes a stretching and whipping process due to the electrostatic forces, which lead to the thinning and solidification of the jet, resulting in the formation of ultrafine fibers. The distance between the spinneret and collector can affect the fiber alignment and diameter [Zhao X., 2022].

A rotating collector to the electrospinning process provides extra force in addition to high shear, and elongation forces that help orient the chains and align the lamellae in the fibre axis direction. The rate of solvent evaporation is also increased, contributing to a decrease in diameter [Ojha S., 2017].

- **Fiber Diameter Control:**

Several parameters can be adjusted to control the diameter of electrospun fibers. These parameters include the viscosity of the polymer solution, the concentration of the polymer in the solution, the applied voltage, and the distance between the spinneret and collector. Higher polymer concentrations, greater applied voltages, and smaller distances between the spinneret and collector can yield smaller fiber diameters [Haider et al., 2018].

- **Post-processing:**

Electrospun fibers may undergo post-processing steps to further enhance their properties. Common post-processing techniques include crosslinking, heat treatment, or surface modification. These steps can improve the mechanical strength, chemical resistance, and bioactivity of the fibers, making them suitable for specific applications, such as tissue engineering or filtration [Zhao X., 2022].

Electrospinning is a versatile and widely used technique, offering precise control over fiber size and morphology. The resulting fibers have an exceptionally high surface area-to-volume ratio, making them ideal for applications in fields like materials science, nanotechnology, drug delivery, and tissue engineering [Haider et al., 2018]. Researchers continue to explore new materials and methods to expand the range of applications for electrospun fibers.

2.4.5. Versatility of different ion containing bioactive glass in wound healing and hemostasis

Various chemical elements from the periodic table exist within human tissues, playing crucial roles in maintaining bodily functions and overall health [Kaur et al., 2014; Chitturi et al., 2015]. These elements are essential for cell functions, enzymatic reactions, maintaining acid-base balance, and regulating body fluids. The physiological effects of these elements are dose-dependent: elements like arsenic and cadmium can be medicinal in low concentrations but toxic in high amounts, while essential elements like calcium, potassium, and sodium can cause life-threatening problems if present in excessive amounts [Anke et al., 2004].

Chemical elements in the body can be categorized based on their concentration and biological roles. One classification relevant to glass composition includes macro-elements, trace elements, and ultratrace elements.

- Macro-elements: These include oxygen (O), carbon (C), hydrogen (H), nitrogen (N), calcium (Ca), phosphorus (P), potassium (K), sodium (Na), sulfur (S), chlorine (Cl), and magnesium (Mg). Their concentration in the body exceeds 0.01%, and they are considered "structural elements" because they form the mass of cells and tissues [Skalnaya et al., 2018].
- Trace elements: These include iron (Fe), zinc (Zn), fluorine (F), strontium (Sr), molybdenum (Mo), copper (Cu), bromine (Br), silicon (Si), cesium (Cs), iodine (I), manganese (Mn), aluminum (Al), lead (Pb), cadmium (Cd), boron (B), and rubidium (Rb). Their concentration ranges from 0.00001% to 0.01%, amounting to hundreds of milligrams to several grams in the human body [Skalnaya et al., 2018].
- Ultratrace elements: These include selenium (Se), cobalt (Co), vanadium (V), chromium (Cr), arsenic (As), nickel (Ni), lithium (Li), barium (Ba), titanium (Ti), silver (Ag), tin (Sn), beryllium (Be), gallium (Ga), germanium (Ge), mercury (Hg), scandium (Sc), zirconium (Zr), bismuth (Bi), antimony (Sb), uranium (U), thorium (Th), and rhodium (Rh). Their concentration is less than 0.000001%, measured in milligrams or micrograms [Skalnaya et al., 2018].

Certain trace elements are vital, such as selenium (Se), iodine (I), zinc (Zn), copper (Cu), cobalt (Co), iron (Fe), manganese (Mn), and molybdenum (Mo) [Skalnaya et al., 2018; Zoroddu et al., 2019]. Others, like boron (B), silicon (Si), arsenic (As), fluorine (F), lithium (Li), bromine (Br), nickel (Ni), and vanadium (V), are considered "conditionally essential" [Skalnaya et al., 2018].

The ionic dissolution products of bioactive glasses play an active role in wound healing by affecting molecular and cellular processes in the body [Zoroddu et al., 2019]. The following sections will discuss the biological significance of elements such as copper, zinc, boron, calcium, cobalt, silicon, aluminum, gallium, and tantalum in wound healing and hemostasis.

a) Wound healing

Copper:

Copper (Cu) is known for its anti-inflammatory properties, often used in complexes to enhance the effects of non-steroidal anti-inflammatory drugs (NSAIDs) while reducing their toxicity [Weder et al., 2002; Hussain et al., 2019; Psomas et al., 2020]. Cu plays a crucial role in wound healing by mitigating inflammation and oxidative stress through various mechanisms: (a) Redox Reactions: Cu participates in redox reactions to scavenge and neutralize harmful reactive oxygen species (ROS) and free radicals, reducing oxidative stress and inflammation [Wilkinson et al., 1987]. (b) Enzymatic Activity: Cu acts as a catalyst for enzymes like matrix metalloproteinases (MMPs), hydroxylases, and oxidases, which break down ROS and prevent inflammation. (c) Superoxide Dismutase Activity: Cu mimics the activity of superoxide dismutase, neutralizing superoxide anions and preventing inflammation. (d) OH^-Inactivation: Cu complexes with OH^- inactivating ligands can neutralize hydroxyl free radicals, mitigating their inflammatory effects [Berthon et al., 1993]. Ceruloplasmin, a protein binding plasma Cu, increases under inflammatory conditions, demonstrating a protective role in inflammation. In Cu-containing mesoporous bioactive glasses (MBGs), Cu stimulates macrophage migration and switches macrophage phenotype from pro-inflammatory M1 to anti-inflammatory M2. This transition is associated with increased expression of cytokines like IL-1 and IL-1ra.

In vivo tests show that Cu-MBGs induce a low inflammatory response and promote angiogenesis. BGs with compositions like $75SiO_2$-15CaO-5CuO-$5P_2O_5$ decrease pro-

inflammatory markers TNF-α and IL-18, increase anti-inflammatory cytokine IL-10, and shift macrophage markers from M1 (iNOS) to M2 (CD206). These results highlight the potential of Cu-containing BGs to modulate inflammation and promote healing [Lin et al., 2019].

Copper is known to promote angiogenesis through various mechanisms, including the activation of signaling pathways that lead to the upregulation of angiogenic factors. In bioactive glasses (BGs), the addition of copper has shown mixed results in stimulating blood vessel formation in animal models, with some concentrations being toxic. However, *in vitro* studies have generally demonstrated positive effects of copper-containing BGs on angiogenesis, promoting vessel density and stimulating VEGF expression and tubule formation. Incorporating copper into BGs loaded into organic scaffolds has also been shown to enhance angiogenesis, making them promising for promoting blood vessel formation in regenerative medicine applications [Berthon et al., 1993].

Copper (Cu) promotes the migration of keratinocytes by influencing integrin activity and enhancing the presence of PCNA and p63 in these cells. Cu-based superoxide dismutase (SOD) stimulates keratinocyte proliferation and migration, while its paracrine effect induces the expression of EGF and IGF as part of its anti-inflammatory properties [Zhao, 2022].

Cu-doped bioactive glass (Cu-BG) fibers, resembling the ECM, promote epithelial cell migration and wound closure. Cu-doped 1393-B3 glass microfibers significantly accelerate wound closure in rodent models, surpassing Cu-free BGs and controls, and promote HUVEC tubule formation *in vitro*. Cu-BGs are incorporated into scaffolds or hydrogels to promote wound closure. For instance, Cu-containing SiO_2-CaO-P_2O_5 BG nanocoating enhances diabetic wound closure, and Cu-doped BG-coated eggshell membranes stimulate faster wound closure in mice. Cu-containing 1393-B2 in PLGA scaffolds promotes wound closure in rat models [Lin et al., 2019].

Copper (Cu) is crucial for connective tissue as it binds with lysyl oxidase, an enzyme necessary for collagen and elastin crosslinking. Copper deficiency can down-regulate collagen synthesis, especially in bone tissue. Cu also stabilizes fibronectins, with concentrations over 0.06 mg/L enhancing stabilization. Cu-containing fibers improve extracellular matrix (ECM) protein attachment and promote greater collagen deposition and organization. Cu-containing bioactive glasses (Cu-BGs) stimulate increased collagen deposition and improved ECM arrangement in

various contexts, including hydrogels, membranes, and dressings. Histological examinations consistently show denser and more aligned ECM in Cu-BG-treated groups compared to controls [Zhao, 2022].

Zinc:

Zinc (Zn) acts as an anti-inflammatory ion through various mechanisms, including its regulatory effects on zinc transporter mRNA and its antioxidant properties. Here are some of the key mechanisms by which zinc exhibits anti-inflammatory effects: (a) Inhibition of NADPH Enzyme: Zinc inhibits the NADPH enzyme, which plays a role in the generation of reactive oxygen species (ROS). By inhibiting this enzyme, zinc helps reduce oxidative stress and inflammation. (b) Induction of Metallothioneins: Zinc induces the production of metallothioneins, which are proteins that bind to and regulate the levels of essential metals like zinc, copper, and cadmium. Metallothioneins can have protective effects against oxidative stress and inflammation. (c) Competition with Iron and Copper: Zinc competes with iron and copper for binding sites on the cell membrane. This competition prevents the production of hydroxyl radicals from iron and copper, which are highly reactive and contribute to oxidative damage. (d) Reduction of Cytotoxic Cytokines: Zinc reduces the production of cytotoxic cytokines, which are inflammatory signaling molecules. By decreasing the levels of these cytokines, zinc helps mitigate inflammation. (e) Promotion of Superoxide Dismutase (SOD): Zinc promotes the proliferation of the enzyme superoxide dismutase (SOD) [Prasad et al., 2002; Prasad et al., 2009]. SOD is responsible for converting superoxide radicals into less harmful molecules, such as hydrogen peroxide, reducing oxidative stress. Zinc also prevents apoptosis (cell death) and has anti-tumorigenic effects on both epithelial and endothelial tissues. It stimulates anti-inflammatory responses and promotes healing by supporting the production of nutrients and proteins that aid in tissue repair [Lansdown et al., 2007]. A deficiency of zinc can impair cytokine function and secretion, affecting the immune system's essential messengers.

In zinc deficiency, chemotaxis of leukocytes (movement of immune cells) and the production of ROS are inhibited, leading to prolonged inflammation. The delayed secretion of cytokines, ROS, and reduced macrophage chemotaxis underscores the potential of zinc for anti-inflammatory effects [Krizkova et al., 2012].

Regarding bioactive glasses (BGs), those containing zinc have demonstrated anti-inflammatory effects. For example, a phosphate BG containing zinc exhibited similar effects to 45S5 BG in terms of down-regulating the pro-inflammatory cytokine IL-6 and up-regulating the anti-inflammatory cytokine IL-10. However, 45S5 BG was found to be more toxic to lipopolysaccharide (LPS)-treated RAW cells [Lang et al., 2007]. In borosilicate glasses with various zinc concentrations, 5 mol% zinc incorporation induced the smallest M1/M2 ratio for THP-1 cells. This led to high expressions of anti-inflammatory markers like ARG and IL-10, as well as a paracrine effect that stimulated the expression of growth factors from human bone marrow stromal cells (hBMSCs). Similar anti-inflammatory effects were observed in chitosan-alginate hydrogels containing zinc-containing 58S BG nanoparticles, resulting in down-regulation of pro-inflammatory factors, enhanced wound closure, and angiogenesis *in vivo*. Compared to copper-containing BGs of the same composition, zinc-containing BGs were found to be more anti-inflammatory, further emphasizing the potential of zinc in modulating inflammation during the wound healing process [Tapiero et al., 2003].

Zinc (Zn) is known to promote angiogenesis by interacting with reactive oxygen species (ROS) and inducing the production of angiogenic factors like FGF-2 and VEGF, stimulating endothelial cell migration, proliferation, and blood vessel formation. However, some studies suggest Zn may also exhibit anti-angiogenic properties. In the context of bioactive glasses (BGs), Zn is often co-loaded with other elements, such as copper (Cu), to enhance angiogenesis. Co-loaded BGs have shown improved cell proliferation, migration, protein expression, angiogenesis, and wound healing in both *in vitro* and *in vivo* studies. Zn-containing BGs have also been found to induce higher VEGF secretion compared to Cu-containing BGs and control materials. Alginate/chitosan hydrogels containing Zn-containing BG nanoparticles have demonstrated a pro-angiogenic effect in rats, promoting sprout angiogenesis and showing a synergistic effect with epidermal growth factor (EGF) to enhance angiogenesis [Zhu et al., 2019].

Zinc (Zn) up-regulates integrins in keratinocytes and promotes their proliferation and migration, aiding in wound healing. Zinc-doped bioactive glass (Zn-BG) stimulates keratinocyte proliferation and re-epithelialization. For example, Zn-doped 58S BG nanoparticles in chitosan-alginate hydrogels promoted faster wound closure in rats. Combining Zn with copper (Cu) in

bioactive glasses (Cu-BGs) enhances wound healing, complicating the assessment of Zn's specific effects on epithelialization.

Zinc (Zn) can disrupt fibronectin and collagen alignment in the extracellular matrix (ECM) by inducing structural changes in the fibronectin binding domain. However, Zn also reduces collagen degradation and stimulates collagen synthesis in bone cells. While it may induce protease expressions like collagenase and elastase, Zn generally inhibits matrix metalloproteinases (MMPs) and prevents ECM degradation. Zn-doped 58S bioactive glass nanoparticle (NPs) enhance collagen deposition in a chitosan-alginate hydrogel, and a commercial product, Mirragen®, containing Zn and copper (Cu), promotes ECM deposition in treating diabetic ulcers [Bai et al., 2021].

Boron:

Borate and borosilicate glasses possess anti-inflammatory properties, primarily demonstrated through the inhibition of key inflammatory mediators like iNOS and COX-2, reduction in nitric oxide (NO) production, and stimulation of ROS metabolism [Demirci et al., 2016]. Boron-containing materials have shown effectiveness in reducing inflammatory responses, especially at higher concentrations. While research on the anti-inflammatory effects of borate bioactive glasses (BGs) is limited, their rapid dissolution kinetics make them promising for delivering therapeutic ions and drugs. For example, boron-containing mesoporous bioactive glass (MBG) scaffolds have been used to incorporate biomimetic anti-inflammatory nano-capsules, effectively blocking the production of pro-inflammatory cytokines and promoting M2 macrophage polarization, which is anti-inflammatory [Nielson et al., 1996; Yin et al., 2020].

Boron plays a significant role in cellular activities by binding to cis diol groups, allowing it to cross cell membranes and interact with RNA ribose moieties. Borate groups stimulate the translation of mRNA for factors like VEGF and TGF-β, promoting their expression in endothelial cells. In bioactive glass (BG), boron enhances angiogenic responses. BG compositions with boron, such as 45S5.2B, stimulate endothelial cell proliferation, migration, and tubule formation through increased ERK phosphorylation. Boron-containing BG fibers and particles also promote angiogenesis *in vitro* and *in vivo*.

Various BG compositions, including '01-06B1' and GL1550, induce higher expressions of angiogenic factors like VEGF and CD31 in endothelial cells. The addition of aluminum to borate BGs further enhances angiogenic factors. These boron-containing BGs show higher angiogenic capabilities compared to silicate-based glasses, making them promising for regenerative applications [Zhao, 2022].

The addition of boron to bioactive glass (BG) formulations enhances their re-epithelialization effects by promoting keratinocyte activities and increasing protein expressions essential for epithelialization. Studies have shown that wounds treated with boron-containing BGs exhibit significantly higher percentages of wound area recovery compared to treatments with pure BGs or BGs combined with growth factors. Boron ions promote keratinocyte migration and stimulate the production of growth factors involved in wound healing, such as G-CGF, GM-CGF, FGF-7, and TGF-β. *In vivo* experiments using rodent models with skin defects have demonstrated that borate-based BGs promote faster wound closure and reduce the extent of damaged tissue compared to traditional BGs and control groups [Demirci et al., 2016].

Boric acid and sodium pentaborate stimulate the deposition of laminin and fibronectin, key extracellular matrix (ECM) proteins, from fibroblasts. Borate-based bioactive glasses (BGs) show promise in promoting ECM deposition due to their rapid dissolution (about 5 times faster than silicate glasses) and ion release [Roy et al., 2023a]. Borate and borosilicate BGs, with non-cytotoxic boron release, outperform silicate-based BGs in collagen deposition for bone regeneration. Borate-based fibers mimic the ECM, aiding in ECM protein migration and deposition. Further research on the mechanisms behind these anti-inflammatory effects could have a significant impact on understanding their therapeutic applications.

Calcium:

Calcium serves as a primary regulator of keratinocyte differentiation [Law et al., 2015] by controlling the expression of specific genes involved in this process, such as transglutaminase, involucrin, loricrin, cytokeratin 1, cytokeratin 10, and filaggrin [Bikle et al., 2012; Subramaniam et al., 2021]. Increased calcium concentrations prompt keratinocytes to initiate differentiation and establish crucial intracellular mechanisms for this purpose. In addition, calcium regulates the formation of cell junctions like desmosomes, adherens junctions, and tight junctions. It also

activates the calcium-sensing receptor (CaSR), which is necessary to trigger the intracellular mechanisms governing keratinocyte differentiation and survival [Bikle et al., 2012; Hennings et al., 1983; Tu et al., 2008].

For fibroblasts, calcium is predominantly used intracellularly for contraction, which is vital for reducing wound size during healing. Intracellular calcium is essential for fibroblast cell adhesion, as it mediates actin remodeling and cadherin recruitment to intracellular junctions [Ko et al., 2001; Xue et al., 2015]. Calcium plays a pivotal role in various signaling pathways regulating angiogenesis [Berridge et al., 1998]. Many mitogens, including angiogenic factors, induce calcium influx by opening plasma membrane calcium channels or releasing calcium from intracellular stores like the endoplasmic reticulum [Munaron et al., 2006]. This influx is crucial for endothelial cell migration, adhesion, proliferation, and vessel formation in both *in vitro* and *in vivo* settings [Alessandro et al., 1996; Kohn et al., 1995].

During the inflammatory phase, high extracellular calcium can enter neutrophils, leading to an increase in intracellular calcium levels, which modulates neutrophil function [Immler et al., 2018]. In the proliferative phase of wound healing, extracellular calcium is crucial for epidermal homeostasis. The calcium-sensing receptor (CaSR) in keratinocytes promotes adhesion, differentiation, and survival by initiating intracellular calcium and E-cadherin-mediated signaling [Tu et al., 2008; Cordeiro et al., 2013]. The rapid increase in calcium ion propagation at the wound site acts as a transcription-independent signal for tissue damage, initiating epithelial healing [Cordeiro et al., 2013].

Cobalt:

Cobalt (Co) promotes angiogenesis by mimicking hypoxia [Tanaka et al., 2005], leading to the up-regulation of hypoxia-responsive factors like VEGF, FGF-2, and TGF-β. In bioactive glasses (BGs), Co-containing scaffolds have shown promise for angiogenesis in bone and cartilage tissues [Chen et al., 2020; Barrioni et al., 2018; de Laia et al., 2021]. Co-containing BGs stimulated higher VEGF secretion from MSCs and increased neo vessel formation in animal models compared to Co-free BGs. Specific types of Co-BGs, such as 58S Co-BG, promoted HIF-1α and VEGF expression in endothelial cells and enhanced tubule formation [Kargozar et al., 2017; Lee et al., 2013]. Composites containing Co-BGs have been proposed for wound

angiogenesis, promoting HUVEC proliferation, migration, and tubule formation [Quinlan et al., 2015]. Increasing Co concentration in BGs generally led to higher HIF-1α and VEGF expression, although higher Co concentrations did not significantly affect VEGF expression [Hoppe et al., 2014].

Silicon:

Silicon is the third most abundant trace element in the human body. It is predominantly found in connective tissues such as bone, skin, and blood vessels. Silicon plays a crucial role in bone mineralization and osteogenesis. Additionally, silicon released during the degradation of silicon-containing biomaterials, like bioactive glasses, has been shown to stimulate the secretion of pro-angiogenic growth factors. Silicon also enhances the strength and elasticity of the skin. It is vital for the optimal synthesis of collagen and the formation of the collagen network, as well as being involved in the synthesis of glycosaminoglycans and the activation of hydroxylation enzymes [Roy et al., 2023b, Zhao X, 2022].

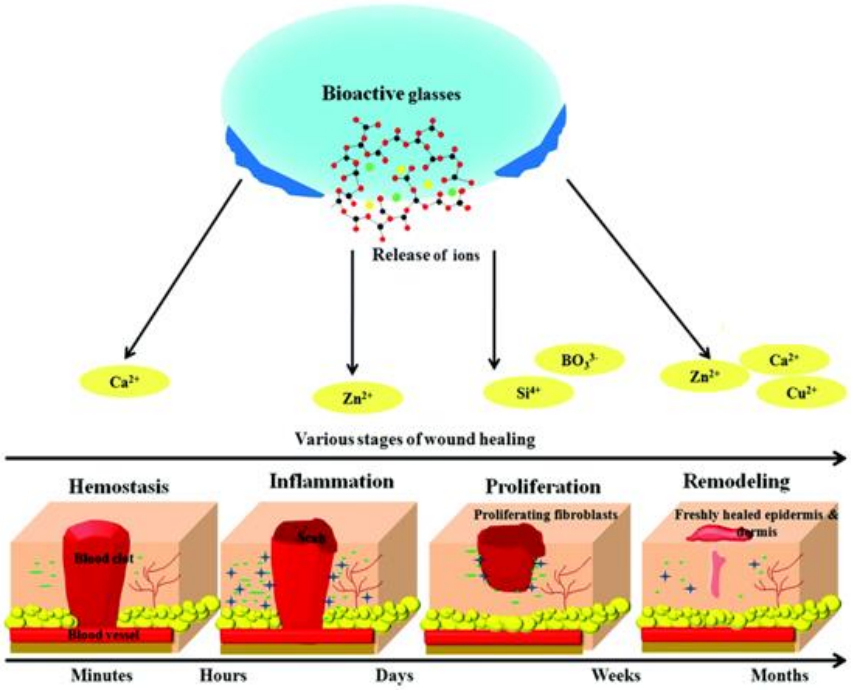

Fig. 2.4. Schematic representation of bioactive glass (BG) dissolution products and their roles in distinct stages of wound healing.

b) Hemostasis

Silica-based inorganic materials have been used in wound healing for their hemostatic properties. Kaolin clay-impregnated gauze, such as QuikClot®, has been used for over a decade to stop severe bleeding. Other materials like silica nanoparticles, mesoporous silica, and silicate clay have also been employed as hemostatic agents. The effectiveness of these materials is attributed to soluble silicate ions, which promote platelet aggregation through pathways involving MMP2 and adenosine diphosphate. They also have high absorption capabilities, condensing coagulation factors and generating Si-O functional groups on their surfaces, which activate factor XII of the intrinsic coagulation pathway.

However, there are limitations to these materials. For example, QuikClot® has poor biodegradability and can induce an exothermic reaction that may lead to tissue damage, foreign-body reactions, and thrombosis. As a result, the FDA has imposed restrictions on their use.

In contrast, bioactive glasses (BGs) are a newer approach in wound healing. BGs release therapeutic ions such as silicon (Si) and calcium (Ca^{2+}), which play crucial roles in the coagulation cascade. For instance, calcium ions are involved in thrombin regeneration and stimulate platelet chemotaxis, adhesion, and enzyme activation. Incorporating calcium into the silicate network of sol-gel glasses increases their pore size and surface area, enhancing their absorption abilities.

Ostomel et al. [2006] developed a hemostatic BG using SiO_2-CaO-CaP sol-gel microspheres and found that it enhanced clot initiation, growth, and ultimate clot strength. Similarly, the addition of calcium to silica has been shown to improve clotting kinetics both *in vitro* and *in vivo* using animal models. However, excessive calcium ions can have a negative hemostatic effect by inducing apatite formation. Incorporating Ca^{2+} into BGs enhances their absorption abilities and pore size, leading to increased clot stiffness and platelet aggregation. Bioactive glasses exhibit hemostatic properties through diverse mechanisms. One significant mechanism involves their capacity to initiate the coagulation cascade, leading to the formation of blood clots. This initiation is facilitated by ions such as Ca^{2+} (clotting factor IV) present in the composition of bioactive glass. These ions interact with proteins within the blood, initiating the clotting process and promoting hemostasis [Pourshahrestani et al., 2016; Pourshahrestani et al., 2019].

Furthermore, the surface characteristics of bioactive glasses play a vital role. Their high surface area and porosity create an environment conducive to platelet adhesion and activation. Platelets adhere to the surface of bioactive glasses, where they become activated and release factors that further promote clot formation [Ostomel et al., 2006].

Recent studies have demonstrated that adding a low concentration (1 mol%) of therapeutic gallium ions (Ga^{3+}) to bioactive glass enhances thrombus formation, activates blood coagulation, and improves its biodegradability and biocompatibility [Pourshahrestani et al., 2017]. In another study, researchers investigated the role of tantalum (Ta)-containing bioactive glass in hemostasis. Although the exact mechanism is not fully understood, it is believed that Ta can modify the glass network to expose more negatively charged silanol groups, providing a highly negatively charged surface that enhances hemostasis [Nagrath et al., 2021].

While such research on heavy metal ion-incorporated bioactive glasses shows promise, prolonged exposure to heavy metals can lead to various health issues, including skin allergies, severe redness, swelling, skin ulcers, cellular death, DNA damage, oxidative stress, neurotoxicity, memory loss, reproductive failure, and carcinogenic effects. Overall, BGs show great promise in hemostasis due to their ability to release therapeutic ions and enhance clotting mechanisms. Further research is needed to optimize their formulations and understand their full potential in clinical applications.

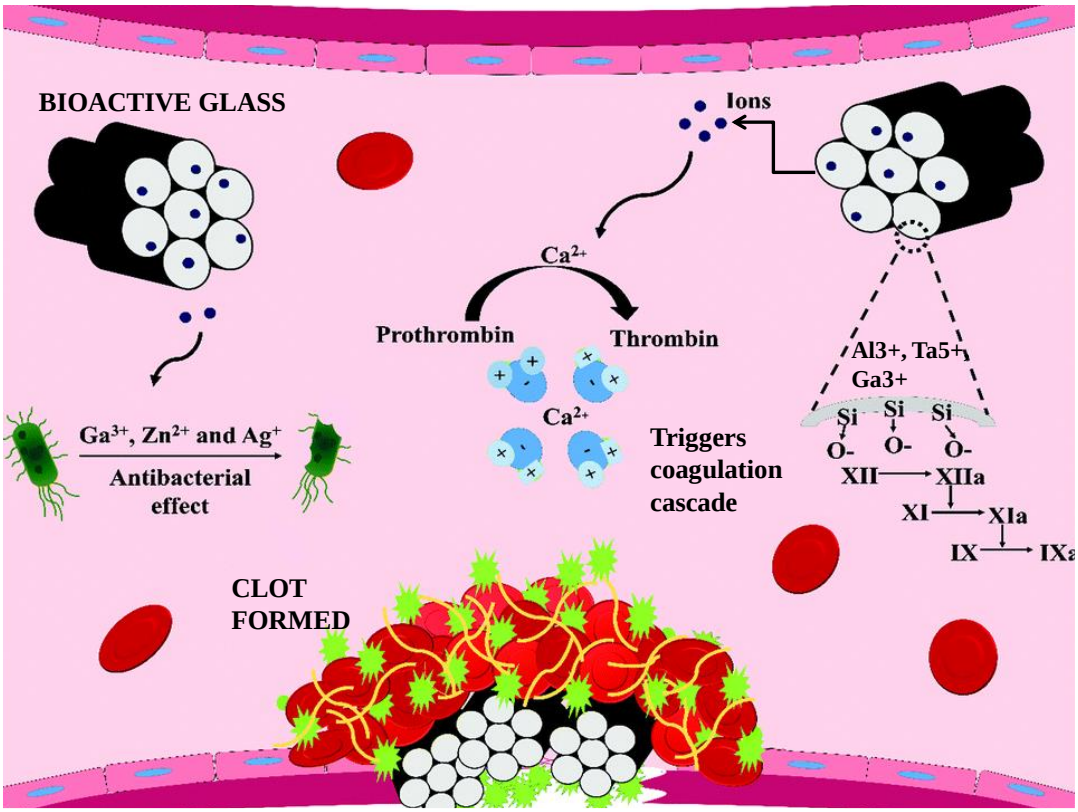

Fig. 2.5. The bioactive glass demonstrates effective hemostatic properties and antibacterial effects through distinct mechanisms. Their negative surface charge activates the intrinsic pathway of the coagulation cascade, leading to rapid hemostasis. Additionally, these materials accelerate thrombin formation by releasing Ca^{2+} and other ions (e.g., Al^{3+}, Ga^{3+}) and concentrate blood components, promoting clot formation. Their high water absorption capacity, facilitated by Ca^{2+} interactions with water molecules in their pores, further supports clotting. Moreover, these materials release therapeutic elements that contribute to their antibacterial effects.

Table 2.2: Role of various ions in wound healing and hemostasis application

Therapeutic ions	Application in wound healing & hemostasis
Zinc (Zn^{2+})	Improving epidermal keratinocyte proliferation and migration, showing antioxidant effects. Also, inhibition of bacterial growth and thereby prevention of infection.
Copper (Cu^{2+})	Regulation of the activity of proteins involved in wound healing such as VEGF (enhancing angiogenesis) and maturation of collagen and elastin. Inhibition of bacterial growth and thereby prevention of infection.
Calcium (Ca^{2+})	Improving hemostasis. Modulation of keratinocyte proliferation and differentiation. Improving fibroblast proliferation. Improving type I collagen synthesis and the increasing ratio of collagen I/III.
Cobalt (Co^{2+})	Cobalt ions (Co^{2+}) are also known as hypoxia mimetic agents which can enhance blood vessel formation by stabilizing hypoxia inducible factor-1 alpha (HIF-1α). The stabilization of this transcription factor in response to hypoxic conditions results in the activation of angiogenic mediators, including vascular endothelial growth factor (VEGF), thus promoting angiogenesis.
Boron[$(BO_3)^{3-}$]	Acceleration of wound healing via activation of angiogenesis (overexpression of VEGF and TGF β). Enhancing the proliferation, migration and production of vital growth factors of dermal cells.
Silicon (Si^{4+})	It has been shown that silicon released during the degradation of silicon-containing biomaterials (e.g., bioactive glasses) stimulates the secretion of pro-angiogenic growth factors. Silicon improves the strength and elasticity of the skin. Moreover, it is an important element for optimal synthesis of collagen and collagen network

	formation, and also it involves in glycosaminoglycans synthesis and activating the hydroxylation enzymes.
Aluminum (Al^{3+})	It can promote hemostasis by interaction with various coagulation factors such as fibrinogen and prothrombin, which are essential for clot formation. Al^{3+} ions influence the platelet activation, leading to formation of platelet plug at the site of injury.
Gallium (Ga^{3+})	Low concentration of therapeutic Galium ions into bioactive glass matrix not only enhanced its capability of platelet aggregation, thrombus formation and blood coagulation activation but also improved its biodegradability and biocompatibility.
Tantalum (Ta^{5+})	Ta accelerates hemostasis is not completely understood. It is believed that Ta can modify the glass network to expose more of negatively charged silanol groups to provide a highly negatively-charged surface to enhance hemostasis.

Chapter 3: Objectives

The specific objective of the present study includes:

3.1. Part A

Objective 1:

Synthesis and characterization of antibacterial (Ag^+ incorporated) bioactive glass (acronym, AgBG) composition.

- Synthesis of AgBG having composition [(70-x) mol% SiO_2, (30-y) mol% CaO, with x ranging from 1 to 5 mol% for B_2O_3, and y ranging from 0.001 to 0.1 mol% for Ag_2O] using the sol-gel method.
- *In vitro* physicochemical characterizations such as XRD, TG-DSC, FTIR, FESEM, zeta potential, BET, and Angle of Repose to assess the properties of AgBG followed by *in vitro* cytotoxicity assay for it's cytocompatibility.

Objective 2:

Fabrication of antibacterial bioactive glass-based micronanofibers (ABGmnf) via electrospinning technique and *in vitro* physicochemical and biological assessments.

- Fabrication of ABGmnf based wound care matrix using the aforementioned glass composition by adding AgBG of a particular particle size range to an FDA-approved polymer solution in a specific ratio to achieve the desired rheological properties for the electrospinning process.
- *In vitro* material characterizations on the as-prepared ABGmnf, such as XRD, FTIR, TG-DSC, FESEM, solubility and mechanical property assessment.
- *In vitro* biological assessments to determine ABGmnf's wound healing potential. This involved conducting an *in vitro* cytotoxicity assay, followed by immunofluorescence staining to visualize cellular morphology and proliferation after ABGmnf based wound care matrix treatment. Subsequently, 2D wound healing assay and antibacterial assays were conducted to determine the minimum inhibitory concentration (MIC) and zone of inhibition (ZOI) following standard protocols.

Objective 3:

Evaluation of the *in vivo* biocompatibility, toxicity, pharmacokinetics and wound healing properties of the fabricated materials using Wistar rats.

- *In vivo* assessment of the biocompatibility and host immunogenic response, followed by toxicity evaluation through hemogram analysis and histological examinations.
- Single-dose dermal pharmacokinetic and biodistribution study of the ABGmnf based wound care matrix.
- *In vivo* comparable efficacy study of the ABGmnf based wound care matrix compared to a market brand, followed by histopathological assessment.

3.2. Part B

Objective 1:

Synthesis and characterization of an antibacterial bioactive glass (Al^{3+} incorporated) composition having hemostatic properties (Al-BAG/AlBG).

- Synthesis of Al-BAG having composition 70 mol% SiO_2, (30-x-y) mol% CaO, x mol% Al_2O_3, and y mol% ZnO, where x ranges from 10 to 18 mol% and y ranges from 0 to 8 mol%, using the sol-gel method.
- Physicochemical characterizations, including XRD, FTIR, TG-DSC, BET, particle size analysis, and FESEM-EDX.
- *In vitro* degradation and ion release studies, as well as assessment of the efficacy of blood absorption.

Objective 2:

Assessment of the *in vitro* cytotoxicity, hemocompatibility, antibacterial properties, and hemostatic potential of the developed Al-BAG following standard protocols.

- *In vitro* biological assays, cytotoxicity assay, immunofluorescence staining to visualize cellular morphology after treatment with Al-BAG. Subsequently, hemocompatibility was assessed through a hemolysis test.
- Antibacterial activity assessment of Al-BAG using a Time-kill test method.

- Evaluating the hemostatic potential of Al-BAG through *in vitro* coagulation assays, including activated partial thromboplastin time (aPTT) and prothrombin time (PT), followed by thrombin generation, thrombus formation, platelet adhesion, red blood cell adhesion, whole blood clotting, and determination of the blood clotting index, all conducted according to standard protocols.

Objective 3:

***In vivo* dermal toxicity assessment histological analyses, to evaluate the material's safety. Additionally, the hemostatic potential of the material was also investigated:**

- Acute dermal toxicity assessment using Wistar rats, followed by histological examination.
- Evaluating the hemostatic potential of Al-BAG wrt clotting time and the percentage of blood loss.

Chapter 4: Experimental Procedures

4.1. Materials

Deionized and decarbonated ultrapure water (Millipore, specific resistivity: 18MΩ) has been utilized for all the experimental preparations and all chemicals were used in this study as received without undergoing purification process.

4.2. Reagents list

1. Tetraethyl orthosilicate (98%, TEOS, TCI)
2. Calcium nitrate tetrahydrate [Ca(NO3)2.4H2O, >99.0%] Emplura
3. Tributyl borate (TBB)- Sigma-Aldrich
4. Silver nitrate ($AgNO_3$) LOBA- ChemieIndoaustranal Co., Bombay
5. Polyvinylpyrrolidone (PVP, MW 40000)- SRL
6. Poly(ethyleneglycol)-block-poly(propyleneglycol)-block-poly(ethyleneglycol)[Pluronic® P123, Sigma-Aldrich]
7. Ethanol (EtOH) Emplura
8. Reagent grade hydrochloric acid (HCl), ACS
9. Reagent grade sulfuric acid (H_2SO_4), ACS
10. Aluminum nitrate nonahydrate [$Al((NO_3)_3.9H_2O$,>99.0%]-MERCK, India
11. Zinc nitrate hexahydrate [$Zn((NO_3)_2.6H_2O$, >99.0%]-MERCK, India
12. Sodium bicarbonate [$NaHCO_3$]- MERCK, India
13. Barium hydroxide [$Ba(OH)_2$]-MERCK, India
14. Dimethyl sulfoxide (BIOREAGENT) $(CH_3)_2SO$ Sigma-Aldrich, USA, 99.9%
15. Dulbecco's modification of Eagle's Medium (DMEM) Invitrogen, Carlsbad, USA, 99.0%
16. Phosphate buffered saline – Sigma-Aldrich, USA, 99.9%
17. 1X Trypsin-EDTA solution-Sigma-Aldrich, USA, 99.9%
18. Fetal Bovine Serum-Invitrogen, Carlsbad, USA, 99.9%
19. Filter (0.2 µm) sterilized-Millipore, USA
20. MTT powder (Thiazolyl blue tetrazolium bromide)3-(4, 5 dimethylthiazol e-2-yl)-2,5-phenyltetrazolium bromide, C18H18BrN5S Sigma-Aldrich,USA, 97.5%
21. TNF-α ELISA assay kit (ImmunoTag, USA)
22. IL-6 ELISA assay kit (ImmunoTag, USA)
23. TAT ELISA kit (ImmunoTag, USA)

24. LDH ELISA kit (ImmunoTag, USA)
25. Paraformaldehyde powder - Sigma-Aldrich, USA, 95%
26. Nutrient agar plate-MP001, HIMEDIA, India
27. Luria Bertani agar plate-MP1151, HIMEDIA, India
28. Sheep blood agar plate-MP1310, HIMEDIA, India
29. Antibiotic Antimycotic Solution 100X Liquid w/10,000 U Penicillin, 10mg Streptomycin and 25 µg Amphotericin B per ml in 0.9% normal saline, HIMEDIA, India
30. Gentamicin Ezy MIC^{TM} Strip (HLG) (0.064-1024 mcg/ml), HIMEDIA, India
31. Luria Bertani Broth, Miller (Miller Luria Bertani Broth), HIMEDIA, India

Sample Preparation:

The detailed synthesis of samples and experimental procedures are described below:

4.3. Experimental: Part A

4.3.1. Fabrication of ABGmnf based wound care matrix

4.3.1.1. Synthesis of AgBG

The bioactive glass composition denoted as AgBG comprises varying proportions: (70-x) mol% SiO_2, (30-y) mol% CaO, with x being within the range of 1 to 5 mol% for B_2O_3, and y ranging from 0.001 to 0.1 mol% for Ag_2O. This glass was synthesized using a straightforward sol-gel technique. The process involved creating a precursor sol by sequentially introducing tetraethyl orthosilicate (TEOS) as the SiO_2 source, calcium nitrate (for CaO), tetraethyl borate (TBB, asthe BO^{3-} source), and silver nitrate ($AgNO_3$, as the Ag source) into a solution of 1N HCl. Continuous stirring was performed until a clear solution formed. To initiate hydrolysis, each precursor was added separately to a predetermined volume of 1N HCl solution. Once the salts were completely dissolved, the subsequent salt was introduced. The resulting sol was then placed in an incubator at 60°C. After gel formation, the bioactive glass was obtained through heat treatment within the temperature range of 600°C to 650°C [Ebrahimi et al., 2023; Azari et al., 2023].

4.3.1.2. Preparation of polymer solution

A requisite quantity of PVP powder was added to ethanol to get a 10-15 % weight/volume PVP polymer solution that was stirred for 1:30-2h at 200 rpm.

4.3.1.3. Preparation of the solution for electrospinning

The previously mentioned AgBG powder was uniformly incorporated into the polymer solution at different weight-to-volume ratios (wt/v) of 6%, 12%, and 18%. Among these options, 6% was selected for the electrospinning process for its optimum rheological property for the electrospinning process. Before being loaded onto the electrospinning machine, the solution underwent a process of removing air bubbles to ensure its quality and performance [Alcaide et al., 2010].

4.3.1.4. Electrospinning procedure

The sol as prepared above was poured into a 5ml disposable syringe. The parameters for electrospinning [E- SPIN NANOTECH, Super ES-1] are optimized after several trials are given as follows:

a. Distance between Spinneret to collector: 7-10cm

b. Flow rate: 2-3 ml/h

c. Applied voltage:10-13kV

The as-spun fibres were collected on aluminum foil throughout the spinning and the fibres were collected from the foil [Fig. 4.1.].

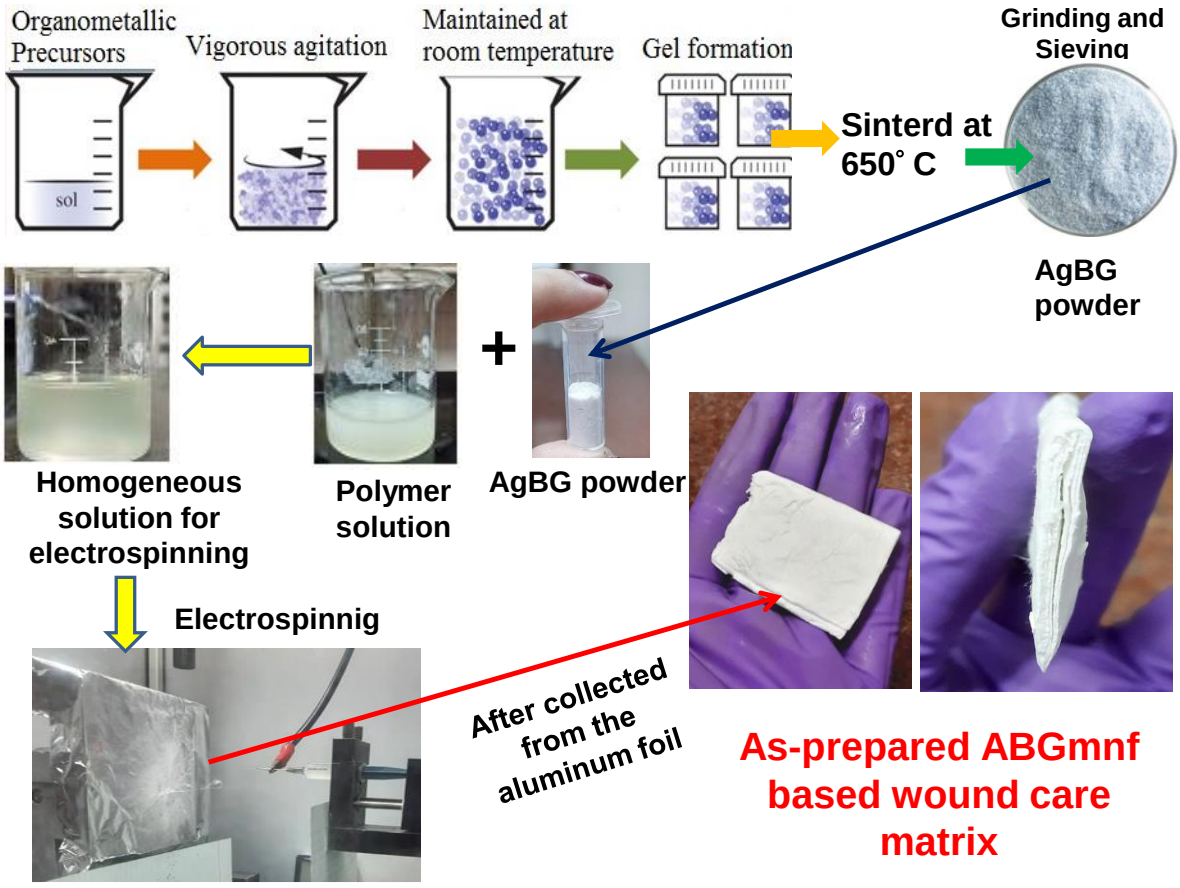

Fig. 4.1. The graphical illustrations of the fabrication of ABGmnf based wound care matrix.

4.3.2. Characterizations of AgBG and ABGmnf based wound care matrix:

4.3.2.1. *In vitro* material characterizations

a) X-ray diffraction (XRD)

X-ray diffraction (XRD) analysis of both the AgBG and ABGmnf based wound care matrix samples was conducted using a X'Pert Pro MPD diffractometer from Panalytical in Almelo, Netherlands. CuK_{α} radiation was employed as the X-ray source. The examination of the samples was performed in a range of 2θ angles from 20° to 80°, with a step size of 0.03° [Roy et al., 2023a].

b)FTIR

Fourier Transform Infrared Spectroscopy (FTIR) analysis of AgBG, both the PVP by itself and the ABGmnf based wound care matrix were performed using the KBr pellet method. This method involves mixing the sample with KBr (Sigma Aldrich, 99%) at a ratio of 1:100 (w/w). The analysis was conducted using a Spectrum 100 FTIR spectrometer from Perkin Elmer. The instrument's settings included a resolution of 4 cm^{-1}, averaging 50 scans, and a wavelength range spanning from 4000 cm^{-1} to 400 cm^{-1} [Roy et al., 2023a].

c)TG-DSC of AgBG and ABGmnf based woundcare matrix

The thermal characteristics of the AgBG and ABGmnf based wound care matrix were assessed using thermogravimetric analysis (TGA) and differential scanning calorimetry (DSC). TGA was conducted on NETZSCH STA 409 CD automatic thermal analyzer, where sealed samples underwent heating in an aluminum pan at a rate of 20°C/min from 50°C to 1000°C, with a constant nitrogen flow of 150 ml/min. For DSC measurements, the temperature range was -50°C to 1000°C, employing a heating rate of 15°C/min under a nitrogen atmosphere [Roy et al., 2023b].

d)FESEM of AgBG and ABGmnf based woundcare matrix

The morphology of AgBG powder and both the PVP matrix and the ABGmnf woundcare matrix were examined using Field Emission Scanning Electron Microscopy (FESEM) conducted with a

Carl Zeiss SMT AG SUPRA 35VP instrument. To prepare the specimens for analysis, they were mounted onto aluminum stubs and then sputter coated with palladium.

e)Zeta potential (ZP) measurement of AgBG

To assess the stability of AgBG particle suspensions, the zeta potential of the AgBG particles was measured using dynamic light scattering (DLS) with a Zetasizer (Malvern Instrument Ltd., UK). To approximate an *in vivo* ionic environment, the AgBG sample was suspended in deionized (DI) water with a pH of 7.4. Zeta potential measurements were conducted six times, with each measurement representing the average of 40 runs. Mean values and standard deviations were calculated. The instrument automatically determined electrophoretic mobility (U) and calculated the Zeta potential based on Smoluchowski's equation [Doostmohammadi et al., 2011].

$$\zeta = (U\eta)/\varepsilon$$

where, ζ is the Zeta potential, *U* is the electrophoretic mobility, η the medium viscosity and ε is the dielectric constant.

f)BET of AgBG

The N_2 adsorption-desorption isotherm was obtained using a [machine name]. Preceding the measurement, the sample underwent a 4-h out gassing procedure at 300°C under vacuum conditions. The specific surface area was determined through the Barrett-Emmett-Teller (BET) method. Pore volume and pore size distribution were assessed using the Barrett-Joyner-Halanda (BJH) method, focusing on the adsorption branches of the isotherms. The total pore volume was approximated based on the adsorbed quantity at the maximum relative pressure [Roy et al., 2024a].

g)Angle of repose of AgBG

By using the funnel method, angle of repose was determined. In a funnel, the accurately weighted blend AgBG was taken. Through the funnel, the AgBG was allowed to flow freely on to the surface. Table shows the relationship between angle of repose and powder flow

[Lechmann et al., 1991]. The radius of the powder cone and angle of repose were calculated by using the following equation:

$$\text{Tan}\theta = h / r$$

Where, 'h' represents the height of the powder cone formed and ‘r’ is the radius of the powder cone formed [Singh et al., 2014].

Table 4.1. Correlation between angle of repose and type of flow of the particles

Angle of repose	Type of flow
25	Excellent
25-30	Good
30-40	Passable
>40	Very poor

h) Mechanical property

To evaluate the tensile strength of the ABGmnf woundcare matrix, the test was performed according to ASTM D 882-10 (2010). The sample (ABGmnf based woundcare matrix and PVP matrix, as control) dimension with 100 mm×25mm×1mm was placed in the machine [Tinius Olsen 5 ST UTM, Aimil Ltd.] and the given load was 25 N. From the results obtained, it is possible to determine the comparative tensile strength of the ABGmnf based woundcare matrix and the PVP matrix [Roy et al., 2024b].

i)Solubility assessment

To conduct the water solubility assay according to OECD 105, we followed a stepwise procedure by adding increasing volumes of water at room temperature to ~ 0.1g of the sample in a 10 ml test tube. After each water addition, the mixture underwent a 10-min shaking period, and visually inspected for any residual undissolved parts of the sample [OECD 105].

In assessing the solubility of the ABGmnf based wound care matrix, a dissolution test was conducted using various polar solvents [5% HCl, 5% NaOH, 5% $NaHCO_3$, Methyl ethyl ketone

(MEK)] and non-polar solvent, Hexane. The test was carried out at room temperature (37^{o}C). The ABGmnf test sample was immersed in each selected solvent, followed by a 10-min shaking period. Any observable changes in appearance were noted and recorded over time.

4.3.2.2. *In vitro* biological assessment

a) *In vitro* cytotoxicity assay

The cell cytotoxicity assessment using the MTT assay was conducted with NIH3T3 cells. This evaluation took place over a span of 24, 48, and 72 h of incubation with extracts from AgBG powder, and ABGmnf based wound care matrix. In summary, the culture media was substituted with 200 µl of MTT solution (1 mg/ml), and the cells were then incubated in darkness for 4 hours at 37°C. This incubation led to the formation of formazan. Following this, 100 µl of dimethyl sulfoxide (DMSO) was introduced to dissolve the formazan after the removal of the MTT solution. Subsequently, the absorbance was measured at 595 nm using an ELISA reader. This absorbance reading is proportional to the number of viable cells. The MTT assay was performed in triplicate for each time point, and the statistical analysis was conducted with a significance level set at a value of $P < 0.05$ at 95% confidence intervals [Roy et al., 2023a].

b)Immunofluorescence staining

The NIH3T3 cells were seeded in 24-well plates at a concentration of 10,000 cell/ml. For cellular proliferation visualization, the NIH3T3 cells were culture with the extract of ABGmnf woundcare matrix for 24, 48 and 72h. Then, the cells were treated with 4% paraformaldehyde to preserve the cellular structure and prevent protein degradation. For permeabilization of the particular immunofluorescence stains (DAPI and FITC), cell membranes may be permeabilized using 0.04% of Triton X-100 and incubated for 30 min at 37^{0}C. Then, buffers were removed and cells were washed twice with 1X PBS. After that, cell nuclei stained with DNA-specific dye, DAPI solution was added to the cells and kept for 5-10 min in shaking at 50 rpm. Then washed twice with 1X PBS. For, stain the cytoskeleton of the cells, cells were treated with FITC solution and kept for 45 mins in dark in shaking at 50 rpm. After incubation, cells were washed three times with 1X PBS for 30 S each wash. Cells must be covered with 1X PBS prior to view under microscope [Bisht et al., 2022].

c)2D *in vitro* wound scratch assay

To assess the impact of the ABGmnf based woundcare matrix on the spreading and migration capabilities of NIH3T3 fibroblasts, a wound scratch assay was employed. Here's how it was carried out:

a) Cell Seeding and Confluence: Initially, 3×10^4 cells per well were seeded into 12-well culture plates and allowed to grow until they reached about 95% confluence.
b) Scratch Creation: A scratch was made on the cell monolayer using the sterile tip of a micropipette (100 µL). The area damaged by the scratch was then rinsed with phosphate-buffered saline (PBS) to eliminate the detached cells.
c) Addition of Extracts: To prepare the ABGmnf based wound care matrix extract, a known amount of the matrix was suspended in DMEM media at a concentration of 1 mg/ml for 24 hours at 37^0C. The resulting homogeneous suspension was filtered and used as extract for the experiment. The extract (as the sample treated) was added to one set of the culture plates, while another set received regular cell media (DMEM only) without the ABGmnf based wound care matrix (as the control).
d) Observation and Imaging: The migration behavior of the cells was observed and images were taken immediately after creating the scratch and up to 24 hours afterward. Microscopy equipped with a digital camera was used to capture these images.
e) Quantification of Wound Healing: The % of wound healing was assessed using the NIH Image J software. The rate of wound healing on the 2D wounds was quantified using the equation (1) mentioned below:

Rate of wound healing (%) = $[(A_0 - A_t) / A_0] \times 100\%$ (Eq. 1)

Where A_0 represents the initial wound area, and A_t represents the wound area at time t [Roy et al., 2023a].

This approach allowed for the evaluation of how the ABGmnf based wound care matrix promoted the migration and healing capabilities of NIH3T3 fibroblasts in response to scratch-induced wounds.

d) Antibacterial assay

Matrix preparation: To prepare PVP matrix, approximately 3g of PVP powder was added into the ethanol and stirred for 2hours to make homogeneous solution and loaded onto electrospinning machine [E- SPIN NANOTECH, Super ES-1]. The parameters are:

a. Distance between Spinneret to collector: 7-10cm
b. Flow rate: 2-3 ml/h
c. Applied voltage:10-13kV

The as-spun fibres were collected on aluminum foil throughout the spinning and the fibres were collected from the foil.

The ABGmnf based wound care matrix preparation has been described in experimental part A (4.3.1. to 4.3.4).

A. **Preparation of Disks:** The PVP matrix and ABGmnf based wound care matrix were cut into disk shapes with a diameter of 6 mm. These disks would be used for testing the antibacterial properties of the materials.
B. **Testing Procedure:** The testing procedure followed the guidelines outlined in the CLSI M02-A12 standard from 2015 [M02-A12, 2015], which is a recognized protocol for determining antimicrobial susceptibility. This standard provides a set of guidelines and recommendations for conducting antimicrobial susceptibility testing.
C. Streak Plate Method:

   A petri plate was held at a 60º angle. A loop containing a bacterial inoculum (a sample of the bacteria to be tested) was placed at one end of the plate. The loop was used to streak the inoculum in a zigzag pattern across the surface of the agar in the petri plate. This process helps evenly distribute the bacteria on the agar surface.

D. **Incubation:** The petri plate with the streaked bacteria was placed in an incubator at a temperature of 37ºC for 10-15 min. This step allows the bacteria to attach and start growing on the agar surface.
E. **Disk Placement**: After the incubation period, the prepared PVP and ABGmnf based woundcare matrix disks were placed onto the surface of the agar plate. These disks likely contain extracts of the respective materials [Roy et al., 2024b].
F. **Incubation for Zone of Inhibition (ZOI):** The agar plates, now containing the disks, were incubated again for a longer period (24 hours) at 37ºC. During this time, if the

materials have antibacterial properties, they will inhibit the growth of bacteria around the disks.

G. **Measurement of Zone of Inhibition (ZOI):** After the incubation period, the plates were examined. The areas around the disks where bacterial growth was inhibited were measured. This area is called the Zone of Inhibition (ZOI). A larger ZOI indicates stronger antibacterial activity of the tested materials.

e)Assessing the antibacterial efficacy through the determination of the minimum inhibitory concentration (MIC)

The bacterial strains were incubated overnight at 37°C in Luria broth (LB), an appropriate growth medium. The bacterial concentration was adjusted to 1.5×10^8 CFU/ml using a 0.5 McFarland Standard. A 96-well plate was used for the MIC determination as follows [Wayne et al., 2018]:

- 50 µl of Luria broth (LB) was added to wells in columns 2-11.
- In column 12, 100 µl of LB was added.
- In column 1, 100 µl of ABGmnf based wound care matrix extract was added. To prepare the extract, a known amount of ABGmnf based wound care matrix was suspended in LB at a concentration of 1 mg/ml for 24 hours under mild rotation (100-150 rpm, overnight). The resulting homogeneous suspension was filtered, and used as extract.
- A 2-fold serial dilution was conducted by transferring 50 µl from each well in column 1 to the subsequent wells in column 2. This mixing was achieved by pipetting up and down four times.
- This serial dilution procedure was repeated until column 10, after which the solution in column 11 was discarded.
- Then, 50 µl of the bacterial suspension was added to each well in columns 1-11.
- The plates were covered with a film and incubated at 37°C for 16-24 hours.
- The bacterial growth was assessed by measuring the optical density (OD) at 450 nm.
- The identical experimental procedure was conducted using both the gram-negative strain *Pseudomonas* and the gram-positive strains *Streptococcus pneumoniae* and

Staphylococcus aureus. The antibiotic Gentamicin was employed as a standard, and the corresponding MIC values for the aforementioned bacterial strains were established.

4.3.2.3. Unveiling the Dynamics: *In Vivo* Explorations for Comprehensive Insights

The animal study followed the OECD guidelines [OECD-402, 2017] at West Bengal University of Animal and Fishery Sciences (WBUAFS, Kolkata). Wistar rats were kept in cages under standard environmental conditions with a consistent temperature (25°C ± 3°C) and received regular provisions of standard diet and water.

a)Assessment of *in vivo* biocompatibility and host immunogenic response

All animal experiments were performed in compliance with OECD guidelines (OECD-402) at the West Bengal University of Animal and Fishery Sciences (WBUAFS, Kolkata) [OECD-402, 2017]. Six Wistar rats were housed in cages under standard environmental conditions, with a constant temperature maintained at 25°C ± 30°C. The rats were fed a standard diet, and water was provided daily.

For the biocompatibility assessment, an intracutaneous reactivity study was conducted following ISO-10993-10 guidelines [2010]. Rats were intradermally injected with ABGmnf based wound care matrix extracts, and the injection sites were observed over time, with edema (swelling) and erythema (redness) being scored. To prepare the ABGmnf based wound care matrix extract, a known amount of the matrix was suspended in DI water at a concentration of 1 mg/ml for 24 hours under mild rotation (100-150 rpm, overnight). The resulting homogeneous suspension was filtered, and intradermal injections were administered to three experimental Wistar rats, followed by the biocompatibility study as described above.

To evaluate the host immunogenic response, levels of pro-inflammatory cytokines like Interleukin-6 (IL-6) and Tumor Necrosis Factor-α (TNF-α) were assessed using ELISA Kits. Skin extracts were collected from the intradermal injection site, and the levels of IL-6 and TNF-α were determined following the manufacturer's guidelines (ImmunoTag).

b)Toxicity evaluation through hemogram analysis and histological examinations of leachable components of ABGmnf based wound care matrix

In this experiment, the ABGmnf based wound care matrix sample, prepared beforehand, was utilized. It was mixed with an appropriate vehicle to ensure adequate moisture and applied to the wound site for a duration of 4 hours. The experimental animals were separated into two groups, each consisting of 6 rats (with a 1:1 ratio of male to female). Wounds were created using the punch biopsy method, and the initial Ca^{2+} ion levels in the blood were determined using standard techniques, alongside the analysis of biochemical and hematological parameters, serving as the baseline at 0 hours. Subsequently, the matrix sample, prepared as mentioned, mixed with a suitable vehicle for improved absorption at the wound site, was applied and covered with transparent cellophane. After 4 hours, blood was collected from the wound site, and any remaining of the matrix was washed out for analysis of Ca^{2+} ion content. The concentration of leached Ca^{2+} ions in the composition was determined by subtracting this value from the initial Ca^{2+} ion concentration (at 0 hours), marking the end of the 4-hour observation period. Following this observation period, the animals were euthanized, and their vital organs, including the lungs, liver, kidneys, heart, and skin, were examined histopathologically [Banerjee et al., 2013].

c)Experimental design for single-dose dermal *in vivo* pharmacokinetic study of ABGmnf based wound care matrix

The *in vivo* dermal pharmacokinetic study of ABGmnf based wound care matrix was carried out in Wistar rats, which were divided into two groups: a control group receiving no treatment and an experimental group treated with ABGmnf on dermal defects created by Punch biopsy. Each group consisted of three rats. The experimental rats, following an overnight fast, were administered 12.5 mg of ABGmnf based wound care matrix dermally. Blood samples were collected at various time points (0h, 2h, 4h, 6h, 24h, 48h, 72h, 7th day, and 10th day post-administration) from the lateral tail-vein of mildly anesthetized rats into heparinized centrifuge tubes. Serum was separated by centrifugation at 4000g for 10 min at 4°C and stored at -80°C for further analysis [Majumdar et al., 2024; Prajapati et al., 2021].

Pharmacokinetic parameters such as the maximum serum concentration of Ca^{2+} (C_{max}) and the time taken to reach C_{max} (T_{max}) of ABGmnf based wound care matrix were determined from the serum concentration-time curve (AUC) using atomic absorption spectroscopy (AAS) with a Varian AA 240 Atomic Absorption Spectrophotometer. All pharmacokinetic parameters are reported as mean ± standard deviation (SD).

d)Experimental design for *in vivo* biodistribution study after single-dose dermal administration of ABGmnf based wound care matrix

To investigate the distribution of calcium ions released from ABGmnf based wound care matrix following dermal administration, rats were randomly assigned to two groups, mirroring the setup of the pharmacokinetics study. Each group received a single dermal dose of 12.5 mg ABGmnf based wound care matrix, consistent with the previous study. Subsequently, at specific time intervals (24h, 48h, 72h, and 7 days, post-administration), rats from each group were anesthetized, euthanized, and their vital organs (liver, spleen, kidney, heart, lung, and skin) were collected for analysis of calcium concentration [Majumdar et al., 2024]. The analysis of ionized calcium was done by using sophisticated technique like atomic absorption Spectroscopy (AAS) [Varian AA 240 Atomic Absorption Spectrophotometer]. After 7 days, the animals were sacrificed humanely using excess dose of Xylazine (5mg/kg BW) and ketamine (40 mg/kg BW) combination and final collection of blood sample was done through cardiac puncture. Followed by that, vital organs like liver, spleen, kidney, heart, lung and skin were collected and estimation of ionic Ca^{2+} was done.

***e)In vivo* wound healing assay**

Each animal underwent a shaving of the back and anesthesia via intraperitoneal injection of 1% pentobarbital sodium (30 mg/kg). Under sterile conditions, a full-thickness skin defect of 1 cm^2 was created on the rat's back using a custom-made stainless steel circular skin punch. In the experimental group (n=3/sex/group), the full-thickness skin wounds were treated with a single daily application of 12.5 mg dosage of ABGmnf based wound care matrix per animal. The positive control group received daily application of the commercially available Betadine onto the wound site, while the negative control group left the wound site untreated throughout the study, with all groups having dressings applied.

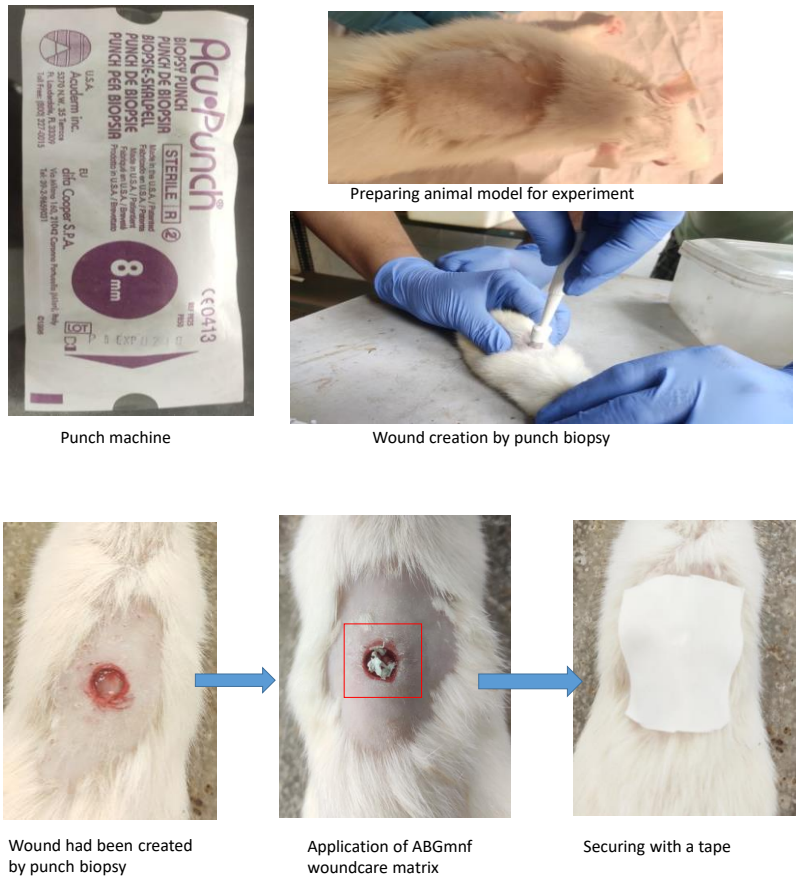

Fig. 4.2. The performance of the wound creation on the animal model and the application of the ABGmnf based wound care matrix for the wound healing experiment.

Photographs of all wound groups were taken on days 0, 7, and 14 using a digital camera, and a gross clinical scoring and assessment were conducted. Additionally, the reduction in wound area was measured at the same time intervals using ImageJ software. The percentage of wound area reduction was calculated using the formula [Dong et al., 2017]:

Wound healing rate = $[(A_0 - A_t) \times 100]/A_0$

Where, A_0 is the initial wound surface area and A_t is the wound surface area after time t.

On the 15th day, the animals were sacrificed, and histological evaluations of various organs (skin, heart, liver, lung, kidney, and spleen) were performed. The organs were fixed in 4% paraformaldehyde for 24 h, embedded in paraffin, and cut into 5 µm sections using a rotary

microtome (RM2016, Leica, Germany). The sections were deparaffinized, rehydrated, and stained with hematoxylin-eosin (H & E). Histological images were captured using a MOTIC A31e microscope.

f)Statistical evaluation

The information is shown as the average value plus or minus the standard deviation, derived from one of three representative experiments, each conducted in triplicate. Statistical significance was determined at a p-value less than 0.05, with a confidence interval of 95%.

Footnote: This work has been filed for an Indian patent.

'Antibacterial bioactive glass micronanofibre composition and process for preparation thereof', J. Chakraborty, S. Saha, P. Roy, R. Saha, App. No. 202111046618, INDIA, Filed, published on 14.04.23 [CSIR]

4.4. Experimental: Part B

4.4.1. Synthesis of Al-BAG/Al-BAG

The bioactive glass composition, denoted as Al-BAG, follows the formulation of 70 mol% SiO_2, (30-x-y) mol% CaO, x mol% Al_2O_3, and y mol% ZnO, where x ranges from 10 to 18 mole% and y ranges from 0 to 8 mole%. The synthesis of this bioactive glass was carried out through the sol-gel method.

For hydrolysis, the precursor sol was prepared by sequentially adding tetraethyl orthosilicate (as a source of SiO_2), calcium nitrate ($Ca(NO_3)_2 \cdot 4H_2O$, as a source of CaO), aluminum nitrate ($Al(NO_3)_3 \cdot 9H_2O$), and zinc nitrate hexahydrate ($Zn(NO_3)_2 \cdot 6H_2O$; as a source of ZnO) into 1N HCl. The mixture was continuously stirred until a clear solution was achieved. After proper dissolution of each salt, the next salt was added. The final sol was then incubated at 60°C. Following gel formation, the bioactive glass was obtained through heat treatment at 650°C.

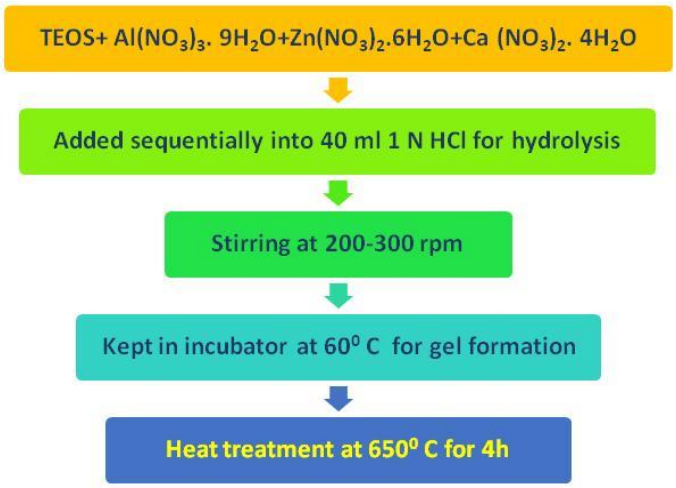

Fig. 4.3. Schematic representation of the synthesis of Al-BAG

4.4.2. Characterization of Al-BAG

4.4.2.1. *In vitro* material characterizations

a) XRD

The Al-BAG powder underwent characterization to analyze its distinctive crystalline phases through powder X-ray diffraction (XRD). The X-ray diffraction patterns were acquired using a CuKα radiation source on an X'Pert Pro MPD diffractometer (Panalytical, Almelo, Netherlands). The scanning of the Al-BAG sample was performed over a 2θ range of 15° to 80° with a step size of 0.03°.

b)FTIR

The Fourier Transform Infrared Spectroscopy (FTIR) spectra of Al-BAG were captured employing the KBr pellet method with a sample to KBr ratio of 1:100. The analysis was conducted on a Spectrum 100 FT-IR spectrometer (PerkinElmer) with a resolution of 4 cm^{-1}, an average of 50 scans, and a wavelength range from 4000 to 400 cm^{-1}.

c)TG-DSC

Thermal analysis, specifically Thermogravimetry and Differential Scanning Calorimetry (TG/DSC), was executed utilizing a NETZSCH STA 409 CD thermal analyzer. The analysis took place in an air atmosphere, and the temperature was gradually increased at a rate of 10°C per minute, reaching up to 1000 °C. This approach allowed for a comprehensive examination of the material's thermal behavior, providing insights into its weight loss and heat flow characteristics under controlled heating conditions.

d)BET

N_2 adsorption-desorption isotherms were produced at 77 K utilizing a Nova Station A instrument to evaluate the textural properties of the bioactive glass Al-BAG. The surface area was calculated employing the Brunauer-Emmett-Teller (BET) method, and the analysis of pore size distribution was conducted using the Barret-Joyner-Halenda method (BJH).

e)Particle size analysis

The determination of the particle size of Al-BAG involved the application of laser Doppler electrophoresis, a technique that measures the electrophoretic mobility of particles in a suspension. This analysis was conducted utilizing the Zetasizer Nano ZS instrument manufactured by Malvern Instruments Ltd, based in England. The instrument provides precise

measurements of particle size distribution in the given material, offering valuable insights into the characteristics of Al-BAG at the particulate level.

f)SEM-EDX

The examination of surface morphology was conducted using a Pro-X Scanning Electron Microscope (SEM) at 15kV. An energy-dispersive X-ray analyzer, coupled with Phenom World software, was integrated with the SEM to facilitate elemental identification and offer quantitative compositional details of the Al-BAG. Prior to imaging, the samples underwent sputter coating with gold, ensuring a maximum coating thickness of 12 nm.

g) *In vitro* ion release and degradation

Known quantity of Al-BAG was suspended in two different pH solutions, pH 7.4 and 5.2, mimicking the pH of the plasma and wound area, as per USP NF-2010 protocol, using USP type II apparatus (Electrolab TDT-08L dissolution tester) at 37^0C with continuous shaking at 120 rpm [Kaur et al., 2019]. Aliquots were collected at specific time intervals, i.e., 0, 4, 8, 12, 16 and 24 hr. throughout the study and the solution was replenished every time with the same volume of the pH solutions. The collected solutions were filtered and the concentration of the leached Ca^{2+}, Al^{3+} and Zn^{2+} ions was estimated by inductively coupled plasma atomic emission spectroscopy (ICP-AES).

The degradation properties were evaluated at 37^0C at two different pH, pH 7.4 and pH 5.2. The samples were immersed in 15 ml falcon tubes containing 10ml of the pH solutions following incubation upto 14 days. At specific time intervals, the samples were separated from the solution and washed with acetone followed by drying in an oven at 60^0C. For quantifying the weight loss (%), the following equation was used:

$$\text{Weight loss (\%)} = [(W_0 - W_t)/ W_0] \times 100$$

Where, W_0 is the initial weight of the sample and W_t is the weight after immersion in the pH solutions [Pourshahrestani et al., 2016].

4.4.2.2. *In vitro* biological assays

a) *In vitro* cytotoxicity assay

Al-BAG samples underwent a 20-minute UV light sterilization, followed by soaking in a known volume of DMEM and 24-hour incubation at 37°C. Subsequently, the leached solution underwent filtration using a 0.22μm membrane filter, and the resulting extract, containing culture media, was utilized for a cytotoxicity experiment. NIH3T3 cells were seeded in a 96-well tissue culture plate, incubated for 24 hours at 37°C in a 5% CO_2 incubator. After removing the culture medium, 100 μL of the extract media was added, with DMEM medium serving as the control. Following incubation for 24, 48, and 72 hours, the MTT assay was conducted using 10 mL of standard MTT reagent at 1 mg mL^{-1} (Sigma-Aldrich) in a 1:9 ratio (MTT:DMEM) across all wells. Incubation in the dark for 4 hours at 37°C was followed by obsoleting the reaction with 100 μL dimethyl sulfoxide after removing MTT and DMEM medium. The absorbance at 570 nm was measured in an ELISA reader (Bio-Rad), and corresponding cell viability was calculated. This cell viability assay, repeated three times at each time point, underwent statistical analysis with a significance level of $P < 0.05$ at 95% confidence intervals [Saha et al., 2020].

b)Immunofluorescence staining

The NIH3T3 cells were seeded in 24-well plates at a concentration of 10,000 cells/ml. For cellular proliferation visualization, the NIH3T3 cells were culture with the extract of Al-BAG for 24, 48 and 72h. Then, the cells were treated with 4% paraformaldehyde to preserve the cellular structure and prevent protein degradation. For permeabilization of the particular immunofluorescence stains (DAPI and FITC), cell membranes may be permeabilized using 0.04% of Triton X-100 and incubated for 30 min at 37^0C. Then, buffers were removed and cells were washed twice with 1X PBS. After that, cell nuclei stained with DNA-specific dye, DAPI solution was added to the cells and kept for 5-10 min in shaking at 50 rpm. Then washed twice with 1X PBS. For, stain the cytoskeleton of the cells, cells were treated with FITC solution and kept for 45 mins in dark in shaking at 50 rpm. After incubation, cells were washed three times with 1X PBS for 30 S each wash. Cells must be covered with 1X PBS prior to view under microscope.

c) *In vitro* antibacterial activity

The test sample underwent moist heat sterilization for 20 minutes at 121°C and 15 psi pressure. The Al-BAG sample was placed in 1ml of normal saline. For the experimental group, the sample

was immersed in normal saline medium inoculated with S. aureus and incubated in a shaker incubator at 37°C for 1-8 hours, with a final titer matching the 0.5 McFarland standards at 1.5×10^8 CFU/ml (Fig.). A 100µl bacterial suspension with the sample was plated on a nutrient agar plate and incubated at 37°C for 48 hours for colony formation. The reduction ratio of the bacteria was assessed using the equation (Eq. 2):

$$R\ (\%) = [(A-B)/A] \times 100\ \%$$

Where R is the percentage reduction ratio, A is the number of bacterial colonies from the untreated bacteria suspension (without testing materials), and B is the number of bacterial colonies from the bacteria culture treated by Al-BAG [Turlybekuly et al., 2019].

d) Hemocompatibility assay

A 2ml citrated (sodium citrate, 3.2% w/v) blood sample was mixed with 5ml dH_2O to form a line of best fit. After 60 minutes of incubation at 37°C, the blood was centrifuged at 2500 G for 10 minutes, and the collected supernatant containing plasma was used. Dilutions of 100%, 50%, 25%, 10%, and 1% were prepared to establish a line of best fit. For the experiment, 500µL of blood was combined with microcentrifuge tubes containing 2.5 mg sample (n= 3 to 5) at a concentration of 5mg/ml, following the ISO 10993-4 standard protocol. The mixture was incubated at 37°C for 60 minutes and then centrifuged at 2500 G for 10 minutes. In the control group, 500µL of blood was incubated and centrifuged similarly. Supernatants from both blood-only and sample-treated blood were collected. A mix of 100µL supernatant and 900µL PBS was prepared, and 200µL of the solution was placed in a 96-well plate for absorbance measurement at 540 nm. PBS served as the background or 'negative control,' and a 'no treatment' group acted as a control. Haemolysis percentage was calculated using below mentioned eqution [Nagrath et al., 2021]:

Hemolysis (%) = (Sample absorbance-negative control)/(positive control-negative control)×100

The absorbance values were correlated with the line of best fit to obtain haemolysis percentage values, and average values are reported with standard error of the mean.

e) *In vitro b*lood absorption efficiency

The blood absorption capacity of Al-BAG was assessed by placing 500µL of citrated whole blood in tissue culture plates. Pre-weighed dry pellets (P_{dry}) were immersed in the blood for adequate absorption. The sealed plates were then incubated at 37°C for an hour. After incubation, the wet pellets (P_{wet}) were extracted from the blood, and any excess moisture and freely drained blood on the pellet surface were gently wiped with absorbent paper. To determine the absorption capacity of the bioactive glass, the pellets were weighed before (P_{dry}) and after immersion (P_{wet}) in blood. The blood absorption efficiency was calculated using the equation below [Dai et al., 2009; Pourshahrestani et al., 2016]:

Blood absorption efficiency (%)=$[(P_{wet} - P_{dry})/P_{dry}]$

f) *In vitro* thrombus formation

A pre-weighed amount of Al-BAG (50 mg) was placed in a 24-well plate and incubated at 37°C for 10 minutes. Subsequently, a citrated blood sample (500 µL) was added and incubated for two different durations, 15 minutes and 45 minutes. To halt the thrombus formation cascade without disturbing the blood clot, double distilled water was added dropwise. A 4% paraformaldehyde solution was introduced to fix the formed thrombus for 10 minutes, and the clot was dried at 40°C overnight. The final weight was then measured again [Pourshahrestani et al., 2016]. The quantitative value was calculated using below mentioned equation [Pourshahrestani et al., 2016]:

Degree of thrombogenicity (%) = $[(P_t-P_0)/P_0]$

g) Exploring *In Vitro* Blood Plasma Coagulation: Insights from Prothrombin Time (PT) and Activated Partial Thromboplastin Time (aPTT) Assays

To assess the coagulation effects of the sample, prothrombin time (PT) and activated partial thromboplastin time (aPTT) tests were conducted at two different concentrations (1 mg and 3 mg) following clinical standard protocols. A semi-automatic coagulation analyzer (BIOMERIEUX, France) was used for the analysis. Blood samples were collected and mixed with one-tenth volume of 3.2% sodium citrate. Platelet poor plasma (PPP) was obtained by centrifugation at 2500G for 15 minutes at 37°C for both PT and aPTT assays [Pourshahrestani et al., 2016; Nagrath et al., 2021].

For the PT test, 50µl of citrated plasma, 100 µl of PT reagent, and the filtered sample extract were separately incubated at 37°C for 2 minutes. PT reagent and the sample were then added to the plasma in the test tube, followed by the measurement of PT.

In the aPTT test, citrated plasma was combined with the aPTT reagent (50 µl: 50 µl). After a 2-minute incubation at 37°C, 50 µl of 0.025 mol/L $CaCl_2$ and the sample extract were simultaneously added to the test tube, and aPTT was measured.

h) In vitro thrombin generation

It's possible that the human thrombin and antithrombin complex (TAT) indicates that thrombin has been neutralized and that it has formed over time. Al-BAG pallet and surgical cotton gauze were utilized as a control, incubated with 1 ml of EDTA-blood for 30 mins at 37°C. To prevent the formation of thrombin-antithrombin complexes, a solution of sodium citrate in the amount of 20 ml was added. An ELISA kit (ImmunoTag, Cat: ITLK01049) was utilized to measure the TAT levels in the blood [Diquelou et al., 1994; Chen et al., 2021].

i) Blood clot formation

Blood samples were obtained from a healthy human volunteer, and an anticoagulant, EDTA was introduces into the blood to prevent the clotting during collection. The collected blood was then subjected to centrifugation at 2500 G for duration of 10 mins at 37°C, which effectively separated the plasma. In the experimental group, a concentration of 5 mg/ml of Al-BAG in a pellet form was used and applied to the blood to induce clot formation. The control group, on the other hand, employed surgical cotton gauze. The process of clot formation was meticulously observed over time after both Al-BAG and surgical cotton gauze came into contact with the blood, and the clotting time was recorded. For scanning electron microscope (SEM) studies, the samples were initially fixed in 3.7% paraformaldehyde and then underwent a dehydration process. Subsequently, the samples were dried and coated with gold before SEM analysis [PHENOM Pro- X] [Ong et al., 2008].

j) *In vitro* assessment of platelet adhesion

To assess platelet adhesion, a lactate dehydrogenase (LDH) assay was employed. Human blood samples were freshly collected from volunteers and anticoagulated with 3.2% sodium citrate.

After that, the citrated blood samples underwent centrifugation at 1500 rpm for 10 mins to eliminate white blood cells and red blood cells. This process produced platelet-rich plasma (PRP), which was further centrifuged at 3000 rpm for 10 min, resulting in a platelet pellet and platelet-poor plasma as the supernatant. The platelet pellet was resuspended in PBS to achieve a concentration of 4×10^8 platelets/ ml. Al-BAG was exposed to the platelets and incubated at 37^{o}C for three different durations (15, 30, and 60 min). At the end of each time interval, the samples were removed and rinsed 10 times in PBS to eliminate non-adherent platelets. Subsequently, the samples were immersed in PBS containing 1% Triton X-100 for 1 h at 37^{o}C to lyse the adherent platelets. The number of platelets adhering to the surface matrix was quantified using an LDH assay kit. A platelet calibration curve was established by performing serial dilutions of a known number of platelets and measuring the optical density (OD) at 450 nm with a BioRad microplate reader. Each measurement was conducted at least three times. Following the assessment of platelet adhesion, the interaction between platelets and Al-BAG was observed using scanning electron microscopy (SEM). To prepare the samples for SEM studies, they were first fixed in 3.7% paraformaldehyde and then dehydrated through a series of ascending ethanol concentrations up to 100% [Pourshahrestani et al., 2016]. Finally, the samples were dried and coated with gold via sputter coating [Pourshahrestani et al., 2016].

k) *In vitro* red blood cell adhesion

After the fresh blood with leached extract of Al-BAG solidified, they were washed several times with PBS. Then, the blood clot was fixed with 4% paraformaldehyde and maintained for 3h. After washing several times with PBS to remove excess paraformaldehyde, the clot was immediately dehydrated with 20%, 40%, 60%, 80% and 100% ethanol/water solution. The red blood cell adhesion *in vitro* was observed by SEM after natural drying.

l) Whole blood clotting and determination of blood clotting index (BCI)

The blood clot indexing (BCI) protocol proposed by Shih et al. has been changed slightly for the current research purpose [Chen et al., 2021]. Anticoagulate containing whole blood (0.2 ml) was distributed to the Al-BAG and surgical cotton gauze, 20 µL of 0.25 M $CaCl_2$ solution was added to initiate coagulation, and the samples were incubated at 37^{o}C with shaking at 100 rpm. The surgical cotton gauze (the "control") and the Al-BAG were placed into tubes and kept at 37^{o}C.

After 10 mins of osmotic lysis of RBCs that were not attached to the clot, a BioRad Microplate Reader was used to measure the optical density (OD) at 540 nm. The BCI was measured using the formula [Ong et al., 2008]:

BCI=100× (Absorbance of Al-BAG/ Absorbance of control)

4.4.2.3. Unveiling *In Vivo* Realms: Exploring the Biological Landscape through *In Vivo* Studies

a) Assessing Acute Dermal Toxicity in Albino Rats: A comprehensive investigation into the effects of topically applied test material, Al-BAG

Eight albino rats were randomly assigned to five groups, each comprising two animals. Group 1, 2, and 3 received dermal applications of the test material at doses of 500 mg/kg, 167 mg/kg (1/3rd of the highest dose), and 100 mg/kg (1/5th of the highest dose) body weight, respectively. Petroleum jelly served as the vehicle for the test material, and Group 4 animals received only petroleum jelly topically at 50 mg. Group 5 animals did not undergo any treatment. A designated area on the back of the animals was shaved for test material application. Body weight was measured before applying the test material and daily in the morning for 14 days. Daily quantities of feed and water were provided, and any leftovers were recorded the next day [Jones et al, 2012].

Histological examinations were conducted on day 15, where animals were euthanized, and tissue samples from the liver, kidney, heart, lungs, and skin were collected post-treatment. The samples were fixed in paraformaldehyde, embedded in paraffin, and cut into 5 μm sections. Hematoxylin-eosin dyes (H&E) were used for staining, following the deparaffinization, rehydration, and washing with dH_2O water of paraffin-embedded sections.

b)Evaluating the *in vivo* hemostatic effectiveness of Al-BAG at varied doses in wistar rats under profuse bleeding conditions

The *in vivo* hemostatic efficacy of Al-BAG at different doses was investigated using femoral artery bleeding scenarios in 7-8-week-old Wistar rats [Hu et al., 2012]. Prior to the experiment, the Al-BAG powder sample was dried at 150-200°C in a vacuum for 4-5 hours and sterilized

through UV irradiation. Wistar rats were anesthetized via intravenous injection with a combination of ketamine and xylazine (40mg/kg BW + 5 mg/kg BW).

During the experiment, the animals were positioned on their backs to expose the groin area, with hind limbs extended. The thigh, including skin, soft tissues, and overlying muscles, was transected with a scalpel to expose the femoral artery and vein. The same vessels were punctured using a 24-gauze needle to induce uncontrolled hemorrhage. Subsequently, various doses of Al-BAG were applied to the injury site. Manual compression with pre-weighed gauze pieces was employed at the wound site to collect the blood lost during the procedure. The time taken for bleeding to cease and the mass of blood loss were observed. These observations were then compared to the control group, which received no test sample (only gauze was used) [Hu et al., 2012; Sundaram et al., 2019].

Statistical evaluation

The information is shown as the average value plus or minus the standard deviation, derived from one of three representative experiments, each conducted in triplicate. Statistical significance was determined at a p-value less than 0.05, with a confidence interval of 95%.

Footnote: This work has been filed for an Indian patent.

'A bioactive glass composition and a process thereof', J.Chakraborty, P.Srivastava, P. Roy, S. Saha and R. Saha, App. No.202211057220, INDIA, Filed, published on 04.08.23 [DRDO]

Chapter 5: Results and Discussions

5.1. Results and Discussion: Part A

5.1.1. Results

5.1.1.1. Results related to AgBG powder

a) XRD

The X-ray diffraction (XRD) pattern of AgBG displays a broad peak at 2θ = 24°, indicating the presence of Si-O-Si linkages in the glass composition, indicative of the amorphous nature of the sample. Our experimental procedure successfully synthesized AgBG [Fig. 5.1(a)] [Roy et al., 2023a].

b)FTIR

Fig. 5.1(b) represents FTIR spectrum of as-prepared AgBG. The three absorption bands at 1090 cm^{-1} matched to the asymmetric stretching vibration of Si-O bonds in (1NBOS) tetrahedral network, 793cm^{-1} and 475 cm^{-1} matched to the symmetric stretching and bending vibration of the Si-O-Si of the silica network, respectively [Zhong et al., 2014]. The vibrational band at 666 cm^{-1} match to the bending of the bridging oxygen (B-O) between trigonal BO_3 groups of the silica network, suggesting the presence of Si-O-B [Rao et al., 2013], although the intensity of the band is too low that corresponds to the presence of very less amount of B_2O_3 in the present composition. The band at about 1398 cm^{-1} with low intensity is attributed to the relaxation of symmetric stretching of the B-O band of the trigonal BO_3 [Moskalewicz et al., 2010]. The vibration at 1636 cm^{-1} is related to the bending vibration of the captivated H_2O molecules and 3453 cm^{-1} related to the stretching vibration of hydroxyl group (O-H) [Shao et al., 2015; Roy et al., 2023a].

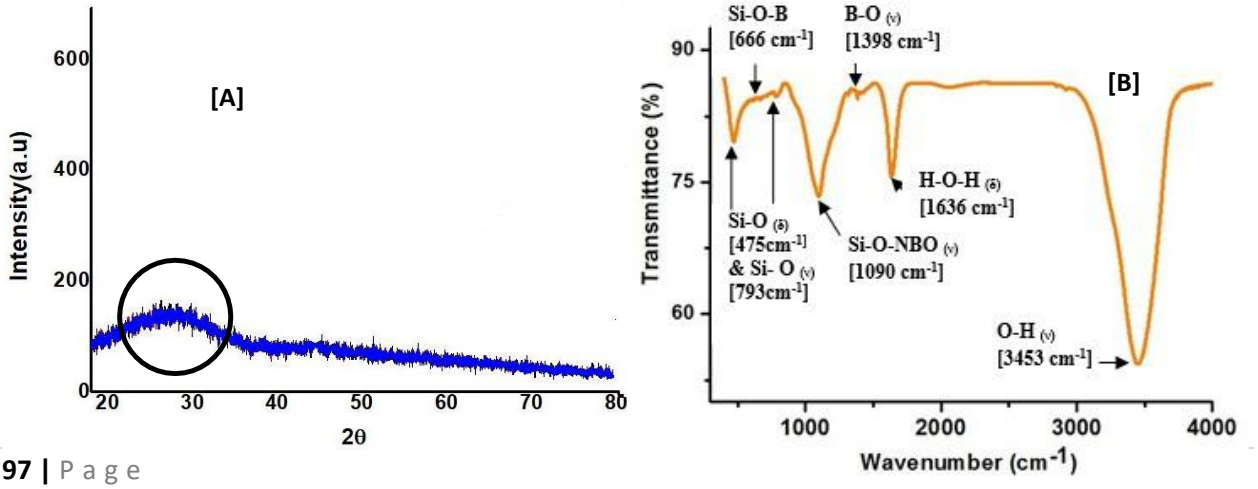

Fig. 5.1. [A] XRD pattern of the as-prepared ABGmnf based wound care matrix.

[B] FTIR spectra of the ABGmnf based wound care matrix showing characteristic vibrations consigned to silicate structural groups and associated with Si-O-B, B-O bonds. ['ν' and 'δ' denotes stretching and bending vibrations, respectively] [Roy et al., 2023a].

c) Differential scanning calorimetry and thermogravimetry analysis (TG-DSC)

TG-DSC was used to study the thermal behavior of the synthesized glass powder. The result is shown in fig. Analysis by TG indicates that the mass of the glass powder gradually decreases at temperature 400^0C and the total mass loss is ~ only 2.5%. Based on the DSC curve, a small kink in the endothermic direction is observed at 400◦C and 650^0C, as well as major peaks at 800^0C and 890^0C. The small kinks at 400◦C indicate the glass transition temperature (TG) and after 650^0C the glass started towards crystallization and the other peaks are attributed to the crystallization and transformation of the crystal structure [Fig. 5.2(a)]. Based on this result, the heat treatment of the glass powder was performed in 650◦C [Roy et al., 2023a].

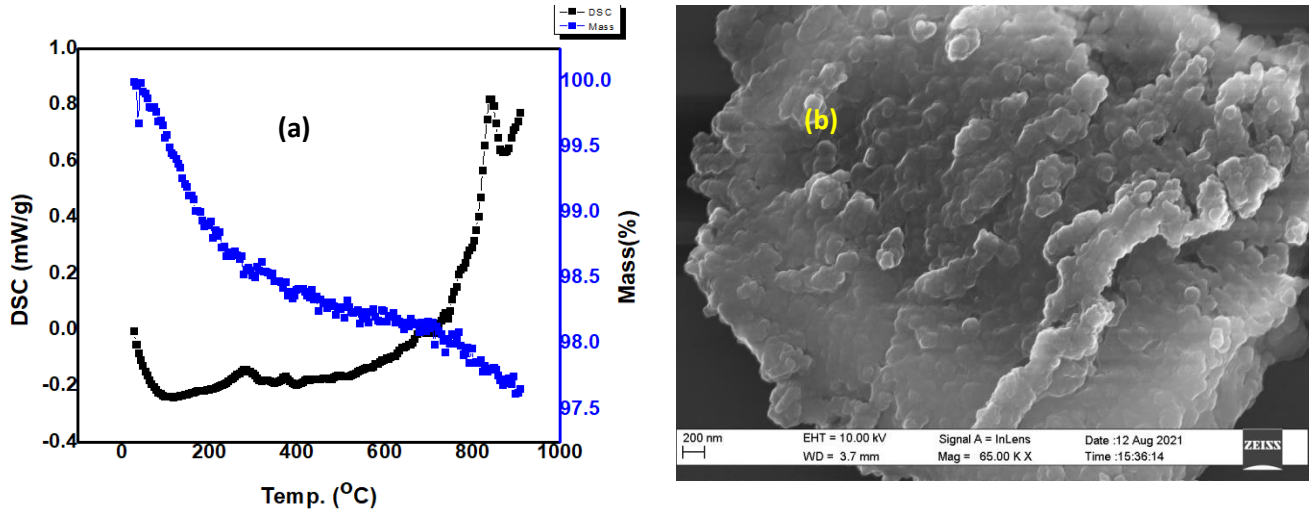

Fig. 5.2. (a) TG-DSC curve of AgBG glass powder, calcined at 650^0C.

(b) FESEM image of AgBG glass powder.

d) FESEM

The microstructure of the powders was examined by FESEM, Fig. .A distribution of nano-sized particles with large agglomerates was observed for the AgBG powder. The nanometric AgBG particles had irregular shapes with particle sizes of 60-100 nm [5.2 (b)].

e) BET

The graph illustrates the N_2 adsorption-absorption isotherm and the corresponding pore size distribution for AgBG. According to the figure, AgBG displayed a type IV isotherm accompanied by a type H1 hysteresis loop. The specific surface area of AgBG was determined to be 78.314 m^2/g, and the average pore size measured 8.984 nm [Fig. 5.3 (a,b)] [Roy et al., 2024b].

f) Zeta potential measurement of AgBG

The zeta potential of AgBG was calculated -15.3 mV at pH 7.4 [Fig. 5.3(c)].

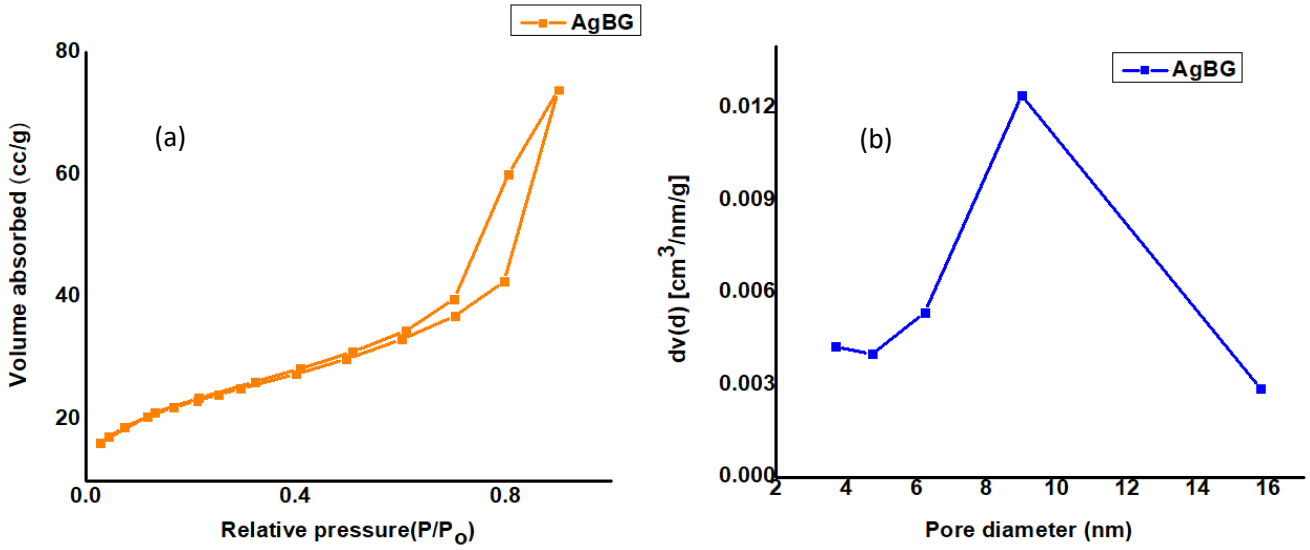

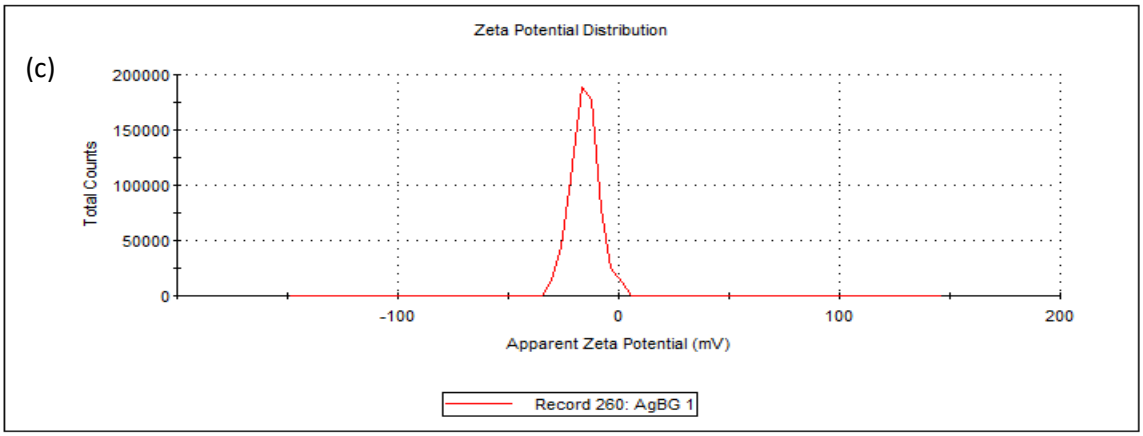

Fig. 5.3. (a) Nitrogen adsorption/desorption isotherm for AgBG, (b) BJH for AgBG, and (c) Zeta potential measurement for AgBG.

g) Angle of repose of AgBG

The calculated angle of repose of the AgBG powder was 26(±1) and the result indicated the good flowability of the AgBG [Fig. 5.4] [Singh et al., 2014].

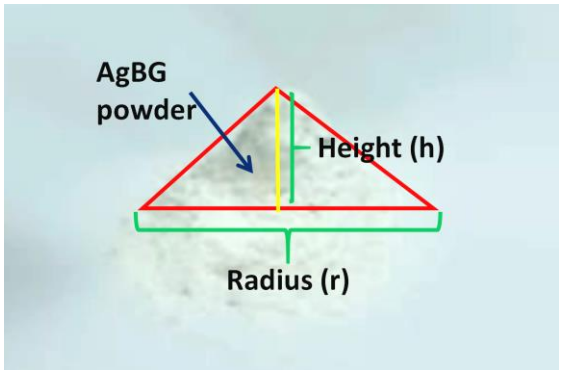

Fig. 5.4. shows angle of repose of AgBG.

5.1.1.2. Results related to ABGmnf based wound care matrix

a) XRD of PVP and ABGmnf based wound care matrix

The X-ray diffraction (XRD) analysis of pure polyvinylpyrrolidone (PVP) revealed two distinct broad peaks at 2θ angles of 11.25° and 21.21°, aligning well with the findings of Li et al. In the

case of the ABGmnf based wound care matrix, the XRD pattern exhibited peaks at 2θ angles of 10.77^{o} and 22.61^{o}, indicative of an amorphous structure characteristic of silicate glass [Fig. 5.5] [Chen et al., 2018]. This observation may be attributed to the low concentration of $AgNO_3$ used in the composition preparation. It is important to note that the incorporation of AgBG into the PVP wound care matrix led to a reduction in peak intensity, resulting in a noisy XRD pattern where small peaks may not be clearly visible [El Hotaby et al., 2017].

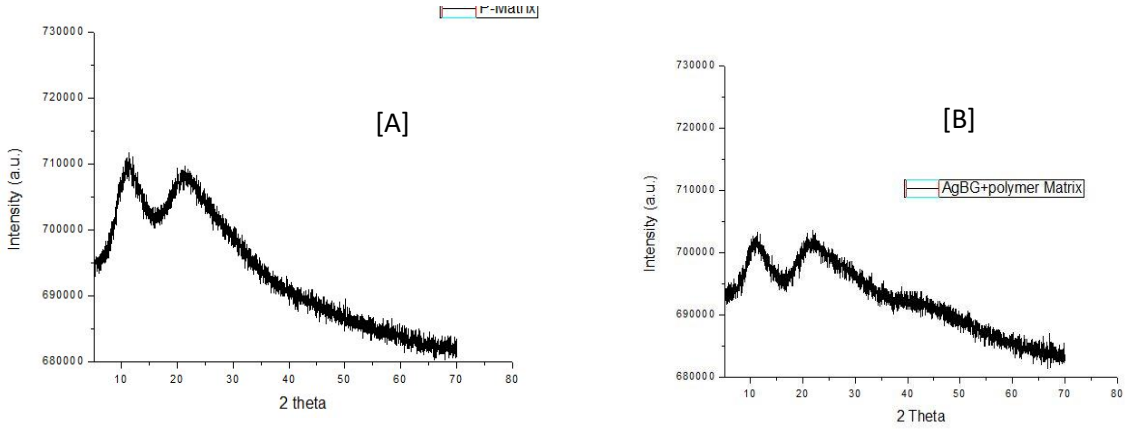

Fig. 5.5. [A] XRD pattern of the PVP matrix

[B] XRD pattern of the as-prepared ABGmnf woundcare matrix.

b)FTIR

The FTIR spectra depicted in the fig. 5.6(a) illustrate the characteristics of PVP and the ABGmnf based wound care matrix. In both spectra, a broad band at 3441 cm^{-1} is evident, signifying the OH stretching vibration. Additionally, a weak peak around 2893 cm^{-1} corresponds to the stretching vibration of $–CH_2$, while a distinct and strong peak at 1663 cm^{-1} is attributed to the C=O stretching vibration. The medium peak at 1439 cm^{-1} is associated with the scissoring vibration of the CH_2 group, and the C-N stretching is observed at 1290 cm^{-1} [Hoppe et al., 2013]. When comparing the PVP spectrum with that of the ABGmnf based wound care matrix, the latter exhibits an absorption peak at 470 cm^{-1}, indicating the Si-O-Si stretching mode [Hoppe et al., 2013]. Symmetrical stretching vibrations of the Si-O(Si) bridge are responsible for the bands at

760-780 cm^{-1}. Additionally, absorption bands in the range of 1150-1300 cm^{-1} are linked to the B-O stretching of trigonal BO_3 units [Yao et al., 2007; Liu et al., 2013].

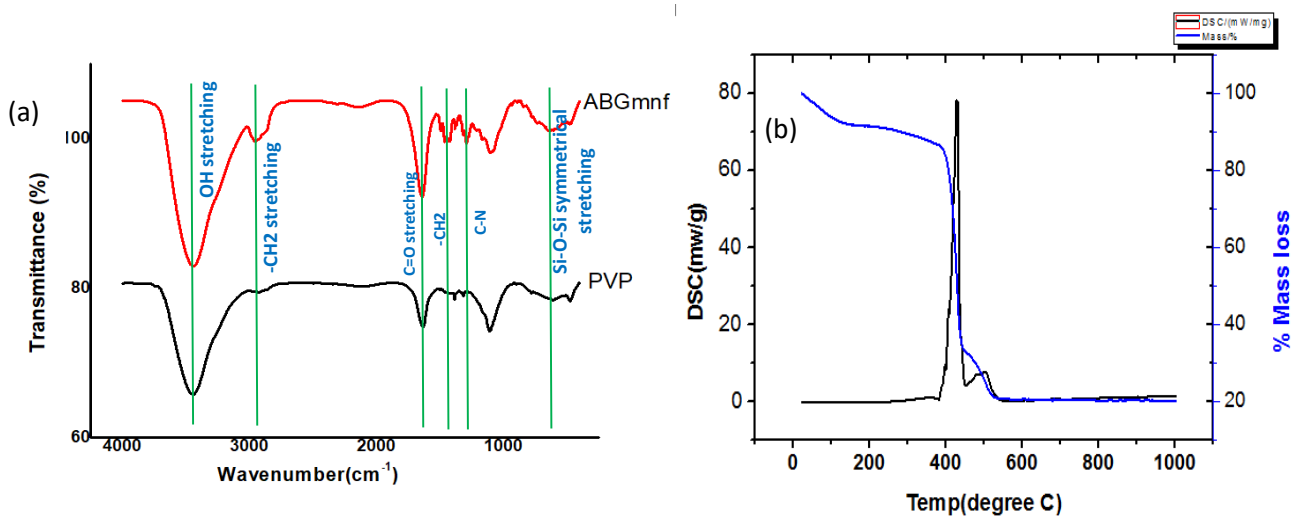

Fig. 5.6. (a) FTIR spectra of the PVP matrix and ABGmnf based wound care matrix heat treated at 600^{o}C showing characteristic vibrations consigned to silicate structural groups and associated with Si-O-B, B-O bonds and PVP related groups.

(b) TG-DSC plot of as-prepared ABGmnf based wound care matrix [AgBG was calcined at 600^{o}C].

c) TG-DSC

The TG-DSC analysis results of the ABGmnf based wound care matrix are presented in Fig. 5.6(b). The TG curve displays four distinct phases of weight reduction: a 22% decrease as the temperature rose from room temperature to 310°C, a significant 45% loss from 310°C to 420°C, another 13% reduction from 420°C to 530°C, with no weight loss detected beyond 530°C. The initial weight loss is ascribed to the evaporation of ethanol and water in the sample. The second weight loss, associated with a prominent peak in the DSC curve, is linked to the composition of the PVP side chain [Roy et al., 2023a]. An exothermic peak is noted during the third weight loss phase, ranging from 440°C to 500°C, indicating the degradation of both the PVP main chain and AgBG. Above 530°C, no transitions or weight loss are observed [Tang et al., 2015].

d)FESEM

Fig. 5.7 exhibits a fibrous network, approximately 1.5 µm diameter of each fibre.

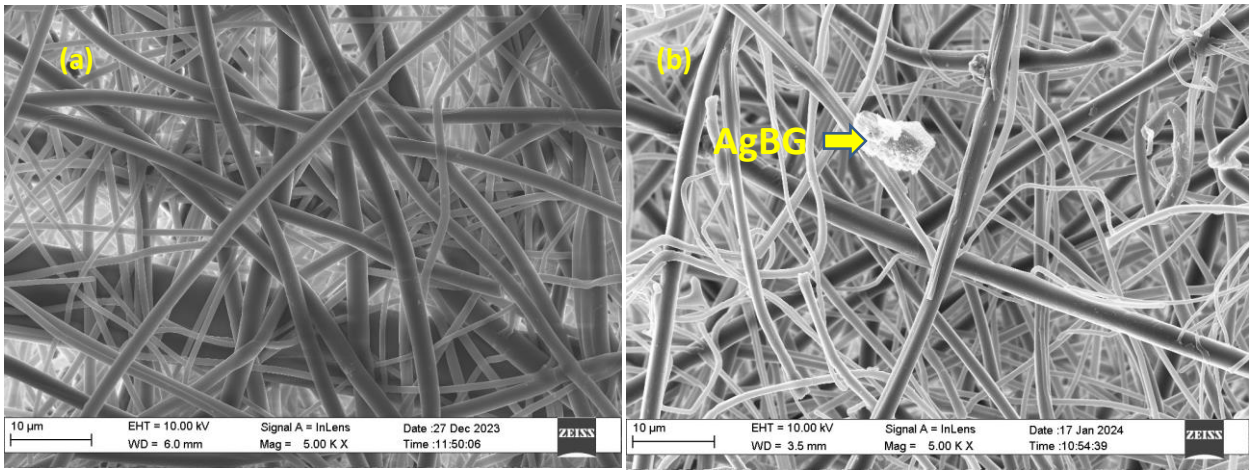

Fig. 5.7. FESEM image (scale bar 10µm) shows the collection of (a) PVP fibre and (b) ABGmnf based wound care matrix with micro-nano ranged diameters of the fibres and entrapped AgBG particles into the matrix.

e) Mechanical property

The comparison between pure PVP matrix and PVP-AgBG (ABGmnf based wound care matrix) stress-strain curve shows that mechanical properties were slightly modified with the AgBG incorporation, shown in Fig. 5.8.

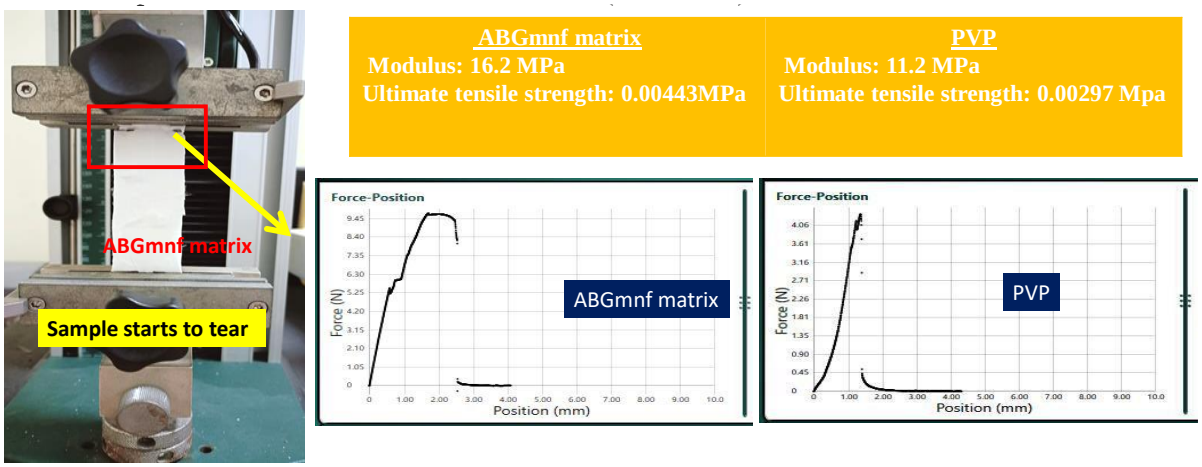

Fig. 5.8. Stress-strain curve of ABGmnf based wound care matrix and PVP matrix.

f) Solubility assessment

The table showed the water solubility as per OECD 105 guideline. The experimental result showed that 0.1g of ABGmnf based wound care matrix was soluble in 0.5 ml water. Hence, from the table, the solubility of ABGmnf based wound care matrix was 1000 to 200 g/l [Table 5.1].

Table 5.1. Water solubility assessment as per OECD 105

ml of water for 0.1g soluble	**0.1**	0.5	**1**	**2**	**10**	**100**	**>100**
~ water solubility in g/l	>1000	**1000 to 200**	200 to 100	100 to 50	50 to 10	10 to 1	<1

It was observed that the ABGmnf based wound care matrix was fully soluble within 1 min in polar solvents whereas in MEK it is partially soluble and in hexane it was insoluble [Fig. 5.9].

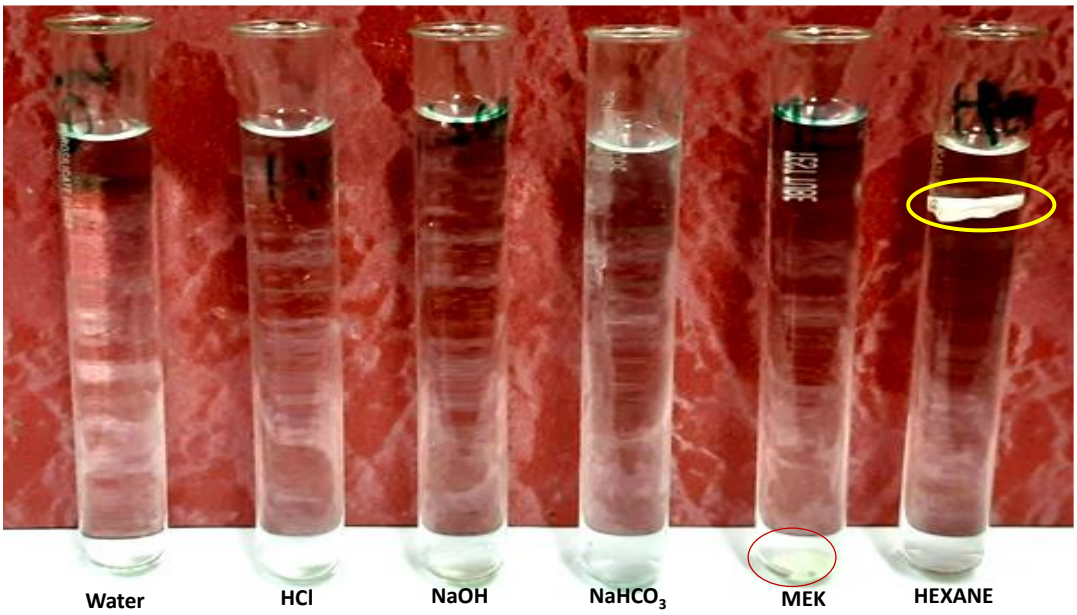

Fig. 5.9. The solubility assessment of ABGmnf based wound care matrix.

5.1.2. Results: *in vitro* biological assessments

5.1.2.1. *In vitro* cytotoxicity assay of AgBG

To check the *in vitro* cytocompatibility of the AgBG, the leached extract (as mentioned in 3.2.7.1.) of the same was obtained by incubation of a known quantity of AgBG for 24 h at 37 ^{0}C. Next, the NIH3T3 cells were treated with the extract of the AgBG for 24, 48 and 72 h. It was observed that the cell viability of NIH3T3 cells in the existence of the extract enhances to some extent with the culture time, suggestive of that AgBG is cytocompatible to NIH3T3 [Fig. 5.10], exhibiting normal cell morphology.

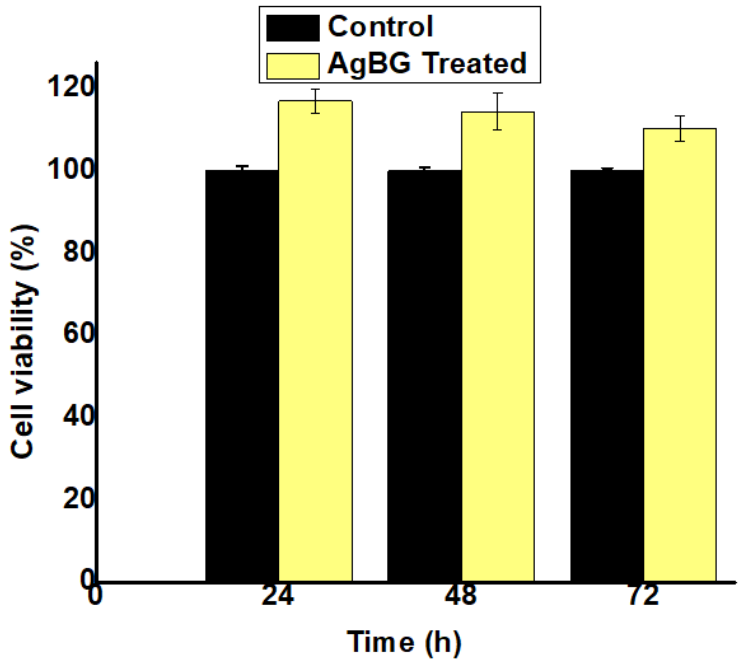

Fig. 5.10. Viability of NIH3T3 cells after 24, 48 and 72h extracts achieved from AgBG. Data shown is mean ± SD of three independent experiments.

5.1.2.2. *In vitro* biological assessment of ABGmnf based wound care matrix

a)*In vitro* cytotoxicity assay

The cytotoxicity of ABGmnf based wound care matrix must be assessed for wound healing applications. About 103(±3.5)%, 105(±4.7)% and 97(±4.3)% of NIH3T3 cells were

metabolically active after 24h, 48h and 72h treatment of ABGmnf based wound care matrix, respectively [Fig. 5.11]. The result indicated the excellent cytocompatibility of the ABGmnf based wound care matrix.

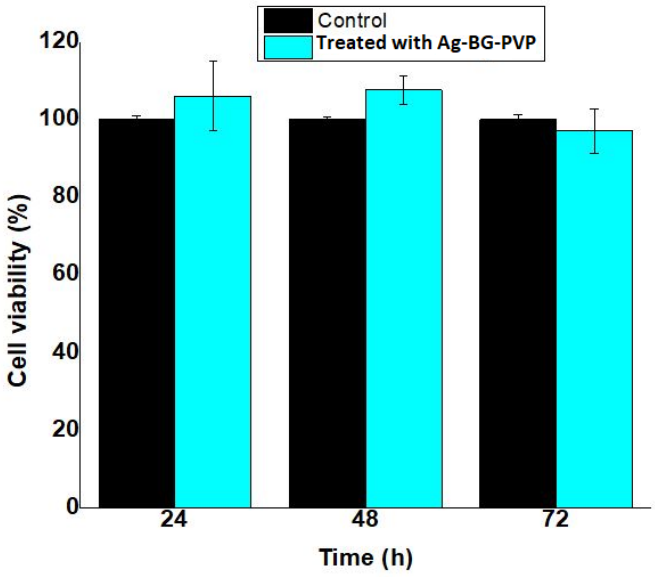

Fig. 5.11. *In vitro* cytotoxicity assay of ABGmnf based wound care matrix showing excellent cell viability, using NIH3T3 cell line.

b)Immunofluorescence staining

Fig. 5.12 represents the fluorescence microscopy images of NIH3T3 cells, stained with DAPI and FITC. Herein, 24h culture was done to observe the adhesion property of cells and showed good cell adhesion [Fig. 5. 12(a)]. After 72h, all attached cells spread properly. Further, cells treated with ABGmnf based wound care matrix, proliferated well and almost reached confluence after 72h incubation [Fig.5.12 (b)]. Fig. 5.12(c) showed the cellular morphology in higher magnification, 20X, after treated with ABGmnf based wound care matrix after 24h and 72h compared with control (untreated cells).

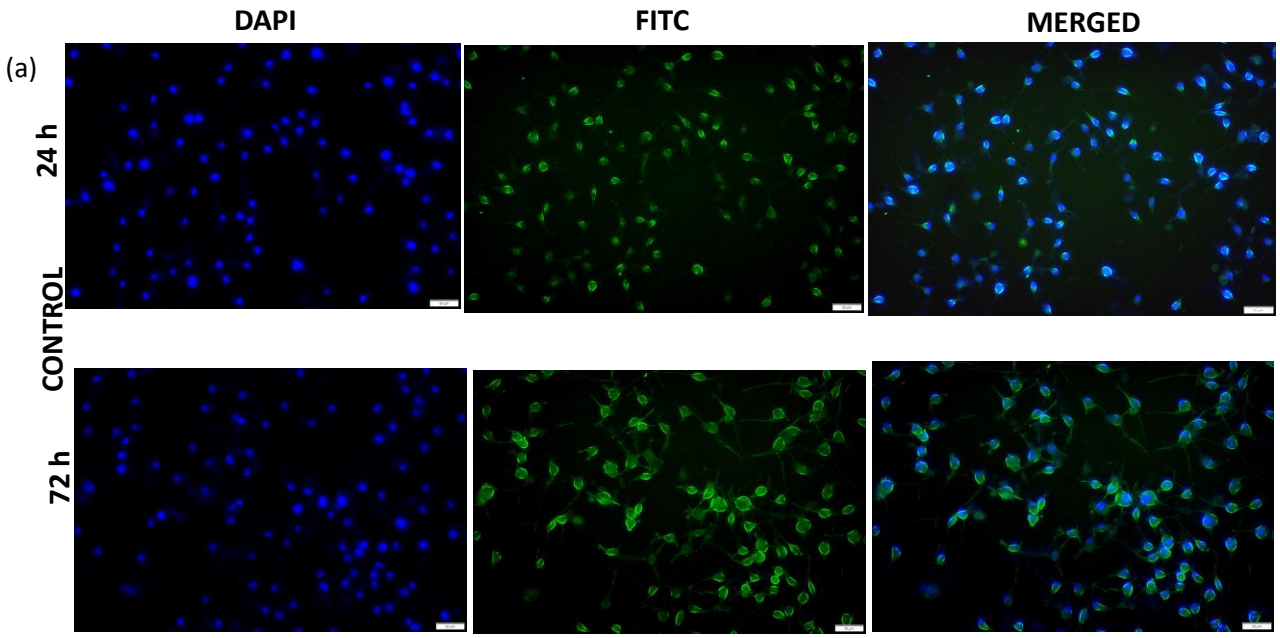

Scale bar: 50 µm and magnification 10X

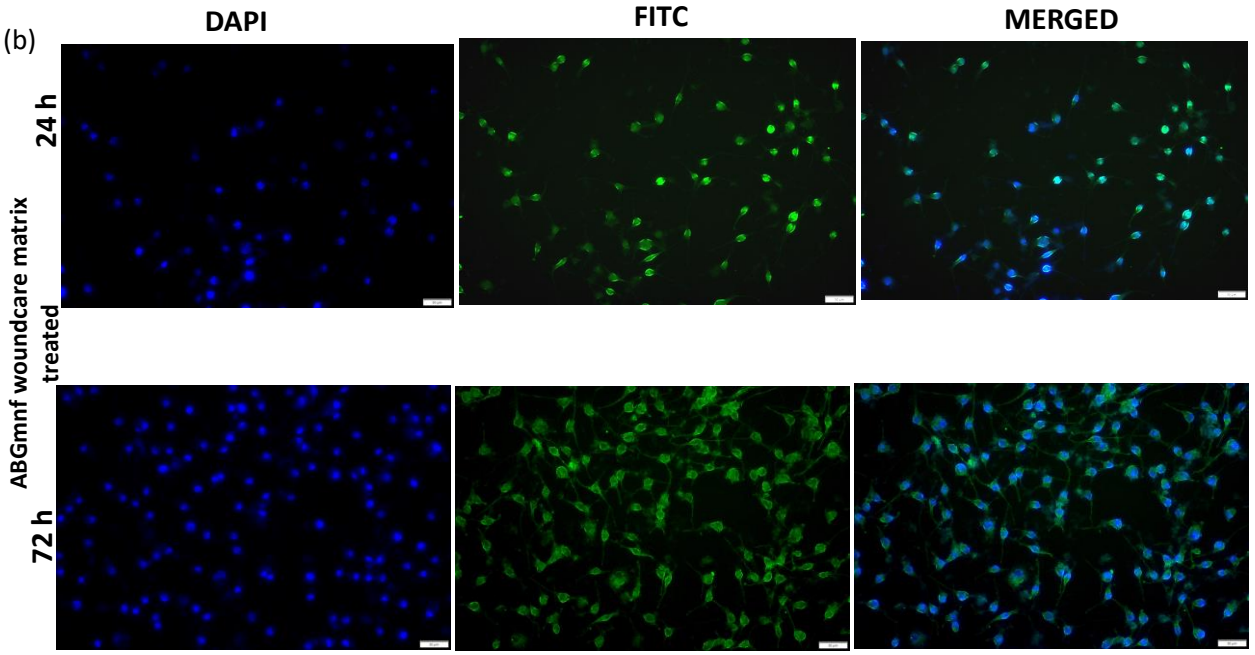

Scale bar: 50 µm and magnification 10X

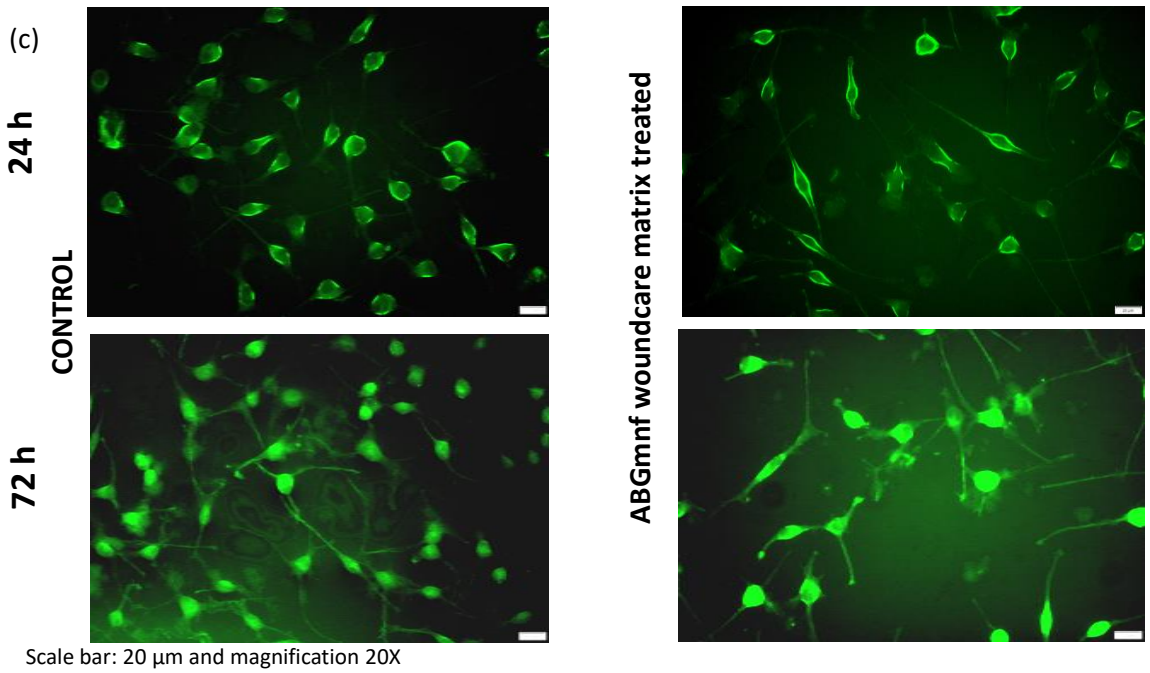

Fig. 5.12. Fluorescence images of cells (a) without any treatment (act as control) and (b) treated with ABGmnf based woundcare matrix extract and incubated for 24h and 72h. The images showed no adverse effects on the cellular morphology after treatment. Magnification: 10X and Scale bar: 50µm. (c) The cellular morphology was showed in higher magnification (20X) and scale bar: 20µm.

c)2 D *in vitro* wound scratch assay

ABGmnf based wound care matrix demonstrated excellent wound contraction, as illustrated in Fig. 5. 13 compared to the control (untreated group). ABGmnf based wound care matrix showed faster wound contraction. These results are in good concurrence with cell proliferation assays. After 24h, rate of the wound contraction was escalated and was found to be around 90(±2)%, which is considerably higher than the result obtained 50(±3)% for the control group [Roy et al., 2023a].

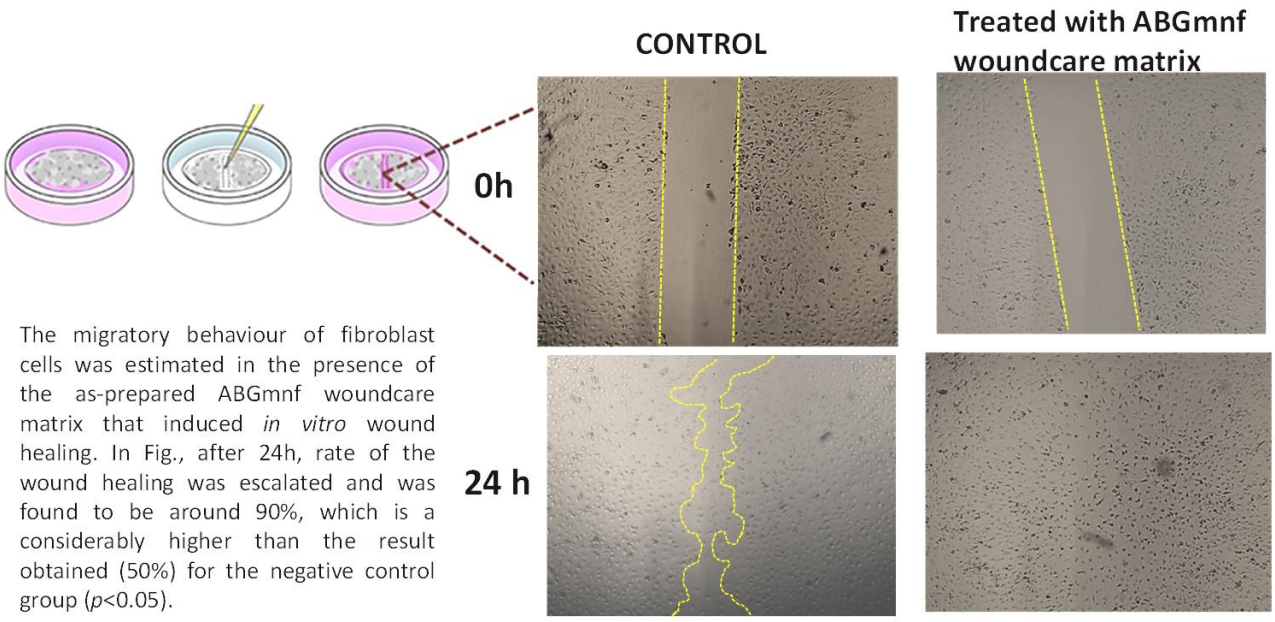

Fig. 5.13. Representative optical image of *in vitro* 2D wound healing assay showing higher cell migration when treated with ABGmnf based wound care matrix compared to the control group. Data shown is mean ± SD of three independent experiments ($p < 0.05$).

d)In vitro antibacterial assay

The antibacterial assay of PVP matrix and ABGmnf based wound care matrix, using *S. aureus* (gram positive strain) and *E. coli* (gram negative strain), cultured on nutrient agar plate, exhibited a ZOI of 13.5±1.5 mm and 19±1.2 mm, respectively. The result was obtained after a period of 24h.

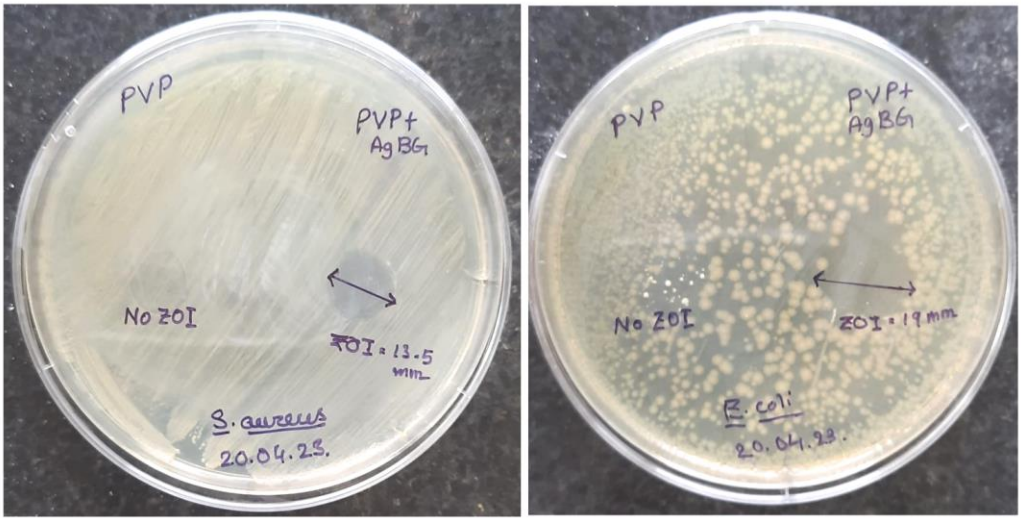

Fig. 5.14. Antibacterial activity of ABGmnf based wound care matrix (PVP-AgBG, showing ZOI) compared with control, pure PVP matrix (no ZOI) after 24h incubation on agar plate at 37^{o}C against (a) *S. aureus* and (b) *E. coli*.

e)Assessment of antibacterial effectiveness through the determination of the minimum inhibitory concentration (MIC)

In Fig. 5.15, the minimum inhibitory concentration (MIC) for the active ingredient against Pseudomonas aeruginosa, a gram-negative bacterium, ranged from 0.43 to 0.5 µg/ml, whereas the MIC for the potent broad-spectrum antibiotic gentamicin was 0.75 µg/ml. Similarly, for Streptococcus pneumoniae, a gram-positive strain, the MIC of the ABGmnf active ingredient was in the range of 0.43-0.5 µg/ml, compared to gentamicin with an MIC of 0.5 µg/ml. In the case of another gram-positive bacterial strain, Staphylococcus aureus, the MIC for the active ingredient of ABGmnf was found to be in the range of 0.425-0.5 µg/ml, while gentamicin had an MIC of 0.5 µg/ml [Roy et al., 2023a].

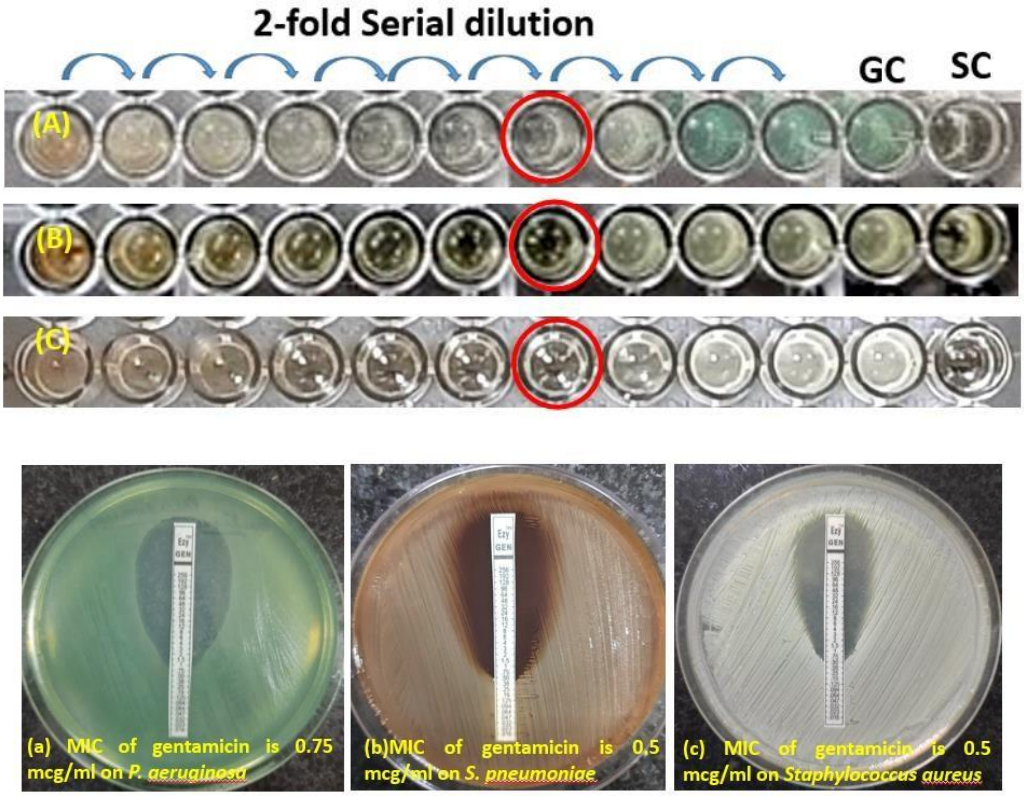

Fig. 5.15. Determine the Minimum Inhibitory Concentration (MIC) of ABGmnf based wound care matrix's active ingredient on both Gram-positive strains (*S. aureus* and *S. pneumoniae*) and the Gram-negative strain (*P. aeruginosa*), in comparison to gentamicin [Roy et al., 2023a].

5.1.3. Results: *In vivo* animal studies

a)Evaluation of *in vivo* biocompatibility and host immunogenic response

The outcomes of the *in vivo* biocompatibility assessment for transdermal injection of the ABGmnf based wound care matrix extract are depicted in Figure 5. Throughout the experiment, none of the animals displayed measurable or overt signs of immune response. There were no local indications of toxicity, such as erythema, edema, or redness, even 24 hours after transdermal application in the Wistar rat model. The locomotor behavior of the test animals remained normal.

Blood samples collected during the study were analyzed to assess the levels of two pro-inflammatory cytokines, TNF-α and IL-6. The TNF-α study revealed that the concentration of the control sample (blood plasma before ABGmnf based wound care matrix extract treatment)

was 32 ± 2 pg/ml, while post-treatment, the concentration of this pro-inflammatory marker was observed to be 28 ± 2 pg/ml [Alcaide et al., 2010], demonstrating comparability. This suggests that ABGmnf based wound care matrix does not elicit significant immune responses. Additionally, in the determination of IL-6 concentration, all samples were run in duplicate, and the results obtained reported a level below the minimum level of detection (LOD) of <7.82 pg/ml (the detection range being 7.82-500 pg/ml, and the normal range of IL-6 being 0-16.4 pg/ml) [Roy et al., 2023a]. This result falls well within the normal range for the cytokine, affirming the biocompatibility of the tested sample.

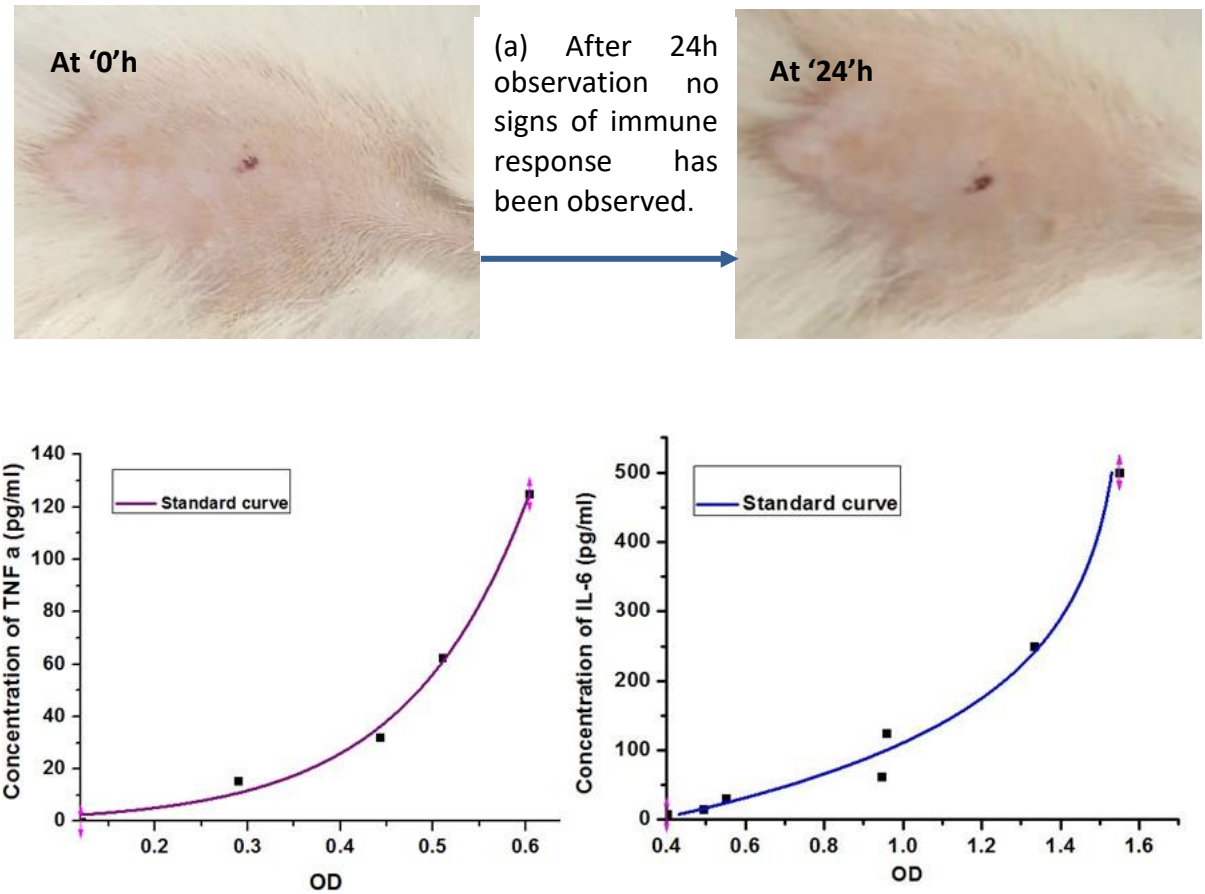

Fig. 5.16. (a) Macroscopic examination reveals the absence of any immune response from the host throughout the observation period. (b) The assessment involves a quantitative analysis of the concentration of the proinflammatory cytokine TNF-α. (c) Similarly, the IL-6 concentration is subjected to quantitative analysis [Roy et al., 2023a].

b)Toxicity by leachable components (Hemogram and histology)

To assess whether leachable compounds from ABGmnf based wound care matrix induce any toxic responses under physiological conditions, we monitored various parameters, including hematology, serum biochemistry, and histopathology. Two groups, denoted as R1 and R2 (with 3 rats per sex per group), were examined at two time points: '0h' before the treatment with the test sample and '4h' after 4 hours of exposure to the test sample. Hematological analysis showed no significant differences between the pre-exposure and post-exposure periods for the ABGmnf based wound care matrix extract. Clinical biochemical parameters, including BUN, ALT, AST, creatinine, and calcium ions, were evaluated and did not exhibit statistically significant differences during the specified time period [refer to Table 5.2.]. Furthermore, histopathological examination of vital organs in the animals revealed normal histo-architecture, indicating the absence of any abnormal findings [refer to Fig. 5.17.] [Doostmohammadi et al, 2011, Roy et al., 2023a].

Table 5.2. presents the hemogram of rats both before ('0h') and after ('4h') the application of ABGmnf based wound care matrix [Roy et al., 2023a]

Parameters	R_1		R_2	
	'O'h	'4'h	'O'h	'4'h
RBC – 10^6/µl	7.6	7.8	7.20	7.32
WBC – 10^3/ µl	2.8	2.6	2.50	2.60
Neutrophil (10^3/ µl)	0.30	0.40	0.50	0.55
Lymphocyte (10^3/ µl)	1.20	1.25	1.40	1.45
Monocyte (10^3/ µl)	0.02	0.02	0.04	0.03
Basophil (10^3/ µl)	0.01	0.01	0.01	0.01
Eosinophil (10^3/ µl)	0.02	0.03	0.02	0.02
Hb(gm/dl)	13.50	13.60	13.40	13.50
Platelet (10^3/ µl)	720	745	710	715
	BIOCHEMICAL			
Bun (mg/dl)	15.50	15.40	16.20	16.20
Creatinine (mg/dl)	0.40	0.40	0.35	0.35
ALT (U/L)	25.00	26.00	24.00	23.00
AST (U/L)	75.00	76.00	80.5	80.00
Ca2+ (in ppm)	1.41	1.42	1.65	1.67

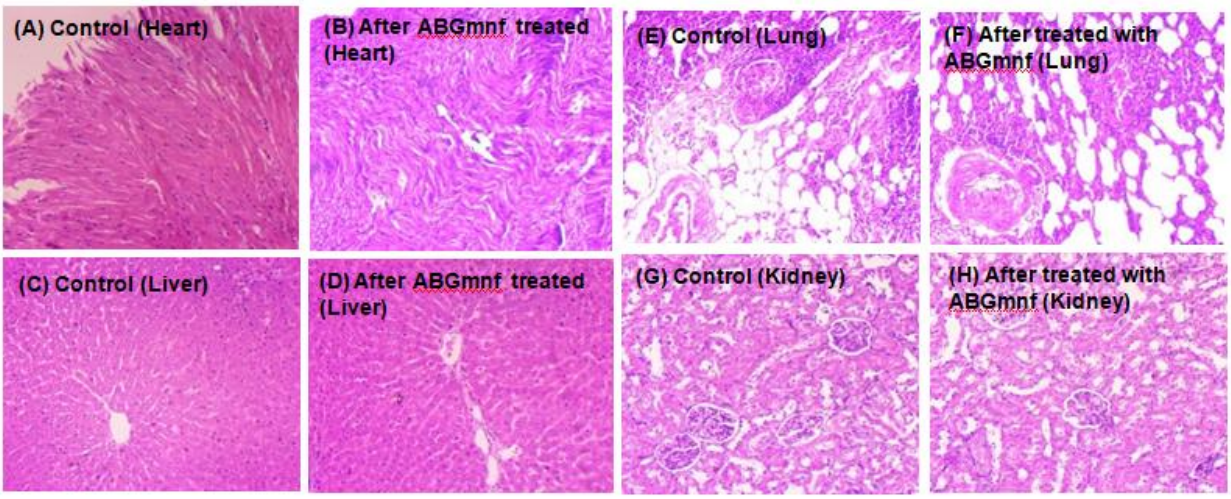

Fig. 5.17. Histological examinations were conducted on sections of the heart, liver, lung, and kidney (labeled A-H) in Wistar rats, with both control and ABGmnf based wound care matrix-treated groups (n>3) [Roy et al., 2023a].

c)In vivo pharmacokinetic study

The serum concentration of the leached Ca^{2+} from AgBG of the ABGmnf based wound care matrix was determined and is represented in Fig. 14. From the graph, it was showed that the Ca^{2+} reached maxima at 45h (T_{max}) with a concentration of 136(±3) ppm (C_{max}) and then decreased to the basal level by the end of the experimental protocol.

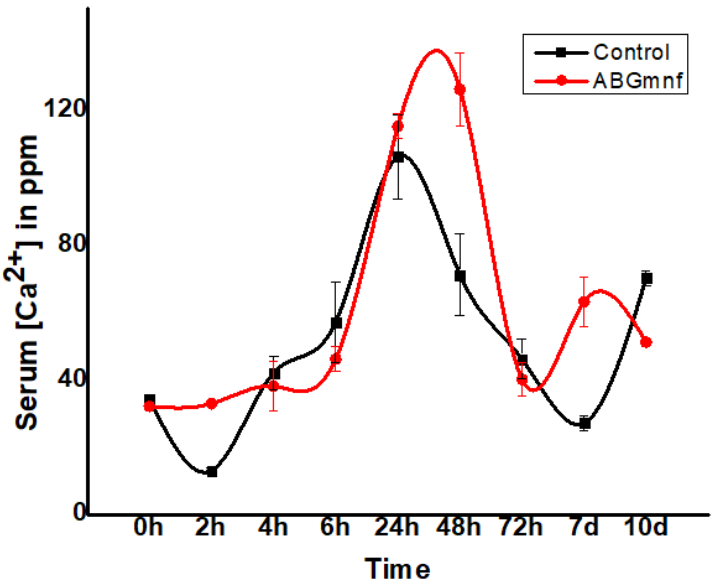

Fig. 5.18. Serum concentration profile of Ca released from AgBG of ABGmnf based wound care matrix. All values are in mean ±SD (n=3/group) [p <0.05].

d) *In vivo* biodistribution study

Tissue calcium level (in ppm) in various vital organs after 7th day of ABGmnf based wound care matrix application compared to the control (untreated). The result did not show any kind of calcium deposition in the vital organs [Fig. 15].

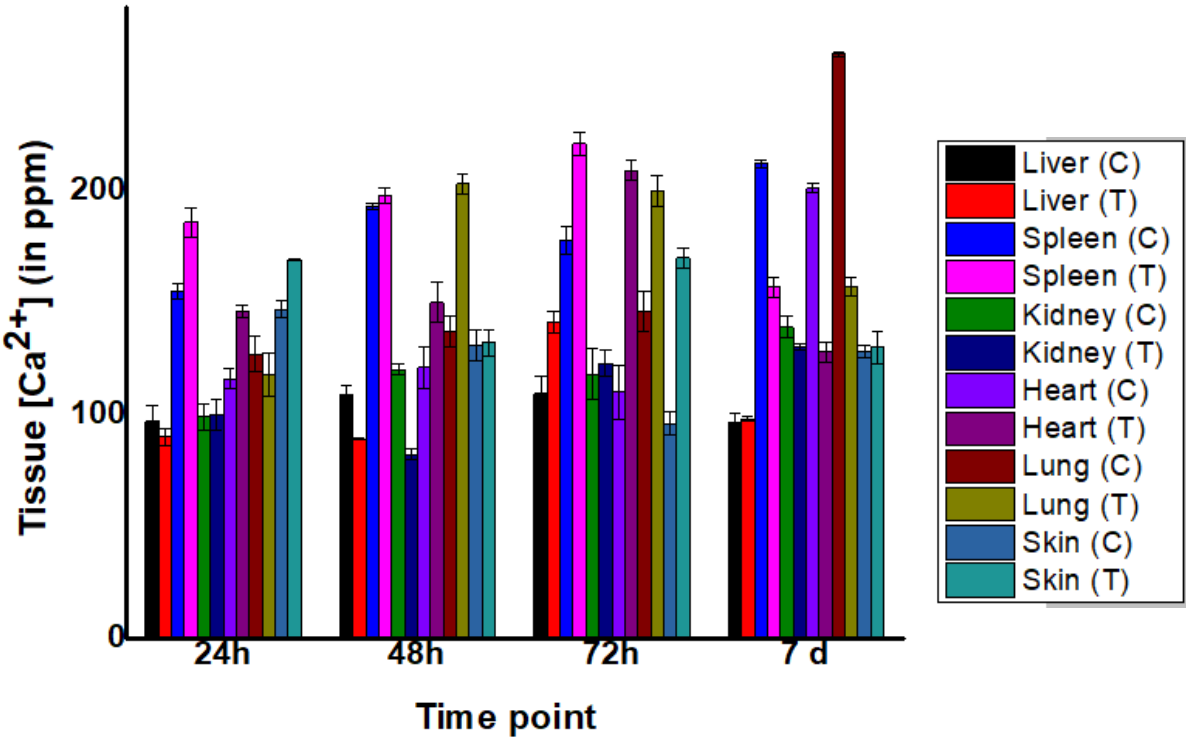

Fig. 5.19. The tissue calcium concentration (in ppm) in different time points after application of ABGmnf based wound care matrix and compared to the control.

***e)In vivo* wound healing assay**

Fig. 14 illustrated the wound healing process on 0, 7, 10 and 14th day following the creation of the wound. The experimental group exhibited initiation of wound healing process much faster compared to control (untreated) and the market available Betadine group. By day 14, the wound was almost completely healed with no scar compared to other two groups. ABGmnf based wound care matrix exhibited a statistically significant ($p<0.05$) wound closure rate reaching

40(±3)% of wound size at the 7th day interval, compared to 22(±1.5)% for the Betadine group and 20(±2)% for control wound. After 10th day of the observation, about 79.9(±2)% wound closure was observed in case of ABGmnf based wound care matrix treated wounds and 55.9(±3)% and 51.8(±3.2)% for the Betadine and control group, respectively. On 14th day, 96.9 (±1.5)% wound closure was observed for the ABGmnf based wound care matrix treated experimental group whereas 81.9 (±2)% and 78 (±1)% for the Betadine and control group, respectively.

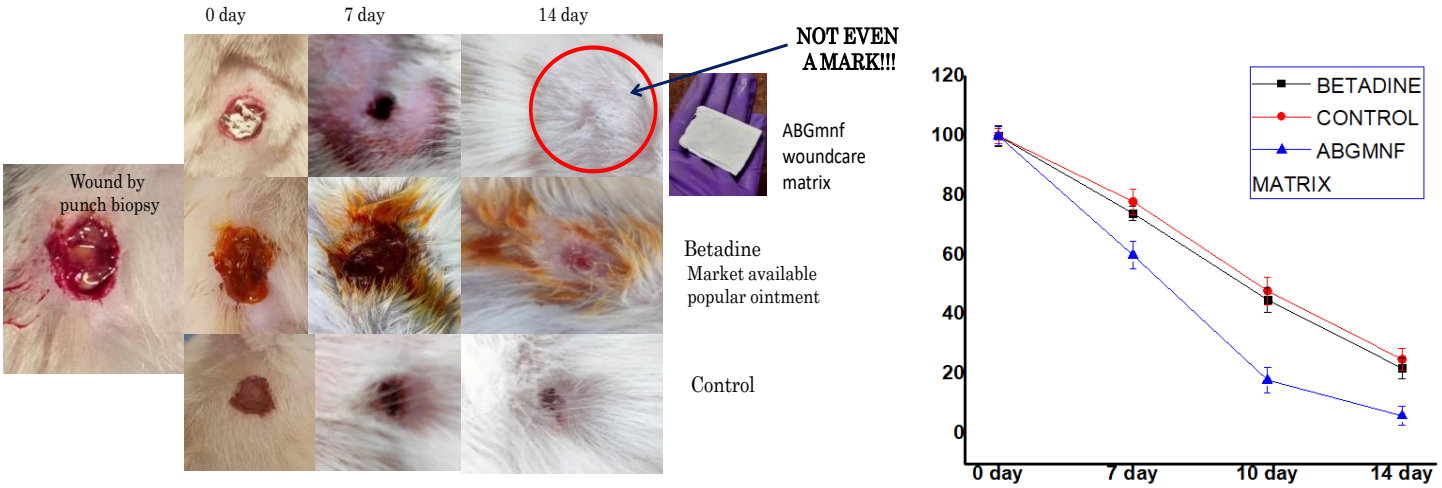

Fig. 5.20. Cascade of full thickness skin wound repair in rats at days 0, 7 and at day 14. Wound treated with ABGmnf based wound care matrix had restored the same texture of normal skin unlike the wound treated with betadine and untreated wound, also it maintained a uniform wound edges throughout the follow up period. The statistical analysis of the % of wound closure in different groups at 0, 7, 10 and 14 days postoperative. All values are demonstrated as mean ± SD (triplicated), ($p \leq 0.05$).

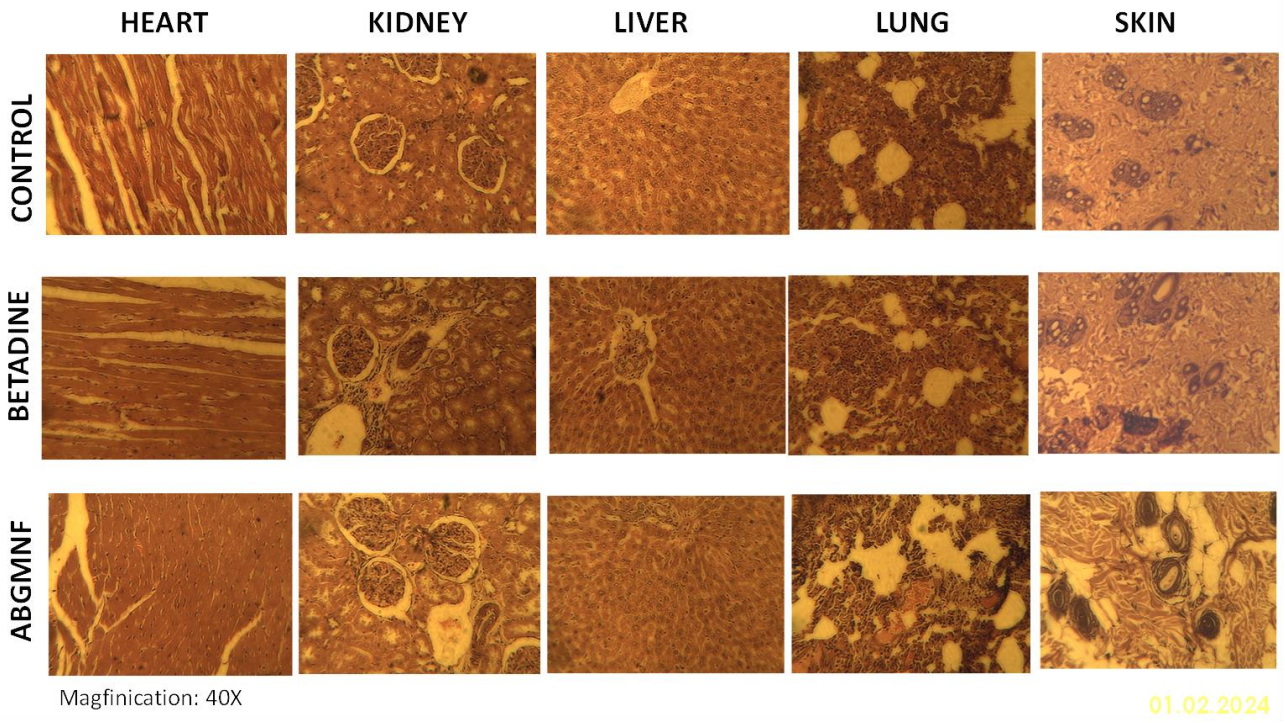

Fig. 5.21. Histological analyses the sections of heart, kidney, liver, lung and kidney in control, betadine and ABGmnf based wound care matrix treated wistar rats (n=3).

In case of heart, the histological analysis showed normal architecture of the cardiomyocytes and myocardium in case of control, betadine as well as ABGmnf based wound care matrix treated groups. Kidney showed normal histoarchitecture of the renal capsule with central vascularized area for the each groups. Bowman's capsule, glomerulus and podocytes were clearly visible. In case of liver, normal hepatic histological architecture was shown and there was no sign of hepatic vein thrombosis in the sinusoids. Central vein, hepatic lobules were surrounded by the hepatocytes, after ABGmnf based wound care treatment also. For the lung, airways and alveolar parenchymal mucosa were shown in normal histo-architecture and absence of any kind of inflammation. In case of skin, the typical histological architecture was shown and no sign of necrosis had been found. Hair follicle, sweat gland, adipocytes, reticular dermis were shown [Roy et al., 2023a].

5.1.4. Discussion

Overall, the primary objectives outlined earlier have been successfully met, validating the initial hypothesis presented at the onset of the investigation. The ABGmnf based wound care matrix

demonstrates qualities that make it suitable for use as a wound care matrix, aiding its consideration in such applications.

The analysis of the AgBG powder and as-prepared ABGmnf based wound care matrix confirmed its suitability for wound healing, as evidenced by its non-toxic impact on the NIH3T3 cell line [Fig. 5.10. 5.11 and 5.12] and enhanced 2D wound healing rates [Fig. 5.13]. This can be attributed to the high solubility of ABGmnf based wound care matrix in various polar solvents, including water [Fig. 5.9]. The increased solubility facilitates the accelerated release of AgBG from the matrix, promoting ion exchange with the surrounding medium. Additionally, AgBG displayed a type IV isotherm with a type H1 hysteresis loop, boasting a specific surface area of approximately 80 m^2/g and an average pore size of 8.9 nm [Fig. 5.3(a, b)]. These properties enable the material to effectively capture and retain water within its pores, expediting the initial phase of the wound healing process [Roy et al., 2024].

Moreover, the use of AgBG as an active material for wound healing is influenced by its capacity to maintain homogeneity and dispersion in a liquid environment. The zeta potential of AgBG, measured at -15.3 mV in dH_2O at pH 7, suggests that the fabricated AgBG is unlikely to agglomerate in a PVP polymer solution [Fig. 5.3 (c)] [Doostmohammadi et al., 2011]. Consequently, the as-spun ABGmnf based wound care matrix contains AgBG in a uniform distribution. The favorable angle of repose of the AgBG further indicates good flow ability [Fig. 5.4].

The successful incorporation of AgBG powder into the PVP fibrous matrix was achieved through electrospinning. XRD analysis confirmed the presence of a broad hump ($2\theta=21^o$) indicating an amorphous glassy network, alongside another broad peak at $2\theta=11^o$ attributed to PVP [Fig. 5.5]. FTIR analysis [Fig. 5.6(a)] captured the distinctive vibrational bands of ABGmnf based wound care matrix. The thermal behavior of the ABGmnf based wound care matrix, evidenced by the TG-DSC curve [Fig. 5.6(c)], revealed the corresponding mass loss. The fibrous nature of both the PVP matrix and the ABGmnf based wound care matrix, resembling a fibrin clot crucial for platelet aggregation and tissue remodeling, was evident in Fig. 5.6 (c). Furthermore, there was a slight modification in the UTS after the incorporation of AgBG into the PVP matrix compared to the PVP matrix alone [Fig. 5.8].

Homaeigohar et al. and other researchers reviewed fibrous wound dressings incorporating bioactive glass [Homaeigohar et al., 2022]. Borate glasses like 13-93B3 have been found to react with simulated body fluid (SBF) five times faster than silicate glass [Huang et al., 2006]. Adding modifier oxides to silicate glasses typically converts oxygen molecules into non-bridging oxygen atoms, reducing network availability. Borate glasses differ from silicate glasses in that they do not always exhibit linear property trends when modifying elements are added. In silicate glasses, the addition of modifiers such as alkali (M_2O) or alkaline-earth (MO) cations disrupts the glass network. This occurs by forming non-bridging oxygens, which help charge balance the modifier cations and reduce the overall glass network connectivity [Shelby, 2005]. Silicate glasses are primarily structured around silicon tetrahedrons. In contrast, vitreous borate glasses are based on planar, trigonally coordinated BO_3 groups, which can form larger structural units like boroxol rings. When modifiers are added to borate glasses, the initial effect is an increase in glass network connectivity due to the formation of 4-coordinated BO^{4-} units. This connectivity increases up to a certain point, after which further additions of modifiers cause a decrease in connectivity, resulting in what is known as the 'borate anomaly' [Fu et al., 2010; Ege et al., 2022]. This change compromises chemical durability and speeds up dissolution, especially with an excess of modifiers and limited network connectivity [Ege et al., 2022].

Nevertheless, the release of borate ions $(BO_3)^{3-}$ at higher concentrations from borate bioactive glass can lead to potential toxicity and unfavorable biological responses [Rahaman et al., 2011]. In this study, a very low concentration of borate has been incorporated into the silicate glass network, well below the toxicity threshold [Institute of Medicine (US) Panel on Micronutrients, 2001]. Following this integration, the cytocompatibility of the composition was evaluated at the *in vitro* level.

In the Fig. 5.11, a comparison of cell viability between experiments using ABGmnf based wound care matrix and the control is evident. Additionally, fluorescent microscopy observations were employed to assess cell proliferation and morphology following exposure to the ABGmnf based wound care matrix, and these results were compared to the control. The DAPI stain, representing cell nuclei, appears blue, while the FITC stain, representing cell cytoplasm, appears green. The figure depicts fluorescent micrographs of cells treated with ABGmnf based wound care matrix and the control after 24h and 72h of incubation. In the images featuring cells treated with the ABGmnf based wound care matrix, a majority exhibited a classical morphology, characterized by colonies

composed of uniformly flat and spread cells, indicating cytocompatibility [Fig. 5.12]. The ABGmnf based wound care matrix showed promising results in promoting the migration of fibroblast cells, indicating its potential for *in vitro* wound healing [Fig.5.13]. Additionally, it exhibited significant antibacterial activity with zone of inhibition (ZOI) measurements of 13.5±1.5 mm and 19±1.2 mm against *S. aureus* and *E. coli*, respectively. These findings highlight its effectiveness in preventing bacterial invasion at the wound site [Fig. 5.14]. The calculated values of MIC of the active ingredient of the ABGmnf based wound care matrix exhibited admirable antibacterial efficacy against both gram positive and gram negative strains that in turn confirms its antibacterial efficacy, taking care of the possibility of bacterial invasion at wound bed [Fig. 5.15].

In vivo biocompatibility assay results shown in Fig. 5.16 confirm that the ABGmnf based wound care matrix is biocompatible and safe for use as a woundcare matrix. Also, it does not induce any kind of immune response, validated by evaluating the levels of proinflammatory cytokines, TNF-α and IL-6 [Fig. 5.16]. As per physiological point of view, TNF-α is a crucial factor for immunogenic response and its excessive activation leads to vasodialation, edema formation, contributes to the oxidative stress at the site of inflammation [Jung et al., 2021]. IL-6, on the other hand, is an upstream inflammatory biomarker that dictates the transition from acute to chronic inflammation [Huang et al., 2006]. Both the above cytokines showed normal concentration range on treatment with the test sample, ABGmnf based wound care matrix, implying good biocompatibility of the test sample.

Another important study, toxicity by leachable components was carried out and the outcomes are shown in Fig.5.17 and Table 5.2. Various parameters related to hematology were tested including RBC and WBC count, WBC Differential count (lymphocyte, monocyte, neutrophil, eosinophil and basophil), hemoglobin level and platelet counts in both cases, i.e., before (denotes ‘0’ h) and after (denotes '4h') application of the ABGmnf [Table 5.2]. Hematological analyses did not exhibit major differences. Clinical biochemical parameters including BUN, Creatinine, AST, ALT and Ca^{2+} concentration were estimated in both sexes of each group and did not indicate any statistical differences. Transaminase indicators, AST and ALT are good indices of damages regarding liver, represent no deleterious impact on the liver in the current case. No unfavorable effects were observed in the levels of BUN and creatinine in serum of the both groups, thus demonstrating the absence of any nephrotoxicity in the test sample. Calcium level was also checked and did not show

statistically significant differences. After sacrifice, the examination of the vital organs such as heart, kidney, liver and lung showed no noteworthy abnormalities. The histological results of the ABGmnf treated and untreated animals were carried on four vital organs, heart, lung, liver and kidney are represented in Fig. 5.17. In case of heart, treated with ABGmnf, showed the normal architecture of the cardiomyocytes and myocardium. There is no sign of increased vacuolization of cardiomyocytes. In case of lungs, airways and alveolar parenchymal mucosa showed normal architecture and absence of any kind of inflammation. In case of liver, treated with the sample, normal hepatic histological architecture is shown and there is no sign of hepatic vein thrombosis in the sinusoids. In case of kidney, treated with ABGmnf, presented the normal histoarchitecture of the renal capsule with central vascularised area was observed [Roy et al., 2023b].

We conducted *in vivo* pharmacokinetic and biodistribution studies to assess various parameters. The serum concentration of leached Ca^{2+} from AgBG of the ABGmnf based wound care matrix was determined and depicted in Fig. 5.18 and 5.19. Evaluating the leaching profile of network modifiers is crucial before using inorganic biomaterials therapeutically, as they can release Ca^{2+} that may exert biological effects at physiological levels. However, elevated levels of Ca^{2+} in the body can lead to various physiological, pharmacokinetic, and pharmacodynamic interactions [Rivadeneira et al., 2015]. Hence, we assessed the *in vivo* release kinetics of leached Ca^{2+} from the ABGmnf based wound care matrix. In our study, the serum concentration-time curve of Ca^{2+} showed an initial increase in serum concentration, peaking at 45 h, and then returning to baseline levels by the end of the experimental period. The maximum serum concentration (C_{max}) was measured at 136 (±3) ppm. Since calcium is an endogenous element in the body, its increased levels are naturally regulated back to baseline through various physiological mechanisms, including influx and efflux through calcium transporters/channels, hormonal regulation involving calcitonin, parathyroid hormone, and vitamin D_3, as well as deposition in organs and bones [Matikainen et al., 2021]. The biodistribution of Ca^{2+} was depicted in Fig. 5.19. On day 1 post-administration of ABGmnf based wound care matrix, significantly higher levels of calcium were detected in the spleen and skin compared to the control rats ($p<0.05$). Over time, by day 3, the calcium levels in all organs increased. This could be attributed to the dermal absorption of leached calcium from ABGmnf based wound care matrix into the systemic circulation, prompting the body to maintain homeostasis. Various physiological calcium stores in the body likely accommodate the surplus calcium. Moreover, the rapid increase in calcium levels was mitigated through urine excretion, evidenced by a significant amount of calcium

detected in the kidneys on day 3 [Patel et al., 2010]. Notably, there was a higher accumulation of calcium in the spleen compared to other organs from day 1 onwards. This could be due to the spleen's role in phagocytosis, clearing foreign particles entering the systemic circulation. Similarly, the liver, rich in resident mononuclear macrophages of the reticuloendothelial system (RES), participates in the endocytosis of foreign entities (in this case, AgBG) [Bhandari et al., 2021]. Subsequently, by day 7, calcium levels showed a decline, with no statistically elevated levels observed in any major organs.

Fig. 5.20 and 5.21 demonstrates the superior wound closure capabilities of the ABGmnf based wound care matrix compared to both Betadine and the untreated control. This improved performance is attributed to the presence of ABGmnf based wound care matrix, which initiates the healing process at both macroscopic [Fig. 5.20] and microscopic levels [Fig. 5.21]. It influences the texture of the wound matrix and modulates proinflammatory cytokines and growth factors like VEGF and FGF, promoting the formation and growth of granulation tissue and ensuring efficient wound closure and healing. [Tanaka et al., 2014; Johnson et al., 2014; Al-Tawarah et al., 2022].

5.2. Results and discussion: Part B

5.2.1. Results: Material characterizations

a)XRD

The X-ray diffraction (XRD) pattern of Al-BAG displays a broad peak at $2\theta = 23°$, indicating the presence of Si-O-Si linkages in the glass composition, indicative of the amorphous nature of the sample. Our experimental procedure successfully synthesized Al-BAG [Fig. 5.22(a)] [Roy et al., 2023b].

b)FTIR

FTIR spectroscopy is a useful tool for examining a sample's absorption of infrared radiation. The analysis of the IR spectrum involves correlating the absorption bands (vibrational bands) with the chemical compounds present in the sample. The FTIR spectrum of the synthesized Al-BAG powder is depicted in Fig. 5.22(b). The peaks observed at 515 cm^{-1} and 736 cm^{-1} are attributed to the stretching of aluminum oxide [Tang et al., 2005]. Additionally, the peak at 450 cm^{-1} corresponds to the bending of the Si-O-Si bond, while two absorption peaks located at approximately 1100 cm^{-1} and 800 cm^{-1} are associated with the asymmetric stretching mode and symmetric stretching or vibration modes, respectively, of the silica ring structure in the Si-O-Si bonds [Pourshahrestani et al., 2016; Roy et al., 2023b].

c)TG-DSC

The Thermogravimetric Analysis (TGA) curve revealed the temperature-dependent mass loss characteristics of the material [Fig. 5.22(c)]. Our findings identified a two-phase sequence of mass loss: the first phase occurred between 30°C and 1830°C, primarily involving the removal of physio-absorbed water, alcoholic products, decomposition of alkoxides, and OH groups [Lefebvre et al., 2007; Kargozar et al., 2019]. The second phase, observed from 200°C to 650°C, was attributed to the simultaneous decomposition of nitrates [Jones et al., 2006]. An endothermic peak at around 470°C indicated the release of water and organic compounds [Li et al., 2016], while another peak at 650°C was linked to the decomposition of residual nitrate compositions and the condensation of silanol [Roy et al., 2023b].

This TGA curve correlated well with the Differential Scanning Calorimetry (DSC) results. Following the decomposition of nitrate groups from the glass network, no further deviations in material mass were observed, suggesting a reduction in decomposition reactions. Notably, all inorganic components were eliminated before reaching 650°C, marking the onset of crystallization around 700°C. The DSC curve exhibited a small endothermic notch around 450°C, indicating the initiation of the transition, specifically nucleation. Another endothermic peak at 523°C was observed, and beyond 650°C, no additional heat absorption was noted. Consequently, the glass transition temperature occurred prior to crystallization, either at or before 650°C [see Fig. 5.22(c)] [Roy et al., 2023b].

d)BET

Fig. 5.22(d) illustrates the N_2 adsorption-desorption isotherm and the corresponding pore size distribution [inset of Fig. 5.22(d)] for Al-BAG. Key textural characteristics of Al-BAG, determined through N_2 adsorption porosimetry, are provided in Table 5.3. As depicted in Fig. 5.22(d), Al-BAG displayed a type IV isotherm with a type H1 hysteresis loop, characteristic of materials with mesoporous structures. The specific surface area of Al-BAG was measured at 333.744 m^2/g, and the average pore size was determined to be 4.617 nm [Fig. 5.22(d)] [Roy et al., 2024a].

Table 5.3. BET analysis of Al-BAG

Sample name	Surface area (m^2/g)	Average pore diameter (nm)	Pore volume (cc/g)
Al-BAG	333.744	4.617	0.450

e)Particle size analysis of Al-BAG

The particle size of Al-BAG falls within the range of 140 nm to 253 nm, and the median particle size (D_{50}) is determined to be 185.6 nm.

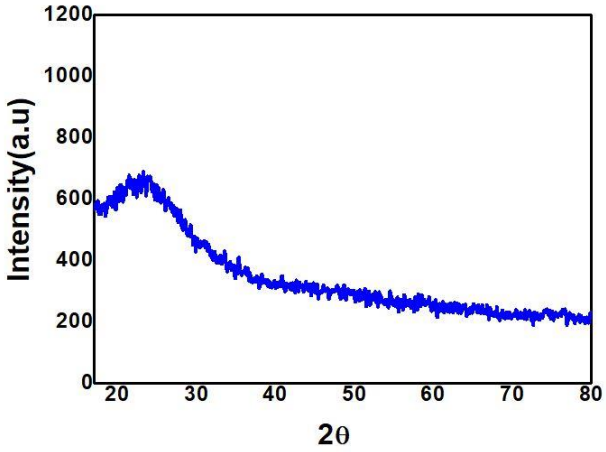
Intensity(a.u)
2θ

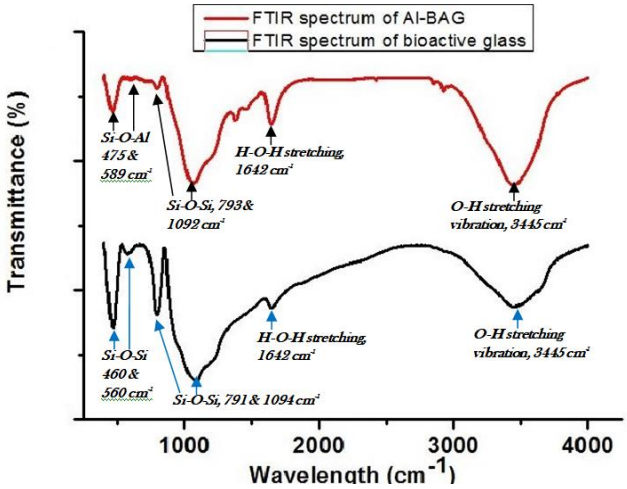
FTIR spectrum of Al-BAG
FTIR spectrum of bioactive glass
Transmittance (%)
Si-O-Al 475 & 589 cm-1
Si-O-Si, 793 & 1092 cm-1
H-O-H stretching, 1642 cm-1
O-H stretching vibration, 3445 cm-1
Si-O-Si 460 & 560 cm-1
Si-O-Si, 791 & 1094 cm-1
H-O-H stretching, 1642 cm-1
O-H stretching vibration, 3445 cm-1
Wavelength (cm-1)

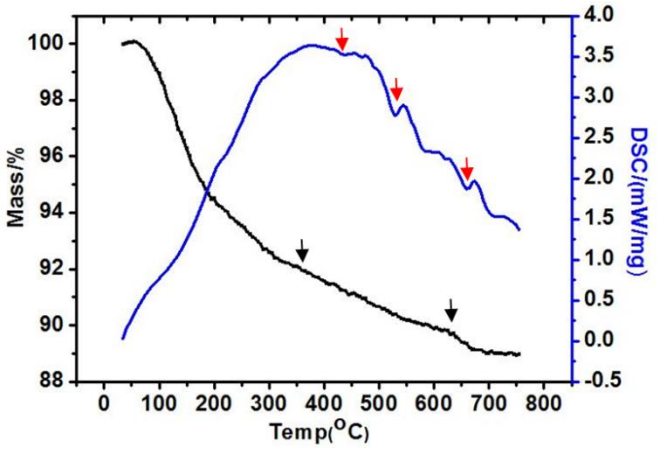
Mass/%
DSC/(mW/mg)
Temp(°C)

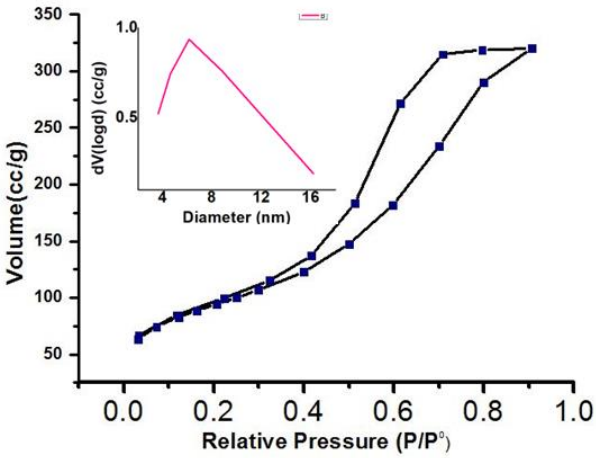
Volume(cc/g)
dV(logd) (cc/g)
Diameter (nm)
Relative Pressure (P/P°)

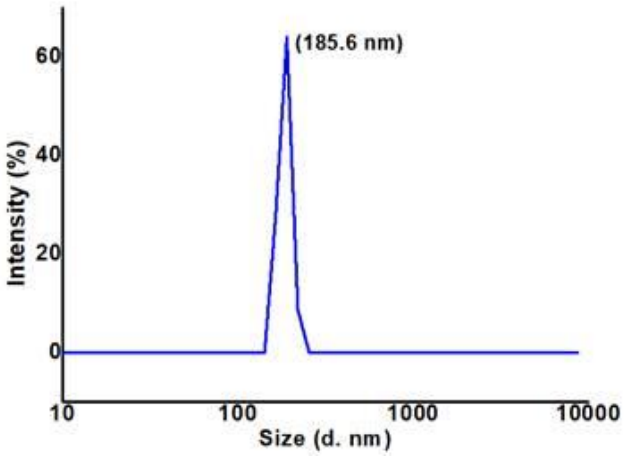
(185.6 nm)
Intensity (%)
Size (d. nm)

Fig. 5.22 (a) XRD pattern of as-prepared Al-BAG powder, calcined at 650^0C.

(b)FTIR spectra of as-prepared Al-BAG calcined at 650^oC and bioactive glass.

(c) TG-DSC plot of as-prepared Al-BAG, calcined at 650^0C.

(d) Displays the N_2 adsorption-desorption isotherm and its associated pore size distribution for Al-BAG [inset of 5.22(d)].

(e) Particle size distribution measurement of Al-BAG.

5.2.1.6. SEM-EDX

The Al-BAG was synthesized successfully according to our experimental procedure. The Al-BAG surface morphology and microstructure was observed by SEM. The surface morphology of Al-BAG is shown in Fig. 5.23 (a, b), exhibits agglomerated particles with granule shapes, having particle size in the range 100-200 nm in a monodisperse manner. The EDX analysis of the freshly prepared Al-BAG validated the presence of Si, Ca, Al, and Zn. According to the EDX results, the composition of the Al-BAG closely aligned with the theoretical values [Roy et al., 2023b].

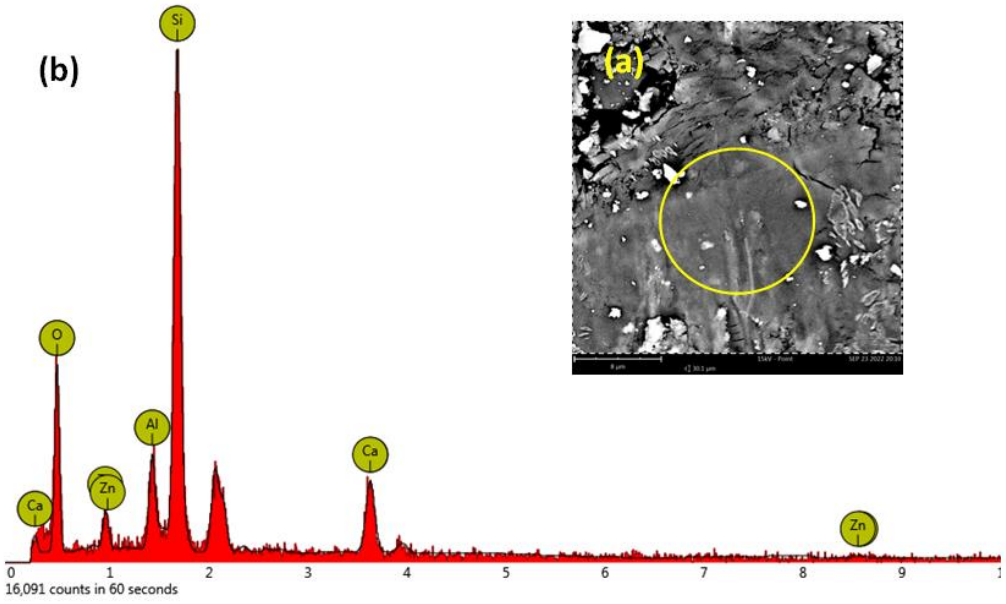

Fig. 5.23. Image (a) depicts the Scanning Electron Microscope (SEM) image, while (b) represents the Energy Dispersive X-ray (EDX) pattern of the as-prepared Al-BAG [Roy et al., 2023b].

g) *In vitro* ion release and degradation study

Changes in the concentrations of Ca^{2+} , Zn^{2+} and Al^{3+} at pH 5.2 and pH 7.4 over different time intervals are illustrated in Figure 4. A significant rise in Ca^{2+} concentration was observed within the first 24 hours under various pH conditions, reaching levels around 30-35 ppm, indicating rapid dissolution.

The *in vitro* degradation characteristics of the samples were assessed by measuring the weight loss ratio after immersion in two distinct pH solutions, namely pH 5.2 and pH 7.4, mimicking the pHs of a wound area and normal blood, respectively. The weight loss increased with prolonged soaking for up to 14 days, after which it gradually continued to degrade, as depicted in Fig. 5.24 [Roy et al., 2023b].

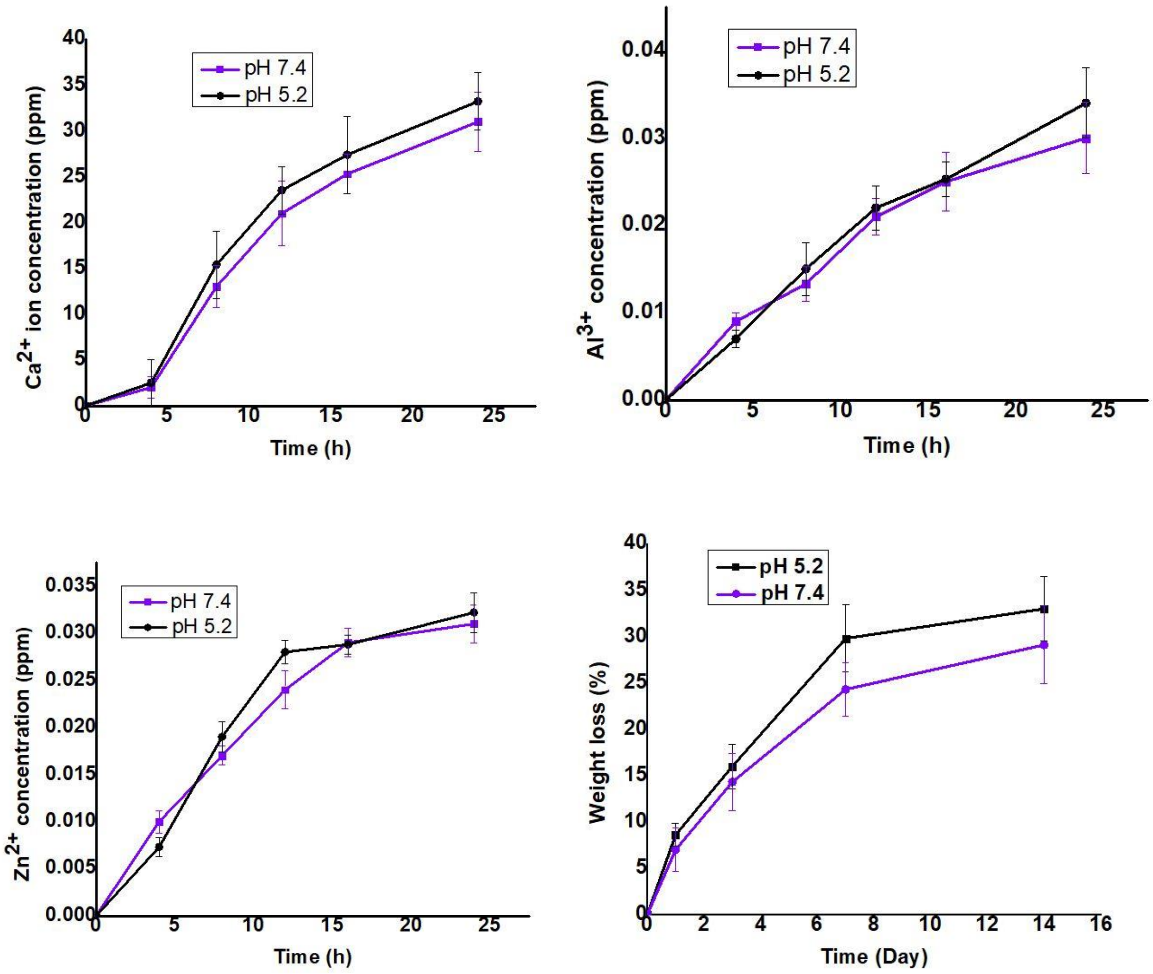

Fig. 5.24. The levels of (a) Ca^{2+}, (b) Al^{3+} and (c) Zn^{2+} were monitored over time during the initial 24 hours in solutions with two different pH values, 5.2 and 7.4. Additionally, (d) illustrates the variation in weight loss of Al-BAG samples under the aforementioned pH conditions [Roy et al., 2023b].

5.2.2. *In vitro* biological assays

a)*In vitro* cytotoxicity assay

To assess the biocompatibility of Al-BAG, the cytotoxicity of NIH3T3 cells was examined following exposure to the leached extract of the sample for 24, 48, and 72 hours. The MTT assay revealed a slight enhancement in cell viability over the culture period, indicating that the sample exhibited non-cytotoxic effects on NIH3T3 cells, as depicted in Fig. 5.25 [Roy et al., 2023b].

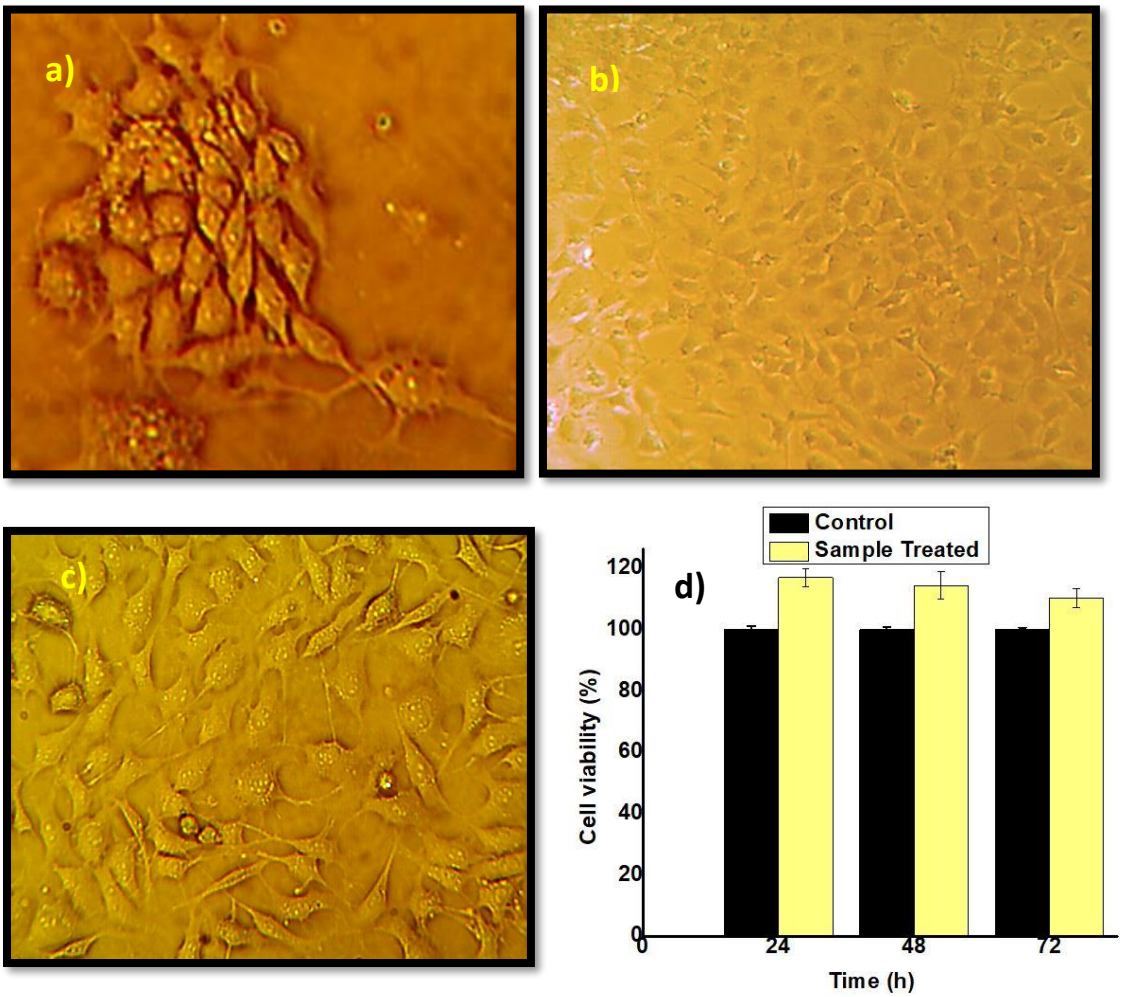

Fig. 5.25 Microscopic pictures of NIH3T3 cells (40X magnification) cultured with the Al-BAG sample are shown for different durations: (a) 24 hours, (b) 48 hours, and (c) 72 hours. (d) illustrates the viability of NIH3T3 cells after exposure to extracts from Al-BAG for 1, 2, and 3 days. The data, obtained through the MTT assay, did not show any statistically significant differences ($p > 0.05$) [Roy et al., 2023b].

b)Immunofluorescence staining

Fig. 5.26 represents the fluorescence microscopy images of NIH3T3 cells, stained with DAPI and FITC. Herein, 24h culture was done to observe the adhesion property of cells and showed good cell adhesion [Fig. 5. 26(a)]. After 72h, all attached cells spread properly. Further, cells treated with Al-BAG, proliferated well and almost reached confluence after 72h incubation [Fig. 5.26(b)]. Fig. 5.26(c) showed the cellular morphology in higher magnification, 20X, after treated with Al-BAG after 24h and 72h compared with control (untreated cells).

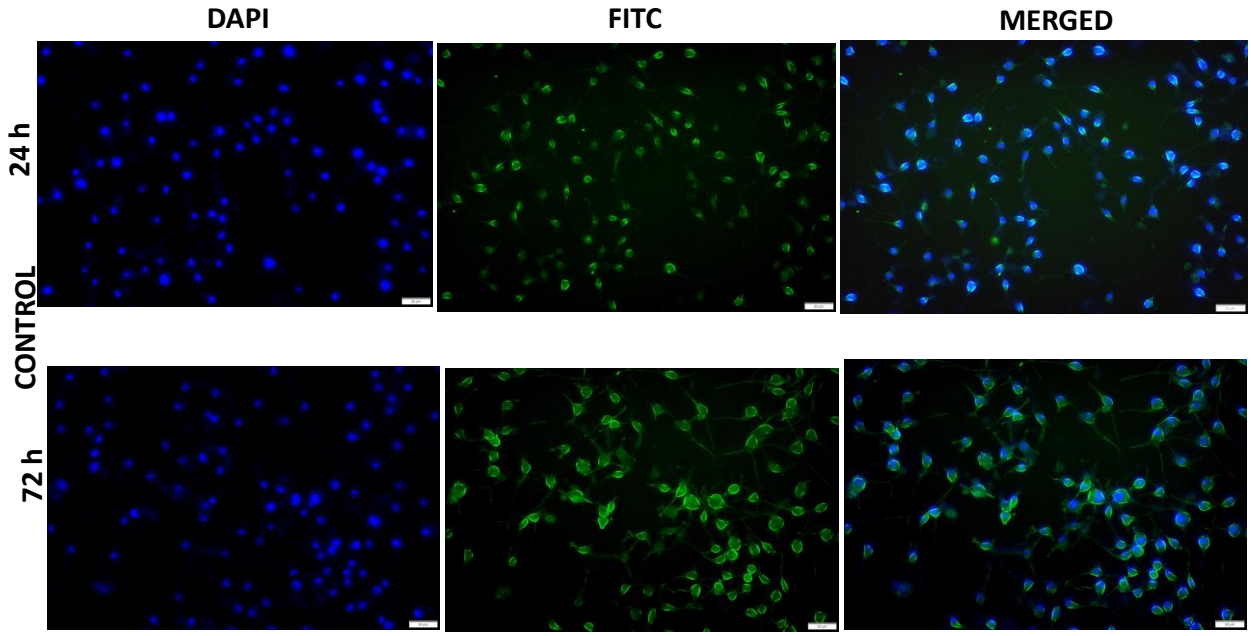

Scale bar: 50 µm and magnification 10X

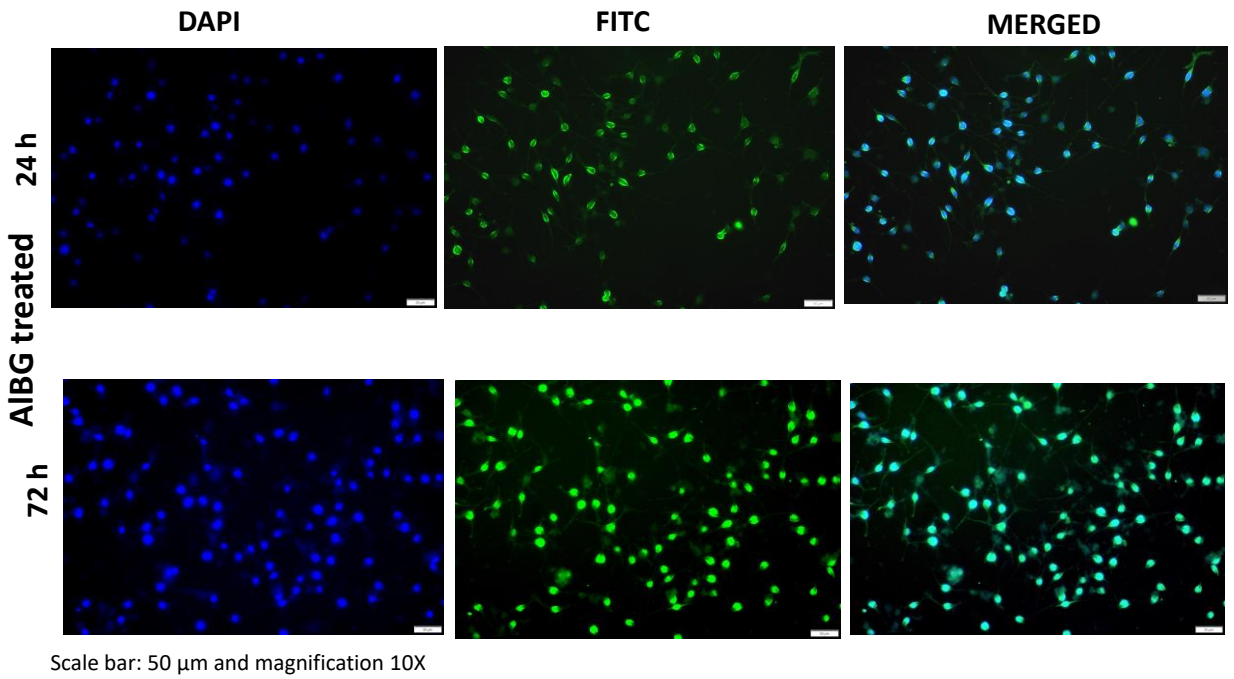

Scale bar: 50 µm and magnification 10X

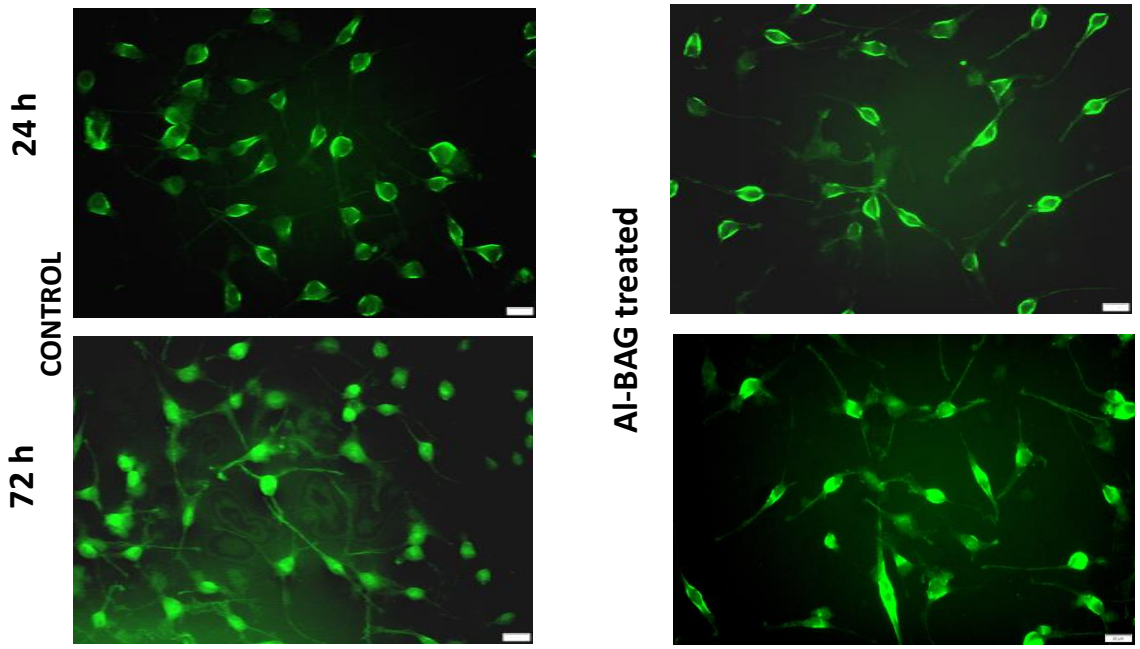

Scale bar: 20 µm and magnification 20X

Fig. 5.26 Fluorescence images of cells (a) without any treatment (act as control) and (b) treated with Al-BAG extract and incubated for 24h and 72h. The images showed no adverse effects on the cellular morphology after treatment. Magnification: 10X and Scale bar: 50µm. (c) The cellular morphology was showed in higher magnification (20X) and scale bar: 20µm.

c) *In vitro* antibacterial activity

The antibacterial efficacy of Al-BAG was investigated against gram-positive strains of *Staphylococcus aureus* for a duration of 8 hours, as illustrated in Fig. 5.27. Al-BAG exhibited strong antibacterial activity against *S. aureus*, primarily attributed to the antibacterial properties of Zn^{2+}. Notably, Al-BAG lacking incorporated Zn^{2+} did not exhibit any antibacterial effects. The inhibitory effect of Al-BAG reached 50% at the 7.5-hour mark [Roy et al., 2023b].

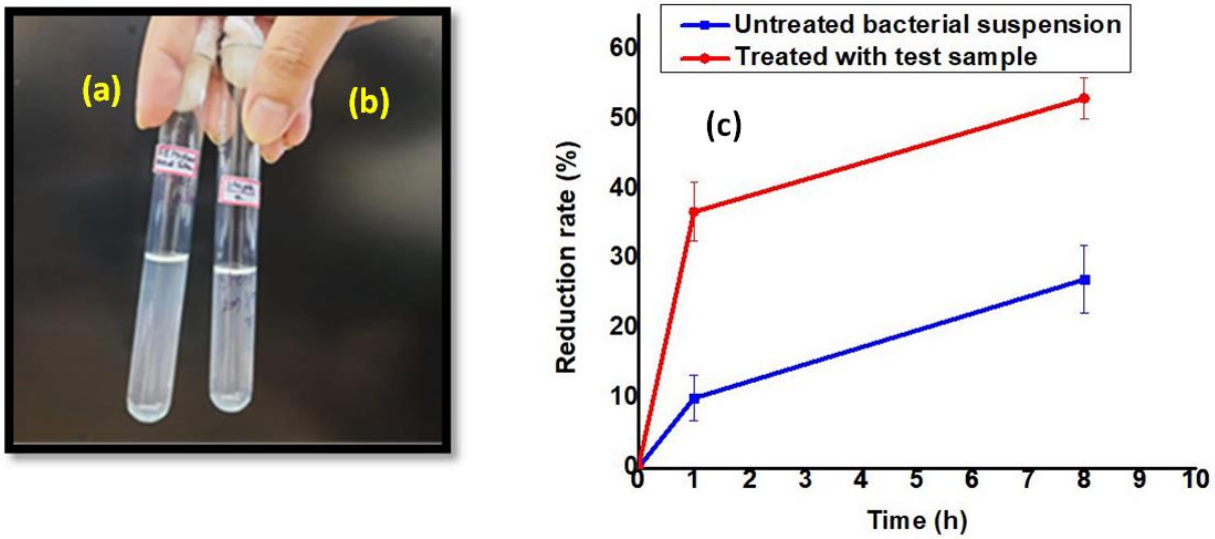

Fig. 5.27 A comparison of turbidity was made between McFarland standard 0.5 (a) and a suspension of *Staphylococcus aureus* (b). The antibacterial effectiveness of Al-BAG against *S. aureus* is depicted in (c).

d) Hemocompatibility test

To assess the hemocompatibility of the prepared sample, it was incubated with human blood to evaluate its ability to induce red blood cell (RBC) lysis. The hemolysis test was conducted, wherein the undesired lysis of RBCs was quantified by measuring the photometric change in absorbance at 540 nm. The findings indicated a hemolysis rate of less than 5% at a concentration of 5 mg/ml, adhering to the recommended level according to standard protocols, as illustrated in Fig. 5.28 [Roy et al., 2023b].

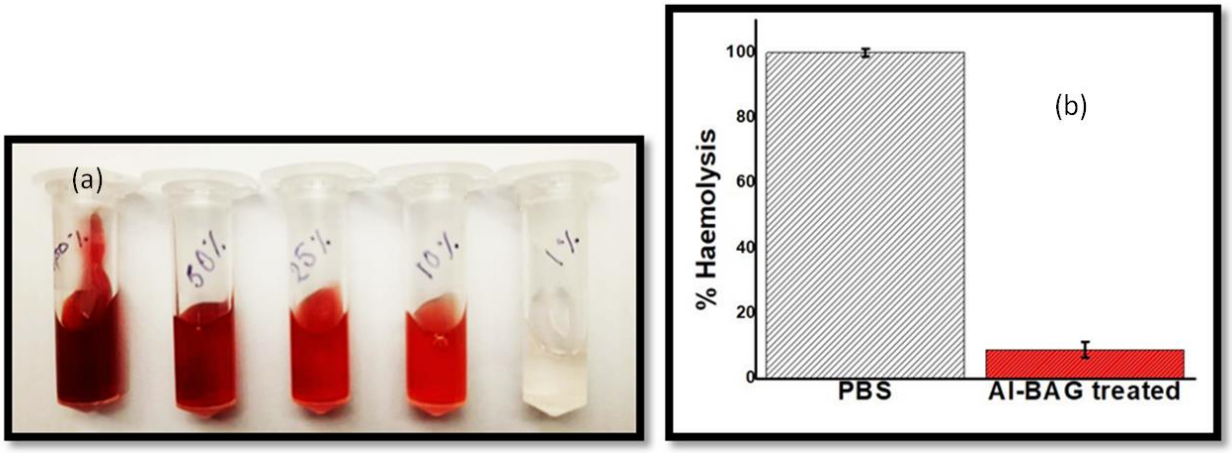

Fig. 5.28 presents the results: (a) a line of best fit was created by making 100, 50, 25, 10, and 1% dilutions, and (b) the hemolysis percentage standard error of the mean for the samples. Absorbance values were matched with the calibration curve to determine hemolysis percentage measurements, demonstrating a statistically significant decrease in hemolysis percentage for Al-BAG compared to PBS only (i.e., no treatment) with a p-value greater than 0.05 [Roy et al., 2023b].

e)*In vitro* blood absorption efficiency

The absorbent capacity of Al-BAG was assessed using both PBS and blood to examine hemostatic responses. The pellets displayed a 36% absorption rate in PBS after 1 hour of incubation, whereas a 45% absorption rate was observed in blood during the same incubation period. After 2 hours of incubation, absorption rates increased to 52% in PBS and 68% in blood, as shown in Fig. 5.29. No further significant absorption was observed after the 2-hour incubation period [Roy et al., 2023b].

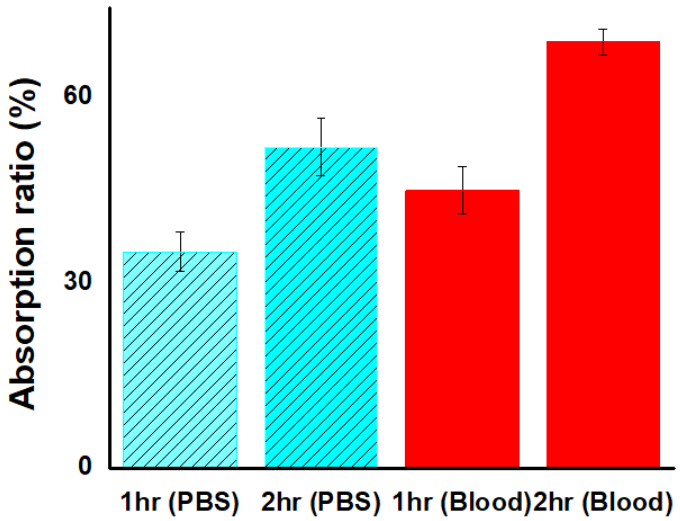

Fig. 5.29 illustrates the absorption of Al-BAG samples in both PBS and blood at two distinct time intervals (1 and 2 hours). The findings indicate a higher absorption capacity in blood compared to PBS, and these differences are statistically significant with a p-value greater than 0.05 [Roy et al., 2023b].

f) *In vitro* thrombus formation

The effective incorporation of Al^{3+} and Zn^{2+} ions into the bioactive glass network was observed to promote thrombus formation, as evidenced by the *in vitro* thrombus formation assay. The thrombus formation exhibited a positive correlation with the incubation time, as depicted in Fig. 5.30 (a, b) [Roy et al., 2023b].

g) *In vitro* blood plasma coagulation assays: PT and aPTT

To assess the impact of Al-BAG on the blood coagulation process, Prothrombin Time (PT) and Activated Partial Thromboplastin Time (aPTT) tests were conducted using two different quantities of Al-BAG (1mg denoted as sample 1 and 3 mg denoted as sample 2). The PT test explores the extrinsic pathway of the blood coagulation cascade, while the aPTT test is associated with the intrinsic pathway. The PT results indicated that all samples significantly activate the extrinsic pathway, leading to reduced PT values (18±1.2 second) compared to the control (blood without sample) (21±1.5 second). Similarly, aPTT values (37.5±1.3 second) were also decreased compared to the control (40±1.2 second), indicating the sample's ability to

activate the intrinsic pathway. The results showed that after Al-BAG treatment, there was a reduction of approximately 14% (±0.9%) in PT and 6.25% (±0.5%) in aPTT compared to the control. However, with a higher quantity of the sample, no significant changes were observed, as illustrated in Fig. 5.30(c, d) [Roy et al., 2023b].

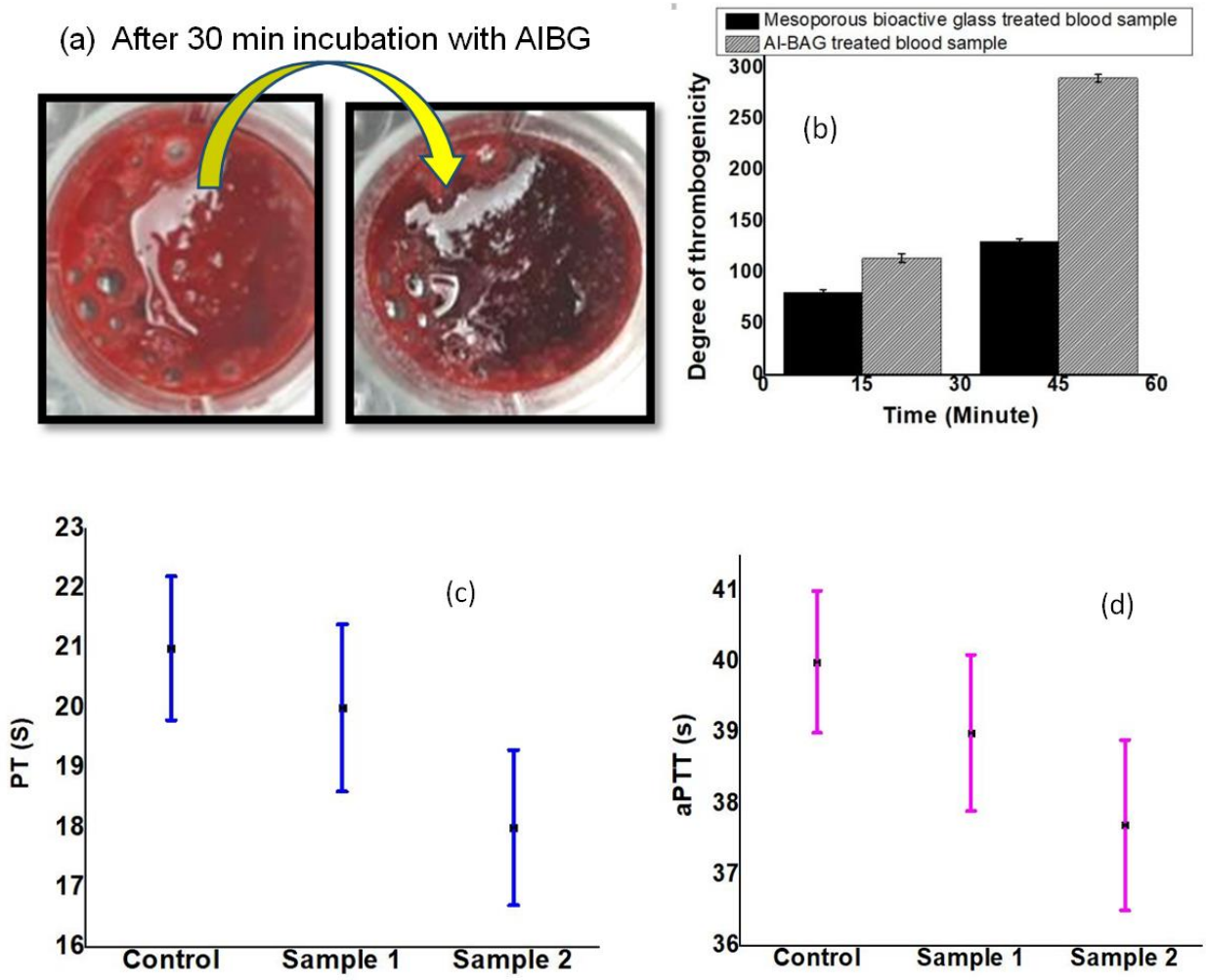

Fig. 5.30 (a) The blood clot formed on Al-BAG surface, captured by a digital camera. (b) Quantitative results of thrombus formation after different incubation times [Roy et al., 2023b].

(c) PT and (d) aPTT results for the sample, observed statistically significant reduction (n=3, p>0.05) in PT specially and aPTT as well compared to control [Roy et al., 2023b].

h)*In vitro* thrombin generation

To quantify the thrombin production over a period, Thrombin-Antithrombin (TAT) levels were assessed in whole blood incubated with Al-BAG and surgical cotton gauze (as control). The TAT concentration in blood exposed to Al-BAG was notably elevated at 62.58 pg/ml ($p<0.05$), in stark contrast to the control with surgical cotton gauze, where TAT measured 6.00 pg/ml [Fig. 5.31] [Roy et al., 2023b].

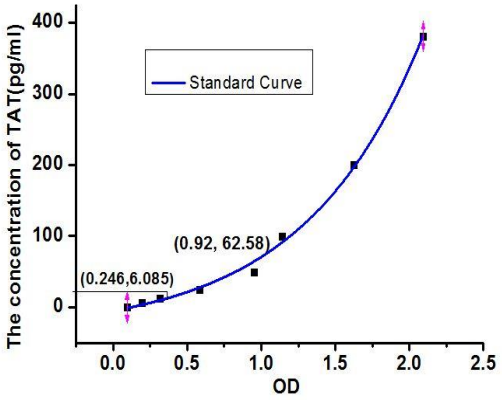

Sample	Concentration of TAT (pg/ml)
1. Control	6
2. Al-BAG	62.50

Fig. 5.31 Thrombin generation over time as measured by the levels of thrombin-antithrombin (TAT) complex, $p<0.05$ by Al-BAG compared to control, n=4 [Roy et al., 2023b].

i)Blood clot formation

SEM analysis revealed the surface of the Al-BAG pellet used for absorbing plasma proteins and blood cells [Fig. 5.32 (b)]. The time taken for blood clot formation was recorded, and it was observed that Al-BAG formed a stable clot in less time compared to the control (surgical cotton gauze) [Fig. 5.32 (a)] [Roy et al., 2024a].

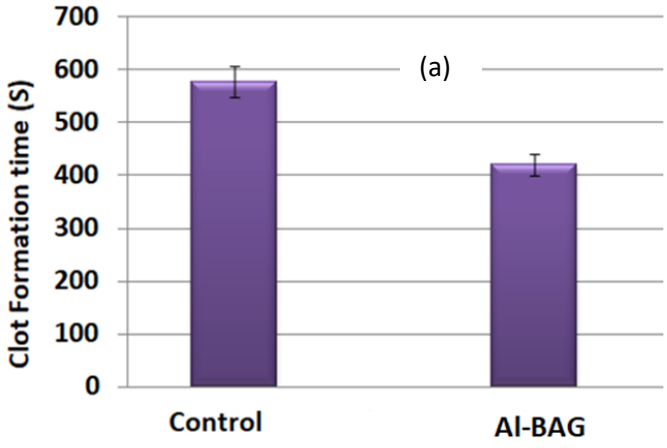

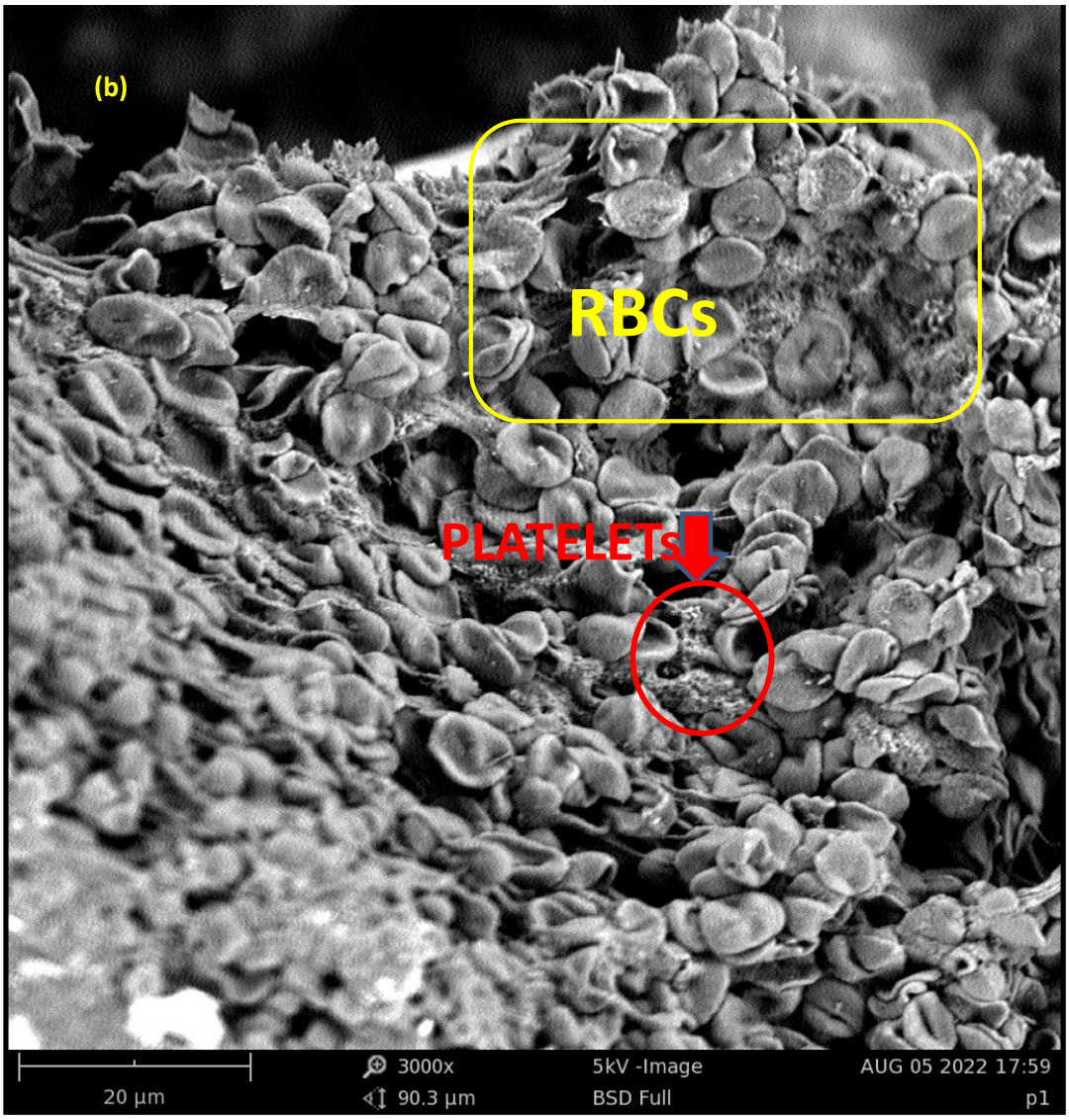

Fig. 5.32 (a) represents the clot formation time, contact with whole blood in the presence of Al-BAG as well as control (n=5).

(b) SEM micrograph exhibit red blood cells (RBCs) and platelets adhered onto the Al-BAG pellet surface, scale bar represents 20 µm and 3000x magnification.

j)*In vitro* assessment of platelet adhesion

In a laboratory study aimed at investigating the influence of Al-BAG on facilitating platelet adhesion and aggregation, Al-BAG and surgical cotton gauze (used as a control) was exposed to a platelet suspension for three different durations (15, 30, and 60 mins). The quantification of platelet adhesion was conducted using an LDH assay kit. Fig. 5.33 presents both qualitative and

quantitative findings related to platelet adhesion on Al-BAG. The results demonstrate that Al-BAG significantly enhances platelet adhesion across various time intervals. No notable differences in the number of adherent platelets on the surfaces were observed after a 15-min incubation period. The most substantial changes in platelet numbers occurred during the subsequent 30 and 60 mins [Fig. 5.33]. The images depict a higher coverage of platelets on the Al-BAG surface, accompanied by the presence of fibrin with a silky appearance, as well as numerous pseudopodia of platelets, indicating increased platelet activation and aggregation [Roy et al., 2024a].

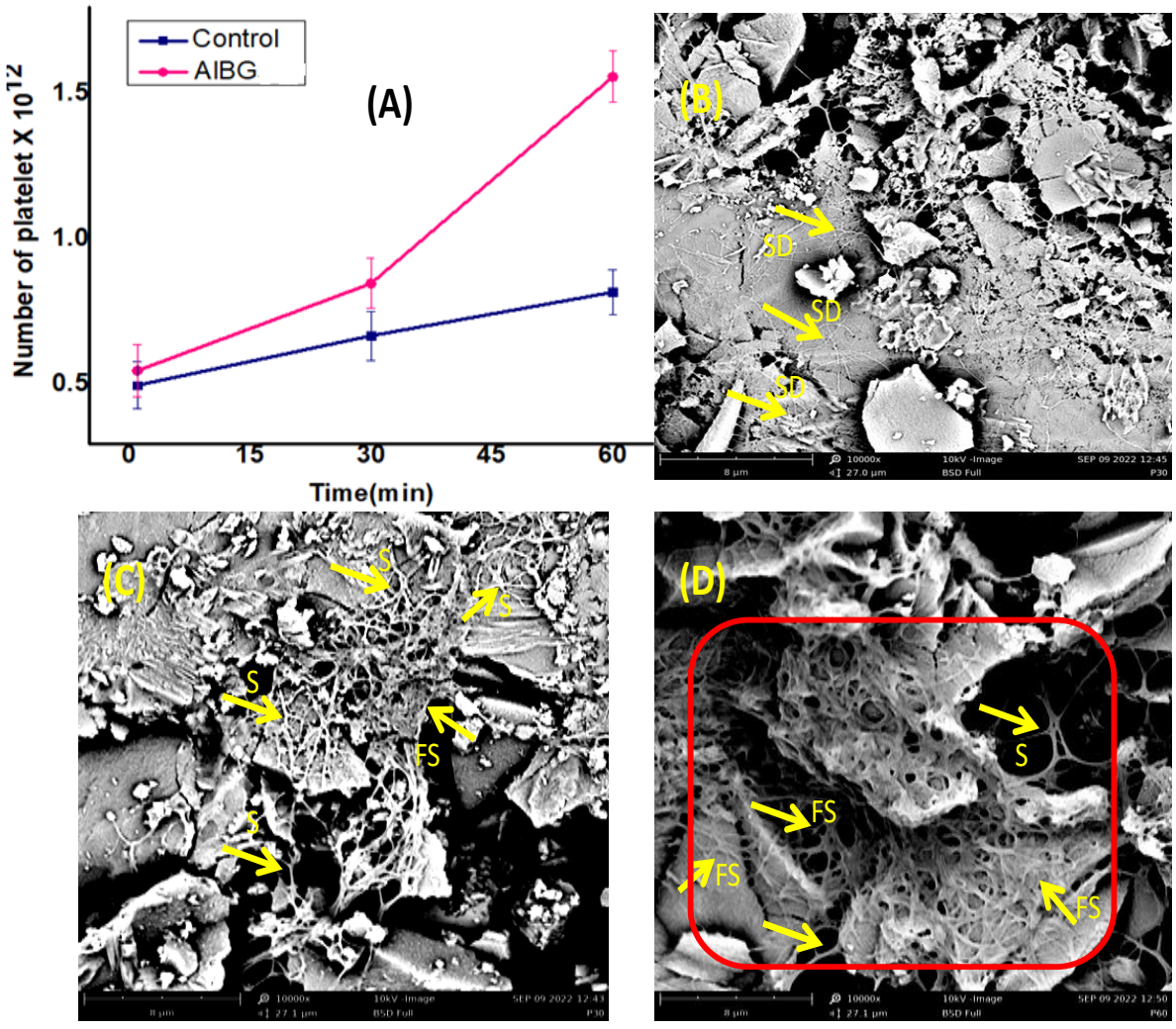

Fig. 5.33 (A) Quantification of platelet adhesion on the Al-BAG surface. (Represented a significant difference, $p > 0.05$). (B), (C) and (D) SEM images illustrating platelet adhesion on the Al-BAG surface at 15, 30, and 60 min (magnification 10000X and scale bar 8 µm).The

arrows indicate the dendrites connecting the platelets. SD=Spread dendritic, S=Spreading, FS=Fully spread [Roy et al., 2024a]. The red box (D) demarcates the active feature of the platelets (S, FS).

k***)In vitro* red blood cell adhesion**

After the fresh blood with leached extract of Al-BAG solidified, they were washed several times with PBS. Then, the blood clot was fixed with 4% paraformaldehyde and maintained for 3h. After washing several times with PBS to remove excess paraformaldehyde, the clot was immediately dehydrated with 20%, 40%, 60%, 80% and 100% ethanol/water solution. RBC adhesion *in vitro* was observed by SEM after natural drying.

The yellow marked arrows are indicating the RBCs with intact cellular morphology [Fig. 5.34].

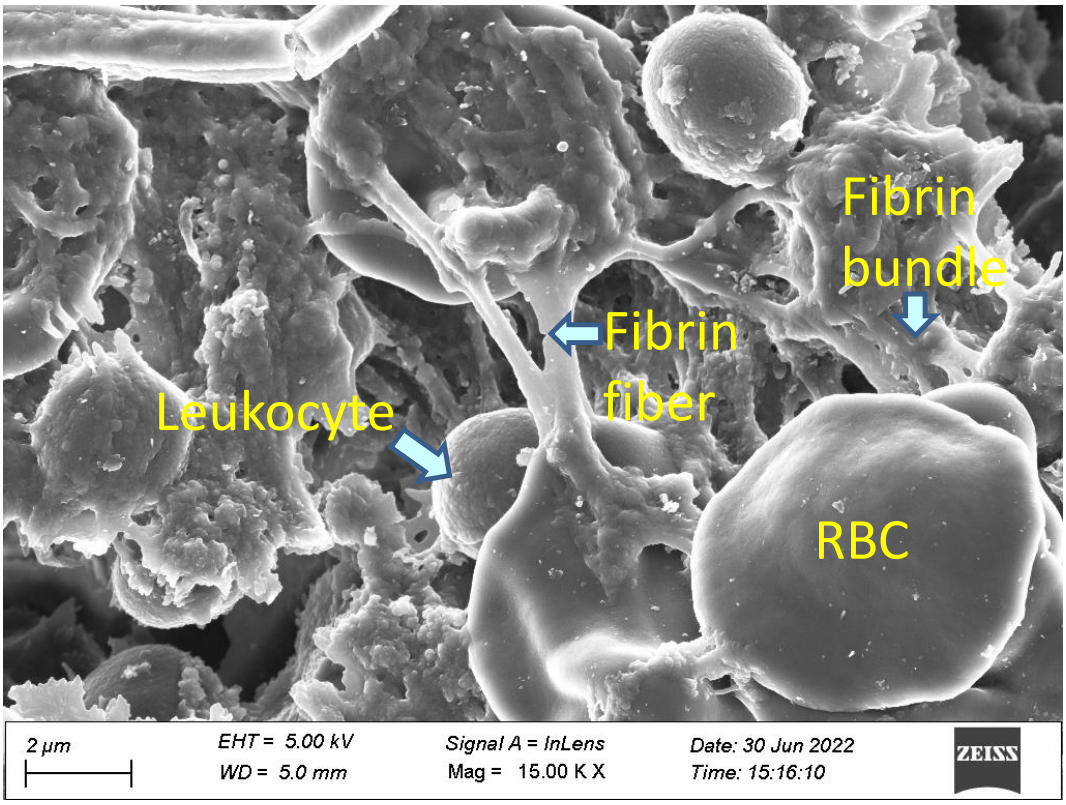

Fig. 5.34 SEM image of a stable hemostatic blood clot, composed of platelet aggregates, RBCs and leukocytes entrapped in the fibrin network [Scale bar= 2µm, Mag= 15 K X]

l) Whole blood clotting and determination of blood clotting index (BCI)

To investigate the potential of Al-BAG to expedite blood clot formation, both Al-BAG and surgical cotton gauze (utilized as the control) were exposed to whole blood. The assessment focused on the presence of hemolyzed, untrapped red blood cells not adhering to the dressing surface, which is directly correlated with slower clotting, leading to higher absorbance. The results indicated that Al-BAG exhibited significantly lower absorbance ($p < 0.05$), indicating a shorter clotting time compared to the control. The calculated Blood Clotting Index (BCI), using the provided equation, was approximately 47(±2.3)%. The remarkably low BCI value suggests that Al-BAG promotes rapid clotting [see Fig. 5.35] [Roy et al., 2024a].

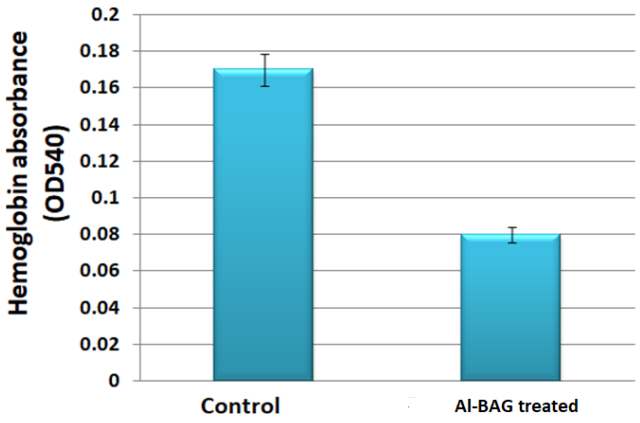

Fig. 5.35 Effect of the Al-BAG on blood clotting rates, as calculated by absorbance of haemoglobin from lysed untrapped RBCs ($p < 0.05$) [Roy et al., 2024a].

5.2.3. Results: *In vivo* animal studies

a) *In vivo* acute dermal toxicity assay

Upon macroscopic examination following the application of Al-BAG with an appropriate vehicle, no clinical indications of erythema, edema, redness, or severe inflammation were observed in both study groups. The results are depicted in Fig. 5.36. After specific time intervals (1 day, 5 days, 10 days, and 14 days), the areas treated with Al-BAG at various concentrations were inspected, revealing complete hair growth within 14 days and the absence of any clinical signs of dermal toxicity [Roy et al., 2023b].

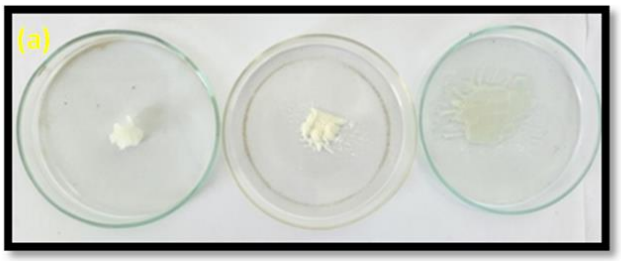

Vehicle (A) | Al-BAG powder (B) | A + B

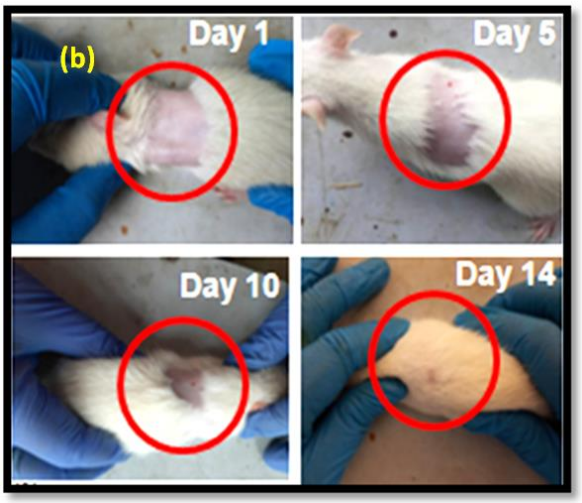

Fig. 5.36 (a) The images depict the mixing of the test material with an appropriate vehicle at a specific ratio, which is then applied to the shaved skin area for the acute dermal study. (b) The images illustrate that the test material does not induce any indications of dermal toxicity after specific time intervals [Roy et al., 2023b].

Histological assessments were conducted on five vital organs—lungs, liver, heart, kidney, and skin—treated with various concentrations of Al-BAG, along with untreated animals. The results are presented in Fig. 5.37. For the lungs, doses of 100 mg/kg BW and 500 mg/kg BW exhibited normal architecture of airways and alveolar parenchymal mucosa without any signs of inflammation. In the liver, treatment with two different doses showed a normal hepatic histological structure, and there was no evidence of hepatic vein thrombosis in the sinusoids. Similarly, in the heart, doses mentioned above displayed the typical architecture of cardiomyocytes and myocardium, with no increased vacuolization observed in cardiomyocytes. The kidney, treated with the mentioned doses, demonstrated a normal histoarchitecture of the renal capsule with a central vascularized area. Regarding the skin, treated with two different doses, it exhibited typical histological architecture, and no signs of necrosis were observed [Roy et al., 2023b].

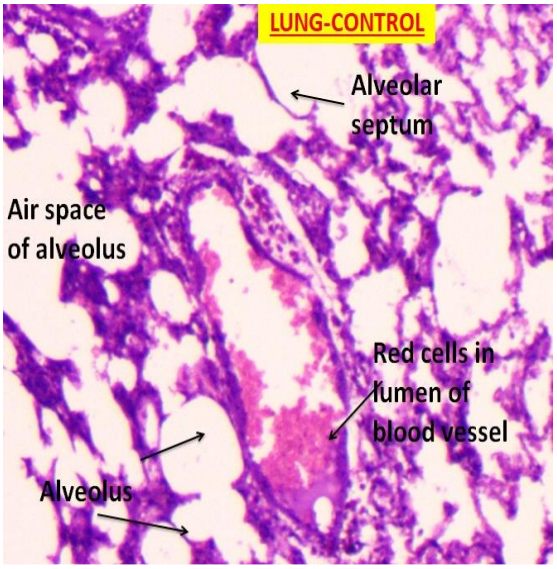

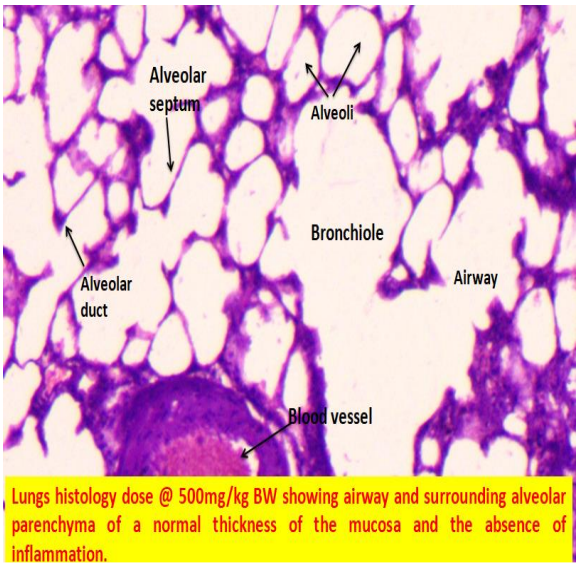

Lungs histology dose @ 500mg/kg BW showing airway and surrounding alveolar parenchyma of a normal thickness of the mucosa and the absence of inflammation.

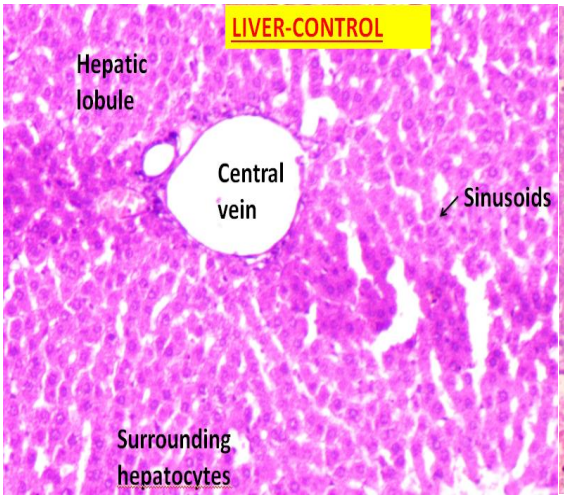

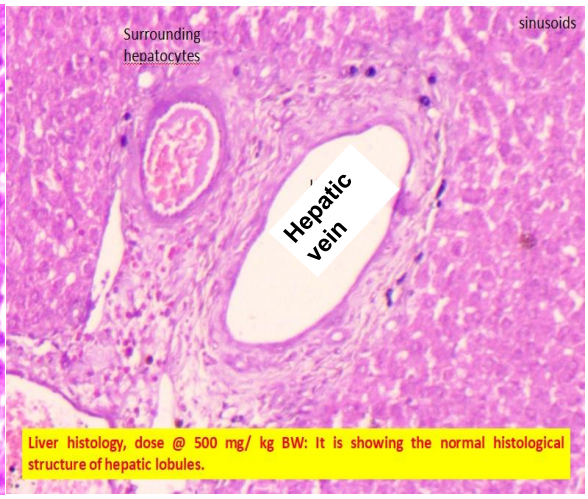

Liver histology, dose @ 500 mg/ kg BW: It is showing the normal histological structure of hepatic lobules.

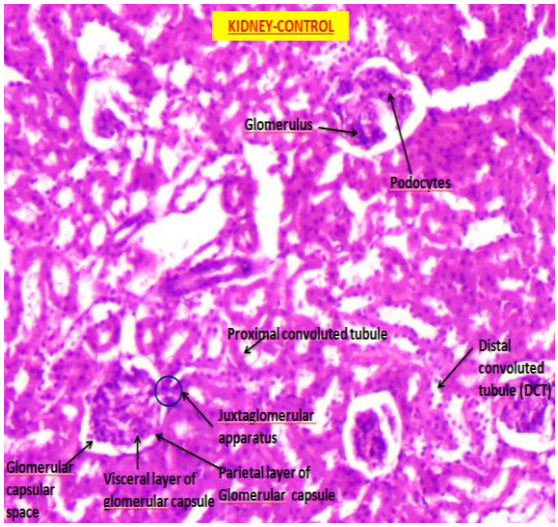

Kidney histology dose @ 500 mg/ kg BW: Typical architecture of renal corpuscle with central vascularized area characterized by a clump of capillaries closed to mesangial cells and podocytes surrounded by Bowman's capsule is shown.

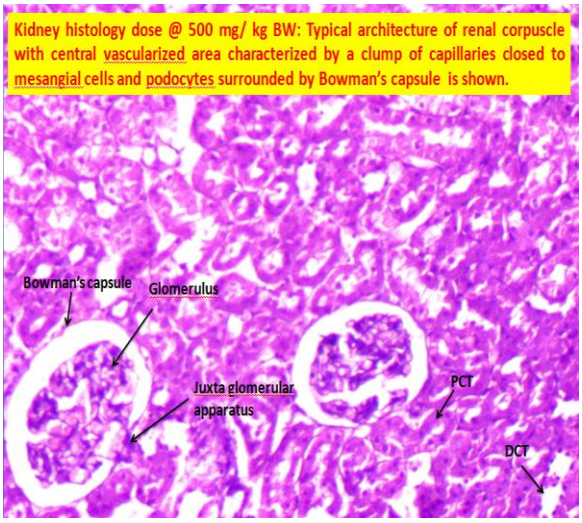

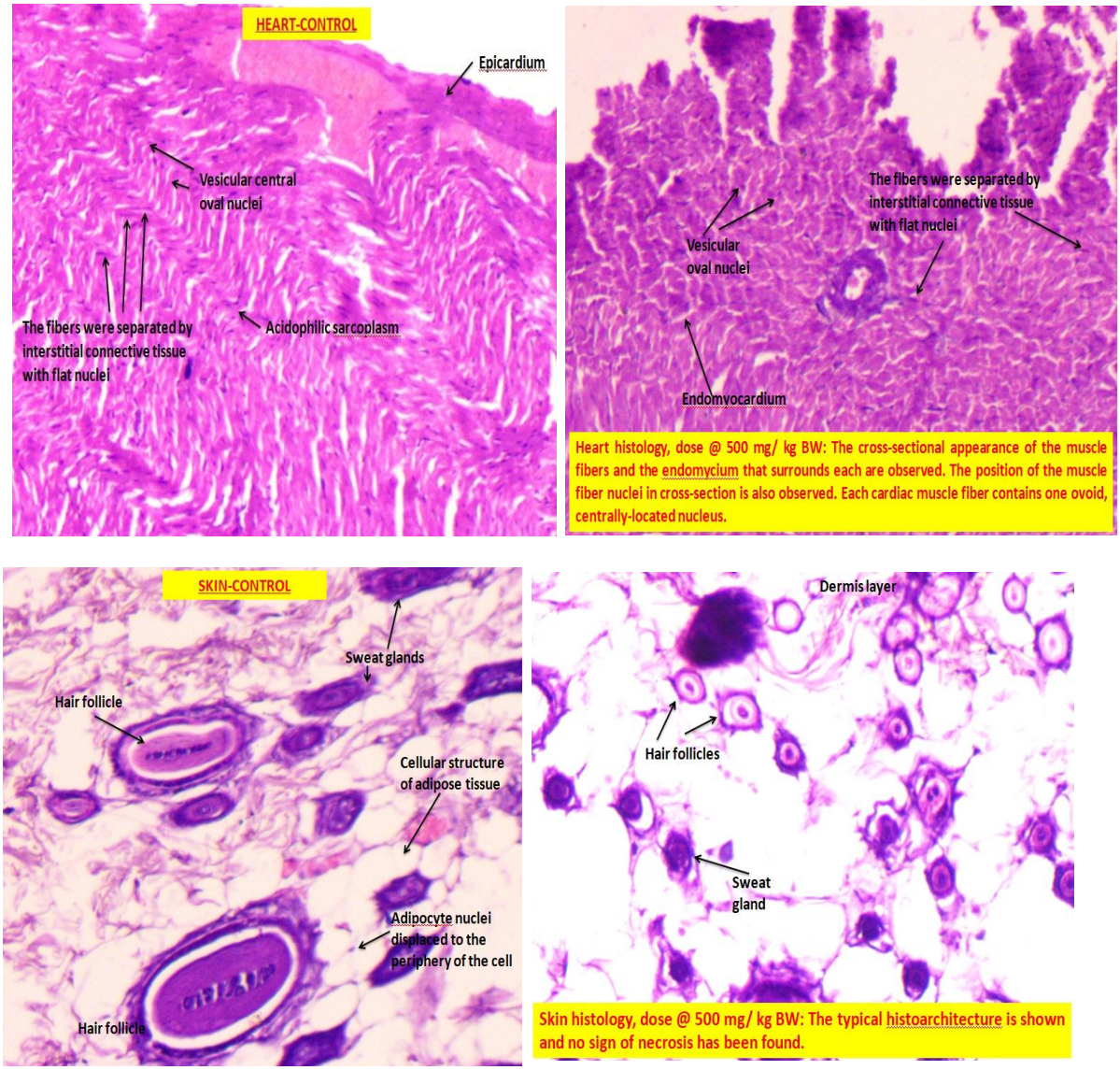

Fig. 5.37 Histological examinations were conducted on sections of lung, liver, kidney, heart and skin in both Al-BAG treated and control Wistar rats (n>5) [Roy et al., 2023b].

b). *In vivo* hemostatic efficacy

The *in vivo* hemostatic efficacy of Al-BAG was assessed using a femoral artery injury model in Wistar rats. The surgical procedure for creating the femoral artery injury is visually represented in photographic images in Fig. 5.38A.

The hemostatic potency was evaluated through the femoral artery injury. In the absence of Al-BAG application, bleeding from the femoral artery injury required 220±15 seconds to achieve firm blood clot formation, with the percentage of blood loss during the surgical procedure

measured at approximately 27%. However, for this experiment, various doses of Al-BAG were applied for a comparative study of efficacy. The highest dose, determined based on the *in vivo* acute dermal toxicity assay (500mg/kg BW), was used. Four doses were selected for the experiment: 1/10th of the highest dose (denoted as R), 1/5th of the highest dose (denoted as K), 1/3rd of the highest dose (denoted as L), and the highest dose (denoted as F). The time taken to halt bleeding for R, K, L, and F were 151.5±10 seconds, 100±9 seconds, 103±6 seconds, and 85±3 seconds, respectively (Fig. 5.38B). Furthermore, the percentage of blood loss at the application site was noted to be 17%, 8%, 7.33%, and 2.22%, respectively (Fig. 5.38C) [Roy et al., 2023b].

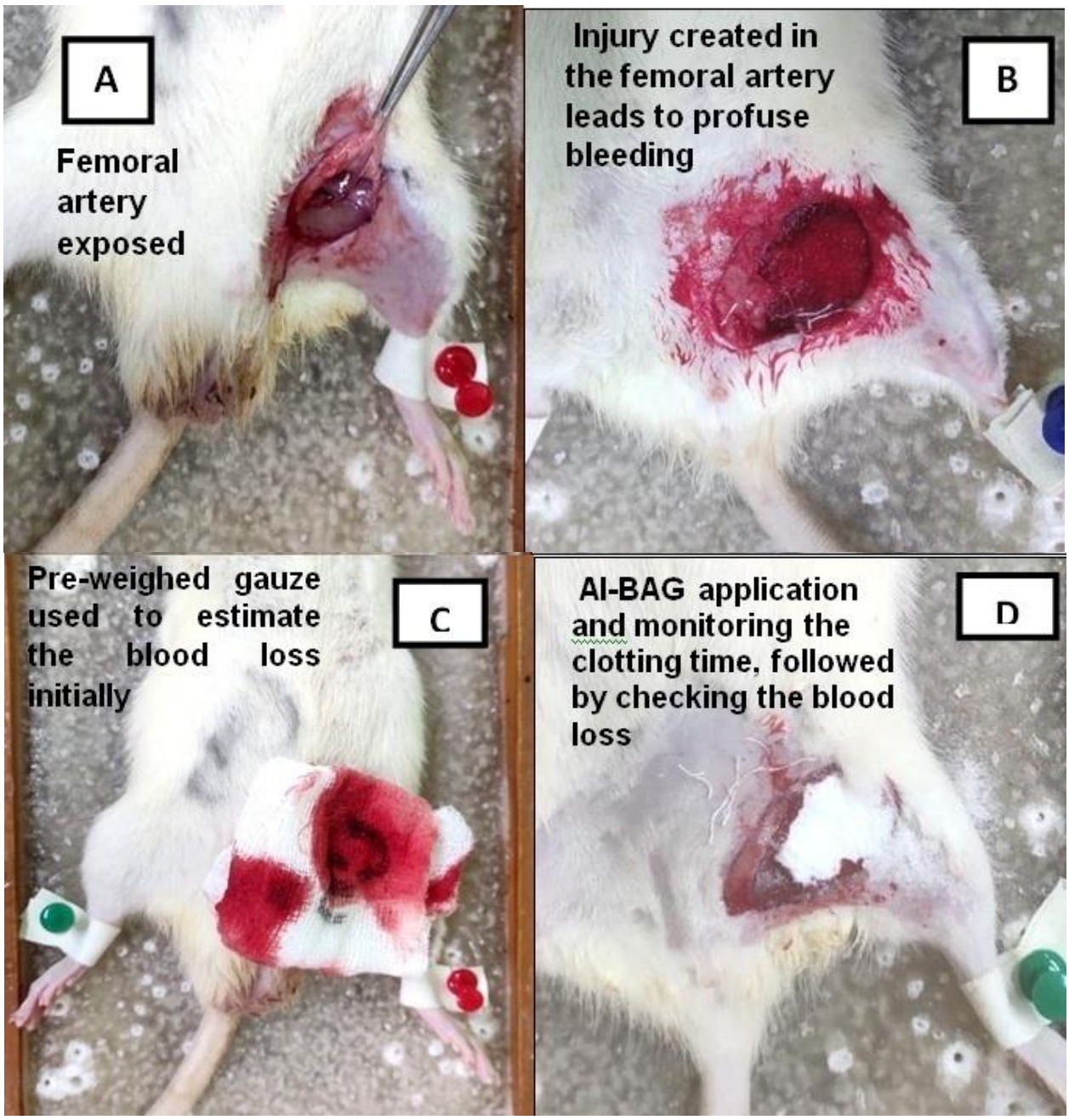
A
Femoral artery exposed
Injury created in the femoral artery leads to profuse bleeding
B
Pre-weighed gauze used to estimate the blood loss initially
C
AI-BAG application and monitoring the clotting time, followed by checking the blood loss
D

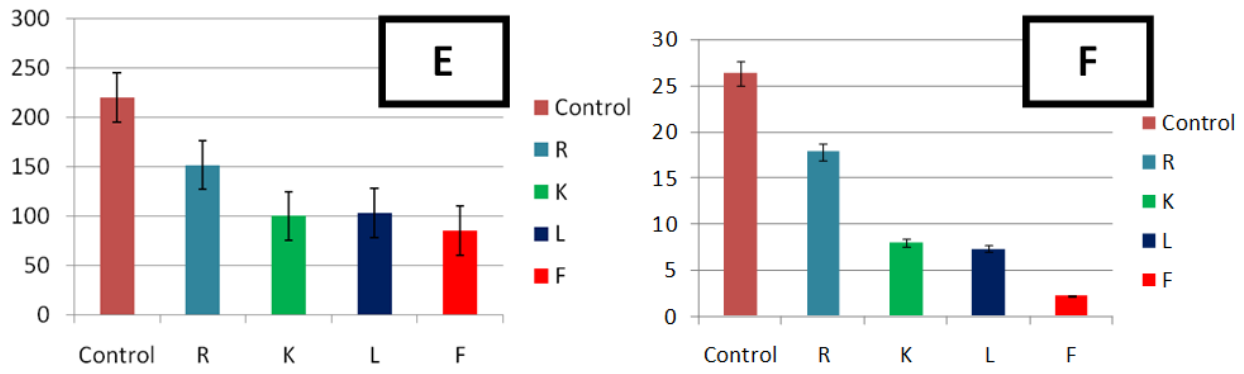

Fig. 5.38 (A) and (B) Photographic images illustrating the surgical process for creating a femoral artery injury. (C) Evaluation of the percentage of blood loss. (D) Application of Al-BAG, monitoring the time for hemostasis/clotting, and subsequent estimation of blood loss. (E) Graphical representation of clotting time/time for hemostasis. (F) Graphical representation of the percentage of blood loss before and after the application of Al-BAG ($p < 0.05$) [Roy et al., 2023b].

5.2.4. Discussion

The control of severe bleeding resulting from trauma or accidents, whether in a military or civilian setting, is essential before receiving definitive medical care. The lack of readily available hemostatic dressings emphasizes the necessity for their development. Upon conducting a meta-analysis of existing market brands such as Quikclot, it was found that they induce a local exothermic reaction leading to tissue injury and exhibit poor degradability. Hemcom/Celox, on the other hand, is associated with allergic reactions and does not adhere well to the wound site, in addition to being relatively expensive [Alam et al., 2005]. In contrast, the hemostatic action of bioactive glass is well-documented, leveraging the 'glass effect'. It acts as a procoagulant, triggering factor XII of the coagulation cascade, and holds promise in addressing the limitations of the aforementioned market brands. The carefully selected composition of the bioactive glass discussed here, known as Al-BAG, has been demonstrated to serve as a potent hemostatic agent in this study.

The physicochemical characteristics of the as-prepared Al-BAG were analyzed through XRD, FTIR, TG-DSC, BET, particle size analysis and SEM-EDX [Fig. 5.22 (a-e), Fig. 5.23], confirming the successful formation of glass. The glass structure consisted of agglomerated

particles with sizes ranging from 100 to 200 nm, and the glass transition temperature (TG) was identified at 650°C. The distinct vibration bands indicative of the composition were observed in the FTIR spectrum. In the BET analysis, Al-BAG displayed type IV isotherms in conjunction with H1 hysteresis loops [Fig. 5.22(d)]. The inset in Fig. 5.22 (d) presented a pore size distribution curve derived from the adsorption using the BJH model. Al-BAG exhibited a notably higher surface area (333.744 m^2/g) and pore volume (0.450 cc/g). This property is particularly valuable as it enables the material to capture and retain a significant volume of water within its pores. These interactions result in the hyperconcentration of coagulation factors and cellular components within the plasma, consequently expediting the coagulation cascade and the subsequent formation of a fibrin clot [Ostomel et al., 2006]. In essence, the porous structure of Al-BAG, with its inherent properties, plays a pivotal role in enhancing the blood coagulation process. Smaller particle sizes provide a larger surface area per unit mass. This increased surface area allows for more efficient interaction with blood components, especially platelets and coagulation factors, can trigger platelet activation more efficiently, leading to a faster and more robust platelet plug formation at the site of the injury, which is a crucial step in hemostasis at the particle size of Al-BAG, 185.6 nm [Fig. 5.22(e)]. This is further correlated with quantitative and qualitative outcomes of the platelet adhesion experiment [Fig. 5.32].

It is well-documented that certain inorganic hemostats exhibit poor biodegradability, which can lead to serious complications such as thrombosis in distal organs like the brain and lungs. Consequently, evaluating the degradability profile of a hemostat is crucial. In this context, we assessed the degradation profile of Al-BAG at two different pH levels (7.4, physiological pH, and 5.2, pH at the wound site). Over a 14-day period, the sample exhibited a weight loss of 33% in pH 5.2, indicating a higher dissolution rate. In contrast, at pH 7.4, the weight loss was lower at 28%, indicating a slower dissolution profile [Fig. 5.24] [Roy et al., 2023b].

The results of the cytotoxicity assay indicate that the as-prepared glass powder showed no toxicity to the NIH3T3 cell line. Additionally, the assay results demonstrated that NIH3T3 cells maintained high viability, slightly exceeding that of the control group, suggesting enhanced cell proliferation and indicating good cytocompatibility of Al-BAG [Fig. 5.25] [Roy et al., 2023b]. Moreover, the *in vivo* acute dermal toxicity study [Fig. 5.35] confirmed the *in vivo* compatibility of Al-BAG, as no significant macroscopic signs of edema, erythema, redness, or inflammation

were observed. Subsequent histopathological analysis of five vital organs, including lungs, liver, heart, kidney, and skin, revealed the normal histoarchitecture of these organs [Fig. 5.36] [Roy et al., 2023b].

Addressing bacterial infections is a significant challenge in the management of open wounds. In this study, we evaluated the antibacterial activity of Al-BAG using a time-kill test [Fig. 5.27]. The results indicated that Al-BAG exhibits enhanced activity against gram-positive strains, specifically *Staphylococcus aureus* [Fig. 5.27] [Roy et al., 2023b]. While the efficacy against gram-negative strains like *Escherichia coli* is not presented here, it is acknowledged that the lower efficacy against gram-negative bacteria may be attributed to the presence of zinc in the Al-BAG composition. Zinc is known to be more sensitive to gram-positive bacteria due to the intricate architecture of the bacterial cell wall. Gram-negative bacteria possess an additional outer plasma membrane with a thick lipopolysaccharide layer, which is considerably thicker than the peptidoglycan layer found in gram-positive bacteria [Turlybekuly et al., 2019].

Hemocompatibility is a crucial factor in assessing the biocompatibility of biomaterials. To evaluate this, an *in vitro* hemolysis assay was conducted [Fig. 5.28]. The results indicate that Al-BAG in this study exhibited a low hemolysis percentage, measuring less than 10%. These findings suggest that if utilized as a hemostatic agent, the metabolic activity of RBCs is unlikely to be significantly affected in the presence of Al-BAG [Roy et al., 2023b].

The intrinsic absorption capacity is a critical criterion for hemostatic agents, and in the case of the Al-BAG sample, it demonstrates time-dependent absorption efficacy in both PBS and blood [Fig. 5.29]. It also exhibits a heightened thrombus formation when in contact with blood and efficiently adheres to platelets for clot formation [Fig. 5.32] [Roy et al., 2024a]. When in contact with blood, Al-BAG activates the coagulation cascade through its intrinsic 'glass effect,' involving coagulation factor XII (Hageman Factor), ultimately leading to fibrin formation.

Moreover, the presence of calcium ions in the glass network acts as a procoagulant by triggering factor IV, expediting the intrinsic pathway of coagulation. Another potential procoagulant is the polar silanol group on the Al-BAG surface, which helps activate factor XII and XI of the intrinsic pathway, leading to fibrin formation. The inclusion of zinc in the Al-BAG composition is a crucial cofactor for both hemostasis and thrombosis. It is known that zinc deficiency can

prolong bleeding time and result in abnormal clotting behavior. At the injury site, activated platelets release Zn^{2+} ions into the local microenvironment, enhancing platelet aggregation and fibrin clot formation [Gordon et al., 1982; Schousboe et al., 1993].

As shown in Fig. 5.30 (c, d), in contact with Al-BAG, the time required for PT and aPTT significantly decreased, indicating that it could have activated both the intrinsic and extrinsic pathways of the coagulation cascade. When a negatively charged substance is connected to body fluids like blood or plasma, triggering the coagulation factors, rapid ion exchange and protonation (H^+ or H_3O^+) occurs on the surface. These protonated groups attracted the negatively charged residues on the membranes of red blood cells, resulting in increased platelet aggregation and strong hemagglutination [Ostomel et al., 2007; Baker et al., 2007; Dai et al., 2009; Chen et al., 2016; Matter et al., 2017; Nagrath et al., 2021]. Al-BAG also increased the quantity of thrombin produced and reduced the delay in thrombin generation [Fig. 5.30(a, b)]. The study involved the measurement of thrombin-antithrombin complex (TAT) formation in whole blood samples that had been exposed to Al-BAG and surgical cotton gauze [Fig. 5.31]. The objective was to understand how the presence of Al-BAG influenced the generation of thrombin, a pivotal factor in blood coagulation. Elevated levels of thrombin trigger the formation of the TAT complex. When treated with Al-BAG, TAT levels were substantially higher, measuring at 62.58 pg/ml. In contrast to the control group, which used surgical cotton gauze, produced only 6.00 pg/ml of TAT, signifying a considerably lower response compared to Al-BAG [Fig. 5.31] [Roy et al, 2024a]. This discrepancy in TAT levels demonstrated that Al-BAG had a pronounced effect on inducing thrombin generation compared to the surgical cotton gauze control. It was hypothesized that the presence of specific ions such as Al^{3+}, Ca^{2+} and Zn^{2+} within the Al-BAG played a role in initiating the blood clotting process, contributing to an increase in thrombin production. Consequently, the study suggested that the porous structure of Al-BAG was effective in managing hemostasis by entrapping red blood cells (RBCs), and the presence of Al-BAG facilitated and accelerated the clotting process [Chen et al., 2021]. Moreover, Al-BAG exhibited an impressive capacity to adhere to red blood cells (RBCs) within the clot, as seen through the entrapment of hemoglobin by fibrin. As the clot formed, the levels of free hemoglobin decreased, while the hemoglobin entrapped by fibrin increased [Long et al., 2018]. Furthermore, the platelets on the surface of Al-BAG display platelet activation in dendritic and early spread states, signifying an activated state. This positive platelet response is likely linked to the wettability of

Al-BAG [Fig. 5.33]. A 47% reduction in BCI corresponded to a faster clot formation, while a decrease in BCI was associated with an increase in the rate of clotting. These findings were further supported by absorbance measurements (OD values). A lower absorbance (OD value) for Al-BAG indicated a faster clotting rate, while a higher absorbance (OD value) for the control (surgical cotton gauze) indicated a slower clotting rate, as demonstrated in Fig. 5.35 [Roy et al., 2024a; Khou et al., 2023].

As per macroscopic observation, following application of the Al-BAG with suitable vehicle, no clinical signs of erythema, edema, redness or severe inflammation were detected in both of the study groups and result shown in Fig. 5.36 and followed by histological analysis [Fig. 5.37]. After specific time interval (1 day, 5 day, 10 day and 14 day), Al-BAG treated area with various concentration was observed and complete hair growth was visible within 14 day and absence of clinical signs of dermal toxicity [Roy et al., 2023b].

The *in vivo* hemostatic efficacy results revealed that the bleeding time for various doses of Al-BAG, with the shortest being 85 seconds for the highest dose (500 mg/kg BW), was significantly shorter compared to the bleeding time in the untreated control group (220 seconds). This indicates the rapid hemostatic potency of Al-BAG, as demonstrated in Fig. 5.38A. Consequently, the faster hemostatic action of Al-BAG effectively reduces blood loss, thereby controlling hemorrhagic bleeding by activating both the intrinsic and extrinsic pathways of the coagulation cascade [Roy et al., 2023b]. The aforementioned coagulation study mechanisms elucidate the subsequent shortened Prothrombin Time (PT) and Activated Partial Thromboplastin Time (aPTT) [5.30 (c, d)] through the involvement of both the extrinsic and intrinsic pathways of coagulation.

6. Conclusions

Chapter 1 of the thesis is the introductory section, highlighting the need for new biomaterials in soft tissue regeneration and providing background information on their application areas, namely wound healing and hemostasis. In this chapter, the wound healing and coagulation cascades have been discussed to provide a comprehensive understanding of these application areas. Additionally, the chapter includes a brief description of bioactive glass, as well.

In Chapter 2, the author reviews the literature on the ongoing research in wound healing and hemostasis applications using bioactive glass, upto the current date. This chapter also includes a list of FDA-approved bioactive glasses used in wound healing applications. For wound healing, studies on zinc-incorporated bioactive glass (BG), gold nanoparticles with BG, and Yunnan baiyao-contained BG in ointment form have been investigated for their wound healing efficacy. Some researchers have prepared multifunctional bioglass (BG)/oxidized sodium alginate (OSA) composite hydrogels with adipic acid dihydrazide (ADH)-modified γ-polyglutamic acid (γ-PGA). In terms of hemostasis, research groups have incorporated various heavy metals, such as Ga^{3+} and Ta^{5+}, into BG compositions and investigated their hemostatic potential. However, there is concern in the use of these heavy metals in healthcare applications. Additionally, all of these are still in the research stage only. This chapter also outlines the structure and synthesis of bioactive glass, highlighting the differences between the melt quench and sol-gel processes, followed by the synthesis of bioactive glass-based micronanofibers. The author briefly discusses the versatility of different ion-containing bioactive glasses in wound healing and hemostasis. In light of the above, the author has made an effort to fabricate sol-gel derived bioactive glass compositions for wound healing and hemostatic applications.

Chapter 3 comprises the thesis objectives. The thesis work is divided into two parts:

Part A describes bioactive glass-based wound care matrix (named ABGmnf-based wound care matrix) designed for non-healing wounds.

Part B describes a hemostatic bioactive glass (named Al-BAG) intended specifically for military wounds and accidental injuries involving profuse bleeding.

Chapter 4 describes all the details of the experimental setup and outlines the experimental procedures according to standard protocols.

Part A describes the synthesis of AgBG, followed by the development of the ABGmnf-based wound care matrix. This matrix was characterized using various *in vitro* material characterization techniques, including XRD, TG-DSC, FTIR, FESEM, BET, and assessments of mechanical properties. After successfully fabricating the ABGmnf-based wound care matrix, *in vitro* biological characterizations were conducted to evaluate cytocompatibility, 2D wound healing efficacy, and antibacterial activity by assessing the zone of inhibition (ZOI) and minimum inhibitory concentration (MIC) against various gram-positive and gram-negative bacterial strains. Subsequently, *in vivo* animal studies were conducted to assess biocompatibility, host immune response, toxicity, pharmacokinetics, biodistribution, and, most importantly, wound healing efficacy compared to the market-available betadine.

Part B describes the synthesis of Al-BAG and various *in vitro* material characterizations, including XRD, TG-DSC, FTIR, SEM-EDX, particle size analysis, and BET. Further, *in vitro* biological characterizations were conducted to evaluate cytocompatibility and hemocompatibility. Additionally, *in vitro* blood coagulation assays (PT and aPTT) and blood absorption capacity tests were performed. Following satisfactory *in vitro* results, the author outlined *in vivo* animal studies, including acute dermal toxicity studies and hemostatic potential studies by inducing femoral arterial bleeding in model animals.

In Chapter 5, the results related to material characterizations, *in vitro* biological studies, and *in vivo* animal studies, followed by a discussion of the outcomes for both Part A and Part B have been presented.

Part A Conclusion:

The author successfully fabricated the ABGmnf-based wound care matrix, which demonstrated excellent *in vitro* and *in vivo* biological outcomes. The material did not induce any immune response, as verified by assessing TNF-α and IL-6 levels after application. Toxicity assessments via hemogram studies showed no adverse effects following application. Pharmacokinetic and biodistribution studies measured serum [Ca^{2+}] and tissue [Ca^{2+}] concentrations, revealing trends similar to normal physiological conditions, balanced by the hormones calcitonin and parathyroid hormone. Additionally, wound closure was significantly faster than in the control and betadine groups. On the 14th day, the ABGmnf based wound care matrix-treated experimental group

exhibited 96.9 (±1.5)% wound closure without a scar mark, compared to 81.9 (±2)% in the Betadine group and 78 (±1)% in the control group. Therefore, this composition in matrix form holds promising prospects in the wound care market, offering a new avenue for soft tissue regeneration.

Part B conclusion:

Part B focuses on hemostatic bioactive glass specifically designed for military wounds and accidental trauma injuries involving profuse arterial bleeding. The author extensively assessed *in vitro* biological studies, establishing Al-BAG's remarkable hemostatic potential. Strikingly, both PT and aPTT were reduced after the application of Al-BAG compared to the control, and SEM images confirmed clot formation, platelet activation, and RBC adhesion onto Al-BAG's surface.

In vivo animal studies included acute dermal toxicity assessments, which demonstrated biocompatibility. The hemostatic potential was evaluated by inducing femoral artery injuries in model animals to simulate profuse bleeding conditions. The *in vivo* hemostatic efficacy results revealed that the bleeding time for various doses of Al-BAG was significantly shorter compared to the untreated control group. For the highest dose (500 mg/kg BW), the bleeding time was as short as 85 seconds, compared to 220 seconds in the control group. The *in vitro* coagulation assay results showed that after Al-BAG treatment, there was a reduction of approximately 14% (±0.9%) in PT and 6.25% (±0.5%) in aPTT compared to the control. Hence, Al-BAG can activate both Intrinsic (from aPTT) and extrinsic (from PT) pathways of the coagulation cascade.

Future scope:

For Part A, long-term pharmacokinetic and biodistribution studies are essential to better understand the trends in serum and tissue [Ca^{2+}] concentration. Any abnormal disposition of calcium can be harmful to physiology, necessitating extensive studies. Over the next year, we plan to investigate the ABGmnf based wound care matrix in a diabetic animal model. This is particularly significant given the high prevalence of diabetic foot ulcers, which are chronic non-healing wounds with detrimental effects. Addressing diabetic wounds with the ABGmnf based wound care matrix presents a significant challenge.

For Part B, extensive animal studies focusing on dermal toxicity and pharmacokinetics are needed to be conducted. Blood clotting assays will be performed using Al-BAG and anticoagulant-treated blood (heparin, citrate, etc.) to determine if clotting can be initiated in patients under anticoagulant therapy or those with coagulopathies. Additionally, developing the prototype using Al-BAG is necessary for the application under discussion.

Footnote:

The research group is pleased to share some exciting news regarding the woundare matrix developed. In this regard, a Memorandum of Understanding (MoU) with a renowned company has been signed. This company has agreed to sponsor the combined Phase I and Phase II clinical trials of ABGmnf based wound care matrix, which will be conducted under the auspices of a Government Medical College.

7. Bibliography

Alam H, Burris D, DaCorta J. Hemorrhage control in the battlefield: role of new hemostatic agents. Mil. Med. 2005, 170: 63–9

Alasvand N, Behnamghader A, Milan PB, Simorgh S, Mobasheri A, Mozafari M. Tissue-engineered small-diameter vascular grafts containing novel copper-doped bioactive glass biomaterials to promote angiogenic activity and endothelial regeneration. Mater Today Bio. 2023, 20: 100647. doi: 10.1016/j.mtbio.2023.100647

Alasvand NA, Behnamghader PB, Mozafari MM. Synthesis and characterization of novel copper-doped modified bioactive glasses as advanced blood-contacting biomaterials. Materials Today Chemistry. 2023, 29: 101465

Alcaide M, P. Portol´es, A. Lopez-Noriega, D. Arcos, M. Vallet-Regí and M.T. Portol´es, Interaction of an ordered mesoporous bioactive glass with osteoblasts, fibroblasts and lymphocytes, demonstrating its biocompatibility as a potential bone graft material, Acta Biomater. 6 (2010) 892–899

Alcaide M, Portol´es P, Lopez-Noriega A, Arcos D, Vallet-Regí M and Portol´es MT. Interaction of an ordered mesoporous bioactive glass with osteoblasts, fibroblasts and lymphocytes, demonstrating its biocompatibility as a potential bone graft material. Acta Biomater. 2010, 6: 892–899

Alessandro R, Masiero L, Liotta LA, Kohn EC. The role of calcium in the regulation of invasion and angiogenesis. *In Vivo*. 1996, 10: 153–160

Ali IH, Ouf A, Elshishiny F, Taskin MB, Song J, Dong M, Chen M, Siam R, and Mamdouh W. Antimicrobial and Wound-Healing Activities of Graphene-Reinforced Electrospun Chitosan/Gelatin Nanofibrous Nanocomposite Scaffolds. ACS Omega. 2022, 7(2): 1838-50

Al-Tawarah MN. Singular and combined healing activity of aqueous extract of Artemisia Jordanica and Achillea Fragrantissima in rabbit's incision, excision and burn models. Biomed. Pharmavol. J. 2022, 15(3)

Anke, MK. Essential and Toxic Effects of Macro, Trace, and Ultratrace Elements in the Nutrition of Man. In Elements and Their Compounds in the Environment; Wiley: Weinheim, Germany, 2004, 343−367. DOI: 10.1002/9783527619634.ch16.

Arcos D, Vallet-Regí M. Sol-gel silica-based biomaterials and bone tissue regeneration. Acta Biomater. 2010, 6: 2874–2888. doi: 10.1016/j.actbio.2010.02.012.

Atluri P. The Surgical Review: An Integrated Basic and Clinical Science Study Guide. Lippincott Williams & Wilkins, 2006

Azari Z, Kermani F, Mollazadeh S, Alipour F, Sadeghi-Avalshahr A, Ranjbar-Mohammadi M, ... & Kargozar S. Fabrication and characterization of cobalt-and copper-doped mesoporous borate bioactive glasses for potential applications in tissue engineering. Ceramics International. 2023, 49(23): 38773-38788.

Bai X, Liu W, Xu L, Ye Q, Zhou H, Berg C, Yuan H, Li J, Xia W. Sequential macrophage transition facilitates endogenous bone regeneration induced by Zn-doped porous microcrystalline bioactive glass. J Mater Chem B. 2021, 9(12): 2885-2898

Baino F, Hamzehlou S, Kargozar S. Bioactive glasses: where are we and where are we going? J. Funct. Biomater. 2018, 9 (1): 25, 10.3390/jfb9010025

Baino F, Novajra G, Miguez-Pacheco V, Boccaccini A, Vitale-Brovarone C. Bioactive glasses: special applications outside the skeletal system. Journal of Non-Crystaline Solids, 2016, 432: 15-30, 10.1016/j.jnoncrysol.2015.02.015

Baker SE, Sawvel AM, Zheng N, Stucky GD. Controlling bioprocesses with inorganic surfaces: layered clay hemostatic agents. Chem. Mater. 2007, 19: 4390–4392,

Banerjee S, Chattopadhyay P, Ghosh A, Pathak MP, Singh S and Veer V. Acute dermal irritation, sensitization, and acute toxicity studies of a transdermal patch for prophylaxis against (±) anatoxin-A poisoning. I. J. T. 2013, 32(4): 308-13

Barbieri L, S. Bruni, F. Cariati, C. Leonelli, G.C. Pellacani, C. Siligardi, U. Russo. Influence of some transition metal cations on the properties of BaO-containing glasses and glass-ceramics, Materials research bulletin. 34(12-13), 1999: 1825-1836.

Barrioni BR, de Laia AGS, Valverde TM, Martins TMD, Caliari MV, de Sa MA, de Goes AM, Pereira MD. Evaluation of *in vitro* and *in vivo* biocompatibility and structure of cobalt releasing sol-gel bioactive glass. Ceramics International. 2018, 44(16): 20337-20347

Baumgarten PK. Electrostatic spinning of acrylic microfibers. J. Colloid Interface Sci. 1971, 36 (1): 71-79

Bellantone M, Coleman NJ, Hench LL. Bacteriostatic action of a novel four-component bioactive glass. J. Biomed. Mater. Res. 2000, 51: 484-490

Bellantone M, Williams HD, Hench LL. Broad-spectrum bactericidal activity of Ag_2O doped bioactive glass. Antimicrob. Agents Chemother. 2002, 46: 1940-1945

Berridge MJ, Bootman MD, Lipp P. Calcium—A life and death signal. Nature. 1998, 395: 645–648

Berthon G. Is copper pro-or anti-inflammatory? A reconciling view and a novel approach for the use of copper in the control of inflammation. Agents and actions. 1993, 39(3): 210-217

Bhandari S, Larsen AK, McCourt P, Smedsrød B, Sørensen KK. The scavenger function of liver sinusoidal endothelial cells in health and disease. Front. Physiol. 2021, 12, No. 757469

Bhardwaj N, Kundu SC, Electrospinning: a fascinating fiber fabrication technique. Biotechnol Adv. 2010, 28(3): 325-47

Bikle DD, Xie Z, Tu CL. Calcium regulation of keratinocyte differentiation. Expert Rev. Endocrinol. Metab. 2012, 7: 461–472

Bisht D, Saxena S, Kharayat NS, Gautam S. Protocols for Immunofluorescence Techniques. In: Deb, R., Yadav, A.K., Rajkhowa, S., Malik, Y.S. (eds) Protocols for the Diagnosis of Pig Viral Diseases. Springer Protocols Handbooks. Humana, New York, NY. 2022

Bosetti M, Hench LL & Cannas M. Interaction of bioactive glasses with peritoneal macrophages and monocytes *in vitro*. Journal of biomedical materials Research. 2002, 60(1): 79-85

Chen J, Qiu L, Li Q, Ai J, Liu H and Chen Q. Rapid hemostasis accompanied by antibacterial action of calcium crosslinking tannic acid-coated mesoporous silica/silver Janus nanoparticles. Materials Science and Engineering: C. 2021, 123: 111958

Chen J, Qiu L, Li Q, Ai J, Liu H and Chen Q. Rapid hemostasis accompanied by antibacterial action of calcium crosslinking tannic acid-coated mesoporous silica/silver Janus nanoparticles. Materials Science and Engineering: C. 2021, 123: 111958

Chen J, Zeng L, Chen X, Liao T & Zheng J. Preparation and characterization of bioactive glass tablets and evaluation of bioactivity and cytotoxicity *in vitro*. Bioactive materials. 2018, 3(3): 315-321.

Chen S, Huan Z, Zhang L, Chang J. The clinical application of a silicate-based wound dressing (Dermfactor®) for wound healing after anal surgery: a randomized study. Int. J. Surg. 2018, 52: 229-232, 10.1016/j.ijsu.2018.02.036

Chen S, Michalek M, Galuskova D, Michalkova M, Svancarek P, Talimian A, Kankova H, Kraxner J, Zheng K, LiveraniL, Galusek D, Boccaccini AR. Multi-targeted B and Co co-doped 45S5 bioactive glasses with angiogenic potential for bone regeneration. Mater Sci Eng C Mater Biol Appl. 2020, 112: 110909

Chen Z, Li F, Liu C, Guan J, Hu X, Du G, Yao X, Wu J, Tian F. Blood clot initiation by mesoporous silica nanoparticles: dependence on pore size or particle size? J. Mater. Chem. B, 2016, 4: 7146–7154

Chitturi R, Baddam VR, Prasad L, Prashanth L, Kattapagari K. A Review on Role of Essential Trace Elements in Health and Disease. J. Dr. NTR Univ. Heal. Sci. 2015, 4 (2): 75

Clinical and Laboratory Standards Institute, M02-A12: Performance standards for antimicrobial disk susceptibility tests, approved standard-12th edition, 2015

Condon EU. Physics of the glassy state. I. constitution and structure, American Journal of

Cordeiro JV, Jacinto A. The role of transcription-independent damage signals in the initiation of epithelial wound healing. Nat. Rev. Mol. Cell Biol. 2013, 14: 249–262

Dai C, Yuan Y, Liu C, Wei J, Hong H, Li X, Pan X. Degradable, antibacterial silver exchanged mesoporous silica spheres for hemorrhage control. Biomaterials, 2009, 30: 5364–5375

Dai C, Yuan Y, Liu C, Wei J, Hong H, Li X, Pan X. Degradable, antibacterial silver exchanged mesoporous silica spheres for hemorrhage control. Biomaterials. 2009, 30(29): 5364-75. doi: 10.1016/j.biomaterials.2009.06.052

Dashnyam K, El-Fiqi A, Buitrago JO, Perez RA, Knowles JC, Kim HW. A mini review focused on the proangiogenic role of silicate ions released from silicon-containing biomaterials. J Tissue Eng. 2017, 8:2041731417707339. doi: 10.1177/2041731417707339

Day RM, Boccaccini AR, Shurey S, Roether JA, Forbes A, Hench LL, Gabe SM. Assessment of polyglycolic acid mesh and bioactive glass for soft-tissue engineering scaffolds. Biomaterials. 2004, 25(27): 5857-66. doi: 10.1016/j.biomaterials.2004.01.043.

Day RM. Bioactive glass stimulates the secretion of angiogenic growth factors and angiogenesis *in vitro*. Tissue Eng. 2005, 11(5-6): 768-77. doi: 10.1089/ten.2005.11.768.

de Laia AGS, Valverde TM, Barrioni BR, Cunha PDS, de Goes AM, de Miranda MC, Gomes DA, Queiroz-Junior CM, de Sá MA, de Magalhães Pereira M. Cobalt-containing bioactive glass mimics vascular endothelial growth factor A and hypoxia inducible factor 1 function. J Biomed Mater Res A. 2021, 109(7):1051-1064. doi: 10.1002/jbm.a.37095

de Laia AGS, Valverde TM, Barrioni BR, Cunha PDS, de Goes AM, de Miranda MC, Gomes DA, Queiroz-Junior CM, de Sa MA, de Magalhaes Pereira M. Cobalt-containing bioactive glass mimics vascular endothelial growth factor A and hypoxia inducible factor 1 function. J Biomed Mater Res. A 2021, 109(7): 1051-1064

Demirci S, Dogan A, Aydin S, Dulger EC, Sahin F. Boron promotes streptozotocin-induced diabetic wound healing: roles in cell proliferation and migration, growth factor expression and inflammation. Mol Cell Biochem. 2016, 417(1-2): 119-33

Deng Z, Lin B, Jiang Z, Huang W, Li J, Zeng X, Wang H, Wang D, Zhang Y. HypoxiaMimicking Cobalt-Doped Borosilicate Bioactive Glass Scaffolds with Enhanced

Angiogenic and Osteogenic Capacity for Bone Regeneration. Int J Biol Sci. 2019, 15(6): 1113-1124

Deshmukh K, Kovářík T, Křenek T, Docheva D, Stich T, and Pola J. Recent advances and future perspectives of sol–gel derived porous bioactive glasses: a review. RSC advances. 2020, 10(56): 33782-33835

Ding X, Tang Q, Xu Z, Xu Y, Zhang H, Zheng D, Wang S, Tan Q, Maitz J, Maitz PK, Yin S, Wang Y, Chen J. Challenges and innovations in treating chronic and acute wound infections: from basic science to clinical practice. Burns Trauma. 2022, 10: tkac014. doi: 10.1093/burnst/tkac014

Diquelou A, Lemozy S, Dupouy D, Boneu B, Sakariassen K, Cadroy Y. Effect of blood flow on thrombin generation is dependent on the nature of the thrombogenic surface. Blood. 1994; 84: 2206-13

doi:10.1016/j.bioactmat.2021.02.041.

Dong X , Chang J , Li H . Bioglass promotes wound healing through modulating the paracrine effects between macrophages and repairing cells. J Mater Chem B. 2017, 5(26): 5240-5250. doi: 10.1039/c7tb01211j.

Dong X, Chang J and Li H. Bioglass promotes wound healing through modulating the paracrine effects between macrophages and repairing cells. J. of Mater. Chem. B 2017, 5: 5240–5250.

Doostmohammadi A, Monshi A, Salehi R, Fathi MH, Golniya Z and Daniels AU. Bioactive glass nanoparticles with negative zeta potential. Ceramics International. 2011, 37(7): 2311-2316.

Ebrahimi M, Manafi S and Sharifianjazi F. The effect of Ag2O and MgO dopants on the bioactivity, biocompatibility, and antibacterial properties of 58S bioactive glass synthesized by the sol-gel method. Journal of Non-Crystalline Solids. 2023, 606: 122189.

Echezarreta-Lopez MM, Miguel TD, Quintero F, Pou J, Landin M. Antibacterial properties of laser spinning glass nanofibers. Int J Pharm. 2014, 477(1-2): 113-21

Echezarreta-Lopez MM, Miguel TD, Quintero F, Pou J, Landin M. Fabrication of Zn-Srdoped laser-spinning glass nanofibers with antibacterial properties. J Biomater Appl. 2017, 31(6): 819-831

El Hotaby W, Sherif H, Hemdan B, Khalil W & Khalil S. Assessment of in situ-prepared polyvinylpyrrolidone-silver nanocomposite for antimicrobial applications. Acta Physica Polonica A. 2017, 131(6): 1554-1560.

El-Okaily MS, Mostafa AA, Dulnik J, Denis P, Sajkiewicz P, Mahmoud AA, Dawood R, Maged A. Nanofibrous Polycaprolactone Membrane with Bioactive Glass and Atorvastatin for Wound Healing: Preparation and Characterization. Pharmaceutics. 2023, 15(7):1990. doi: 10.3390/pharmaceutics15071990.

Filip GA, Achim M, Mihalte P, Miclaus MA, Cristea C, Melinte, Gheban GB, Munteanu DM, Cadar O, Simon I, Pana O, Tudoran c LB, Clichici S, Stefan R. Design, *in vitro* bioactivity and *in vivo* influence on oxidative stress and matrix metalloproteinases of bioglasses in experimental skin wound. Journal of Trace Elements in Medicine and Biology. 2021, 68: 126846

Fiume E, Migneco C, Verné E, Baino F. Comparison Between Bioactive Sol-Gel and Melt-Derived Glasses/Glass-Ceramics Based on the Multicomponent SiO_2-P_2O_5-CaO-MgO-Na_2O-K_2O System. Materials (Basel). 2020, 13(3): 540. doi: 10.3390/ma13030540

Fu QA, Rahaman MN, Fu HL, Liu X. Silicate, borosilicate, and borate bioactive glass scaffolds with controllable degradation rate for bone tissue engineering applications. I. Preparation and *in vitro* degradation. J. Biomed. Mater. Res. A. 2010, 95: 164–71

Gao C, Gao Q, Bao X, Li Y, Teramoto A, Abe K. Preparation and *in vitro* bioactivity of novel mesoporous borosilicate bioactive glass nanofibers. J. Am. Ceram. Soc. 2011, 94: 2841– 2845

Gao C, Zhang L, Wang J, Jin M, Tang MQ, Chen Z, Cheng Y, Yang R, Zhao G. Electrospun nanofibers promote wound healing. J. Mater. Chem. B. 9 2021, 3106–3130. doi:10.1039/d1tb00067e

Gao, L., Zhou, Y., Peng, J. et al. A novel dual-adhesive and bioactive hydrogel activated by bioglass for wound healing. NPG Asia Mater. 2019, 11: 66 https://doi.org/10.1038/s41427-019-0168-0

Gillette RL, Swaim SF, Sartin EA, Bradley DM, Coolman SL. Effects of a bioactive glass on healing of closed skin wounds in dogs. Am J Vet Res. 2021, 62(7):1149-53. doi: 10.2460/ajvr.2001.62.1149.

Gordon PR, Woodruft CW, Anderson HL and O'Dell BL. Effect of acute zinc deprivation on plasma zinc and platelet aggregation in adult males. Am. J. Clin. Nutr. 1982, 35(1): 113-119

Haider A, HaiderS, Kang IK. A comprehensive review summarizing the effect of electrospinning parameters and potential applications of nanofibers in biomedical and biotechnology. Arabian Journal of Chemistry. 2018, 11(8): 1165-118

Haider S, Al-Zeghayer Y, Ali FA, Haider A, Mahmood A, Al-Masry W, Imran M, Aijaz M. Highly aligned narrow diameter chitosan electrospun nanofibers. J. Polym. Res. 2013, 20(4): 1-11

healing in diabetic rats. Bioact. Mater. 2021, 6: 3496–3506

Heher P, Muhleder S, Mittermayr R, Redl H, Slezak P. Fibrin-based delivery strategies for acute and chronic wound healing. Adv. Drug Deliv. Rev. 2018, 129: 134–147

Hennings H, Holbrook KA. Calcium regulation of cell-cell contact and differentiation of epidermal cells in culture: An ultrastructural study. Exp. Cell Res. 1983, 143: 127–142

Hoffman M, Monroe DM. A Cell-based Model of Hemostasis. Thromb. Haemostasis. 2001, 85: 958-965.

Holl J, Kowalewski C, Zimek Z, Fiedor P, Kaminski A, Oldak T, Moniuszko M, Eljaszewicz A. Chronic Diabetic Wounds and Their Treatment with Skin Substitutes. Cells. 2021, 10(3):655. doi: 10.3390/cells10030655

Homaeigohar S, Boccaccini AR. Antibacterial biohybrid nanofibers for wound dressings. Acta Biomater. 2020, 107: 25-49.

Homaeigohar S, Li M, Boccaccini AR. Bioactive glass-based fibrous wound dressings, Burns Trauma. 2022, 10(tkac038): 1-16

Hoppe A, Jokic B, Janackovic D, Fey T, Greil P, Romeis S, Schmidt J, Peukert W, Lao J, Jallot E, Boccaccini AR. Cobalt-releasing 1393 bioactive glass-derived scaffolds for bone tissue engineering applications. ACS Appl Mater Interfaces. 2014, 6(4): 2865-77

Hoppe A, Meszaros R, Stähli C, Romeis S, Schmidt J, Peukert W, ... & Boccaccini AR. *In vitro* reactivity of Cu doped 45S5 Bioglass® derived scaffolds for bone tissue engineering. Journal of Materials Chemistry B. 2013, 1(41): 5659-5674.

Hou Y, Xu X, Zhou Y, Li Q, Zhu L, Liu C, Chen S, and Pang J. Versatile Bioactive Glass/Zeolitic Imidazolate Framework-8-Based Skin Scaffolds toward High-Performance Wound Healing. ACS Appl. Mater. Interfaces. 2024, 16(7): 8228–8237

Hu et al. Antibacterial hemostatic dressings with nanoporous bioglass containing silver. Int. J. of Nanomedicine. 2012, 7: 2613-2620

Hu H, Tang Y, Pang L, Lin C, Huang W, Wang D, and Jia W. Angiogenesis and full-thickness wound healing efficiency of a copper-doped borate bioactive glass/poly (lactic-co-glycolic acid) dressing loaded with vitamin E *in vivo* and *in vitro*. ACS applied materials & interfaces. 2018, 10(27): 22939-22950

Huang WH, Day DE, Kittiratanapiboon K, Rahaman MN. Kinetics and mechanisms of the conversion of silicate (45S5), borate, and borosilicate glasses to hydroxyapatite in dilute phosphate solutions. J. Mater. Sci. Mater. Med. 2006, 177: 583–96

Huang WH, Day DE, Kittiratanapiboon K, Rahaman MN. Kinetics and mechanisms of the conversion of silicate (45S5), borate, and borosilicate glasses to hydroxyapatite in dilute phosphate solutions. J. Mater. Sci. Mater. Med. 2006, 177: 583–96

Hunault MO, Galoisy L, Lelong G, Newville M, Calas G. Effect of cation field strength on Co^{2+} speciation in alkali-borate glasses. Journal of Non-Crystalline Solids. 2016, 451: 101-110

HussainA, Alajmi MF, Rehman MT, Amir S, Husain FM, Alsalme A, Siddiqui MA, Alkhedhairy AA, KhanRA. Copper(II) complexes as potential anticancer and Nonsteroidal antiinflammatory agents: *In vitro* and *in vivo* studies. Scientific Reports. 2019, 9(1): 1-17

Hvas CL, Larsen JB. The Fibrinolytic System and Its Measurement: History, Current Uses and Future Directions for Diagnosis and Treatment. Int J Mol Sci. 2023, 24(18):14179. doi: 10.3390/ijms241814179

Immler R, Simon SI, Sperandio M. Calcium signalling and related ion channels in neutrophil recruitment and function. Eur. J. Clin. Investig. 2018, 48 (Suppl. 2): e12964

Institute of Medicine (US) Panel on Micronutrients. Dietary Reference Intakes for Vitamin A, Vitamin K, Arsenic, Boron, Chromium, Copper, Iodine, Iron, Manganese, Molybdenum, Nickel, Silicon, Vanadium, and Zinc. Washington (DC): National Academies Press (US); 2001. 13, Arsenic, Boron, Nickel, Silicon, and Vanadium.

ISO, Part 10: Test for irritation and skin sensitization (ISO 10993-10-33), (2010)

Izquierdo-Barba I, Vallet-Regi M. Mesoporous bioactive glasses: Relevance of their porous structure compared to that of classical bioglasses. Biomed. Glas. 2015, 1: 140–150. doi: 10.1515/bglass-2015-0014.

Jang DI, Lee AH, Shin HY, Song HR, ParkJH, Kang TB, Lee SR and Yang SH. The Role of Tumor Necrosis Factor Alpha (TNF-α) in Autoimmune Disease and Current TNF-α Inhibitors in Therapeutics. Int. J. Mol. Sci. 2021, 22(5): 2719

Johnson KE and TA Wilgus. Vascular endothelial growth factor and angiogenesis in the regulation of cutaneous wound repair. Adv. Wound Care. 2014, 3(10): 647-61

Jones M, J. Ganopolsky G, Labbe A et al. Novel nitric oxide producing probiotic wound healing patch: preparation and in-vivo analysis in a new Zealand white rabbit model of ischaemic and infected wounds. Int. Wound J. 2012, 9(3): 330-343

Jones R, Ehrenfried LM, Hench LL. Optimising bioactive glass scaffolds for bone tissue engineering. Biomaterials. 2006, 27: 964-973

Ju Q, Zenji T, Anthony L.B. Maçon, Norris E, Poologasundarampillai G, Obata A, Jones J R, and Kasuga T. Silver-doped calcium silicate sol-gel glasses with a cotton-wool-like structure for wound healing. Biomaterials Advances. 2022, 134: 112561

Jung SB, Day DE, Wound care, Google Patents, 2011.

Kaou MH, Furkó M, Balázsi K and Balázsi C. Advanced Bioactive Glasses: The Newest Achievements and Breakthroughs in the Area. Nanomaterials. 2023, 13(16): 2287. https://doi.org/10.3390/nano13162287

Kargozar S, Baino F, Banijamali S, Mozafari M. Synthesis and physico-chemical characterization of fluoride (F)- and silver (Ag)-substituted sol-gel mesoporous bioactive glasses. Biomed. Glasses. 2019, 5: 185-192.

Kargozar S, Baino F, Hamzehlou S, Hill R, Mozafari M. Bioactive glasses: sprouting angiogenesis in tissue engineering. Trends Biotechnol. 2018, 36 (4): 430-444, 10.1016/j.tibtech.2017.12.003

Kargozar S, Lotfibakhshaiesh N, Ai J, Mozafari M, Milan PB, Hamzehlou S, Barati M, Baino F, Hill R, Joghataei MT. Strontium- and cobalt-substituted bioactive glasses seeded with human umbilical cord perivascular cells to promote bone regeneration via enhanced osteogenic and angiogenic activities. Acta Biomater. 2017, 58: 502-514.

Kaur G, Kumar V, Baino F, Mauro JC, Pickrell G, Evans I, and Bretcanu O. Mechanical properties of bioactive glasses, ceramics, glass-ceramics and composites: State-of-the-art review and future challenges. Mater. Sci. and Engg: C. 2019, 104: 109895.

Kaur G, Pickrell G, Sriranganathan S, Kumar V and Homa D. Review and the state of the art: sol–gel and melt quenched bioactive glasses for tissue engineering. J. Biomed. Mater. Res. Part B, 2016, 104: 1248–1275

Kermani F, Hossein S, Ali A, Seyed J H, Seyed H T, Alireza R, Simin N, Seyede A H, Sahar M, and Kargozar S. Modified sol–gel synthesis of mesoporous borate bioactive glasses for potential use in wound healing. Bioengineering. 2022, 9(9): 442.

Kermani F, Nazarnezhad S, Mollaei Z, Mollazadeh S, Ebrahimzadeh-Bideskan A, Askari, Reza Kazemi Oskuee et al. "Zinc-and copper-doped mesoporous borate bioactive glasses: Promising additives for potential use in skin wound healing applications. International Journal of Molecular Sciences. 2023, 24(2): 1304

Kim HW, Kim HE, Knowles JC. Production and potential of bioactive glass nanofibers as a next-generation biomaterial. Adv. Funct. Mater. 2006, 16: 1529–1535

Ko KS, Arora PD, Bhide V, Chen A, Mcculloch CAG. Cell-cell adhesion in human fibroblasts requires calcium signaling. J. Cell Sci. 2001, 114: 155–1167

Kohn EC, Alessandro R, Spoonster J, Wersto RP, Liotta LA. Angiogenesis: Role of calcium-mediated signal transduction. Proc. Natl. Acad. Sci. USA 1995, 92: 1307–1311

Kong LZ, Wu Z, Zhao HK, Cui HM, Shen J, Chang J, Li HY, He YH. Bioactive injectable hydrogels containing desferrioxamine and bioglass for diabetic wound healing. ACS Appl. Mater. Interfaces. 2018, 10: 30103–30114.

Krizkova S, Ryvolova M, Hrabeta J, Adam V, Stiborova M, Eckschlager T, Kizek R. Metallothioneins and zinc in cancer diagnosis and therapy. Drug Metab Rev. 2012, 44(4): 287-301

Kwaan HC. From fibrinolysis to the plasminogen-plasmin system and beyond: A remarkable growth of knowledge, with personal observations on the history of fibrinolysis. Semin. Thromb. Hemost. 2014, 40: 585–591. doi: 10.1055/s-0034-1383545

Lang C, Murgia C, Leong M, Tan LW, Perozzi G, Knight D, Ruffin R, Zalewski P. Antiinflammatory effects of zinc and alterations in zinc transporter mRNA in mouse models of allergic inflammation. Am J Physiol Lung Cell Mol Physiol. 2007, 292(2): L577-84.

Lansdown AB, Mirastschijski U, Stubbs N, Scanlon E, Agren MS. Zinc in wound healing: theoretical, experimental, and clinical aspects. Wound Repair Regen. 2007, 15(1): 2-16

Lansdown AB, Sampson B, Laupattarakasem P, Vuttivirojana A. Silver aids healing in the sterile skin wound: experimental studies in the laboratory rat. Br. J. Dermatol. 1997, 137: 728-735

Lansdown AB, Williams A, Chandler S, Benfield S. Silver absorption and antibacterial efficacy of silver dressings. J. Wound Care. 2005, 14: 155-160

Law JX, Chowdhury SR, Aminuddin BS, Ruszymah BHI. Effect of calcium concentration on keratinocyte differentiation in 2-D culture and 3-D construct. Regen. Res. 2015, 4: 22–29

Lechmann L, Lieberman HA, Kanig JH. The theory and Practice of Industrial Pharmacy Tablets, 4th ed., Varghese Publishing House; Bombay, 1991, 293-345.

Lee IH, Yu HS, Lakhkar NJ, KimHW, Gong MS, Knowles JC, Wall IB. Development, characterisation and biocompatibility testing of a cobalt-containing titanium phosphate-based glass for engineering of vascularized hard tissues. Mater Sci Eng C Mater Biol Appl. 2013, 33(4): 2104-12

Lefebvre L, Chevalier J, Gremillard L, Zenati R, Thollet G, Bernache-Assolant D, Govin A. Structural transformations of bioactive glass 45S5 with thermal treatments. Acta Materialia. 2007, 55: 3305-3313

Lei D, Zhao J, Zhu C, Jiang M, Ma P, Mi Y, Fan D. Multifunctional Oxidized Dextran Cross-Linked Alkylated Chitosan/Drug-Loaded and Silver-Doped Mesoporous Bioactive Glass Cryogel for Hemostasis of Noncompressible Wounds. Gels. 2023, 9(6): 455. doi: 10.3390/gels9060455

Li B, Qing Z, Li Y, Li H, Zhang S. Effect of CaO content on structure and properties of low temperature co-fired glass-ceramic in the Li_2O-Al_2O_3-SiO_2 system, J. Mater Sci: Mater. Electron. 2016, 27: 455-2459.

Li H, Jin H, Yu H, Green CR, and Chang J. Bioglass promotes wound healing by affecting gap junction connexin 43 mediated endothelial cell behavior. Biomaterials. 2016, 84: 64-75.

Li J, Zhang T, Pan M, Xue F, Lv F, Ke Q et al. Nanofiber/hydrogel core-shell scaffolds with three-dimensional multilayer patterned structure for accelerating diabetic wound healing. J. Nanobiotechnol. 2022, 20: 28

Li M, Dai Q, Zhu S, FengQ, Qin Z, Gao H, Cao X. An ultrafast water absorption composite cryogel containing Iron-doped bioactive glass with rapid hemostatic ability for non-compressible and coagulopathic bleeding. Chemical Engineering Journal. 2023, 469: 143758

Li Y and Bou-Akl T. Electrospinning in Tissue Engineering, in Electrospinning -Material, Techniques, and Biomedical Applications, InTech, 2016.

Lin C, Mao C, Zhang J, Li Y and Chen X. Healing effect of bioactive glass ointment on full thickness skin wounds, Biomed. Mater. 2012, 7: 045017

Lin R, Deng C, Li X, Liu Y, Zhang M, Qin C, Yao Q, Wang L, Wu C. Copper-incorporated bioactive glass-ceramics inducing anti-inflammatory phenotype and regeneration of cartilage/bone interface. Theranostics, 2019, 9(21): 6300-6313

Lin Y, Brown RF, Jung SB, Day DE. Angiogenic effects of borate glass microfibers in a rodent model. J Biomed Mater Res A. 2014, 102(12): 4491-9. doi: 10.1002/jbm.a.35120.

Liu J, Zhou X, Zhang Y, Zhu W, Wang A, Xu M, and Zhuang S. Rapid hemostasis and excellent antibacterial cerium-containing mesoporous bioactive glass/chitosan composite sponge for hemostatic material. Materials Today Chemistry. 2022: 100735

Liu M, Xiangsheng W, Jie C, Hongsheng W, Binbin S, Jufang Z, Bernd R et al. Electrospun flexible magnesium-doped silica bioactive glass nanofiber membranes with anti-inflammatory and pro-angiogenic effects for infected wounds. Journal of Materials Chemistry B. 2023, 11(2): 359-376.

Liu R, Chen S, Huang P, Liu G, Luo P, Li Z, Xiao Y, Chen Z. Immunomodulation-based strategy for improving soft tissue and metal implant integration and its implications in the development of metal soft tissue materials. Adv. Funct. Mater. 2020, 1910672: 1-15, 10.1002/adfm.201910672

Liu X, Rahaman MN, and Day DE. Conversion of melt-derived microfibrous borate (13-93B3) and silicate (45S5) bioactive glass in a simulated body fluid. J. Mater. Sci. Mater. Med. 2013, 24(3): 583–595

Long M, Zhang Y, Huang P, Chang S, Hu Y, Yang Q, Mao L, Yang H. Emerging nanoclay composite for effective hemostasis. Adv. Funct. Mater. 2018, 28: 1–9

Mahmoudi M, Alizadeh P, Soltani M. Wound healing performance of electrospun PVA/70S30C bioactive glass/Ag nanoparticles mats decorated with curcumin: *In vitro* and *in vivo* investigations. Biomater Adv. 2023, 153:213530. doi: 10.1016/j.bioadv.2023.213530

Majumdar S, Tiwari A, Mallick D, Patel DK, Trigun SK, & Krishnamurthy S. Oral Release Kinetics, Biodistribution, and Excretion of Dopants from Barium-Containing Bioactive Glass in Rats. ACS omega. 2024

Mao C., Lin C and Chen X. Enhanced healing of full-thickness diabetic wounds using bioactive glass and Yunnan baiyao ointments. Journal of Wuhan University of Technology-Mater Sci Ed, 2014, 29(5):1063-1070. DOI:10.1007/s11595-014-1044-y

Martini F. et al., Fundamentals of anatomy & physiology. 2018

Mârza SM, Magyari K, Bogdan S, Moldovan M, Peştean C, Nagy A, Tăbăran F, Licarete E, Suarasan S, Dreanca A, Baia L, Papuc I. Skin wound regeneration with bioactive glass-gold nanoparticles ointment. Biomed Mater. 2019, 14(2): 025011. doi: 10.1088/1748-605X/aafd7d.

Masoud M. Cellular response to bioactive glass, and glass ceramic. Handbook of Biomaterials Biocompatibility, 2020, 413, 10.1016/b978-0-08-102967-1.00019-0

Matabola KP, Moutloali RM. The influence of electrospinning parameters on the morphology and diameter of poly(vinyledene fluoride) nanofibers-effect of sodium chloride. J. Mater. Sci. 2013, 48 (16): 5475

Matikainen N, Pekkarinen T, Ryhänen EM, Schalin-Jäntti C. Physiology of calcium homeostasis: an overview. Endocrinol. Metab. Clin. North Am. 2021, 50(4): 575−590.

Matter MT, Starsich F, Galli M, Hilber M, Schlegel AA, Bertazzo S, Pratsinis SE, Herrmann IK. Developing a tissue glue by engineering the adhesive and hemostatic properties of metal oxide nanoparticles. Nanoscale, 2017, 9: 8418–8426

Maynard JR, Dreyer BE, Stemermaan MB and Pitlick FA. Blood, 1977, 50: 387-396

Maynard JR, Heckman CA, Pitlick FA, and Nemerson Y. J. Clin. Invest. 1975, 55: 814-824

Meddahi-Pelle A, Legrand A, Marcellan A, Louedec L, Letourneur D, Leibler L. Organ repair, hemostasis, and *in vivo* bonding of medical devices by aqueous solutions of nanoparticles. Angew. Chem. Int. Ed. 2014, 53: 6369–6373

Mehrabi A, Karimi A, Mashayekhan S, Samadikuchaksaraei A, Milan PB. In-situ forming hydrogel based on thiolated chitosan/carboxymethyl cellulose (CMC) containing borate bioactive glass for wound healing. Int J Biol Macromol. 2022, 222(Pt A): 620-635. doi: 10.1016/j.ijbiomac.2022.09.177

Monavari M, Homaeigohar S, Medhekar R, Nawaz Q, Monavari M, Zheng K, Boccaccini AR. A 3D-Printed Wound-Healing Material Composed of Alginate Dialdehyde-Gelatin Incorporating Astaxanthin and Borate Bioactive Glass Microparticles. ACS Appl Mater Interfaces. 2023. doi: 10.1021/acsami.2c23252

Moskalewicz T, Smeacetto F, Cempura G, Ajitdoss LC, Salvo M and Czyrska-Filemonowicz A. Microstructure and properties characterisation of the double layered glass–ceramic coating on near-α titanium alloy. Surf. Coat. Technol. 2010, 204(21-22): 3509-16

Munaron L. Intracellular calcium, endothelial cells and angiogenesis. Anti-Cancer Drug Discov. 2006, 1: 105–119.

Nagrath M, AlhalawaniA, Yazdi AR, Towler MR. Bioactive glass fiber fabrication via a combination of sol-gel process with electro-spinning technique. Mater Sci Eng C Mater Biol Appl. 2019, 101: 521-538.

Nagrath M, Alireza Y, Aran R, Dermot D, Saeed UR, Reid C. Gallant, Heyu N, Praveen RA, and Mark RT. Tantalum-containing meso-porous glass fibres for hemostatic applications. Materials Today Communications. 2021, 27: 102260.

Nagrath M, Danielle B, Corwyn R, Deanna P, Joao R, and Mark T. Porcine liver injury model to assess tantalum-containing bioactive glass powders for hemostasis. Journal of Materials Science: Materials in Medicine. 2022, 33(6): 2022: 53.

Nagrath M, Reid G, Alireza RY, Andrew M, Saidur R, Loraine C, Stephen DW, Heyu N, and Mark RT. Tantalum-containing mesoporous bioactive glass powder for hemostasis. Journal of Biomaterials Applications. 2021, 35(8): 924-932

Nagrath M, Yazdi AR, Rafferty A, Daly D, Rahman SU, Gallant RC, Ni H, Arany PR and Towler MR. Tantalum-containing meso-porous glass fibres for hemostatic applications. Materials Today Communications. 2021, 27: 102260.

Naseria S, William C. Leprya, Vimal B. Maisuriab, Nathalie Tufenkjib, Showan N. Nazhat. Development and characterization of silver-doped sol-gel-derived borate glasses with anti-bacterial activity. Journal of Non-Crystalline Solids. 2019, 505: 438–446

Nie R, Zhang QY, Feng ZY, Huang K, Zou CY, Fan MH, Zhang YQ, Zhang JY, Li-Ling J, Tan B, Xie HQ. Hydrogel-based immunoregulation of macrophages for tissue repair and regeneration. Int J Biol Macromol. 2024, 268(Pt1): 131643. doi: 10.1016/j.ijbiomac.2024.131643.

Nielsen FH. Evidence for the nutritional essentiality of boron. Journal of Trace Elements in Experimental Medicine. 1996, 9(4): 215-229

Nurden AT. Molecular basis of clot retraction and its role in wound healing. Thromb Res. 2023, 231:159-169. doi: 10.1016/j.thromres.2022.08.010.

OECD Guidelines for the Testing of Chemicals, Section 1: Test number 105

OECD, Section 4: Test No. 402: Acute Dermal Toxicity, OECD guidelines for the testing of chemicals, (2017) 1-13

Ojha, S. Structure–property relationship of electrospun fibers. In Electrospun nanofibers, pp. 239-253. Woodhead Publishing, 2017

Ong SY, Wu J, Moochhala SM, Tan MH, Lu J. Development of a chitosan-based wound dressing with improved hemostatic and antimicrobial properties. Biomaterials. 2008, 29: 4323-4332

Ostomel T, Shi Q, Tsung C, Liang H, Stucky G. Spherical bioactive glass with enhanced rates of hydroxyapatite deposition and hemostatic activity. Small, 2006, 2(11): 1261-1265, 10.1002/smll.200600177

Ostomel TA, Shi Q, Stoimenov PK, Stucky GD. Metal oxide surface charge mediated hemostasis. Langmuir. 2007, 23: 11233–11238

Ostomel TA, Shi QH, Stucky GD. Oxide hemostatic activity. J. Am. Chem. Soc. 2006, 128: 8384–8385.

Özarslan AC, Özel C, Okumuş MD, Doğan D, Yücel S. Development, structural and rheological characterization, and *in vitro* evaluation of the zinc-doped 45S5 bioactive glass-vaseline ointment for potential wound healing applications. Journal of Materials Research, 2013, 38(6): 1557-1572

Parham S, Kharazi AZ, Bakhsheshi-Rad HR, Ghayour H, Ismail AF, Nur H, Berto F. Electrospun Nano-Fibers for Biomedical and Tissue Engineering Applications: A Comprehensive Review. Materials (Basel), 2020, 13(9)

Patel S, Docampo R. Acidic calcium stores open for business: expanding the potential for intracellular Ca^{2+} signaling. Trends Cell Biol. 2010, 20(5): 277−286.

Pawar V and Shinde V. Bioglass and hybrid bioactive material: a review on the fabrication, therapeutic potential and applications in wound healing. Hybrid Advances. 2024, 6: 100196

Physics. 1954, 22(2): 43-53.

Pillay V, Dott C, Choonara YE, Tyagi C, Tomar L, Kumar P, Toit LC, Ndesendo VMK. A review of the effect of processing variables on the fabrication of electrospun nanofibers for drug delivery applications. J. Nanomater. 2013 (2013): 22

Pourshahrestani S , Zeimaran E , Adib Kadri N , Gargiulo N , Samuel S , Naveen SV , Kamarul T , Towler MR . Gallium-containing mesoporous bioactive glass with potent hemostatic activity and antibacterial efficacy. J Mater Chem B. 2016, 4(1): 71-86. doi: 10.1039/c5tb02062j.

Pourshahrestani S, Nahrizul AK, Ehsan Z, Nicola G, Shani S, Sangeetha VN, Khairunnisa H, Tunku K, and Mark R. T. Comparative efficacy of hemorrhage control of a novel mesoporous bioactive glass versus two commercial hemostats. Biomedical Materials. 2018, 13(2): 025020

Pourshahrestani S, Zeimaran E, Kadri NA, Gargiulo N, Jindal HM, Naveen SV, Sekaran SD, Kamarul T, Towler MR. Potency and Cytotoxicity of a Novel Gallium-Containing Mesoporous Bioactive Glass/Chitosan Composite Scaffold as Hemostatic Agents. ACS Appl Mater Interfaces. 2017, 9(37): 31381-31392. doi: 10.1021/acsami.7b07769

Pourshahrestani S, Zeimaran E, Kadri NA, Gargiulo N, Samuel S, Naveen S, Kamarul T, Towler M. Gallium-containing mesoporous bioactive glass with potent hemostatic activity and antibacterial efficacy. J. Mater. Chem. B, 2016, 4(1):. 71-86, 10.1039/C5TB02062

Pourshahrestani S, Kadri NA, Zeimaran E, Towler M. Well-ordered mesoporous silica and bioactive glasses: promise for improved hemostasis. Biomater. Sci. 2019, 7(1): 31-50, 10.1039/C8BM01041B

Prajapati SK, Krishnamurthy S. Development and treatment of cognitive inflexibility in sub-chronic stress−re-stress (SRS) model of PTSD. Pharmacol. Rep. 2021, 73: 464−479

Prasad AS, Beck FW, Snell DC, Kucuk O. Zinc in cancer prevention. Nutr Cancer. 2009, 61(6): 879-87

Prasad AS, Kucuk O. Zinc in cancer prevention. Cancer Metastasis Rev. 2002, 21(3-4): 291-5

Psomas G. Copper(II) and zinc(II) coordination compounds of non-steroidal antiinflammatory drugs: Structural features and antioxidant activity. Coordination Chemistry Reviews. 2020, 412: 213259

Quinlan E, Partap S, Azevedo MM, Jell G, Stevens MM, O'Brien FJ. Hypoxia-mimicking bioactive glass/collagen glycosaminoglycan composite scaffolds to enhance angiogenesis and bone repair. Biomaterials. 2015, 52: 358-66

Quintero F, Pou J, Comesana R, Lusquinos F, Riveiro A, Mann AB, Hill RG, Wu ZY, Jones JR. Laser Spinning of Bioactive Glass Nanofibers, Advanced Functional Materials. 2009, 19(19): 3084-3090

Rabul RA, Jewena N, Das SK, Khandaker JI, Ahmed F. Synthesis of Metal- Oxide (Al2O3) Nanoparticles by using Autoclave for the Efficient Absorption of Heavy Metal Ions, J. Nanomater. Mol. Nanotechnol. 2020, 9: 6.

Rahaman MN, Day DE, Bal BS, Fu Q, Jung SB, Bonewald LF et al. Bioactive glass in tissue engineering. Acta Biomater. 2011, 76: 2355–73

Rao TG, Kumar AR, Neeraja K, Veeraiah N and Reddy MR. Optical and structural investigation of Eu^{3+} ions in Nd^{3+} co-doped magnesium lead borosilicate glasses. J. Alloys Compd. 2013, 557: 209-17

Reneker DH, Yarin AL, FongH, Koombhongse S. Bending instability of electrically charged liquid jets of polymer solutions in electrospinning. Journal of Applied Physics. 2000, 87(9): 4531-4547

Rivadeneira J, Luz GM, Audisio MC, Mano JF, Gorustovich AA. Novel antibacterial bioactive glass nanocomposite functionalized with tetracycline hydrochloride. Biomed. Glasses. 2015, 1 (1): 128−135

Rodrigues M, Kosaric N, Bonham CA, Gurtner GC. Wound healing: a cellular perspective. Physiol. Rev. 2019, 99:665–706

Roy P, Saha R, Saha S, Dattaray D, Mandal TK, ElShazly N, Marei MK, Chakraborty J. Facile synthesis of electrospun antibacterial bioactive glass based micronanofibre (ABGmnf)

for exalted wound healing: *In vitro* and *in vivo* studies. Materials Chemistry and Physics, 2023a, 305: 127874

Roy P, Saha R and Chakraborty J. A novel composition of bioactive glass with potent haemostatic action and antibacterial competence. Ceramics International. 2023b, 49: 6389-6400

Roy P, Saha R, Dattaray D, Saha S, Mandal TK, Srivastava P, and Chakraborty J. Bioactive glass incorporated dressing matrix for rapid hemostatic action with antibacterial activity. Materials Chemistry and Physics. 2024a, 315: 128942

Roy P, Saha R, Pawlik J, Samol Z, Dziadek M, Cholewa-Kowalska K, and Chakraborty J. Cobalt containing antimicrobial bioactive glass coated urinary catheter towards management of catheter associated urinary tract infection (CAUTI): Significant *in vitro* characterizations. Ceramics International. 2024b, 50(7): 11625-11638.

Ruggeri Z. Structure and Function of von Willebrand Factor. Thromb. Haemost. 1999, 82(08): 576–584

Saha S, Bhattacharjee A, Hasanur SK, Ray S, Marei M, Jain H, Chakraborty J. Prospects of antibacterial bioactive glass nanofibers for wound healing: An *in vitro* study. 2020, 11(1). DOI:10.1111/ijag.15029

Saha S, Bhattacharjee A, Rahaman SH, Ray S, Marei MK, Jain H and Chakraborty J. Prospects of antibacterial bioactive glass nanofibers for wound healing: An *in vitro* study. Int. J. of Appli. Glass Sci. 2020, 11(2): 320-328

Saravanapavan P, Jones JR, Pryce RS, Hench LL. Bioactivity of gel-glass powders in the CaO-SiO_2 system: a comparison with ternary (CaO-P_2O_5-SiO_2) and quaternary glasses (SiO_2-CaO-P_2O_5-Na_2O) J. Biomed. Mater. Res. A. 2003, 66: 110–119. doi: 10.1002/jbm.a.10532.

Scholze H. Glass: nature, structure, and properties, Springer Science & Business Media, 2012

Schousboe I. Contact activation in human plasma is triggered by zinc ion modulation of factor XII (Hageman factor). Blood coagulation fibrinolysis, 1993, 4(5): 671-678

Sepulveda P, Jones JR, Hench LL. Characterization of Melt-Derived 45S5 and sol-gel-derived 58S Bioactive Glasses. J. Biomed. Mater. Res. 2001, 58: 734–740. doi: 10.1002/jbm.10026.

Sepulveda P, Jones JR., Hench LL. *In vitro* dissolution of melt derived 45 S5 and sol–gel derived 58 S bioactive glasses. Biomed. Mater. Res. 2002, 61: 301–311. doi: 10.1002/jbm.10207.

Shao G, Wu X, Kong Y, Cui S, Shen X, Jiao C and Jiao J. Thermal shock behavior and infrared radiation property of integrative insulations consisting of $MoSi_2$/borosilicate glass coating and fibrous ZrO_2 ceramic substrate. Surf. Coat. Technol. 2015, 270: 154- 63

Sharaf S, El-Shafei AM, Refaie R, Gibriel AA, and Abdel-Sattar R. Antibacterial and wound healing properties of cellulose acetate electrospun nanofibers loaded with bioactive glass nanoparticles; *in-vivo* study. Cellulose. 2022, 29(8): 4565-4577

Sharifi E, Sadati SA, Yousefiasl S, Sartorius R, Zafari M, Rezakhani L, Alizadeh M, Nazarzadeh Zare E, Omidghaemi S, Ghanavatinejad F, Jami MS, Salahinejad E, Samadian H, Paiva-Santos AC, De Berardinis P, Shafiee A, Tay FR, Pourmotabed S, Makvandi P. Cell loaded hydrogel containing Ag-doped bioactive glass-ceramic nanoparticles as skin substitute: Antibacterial properties, immune response, and scarless cutaneous wound regeneration. Bioeng Transl Med. 2022, 7(3): e10386. doi: 10.1002/btm2.10386.

Sharifi E, Satar Yousefiasl, Nilofar Laderian, Navid Rabiee, Pooyan Makvandi, Samiramis Pourmotabed, Milad Ashrafizadeh, Fatemeh Familsattarian, Wei Fang Cell-loaded genipin cross-linked collagen/gelatin skin substitute adorned with zinc-doped bioactive glass-ceramic for cutaneous wound regeneration. International Journal of Biological Macromolecules. 2023, 251: 125898

Shelby JE. Introduction to glass science and technology, Royal Society of Chemistry, 2005

Sherwood L and Ward C. Human physiology: from cells to systems, 3rd ed. 2016.

Shi M, Zhao F, Sun L, Tang F, Gao W, Xie W, Cao X, Zhuang J and Chen X. Bioactive glass activates VEGF paracrine signaling of cardiomyocytes to promote cardiac angiogenesis. Materials Science and Engineering: C, 2012, 124: 112077

Singh H, Arora S, Mani M, Mahaur KK, and Chandra P. Development of multicomponent formulation of herbal drugs for evaluation of Antidiabetic activity. Pharm. Lett, 2014, 6: 219-223.

Skalnaya MG, Skalny AV, Radysh IV. In Essential trace elements in human health: a physician's view; Publishing House of Tomsk State University: Tomsk, Russia, 2018, 6−16

Spiller KL, Nassiri S, Witherel CE, Anfang RR, Ng J, Nakazawa KR, Yu T, Vunjak-Novakovic G. Sequential delivery of immunomodulatory cytokines to facilitate the M1-to-M2 transition of macrophages and enhance vascularization of bone scaffolds. Biomaterials. 2015, 37: 194-207, 10.1016/j.biomaterials.2014.10.017

Spiller KL, Koh TJ. Macrophage-based therapeutic strategies in regenerative medicine. Adv. Drug Deliv. Rev. 2017, 122: 74-83, 10.1016/j.addr.2017.05.010

Sridharan R, Cameron AR, Kelly DJ, Kearney CJ, O'Brien FJ. Biomaterial based modulation of macrophage polarization: a review and suggested design principles. Mater. Today. 2015, 18: 313-325, 10.1016/j.mattod.2015.01.019

Stocco TD, Bassous NJ, Zhao S, Granato AEC, Webster TJ, and Lobo AO. Nanofibrous scaffolds for biomedical applications. Nanoscale. 2018, 10(26): 12228–12255

Stoor P, Soderling E, Grenman R. Bioactive glass S53P4 in repair of septal perforations and its interactions with the respiratory infection-associated microorganisms *Heamophilus influenzae* and *Streptococcus pneumonia*. J. Biomed. Mater. Res. 2001, 58: 113-120

Stoor P, Soderling E, Grenman R. Interactions between the bioactive glass S53P4 and the atrophic rhinitis-associated microorganism *Klebsiella ozaenae*. J. Biomed. Mater. Res. 1999, 48: 869-874

Stoor P, Soderling E, Salonen JI. Antibacterial effects of a bioactive glass paste on oral microorganisms. Acta Odontol. Scand. 1998, 56: 161-165

Subramaniam T, Fauzi MB, Lokanathan Y, and Law JX. The role of calcium in wound healing. International journal of molecular sciences. 2021, 22(12): 6486.

Sundaram et al., Injectable chitosan-nano bioglass composite hemostatic hydrogel for effective bleeding control. Int. J. of Biological Macromolecules. 2019, 129: 936-943

Tan SH, Inai R, Kotaki M, Ramakrishna S. Systematic parameter study for ultra-fine fiber fabrication via electrospinning process. Polymer. 2005, 46(16): 6128-6134

Tanaka M, Narazaki and Kishimoto T. IL-6 in inflammation, immunity, and disease, Cold Spring Harb Perspect Biol. 2014, 6(10): a016295

Tanaka T, Kojima I, Ohse T, Ingelfinger JR, Adler S, Fujita T, Nangaku M. Cobalt promotes angiogenesis via hypoxia-inducible factor and protects tubulointerstitium in the remnant kidney model. Lab Invest. 2005, 85(10): 1292-307

Tang B, Ge J, Zhou L, Wang G, Niu J et al. A facile and controllable synthesis of alumina nanostructure without a surfactant. Eur. J. Inorg. Chem. 2005, 4366-4369

Tang C, Hu M, Fang M, Liu Y, Wu X, Liu W, Wang M, Huang Z. Photocatalytic Property of TiO_2-Vermiculite Composite Nanofibers via Electrospinning. Nanoscale Res Lett. 2015, 10(1):977. doi: 10.1186/s11671-015-0977-1.

Tang F, Li J, Xie W, Mo Y, Ouyang L, Zhao F, Fu X, Chen X. Bioactive glass promotes the barrier functional behaviors of keratinocytes and improves the Re-epithelialization in wound healing in diabetic rats. Bioact Mater. 2021, 6(10): 3496-3506. doi: 10.1016/j.bioactmat.2021.02.041

Tapiero H, Tew KD. Trace elements in human physiology and pathology: zinc and metallothioneins. Biomed Pharmacother. 2003, 57(9): 399-411

Tenda Heal Home Page. https://tendaheal.com/products/, 2023

The coagulation cascade: initiation, maintenance, and regulation - Biochemistry (ACS Publications).[Online].Available:https://pubs.acs.org/doi/abs/10.1021/bi00107a001?journalCode=bichaw. [Accessed: 23.05.23]

Thomas AC and Wysocki AB. The healing wound: a comparison of three clinically useful methods of measurement. Decubitus 3, 1990, 18-20: 24–5

Tomar S, Pandey R, Surya P, Verma R, Mathur R, Gangenahalli G, Singh S. Multifunctional, Adhesive, and PDA-Coated Bioactive Glass Reinforced Composite Hydrogel for Regenerative Wound Healing. ACS Biomater Sci Eng. 2023, 9(3): 1520-1540. doi: 10.1021/acsbiomaterials.2c01223

Tu CL, Chang W, Xie Z, Bikle DD. Inactivation of the Calcium Sensing Receptor Inhibits E-cadherin-mediated Cell-Cell Adhesion and Calcium-induced Differentiation in Human Epidermal Keratinocytes. J. Biol. Chem. 2008, 283: 3519–3528

Turlybekuly A, Pogrebnjak AD, Sukhodub LF, Sukhodub LB, Kistaubayeva AS, Savitskaya IS, Shokatayeva DH et al. Synthesis, characterization, *in vitro* biocompatibility and antibacterial properties study of nanocomposite materials based on hydroxyapatite-biphasic ZnO micro-and nanoparticles embedded in Alginate matrix. Mater. Sci. and Engg: C. 2019, 104: 109965.

Valappil SP, Ready D, Neel EA, Pickup DM, Chrzanowski W, O'Dell LA, Newport RJ, Smith ME, Wilson M, Knowles JC. Antimicrobial gallium-doped phosphate-based glasses. Adv. Funct. Mater. 18, 2008: 732-741

Valappil SP, Ready D, Neel EA, Pickup DM, O'Dell LA, Chrzanowski W, Pratten J, Newport RJ, Smith ME, Wilson M, Knowles JC. Controlled delivery of antimicrobial gallium ions from phosphate-based glasses. Acta Biomater. 5, 2009: 1198-1210

Versteeg HH, Heemskerk JWM, Levi M, Reitsma PH, New Fundamentals in Hemostasis. Physiological Reviews. 2013, 93(1): 327-358.

Vinayak MN and Jana S, Datta P and Das H and Chakraborty B, Mukherjee P, Mondal S and Kundu B, Nandi SK. Accelerating Full-Thickness Skin Wound Healing Using Zinc and Cobalt Doped-Bioactive Glass Coated Eggshell Membrane. http://dx.doi.org/10.2139/ssrn.4213299

Wang C, Zhu F, Cui Y, Ren H. An easy-to-use wound dressing gelatin-bioactive nanoparticle gel and its preliminary *in vivo* study. Journal of Materials Science: Materials in Medicine. 2016, 28(1) DOI:10.1007/s10856-016-5823-1

Wang T, Kumar S. Electrospinning of polyacrylonitrile nanofibers. J. Appl. Polym. Sci. 2006, 102(2): 1023-1029

Wang X, Fang C, Jun L, Smått JH, Gepperth D, LastusaariM, XuC, and Hupa L. Biocomposites of copper-containing mesoporous bioactive glass and nanofibrillated cellulose: Biocompatibility and angiogenic promotion in chronic wound healing application. Acta Biomaterialia. 2016, 46: 286-298.

Wang Y, Luo M, Li T, Xie C, Li S, Lei B. Multi-layer-structured bioactive glass nanopowder for multistage-stimulated hemostasis and wound repair. Bioactive Materials. 2023, 25: 319-332. doi: 10.1016/j.bioactmat.2023.01.019

Waugh AA, Grant, JS, Ross, and K. J. W. Wilson, Ross and Wilson anatomy and physiology in health and illness, 9th ed., repr. Edinburgh: Churchill Livingstone, 2001

Wayne PA, Clinical and Laboratory Standards Institute. Performance standards for dilution antimicrobial susceptibility tests for bacteria that grow aerobically, 11th Ed. CLSI standard M07, Clinical and Laboratory Standards Institute, 2018

Weder JE, Dillon CT, Hambley TW, Kennedy BJ, Lay PA, Biffin JR, Regtop HL, Davies NM. Copper complexes of non-steroidal anti-inflammatory drugs: an opportunity yet to be realized. Coordination Chemistry Reviews. 2002, 232(1-2): 95-126

Weiss HJ, Turitto VT, Baumgartner HR, Nemerson Y and Hoffman T. Blood, 1989, 73: 968-975

Wilcox JN, Smith KM, Schwartz SM and Gordon D. Proc. Natl. Acad. Sci. USA 1989, 86: 2839-2843

Wilkinson G, Gillard RD, McCleverty JA. Comprehensive coordination chemistry. The synthesis, reactions, properties and applications of coordination compounds. V. 3. Main group and early transition elements, 1987.

Wu HB, Li FY, Wang SF, Lu JX, Li JQ, Du Y, Sun XL, Chen XY, Gao JQ, Ling DS. Ceria nanocrystals decorated mesoporous silica nanoparticle based ROS-scavenging tissue adhesive for highly efficient regenerative wound healing. Biomaterials. 2018, 151: 66–77

Wu J, Stebbins JF, Cation field strength effects on boron coordination in binary borate glasses, Journal of the American Ceramic Society. 2014, 97(9): 2794-2801.

Wu J, Stebbins JF. Effects of cation field strength on the structure of aluminoborosilicate glasses: high-resolution 11B, 27Al and 23Na MAS NMR. Journal of Non-Crystalline Solids. 2009, 355(9): 556-562.

Wu X, Li H. Incorporation of Bioglass Improved the Mechanical Stability and Bioactivity of Alginate/Carboxymethyl Chitosan Hydrogel Wound Dressing. ACS Appl Bio Mater. 2021, 4(2): 1677-1692. doi: 10.1021/acsabm.0c01477.

Xia W, Zhang D, Chang J. Fabrication and *in vitro* biomineralization of bioactive glass (BG) nanofibres. Nanotechnol. 2007, 18(13): 135601

Xu Y, Peng JL, Dong X, Xu YH, Li HY, Chang J. Combined chemical and structural signals of biomaterials synergistically activate cell-cell communications for improving tissue regeneration. Acta Biomater. 2017, 55: 249–261

Xue J, Wu T, Dai Y, Xia Y. Electrospinning and Electrospun Nanofibers: Methods, Materials, and Applications. Chem Rev. 2019, 119(8): 5298-5415.

Xue M, Jackson CJ. Extracellular Matrix Reorganization during Wound Healing and Its Impact on Abnormal Scarring. Adv. Wound Care. 2015, 4: 119–136

Yang Q, Chen S, Shi H, Xiao H, Ma Y. *In vitro* study of improved wound-healing effect of bioactive borate-based glass nano-/micro-fibers. Materials Science and Engineering: C, 2015, 55: 105-117

Yao A, Rahaman MN, Lin J, and Huang W. Structure and crystallization behavior of borate-based bioactive glass. J. Mater. Sci. 2007, 42(23): 9730–9735

Yin C, Zhao Q, Li W, Zhao Z, Wang J, Deng T, Zhang P, Shen K, Li Z, Zhang Y. Biomimetic anti-inflammatory nano-capsule serves as a cytokine blocker and M2 polarization inducer for bone tissue repair. Acta Biomater. 2020, 102: 416-426

Yu H, Peng J, Xu Y, Chang J, Li H. Bioglass Activated Skin Tissue Engineering Constructs for Wound Healing. ACS Appl Mater Interfaces. 2016, 8(1): 703-15. doi: 10.1021/acsami.5b09853

Yuan C, Daixing Zhang, Yujing Tang, Zifang Guo, Kai Lin, Yingjie Yu, Jinghua Li, Qing Cai . Fibrous dressing containing bioactive glass with combined chemotherapy and wound healing promotion for post-surgical treatment of melanoma. Biomaterials Advances. 2023, 149: 213387

Z.T. Birgani, N. Gharraee, A. Malhotra, C.A. van Blitterswijk, P. Habibovic, Combinatorial incorporation of fluoride and cobalt ions into calcium phosphates to stimulate osteogenesis and angiogenesis, Biomedical Materials 11(1) (2016) 015020.

Zanotto ED, Mauro JC. The glassy state of matter: Its definition and ultimate fate, Journal

Zarzycki J. Glasses and the vitreous state, Cambridge university press, 1991

Zeng Q, Han Y, Li H and Chang J. Design of a thermosensitive bioglass/agarose–alginate composite hydrogel for chronic wound healing. J. Mater. Chem. B, 2015, 3**:** 8856-8864

Zhang X , Ying Li, Zhijie Ma, Dan He, Haiyan Li. Modulating degradation of sodium alginate/bioglass hydrogel for improving tissue infiltration and promoting wound healing. Bioactive Materials. 2021, 6(11): 3692-3704

Zhang K, Chai B, Ji H, Ma Y, Zhu L, Xu J, Wu Y et al. Bioglass promotes wound healing by inhibiting endothelial cell pyroptosis through regulation of the connexin 43/reactive oxygen species (ROS) signaling pathway. Laboratory Investigation. 2022, 102(1): 90-101.

Zhang M, Fan Z, Zhang J, Yang Y, Huang C, Zhang W, Ding D, Liu G, Cheng N. Multifunctional chitosan/alginate hydrogel incorporated with bioactive glass nanocomposites enabling photothermal and nitric oxide release activities for bacteria-infected wound healing. Int J Biol Macromol. 2023, 232: 123445. doi: 10.1016/j.ijbiomac.2023.123445

Zhang Y, Jiaxi Liu, Zhenning Wu, Xianhui Mei, Wei Zhu, Anping Wang. Rapid promoting thrombus formation and fibrin cross-linked Bi-doped mesoporous bioglass for hemostatic agent. Materials Today Chemistry. 2022, 25: 100980

Zhao S, Li L, Wang H, Zhang Y, Cheng X, Zhou N, Rahaman MN, Liu Z, Huang W, Zhang C. Wound dressings composed of copper-doped borate bioactive glass microfibers stimulate angiogenesis and heal full-thickness skin defects in a rodent model. Biomaterials, 2015, 53: 379-391, 10.1016/j.biomaterials.2015.02.112

Zhao S, Li L, Wang H, Zhang Y, Cheng X, Zhou N, Rahaman MN, Liu Z, Huang W, and Zhang C. Wound dressings composed of copper-doped borate bioactive glass microfibers stimulate angiogenesis and heal full-thickness skin defects in a rodent model. Biomaterials. 2015, 53: 379-391.

Zhao X. PhD thesis. 2022

Zheng C, Liu J, Bai Q, Quan Y, Li Z, Chen W, Gao Q, Zhang Y, Lu T. Preparation and hemostatic mechanism of bioactive glass-based membrane-like structure camouflage composite particles. Materials & Design. 2022, 223: 111116

Zheng K, Niu W, Lei B & Boccaccini A R. Immunomodulatory bioactive glasses for tissue regeneration. Acta Biomaterialia. 2021, 133: 168-186

Zhong J, Ma X, Lu H, Wang X, Zhang S and Xiang W. Preparation and optical properties of sodium borosilicate glasses containing Sb nanoparticles. J. Alloys Compd. 2014, 607: 177-82.

Zhong JP and Greenspan DC. Processing and properties of sol–gel bioactive glasses, J. Biomed. Mater. Res. 2000, 53: 694–701

Zhou J, Wang H, Zhao S, Zhou N, Li L, Huang W, Wang D, and Zhang C. *In vivo* and *in vitro* studies of borate based glass micro-fibers for dermal repairing. Materials Science and Engineering: C, 2016, 60: 437-445

Zhou J, Wang H, Zhao S, Zhou N, Li L, Huang W, Wang D, Zhang C. *In vivo* and *in vitro* studies of borate based glass micro-fibers for dermal repairing, Mater Sci Eng C Mater Biol Appl. 2016, 60: 437-445

Zhou Y, Gao L, Peng J, Xing M, Han Y, Wang X, Xu Y, Chang J. Bioglass Activated Albumin Hydrogels for Wound Healing. Adv Healthc Mater. 2018, 7(16): e1800144. doi: 10.1002/adhm.201800144.

Zhu J, Jiang G, Song G, Liu T, Cao C, Yang Y, Zhang Y, Hong W. Incorporation of ZnO/Bioactive Glass Nanoparticles into Alginate/Chitosan Composite Hydrogels for Wound Closure. ACS Appl Bio Mater. 2019, 2(11): 5042-5052. doi: 10.1021/acsabm.9b00727

Zhu JY, Jiang GH, Song G, Liu TQ, Cao C, Yang YH, Zhang YJ, Hong WJ. Incorporation of ZnO/Bioactive Glass Nanoparticles into Alginate/Chitosan Composite Hydrogels for Wound Closure. ACS Applied Bio Materials. 2019, 2(11): 5042-5052

Zhu Y, Ma Z, Kong L, He Y, Chan HF, Li H. Modulation of macrophages by bioactive glass/sodium alginate hydrogel is crucial in skin regeneration enhancement. Biomaterials. 2020, 256: 120216, 10.1016/j.biomaterials.2020.120216

Zhu Y, Ma Z, Kong L, He Y, Chan HF, Li H. Modulation of macrophages by bioactive glass/sodium alginate hydrogel is crucial in skin regeneration enhancement. Biomaterials. 2020, 256:120216. doi: 10.1016/j.biomaterials.2020.120216.

Zoroddu MA, Aaseth J, Crisponi G, Medici S, Peana M, Nurchi VM. The Essential Metals for Humans: A Brief Overview. J. Inorg. Biochem. 2019, 195: 120−129

APPENDIX

Materials Chemistry and Physics 305 (2023) 127874

Contents lists available at ScienceDirect

Materials Chemistry and Physics

journal homepage: www.elsevier.com/locate/matchemphys

Facile synthesis of electrospun antibacterial bioactive glass based micronanofibre (ABGmnf) for exalted wound healing: *In vitro* and *in vivo* studies

Payal Roy [a], Rupam Saha [a,b], Suman Saha [a], Debolina Dattaray [c], Tapan Kumar Mandal [c], Noha ElShazly [d,e], Mona K. Marei [d,f], Jui Chakraborty [a,b,*]

[a] Bioceramics and Coating Division, CSIR-Central Glass and Ceramic Research Institute (CSIR- CGCRI), 196, Raja S. C. Mullick Road, Kolkata, 700 032, India
[b] Academy of Scientific and Innovative Research (AcSIR), Ghaziabad, 201002, India
[c] Department of Veterinary Pharmacology and Toxicology, West Bengal University of Animal and Fishery Sciences, Belgachia, Kolkata, 700 037, India
[d] Tissue Engineering Laboratories, Faculty of Dentistry, Alexandria University, Alexandria, Egypt
[e] Department of Comparative Biomedicine and Food Science, University of Padova, Legnaro, PD, Italy
[f] Departmentof Removable Prosthodontics, Faculty of Dentistry, Alexandria University, Alexandria, Egypt

HIGHLIGHTS

- Electrospinning and the sol-gel method were used to fabricate ABGmnf.
- ABGmnf showed brilliant cyto-and biocompatibility with antibacterial action.
- Its fibrous texture expedites wound healing.
- That might expand another domain of chances and headings to recuperate wounds.

GRAPHICAL ABSTRACT

ARTICLE INFO

Keywords:
Antibacterial bioactive glass based micronanofibre
In-vivo wound healing assay
In-vivo biocompatibility
TNF-α-IL-6
MIC

ABSTRACT

Recently, bioactive glass has shown an incredible potential to address the assortment of chronic wounds including diabetic and venous ulcers. In this regard, the textural properties of bioactive glass (BG)-based micronanofibre, which are analogous to the fibrin clot that aggregates platelets, provide advantages that support the coagulation cascade and subsequent soft tissue regeneration by providing mechanical support and a source of various therapeutic ions. In this correspondence, we synthesized a binary composition comprising (70-x) mol% SiO_2, (30-y) mol% CaO, $1 < x < 5$ mol% B_2O_3 and $0.001 < y < 0.1$mol% Ag_2O composition (ABGmnf) via sol-gel method followed by fabrication of the electrospun fibres, and state-of-art characterizations, XRD, FTIR, and FESEM-EDXalong with biological studies including *in-vitro* cytocompatibility, 2D wound healing, antibacterial activities by determination of minimum inhibitory concentration (MIC). In addition, the concentration of proinflammatory cytokines (TNF-α and IL-6) and various hematological, biochemical, and histopathological parameters were used to establish the *in vivo* biocompatibility. The *in vivo* wound healing assay, which

* Corresponding author.Jui Chakraborty, Bioceramics and Coating Division, CSIR- Central Glass and Ceramic Research Institute, (CSIR-CGCRI), 196, Raja S. C. Mullick Road, Kolkata, 700 032, India.
E-mail address: jui@cgcri.res.in (J. Chakraborty).

https://doi.org/10.1016/j.matchemphys.2023.127874
Received 12 February 2023; Received in revised form 28 April 2023; Accepted 1 May 2023
Available online 9 May 2023
0254-0584/

Ceramics International 49 (2023) 6389–6400

Contents lists available at ScienceDirect

Ceramics International

journal homepage: www.elsevier.com/locate/ceramint

A novel composition of bioactive glass with potent haemostatic action and antibacterial competence

Payal Roy [a], Rupam Saha [a,b], Jui Chakraborty [a,b,*]

[a] Bioceramic and Coating Division, CSIR-Central Glass and Ceramic Research Institute (CSIR-CGCRI), 196, Raja S. C. Mullick Road, Kolkata, 700 032, India
[b] Academy of Scientific and Innovative Research (AcSIR), Ghaziabad, 201002, India

ARTICLE INFO

Keywords:
Haemostasis
Antibacterial activity
Bioactive glass
Haemocompatibility
PT-aPTT
Acute dermal toxicity

ABSTRACT

Haemorrhagic bleeding is a crucial area of concern related to military as well as civilian trauma. In recent years, bioactive glass is gaining attention in a number of healthcare applications, including haemostasis. Herewith, we report a unique composition of bioactive glass, 70 SiO_2: (30-x-y) CaO: x.Al_2O_3: y.ZnO, where x = 10–18 mole% and y = 0–8 mole%, (Al-BAG) exhibiting haemostatic property as well as antibacterial activity. The as-prepared glass was characterized using XRD, SEM-EDX, FTIR and TG-DSC along with *in-vitro* degradation study and biological studies e.g., cytocompatibility, haemocompatibility, *in-vitro* thrombus formation, *in-vitro* blood absorption capacity, blood coagulation assays (PT, aPTT), *in-vitro* antibacterial assay against *Staph. aureus* as well as *in-vivo* acute dermal toxicity followed by histopathological analysis) and *in-vivo* haemostasis efficacy were undertaken. The novel bioactive glass composition exhibits promises to be an efficient haemostatic agent with antibacterial activity.

1. Introduction

Haemorrhagic bleeding control is crucial on account of trauma, major surgeries or to combat mortality, and effective control of blood loss, positively correlated to reduce the mortality incidents [1,2]. Haemostasis is a physiological process, highly orchestrated and complex retort at the injury site, comprising the vessel wall, platelets and coagulation factors to staunch [3]. At the injury site, blood and blood components, e.g., erythrocytes, white blood cells etc. leak out of the damaged vessel wall and the smooth muscle in the wall contracts near the injury point to reduce the blood loss, termed as 'vascular spasm'. At this moment, platelets are activated by chemicals (platelet-derived growth factor, VEGF, coagulation factors etc.) released from the injury site and and become spiked and stick to each other at the underlying collagen matrix leading to formation of the platelet plug [4]. In the next step, fibrinogen is converted to fibrin, which forms a mesh that traps more platelets and erythrocytes to produce clots [3–7]. There are various market available haemostatic agents e.g., natural polymer/-synthetic polymer/kaolin clay based, e.g., HemCon, Celox, QuikClot, have been proven clinically effective for the rapid control of bleeding. Nevertheless, the pad like HemCon dressings, Celox has poor adhesion at the injury site and occurrence of rebleeding on refreshing the dressing [8]. The kaolin clay based QuikClot specifically functions with a local exothermic reaction, leading to additional tissue injury [9,10]. Poor biodegradability is worth mentioning and some studies shows that these materials do not often provide immediate haemostasis when applied to the site, resulting in larger blood loss compared with other agents [11]. A chitosan based indigenous haemostatic material (e.g., Axiostat) has been reported of variation in performance among batches [12]. Furthermore, such dressing may not be reliable for controlling hemorrhage in coagulopathy since its haemostatic aptitudes depend exclusively on the blood-clotting activity of the host [13]. Another major problem related to the delay or impairment of the wound healing cascade is the microbial infection [14] and that can be treated with antibiotics but the most important challenge is the increasing rate of antibiotic-resistant bacterial infections for instance ESKAPE pathogens [15,16], so an alternative to antibiotics is need of the hour for controlling infection and expedite the healing cascade. Hence, the development of a promising haemostatic agent with bacteriostatic or bactericidal efficacy is highly desirable.

In this regard bioactive glass with high surface area and anionicity (glass effect) can induce hemostasis via activation of factor XII and other

Abbreviations: PT, Prothombin Time; aPTT, Activated Partial Thromboplastin Time.

* Corresponding author. Bioceramic and Coating Division, CSIR-Central Glass and Ceramic Research Institute (CSIR-CGCRI),196, Raja S. C. Mallick Road, Kolkata, 700 032, India.
E-mail address: jui@cgcri.res.in (J. Chakraborty).

https://doi.org/10.1016/j.ceramint.2022.10.114
Received 21 July 2022; Received in revised form 28 September 2022; Accepted 9 October 2022
Available online 11 October 2022

Materials Chemistry and Physics 315 (2024) 128942

Contents lists available at ScienceDirect

Materials Chemistry and Physics

journal homepage: www.elsevier.com/locate/matchemphys

Bioactive glass incorporated dressing matrix for rapid hemostatic action with antibacterial activity

Payal Roy [a], Rupam Saha [a,b], Debolina Dattaray [c], Suman Saha [a], Tapan Kumar Mandal [c], Pooja Srivastava [d], Jui Chakraborty [a,b,*]

[a] Bioceramics and Coating Division, CSIR-Central Glass and Ceramic Research Institute (CSIR- CGCRI), 196, Raja S. C. Mullick Road, Kolkata, 700 032, India
[b] Academy of Scientific and Innovative Research (AcSIR), Ghaziabad, 201002, India
[c] Department of Veterinary Pharmacology and Toxicology, West Bengal University of Animal and Fishery Sciences, Belgachia, Kolkata, 700 037, India
[d] Institute of Nuclear Medicine & Allied Sciences, Brig SK Mazumdar Marg, Timarpur, Delhi, 110054, India

HIGHLIGHTS

- AlBGscg is cytocompatible, **has** rapid hemostasis **and** antibacterial activity.
- It can **initiate** both intrinsic and extrinsic coagulation **cascades.**
- It shows **rapid** thrombin generation and **improves** hemostasis *in vivo.*

GRAPHICAL ABSTRACT

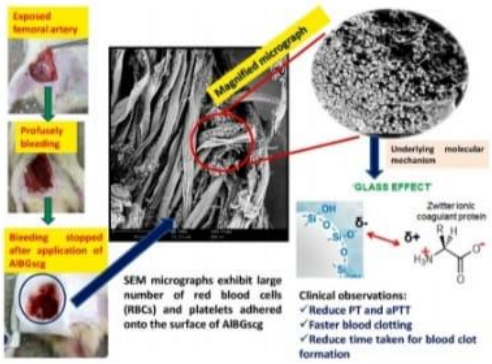

ARTICLE INFO

Keywords:
AlBGscg
Platelet adhesion
PT-aPTT
Antibacterial activity
Thrombin generation
In-vivo hemostatic efficacy

ABSTRACT

Uncontrolled bleeding stands as a leading cause of preventable death in both civilian trauma and military battlefield scenarios. Existing hemostatic dressings like HemCon, Celox, and QuickClot, often lack instant hemostasis at the bleeding site and may have biodegradability and exothermic issues. To address the above in this communication, we have synthesized a hemostatic glass (acronym AlBG, $CaO\text{-}SiO_2$ system, incorporated with Al_2O_3 and ZnO) by sol gel route and carried out detail physicochemical characterizations, e.g., XRD, FESEM, FTIR, BET and particle size analysis etc. The AlBG of particle size range 140–253 nm was incorporated into the nonwoven surgical cotton gauze to obtain AlBGscg. *In vitro* biological assays including cytocomtability, hemocompatibility assays of the above coated gauze was undertaken using NIH3T3 of which, the later showed optimum hemocompatibility with <6 % lysis of red blood cells. Potent antibacterial action on both gram positive

* Corresponding author. Bioceramics and Coating Division, CSIR-Central Glass and Ceramic Research Institute (CSIR- CGCRI), 196, Raja S. C. Mullick Road, Kolkata, 700 032, India.
E-mail address: jui@cgcri.res.in (J. Chakraborty).

https://doi.org/10.1016/j.matchemphys.2024.128942
Received 3 May 2023; Received in revised form 8 January 2024; Accepted 11 January 2024
Available online 13 January 2024

ARTICLE IN PRESS

Ceramics International xxx (xxxx) xxx

Contents lists available at ScienceDirect

Ceramics International

journal homepage: www.elsevier.com/locate/ceramint

Cobalt containing antimicrobial bioactive glass coated urinary catheter towards management of catheter associated urinary tract infection (CAUTI): Significant *in vitro* characterizations

Payal Roy [a,1], Rupam Saha [a,b,1], Justyna Pawlik [c], Zuzanna Samol [c], Michał Dziadek [c], Katarzyna Cholewa-Kowalska [c], Jui Chakraborty [a,b,*]

[a] Bioceramics and Coating Division, CSIR-Central Glass and Ceramic Research Institute (CSIR- CGCRI), 196, Raja S. C. Mullick Road, Kolkata, 700 032, India
[b] Academy of Scientific and Innovative Research (AcSIR), Ghaziabad-201002, India
[c] Faculty of Materials Science and Ceramics, Department of Glass Technology and Amorphous Coatings, AGH University of Krakow, 30 Mickiewicza Ave., 30-059, Krakow, Poland

ARTICLE INFO

Handling Editor: Dr P. Vincenzini

Keywords:
CAUTI
Bacterial adhesion study
Antimicrobial potency
MBGCo based coating
Coating adhesion study
Sol gel EISA

ABSTRACT

Catheter associated urinary tract infections (CAUTI) contributes to about 75 % of nosocomial urinary tract infections (UTI) and the risk potential is further escalated upon prolonged usage of the urinary catheter. Additionally, there is an increased risk for bloodstream infection from urinary source resulting in neutropenia and plethora of renal diseases. Over the past decades, numerous antibiotics/antimicrobial agents have been surface functionalized on catheter tubes but none proved effective owing to biofilm's tolerance. Further, in case of the indwelling urinary catheters, a thin fibrous capsule develops around the catheter, with no adhesion of the epithelial tissue. Additionally, recent reports of Co based bioactive glass exhibited potent antimicrobial action on both *E. coli*, *P. aeruginosa* (gram negative) and *Candida albicans* (fungus) which are primary causative organisms for CAUTI.

In view of the above, we propose to fabricate a Co containing antimicrobial mesoporous bioactive glass (MBGCo) coated indwelling urinary catheter tubing, followed by its *in vitro* material (XRD, TG-DSC, FTIR, FESEM, BET and water contact angle determination), *in-vitro* bioactivity study and biological characterization (*in-vitro* cell cytotoxicity, antibacterial, antifungal studies, initial bacterial adhesion study etc.) of MBGCo coated urinary catheter tubing, along with antimicrobial studies and optimization of the same to obtain a preliminary prototype that is expected to address the issues of the existing urinary catheters.

1. Introduction

Catheters are susceptible to microbial accumulation; a multispecies biofilm can form, causing serious infections [1–4]. Foley catheters are most susceptible to infection because bacteria can accumulate and grow rapidly over time if left unnoticed. This infection is called catheter-associated urinary tract infection (CAUTI), which has stimulated research into antimicrobial materials for urinary catheters. Catheter-associated urinary tract infections (CAUTIs) account for approximately 75% of hospital-acquired urinary tract infections (UTIs), and the risk increases further with prolonged urinary catheter use [4–6]. A significant factor in the risk of CAUTI is the length of the catheterization. The likelihood of an infection occurring as a result of the catheterization increases with time [6]. Garibaldi et al. claim that [7] for every day the catheter is in the body, the risk of developing bacteremia rises by 5%; by the tenth day, 50% of patients develop CAUTI, and by day 30, 100% of patients contract infection. In addition, there is an increased risk of urinary tract infections, which cause neutropenia and many kidney diseases. In recent decades, many antibiotics/antimicrobial agents have been functionalized on the surface of catheter tubes, but none have been shown to be effective due to biofilm tolerance [8–10]. In addition, indwelling catheters develop a thin

* Corresponding author. Bioceramics and Coating Division, CSIR-Central Glass and Ceramic Research Institute (CSIR- CGCRI), 196, Raja S. C. Mullick Road, Kolkata, 700 032, India.
E-mail address: jui@cgcri.res.in (J. Chakraborty).
[1] Rupam Saha(Co-first author) has equal contribution to the manuscript as Payal Roy.

https://doi.org/10.1016/j.ceramint.2024.01.065
Received 11 October 2023; Received in revised form 26 December 2023; Accepted 4 January 2024
Available online 23 January 2024

Please cite this article as: Payal Roy et al., *Ceramics International*, https://doi.org/10.1016/j.ceramint.2024.01.065

Materials Chemistry and Physics 320 (2024) 129416

Contents lists available at ScienceDirect

Materials Chemistry and Physics

journal homepage: www.elsevier.com/locate/matchemphys

Synthesis and *in-vitro* evaluation of Zr-doped radiopaque bioactive glass: A possible biomaterial for endodontic application

Rupam Saha [a,b], Payal Roy [a], Jui Chakraborty [a,b,*]

[a] CSIR-Central Glass and Ceramic Research Institute, Jadavpur, Kolkata, 700 032, India
[b] Academy of Scientific and Innovative Research (AcSIR), Ghaziabad, 201002, India

HIGHLIGHTS

- As-Prepared Zr-BG exhibits optimum radiopacity needed for endodontic applications.
- Zr-BG composition as above is cyto-compatible and aids in cell proliferation.
- Zr-BG is able to promote matrix mineralization that would be beneficial for dentin repairment process.
- Zr-BG promotes cell migration that could be useful for pulp repair.
- Zr-BG suppresses the bacterial growth synergistically owing to the presence of Zr^{4+} and Ag^{+} in the composition.

GRAPHICAL ABSTRACT

ARTICLE INFO

Keywords:
In situ radiopacity
Antibacterial potency
Endodontic application
Sol-gel
Multifunctional bioactive glass
Pulp capping

ABSTRACT

We have synthesized a sol-gel derived multifunctional silicate based bioactive glass composition[(70-x)SiO_2-(30-y-z)CaO-xB_2O_3-yAg_2O-zZrO_2,wherein 1<x < 5,0.5<y < 2,0.005<z < 2 mol%] with radiopacity and antibacterial potency, for possible endodontic applications such as vital pulp therapy of paediatric population worldwide with a prevalence of dental caries and primary tooth decay. The composition was physicochemically characterized by X-ray Diffraction (XRD), Field Emission Scanning Electron Microscopy –Energy Dispersive X-ray Analysis (FESEM-EDX), Fourier Transform Infrared Spectroscopy (FTIR), and ThermoGravimetric analysis –Differential Scanning Calorimetry (TG-DSC). The textural properties were measured by Brunauer-Emmett-Teller (BET) surface area measurement and N_2 adsorption/desorption study. Next, the *in-vitro* bioactivity was assessed by soaking the sample in simulated body fluid (SBF).Apart from these, the *in-vitro* biological properties were assessed by performing cell migration assay, MTT[(3-[4,5-dimethylthiazol-2-yl]-2,5 diphenyl tetrazolium bromide] colorimetric assay for cytotoxicity and proliferation assay, matrix mineralization assay on a embryonic fibroblast cell line which can differentiate into other type of cells depending upon the medium. *In vitro* antibacterial assay was performed on a gram + ve *streptococcus.sp.* bacterial strain which is the most susceptible oral bacteria and *in situ*

* Corresponding author.
E-mail address: jui@cgcri.res.in (J. Chakraborty).

https://doi.org/10.1016/j.matchemphys.2024.129416
Received 24 January 2024; Received in revised form 10 April 2024; Accepted 30 April 2024
Available online 7 May 2024
0254-0584/

Journal of Drug Delivery Science and Technology 66 (2021) 102830

Contents lists available at ScienceDirect

Journal of Drug Delivery Science and Technology

journal homepage: www.elsevier.com/locate/jddst

Looking into the possibilities of cure of the type 2 diabetes mellitus by nanoparticle-based RNAi and CRISPR-Cas9 system: A review

Payal Roy, Suman Saha, Jui Chakraborty *

CSIR- Central Glass & Ceramic Research Institute, 196, Raja S. C. Mallick Road, Kolkata, 700 032, India

ARTICLE INFO

Keywords:
Type 2 diabetes mellitus
Ominous octet
GWAS
Chitosan nanomicelle
Nanoparticle-based RNAi therapy
CRISPR-Cas9

ABSTRACT

Hyperglycemia is the hallmark of T2DM, related to many candidate genes, e.g., MAPK4, GCKR, STAT3, SOCS3, PTPN1 and PEPCK. To detect new variants of the susceptible genes related to T2DM, a genome-wide association study (GWAS) is being undertaken as well. The existing treatments are unable to address the root cause of the disease at the genetic level and in this regard, the concept of RNAi and most recently, the invention of CRISPR-Cas9 system holds a huge promise and paves a new direction in the treatment strategy of the disease at the genetic level, with a possibility for complete cure, although, issues like low efficiency and off-target problems have impeded their applicability. Additionally, the target-specific delivery using viral carriers also poses serious safety issues. Hence, the current scenario underscores the need for suitable nanocarriers for delivery of the above payloads to the target site and in the present narrative review, we attempt to draw the current understanding of RNAi on the T2DM treatment with the help of nanoparticle encapsulated *anti*-miR, siRNA, shRNA delivery, also nanoparticle-based CRISPR-Cas9 delivery, to explore the prospect of the complete cure of the disease.

1. Introduction-

The incidence of diabetes is an important global issue nowadays and the number of affected patients worldwide is expected to be over 400 million adults by 2030 [1,2]. T2DM is often called 'lifestyle disease' and is linked with obesity and lack of physical activity [3], leading to disruption of glucose homeostasis, affecting several vital organs, including liver, kidney, brain, skeletal muscles, adipose tissue, pancreatic α and β cells, and GI tract, altogether referred as 'ominous octet' by Dr. R.A. DeFronzo [4]. To control T2DM, patients have to take time to time medicines, diet and should follow the right lifestyle which might be difficult to continue life-long. Often patients miss taking medicines which in turn, might fluctuate their plasma glucose level significantly [5]. Hence, controlling the disease by such conventional medications is difficult and they are unable to address the root cause of the same at genetic level.

In view of the above, medical research is underway, looking into new directions of the T2DM treatment strategy at the genetic level, based on the molecular mechanism of the candidate gene expression, followed by regulation of the same, as per requirement [6]. The pathogenesis of T2DM is regulated by many genes, including the candidate genes, MAPK4, STAT3, SOCS3, PTPN1 genes are upregulated leading to TNF-α and IL-6 mediated insulin resistance and blockade of insulin and leptin signalling. Additionally, the upregulation of PGC1A, PEPCK, CRTC2, TRIB3, TSC22D4, adiponectin, and GCGR genes, etc., are related to gluconeogenesis, and they are the negative regulator of insulin signalling pathway intermediate, Akt [7–9].

In gene therapy, RNAi leads to knock down of the causative gene of the chronic disease, thereby taking care of the gene expression. It comprises a class of small non-coding RNA molecules that are directly involved in the pathogenesis of the disease and are emerging key factor for biological processes [10]. The excitement surrounding RNAi encompasses the delivery of the exogenous RNAi-based therapeutics, e.g., mature siRNA and short hairpin (shRNA) molecules, to reduce the expression of a causative target gene, in another way, endogenously circulating upregulated miRNAs that are involved in T2DM are also targeted for silencing via administration of an antagonist of the particular miRNA [11]. The miRNA functions as post-transcriptional suppressors, and are commercially available as miRNA-mimics [11,12] whereas the synthetic dsRNAs (siRNA, shRNA) are exogenously administered and the siRNAs are available as duplex RNAs [13]. The shRNAs undergo DICER processing, an endoribonuclease that can cleave the double-stranded RNA into small fragments [14], which activates a catalytic component of RNA-induced silencing complex (RISC) that can

* Corresponding author.
E-mail address: jui@cgcri.res.in (J. Chakraborty).

https://doi.org/10.1016/j.jddst.2021.102830
Received 24 March 2021; Received in revised form 26 August 2021; Accepted 27 August 2021
Available online 28 August 2021
1773-2247/

c0010 Mesoporous silica-biopolymer-based systems in drug delivery applications

10

Suman Saha, Payal Roy and Jui Chakraborty
Bioceramics and Coating Division, CSIR-Central Glass & Ceramic Research Institute, Kolkata, India

s0010 10.1 Introduction

p0010 Since the late 20th century, mesoporous silica materials have gained considerable attention after unearthing the recent family of molecular sieve identified as M41S (Yang, Gai, & Lin, 2012). Further MCM-41, MCM-48, and SBA-15 are the most common mesoporous silica materials having a 2D-hexagonal and 3D-cubic structural property with the pore size in the range between 2 and 10 nm. Zhao, Sun, Li, and Stucky (2000) inflated the scope of these molecules further by synthesizing the materials with bigger pore size of around 30 nm. Eventually, these inorganic nanoparticles have gained considerable interest in the area of drug delivery during the last few years. The first reported mesoporous silica material that was used in drug delivery system is MCM-41 in the year 2001 (Vallet Regi, Ramila, Del Real, Pérez, & Pariente, 2001). Further many research teams explored the mesoporous silica materials as excellent carriers for drug delivery owing to their intrinsic textural properties that enable them to load higher amount of drug molecule inside the pore channel structure. Among those mesoporous silicas, MCM-41 and SBA-15 contain a honeycomb-like porous structure with empty channels that can encapsulate large amounts of bioactive molecules. The unique properties of high surface area (N900 m^2/g), large pore volume (N0.9 cm^3/g), and tunable pore size with a narrow distribution (2−10 nm) make them appropriate for various controlled release applications (Slowing, Vivero-Escoto, Wu, & Lin, 2008). On the other hand, mesoporous silica nanoparticles (MSNs) protect the drug molecule from premature release and unwanted degradation in stomach and intestines before reaching the target organs. Moreover, their excellent biocompatibility, controllable particle size, and ease of surface modification that makes them promising candidates for various biomedical applications and as effective carriers for numerous therapeutic agents for various diseases including cancer (Lu, Liong, Li, Zink, & Tamanoi, 2010), diabetes (Zhao, Trewyn, Slowing, & Lin, 2009), and inflammation (Liong, Lu, Tamanoi, Zink, & Nel, 2018; Lozano et al., 2010; Moulari, Pertuit, Pellequer, & Lamprecht, 2008; Poorakbar et al., 2018; Suwalski et al., 2010; Zhu, Wang, et al., 2011). To prevent

Tailor-Made and Functionalized Biopolymer Systems. DOI: https://doi.org/10.1016/B978-0-12-821437-4.00002-5

Bera-TFBS-1632744 978-0-12-821437-4 00002

S/W Developed by Computer Section and
Database Managed by IPR Cell

CENTRAL GLASS AND CERAMIC RESEARCH INSTITUTE

196 RAJA S C MULLICK ROAD KOLKATA-700 032
IPR CELL

Patent Search Result

FILENO 307 REFNO 0167NF2021 APPNO 202111046618 PATNO COUNTRY INDIA

INVENTOR(S) J CHAKRABORTY
S SAHA
P ROY
R SAHA

TITLE: ANTIBACTERIAL BIOACTIVE GLASS MICRONANOFIBRE COMPOSITION AND PROCESS FOR PREPARTION THEREOF

Date of

COMMUNICATION 28/09/2021 PUBLICATION : SEAL :
FILING : 12/10/2021 ACCEPTANCE : RENEWAL :

ABSTRACT

It is known that the chronic wounds fail to proceed through the normal process of wound healing and often stall in the inflammation phase of healing. Examples of Chronic wounds are categorized into diabetic foot ulcers, venous leg ulcers, arterial insufficiency and pressure ulcers. Some of the most common complications include infection, tissue necrosis, periwound dermatitis etc. There are many problems related to the published prior arts as well as market available dressing materials and matrices. The existing prior art focusing on the borate bioactive glass, having a chance of toxicity. The processing methods described by other prior art, are time-consumiing, as well as complicated steps. The market available dressing materials also exhibits lot of problems related to adherence to wound, cannot give protection from bacterial infection fail to maintain an optimal moisture environment, may be immunogenic.

The proposed invention can address the above mentioned problems in many ways. From the processing point of view, it is much simpler and take less time, readily prepare the final solution for electrospinning which is advantageous from the industrial view point. In this innovation, an FDA approved water soluble polymer is used for achieving an optimal rheological property. The final product is effective for wound healing and take much less time (15 days) toclose the open wound and not showing any local signs of local toxicity (edema, erythema etc.) and also helps in tissue regeneration.

The complete specification filed on 28/09/2022
U'll get priority date from 12/10/2021

Payal Roy
24.01.2023.

1/11/22

669

Tele: 23818132
Fax: 23902719

No. ERIP/IP/2201058/M/01
Ministry of Defence
Defence R&D Organisation
Dte of ER & IPR, IPR Group
V[th] Floor, DRDO HQrs Annexe
Metcalfe House, Civil Lines
New Delhi -110 054
Dated 10 Oct 2022

The Member Secretary
LSRB
IV[th] Floor, DRDO HQrs Annexe
Metcalfe House, Civil Lines
New Delhi -110 054

Subject: FILING OF PATENT APPLICATION

A patent application on the following invention has been filed with Indian Patent Office, New Delhi Jointly in the name of Chairman, DRDO & CSIR.

"A Bioactive Glass Composition and a Process thereof"

2. The following have been named as the inventors for the above mentioned invention:

Inventor from INMAS, Delhi

(i) Dr. Pooja Srivastava

Inventors from CSIR, Kolkata

(i) Dr. Jui Chakraborty
(ii) Ms. Payal Roy
(iii) Mr. Suman Saha
(iv) Ms. Rupam Saha

3. The above application has been accorded **202211057220** as application number.

4. A copy of this letter may please be given to the concerned scientists for their record/retention.

Romi 10/10/22

(Romi Sinha)
Assoc. Director (IPR)

Dr Archana
Pl send a copy to all
inventors

12/10

Payal Roy
24.01.2023.

Welcome Dr Seema Sign out

Controller General of Patents, Designs & Trade Marks

सत्यमेव जयते

INTELLECTUAL PROPERTY INDIA
PATENTS | DESIGNS | TRADE MARKS
GEOGRAPHICAL INDICATIONS

G.A.R.6
[See Rule 22(1)]

RECEIPT

Docket No 50356

Date/Time 2022/05/17 12:23:00

Dr Seema Innovation Protection Unit (IPU), CSIR
NISCAIR Building 3rd Floor 14 Satsang Vihar Marg
Email: seema.ipu@niscair.res.in

Sr. No.	Ref No./Application	App. Number	Amount Paid	CBR No.	Form Name	Fee Payment	Remarks
1	202211028466	TEMP/E-1/26211/2022-DEL	8000	18784	FORM 1	Full	A PROCESS FOR THE SYNTHESIS OF A POLYMER–CERAMIC/BIOACTIVE GLASS COMPOSITE MATERIAL WITH BIODEGRADABLE AND ANTIMICROBIAL PROPERTIES

Transaction ID	Payment Mode	Challan Identification Number	Amount Paid	Head of Acc. No.
N-0000965965	Online Bank Transfer	1705220007619	8000.00	1475001020000001

Total Amount : ₹ 8000.00
Amount in Words: Rupees Eight Thousand Only

Received from Dr Seema the sum of ₹ 8000.00 on account of Payment of fee for above mentioned Application/Forms.

* This is a computer generated receipt, hecnce no signature required.

Print

Payal Roy.
24.01.2023.

Home About Us Contact Us

Welcome Dr Seema Sign out

Controller General of Patents, Desigos & Trade Marks

सत्यमेव जयते

INTELLECTUAL PROPERTY INDIA
PATENTS | DESIGNS | TRADE MARKS
GEOGRAPHICAL INDICATIONS

G.A.R.6
[See Rule 22(1)]
RECEIPT

Docket No 11280

Date/Time 2022/02/02 15:15:00

Dr Seema Innovation Protection Unit (IPU),
CSIR NISCAIR Building 3rd Floor I4
Satsang Vihar Marg Email:
seema.ipu@niscair.res.in

1	202211005734	TEMP/E-1/4985/2022-DEL	8000	4132	FORM 1	Full	In situ Radiopaque Bioactive Glass and its composition thereof

N-0000916333	Online Bank Transfer	0202210012358	8000.00	1475001020000001

Total Amount : ₹ 8000

Amount in Words: Rupees Eight Thousand Only

Received from Dr Seema the sum of ₹ 8000 on account of Payment of fee for above mentioned Application/Forms.

* This is a computer generated receipt, hecnce no signature required.

Home About Us Contact Us

Payal Roy.
24.01.2023.